

UC Riverside

UC Riverside Electronic Theses and Dissertations

Title

Design and Charge-Transfer Properties of Bioinspired Electrets

Permalink

<https://escholarship.org/uc/item/0kw3s2z5>

Author

Bao, Duoduo

Publication Date

2013

Peer reviewed|Thesis/dissertation

UNIVERSITY OF CALIFORNIA
RIVERSIDE

Design and Charge-Transfer Properties of Bio-inspired Electrets

A Dissertation submitted in partial satisfaction
of the requirements for the degree of

Doctor of Philosophy

in

Bioengineering

by

Duoduo Bao

March 2013

Dissertation Committee:
Dr. Valentine I. Vullev, Chairperson
Dr. Bahman Anvari
Dr. Mihri Ozkan

Copyright by
Duoduo Bao
2013

The Dissertation of Duoduo Bao is approved:

Committee Chairperson

University of California, Riverside

ACKNOWLEDGEMENTS

I greatly appreciate my advisor, Dr. Valentine I. Vullev's guidance, advice, encouragement, and friendship in my graduate school. I feel so blessed that I can work with him. He is such a positive person that he never lets me down, and he never gives up on me. I appreciate the time and energy he put on me in order to figure me as a scientific researcher. As a great mentor, he not only trained me how to do experiments in lab, but also shaped me as an effective communicator in interacting with other researchers. He corrected my dissertation line by line and wrote commences as detailed as possible; he did the same to all my manuscripts and proposals, too. He is such a considerate teacher that he always motivates me with heartwarming words. All he passed to me is encouragement and positive feedback. Dr. Vullev is also a knowledgeable friend. I enjoyed every conversation with him. I will keep his scientific guidance and professional advice and imply them as guidelines in my career.

I would like to thank Dr. Bahman Anvari for providing valuable advice, comments, and time during serving on the guidance, qualifying, and dissertation committees. I want to thank Dr. Mihri Ozkan for her encouraging words, patient guidance and for serving as my oral qualifying exam committee and dissertation defense committee. Special thanks to Dr. Roger Lake served as a member of my oral qualifying exam committee and his research group for great help in theoretical calculations of bioinspired electrets. I want to thank Dr. Jerome Schultz for strong financial supports and helpful discuss in my research. I appreciate him for being my qualifying exam committee member. As a distinguished

professor, he sets great example of being successful. A special thanks to Dr. Jane Schultz for hosting welcome parties for graduate students. These parties are so cozy and amazing that I felt the whole department is a big family.

A special thanks to our current department Chair Dr. Victor G. J. Rodgers for his hard work in organizing Bioengineering Interdepartmental Graduate (BIG) program. A special thanks to Dr. Demitrios Morikis for his time and consideration in helping my academic and career affairs. Thanks to Dr. Julia Lyubovitsky, Dr. Huinan Liu, Dr. Jiayu Liao and Dr. B. Hyle Park for their helpful advice and encouragement in my research and career affairs. Thanks to Dr. Gregory Beran at Chemistry Department for strong supporting in collaborations of theoretical calculations in quinone project. Thanks to staffs in Analytical Chemistry Instrumentation Facility at Chemistry Department, UCR. Great thanks to Dr. Dan Borchardt and Mr. Yi Meng for their guidance and training in using NMR facilities. A special thanks to Graduate Division, especially Dean Dr. Joseph Childers at UCR for supporting my graduate study here.

A special thanks to Ms. Denise Sanders, our department office manager and my school 'Mom'. She helped me to start my first day at UCR and she is always patient to help me out. She has been the most impressive woman I've seen in my life. Thank Ms. Crissy Reising, Ms. Corena Valencia-McBride, Ms. Jennifer Morgan for their tremendous work to support my research. Without them, I even could not attain a bottle of ethanol. They are awesome in doing their jobs. A special thanks to Ms. Hong Xu, our department engineer. She is smart, handy, decisive, and supportive. I would like thank

her for working so hard to ensure lab safety. I enjoyed the time spending with her and I appreciate friendship from her.

I would like to thank all my friends at UCR. Thanks for their support in my research and for the happy times I have been had with them.

Special thanks to Dr. Daniel T. Gryko, Dr. Dorota Gryko and their research group members in the Institute of Organic Chemistry of the Polish Academy of Sciences for their enormous guidance to train me as a real chemist in organic chemistry field. Thank Dr. Gryko for all the time and efforts he put on me. I had a wonderful lab time and amazing experiences in Warsaw. I greatly appreciate the time and energy that Dr. Jan P. Lewtak, my lab mate in Dr. Gryko's group, put on me. He is my 'Shifu' in the lab who taught me hand by hand with each synthetic reactions; he is a perfect friend who shared home-made Pierogi and Bigos with me; he is a patient language teacher who taught me Polish and practice with me every day. Special thanks to Mr. Jan Klajn, Dr. Roman Voloshchuk, Dr. Olena Vakuliuk, Dr. Beata Koszarna, Dr. Joanna Piechowska, Ms. Jin Li for all their friendly help while I was in Warsaw. I could not have such a great time there without their help. The experience will always shine in my whole life and warm my heart whenever I think of them all.

I would like to thank all Vullev research group members I worked with. A special thanks to former lab member and my great friend Dr. Wei Xia for his selfless help in the lab. Wei has been such a professional and smart man and he always set high standards for us to follow. The time I spent with him was not long but was cheerful. A special thanks

to Dr. Marlon Thomas, my academic brother, for his help in my research and strong support with my job-hunting. I am grateful for helpful discussion, suggestions and productive cooperation of Dr. Jiandi Wan from Princeton University and Dr. Bing Xia from Boston University in my research. A special thanks to my current lab member and a great friend, Mr. Srigokul Upadhyayula for his great support in my research and personal life. I will always remember the friendship, the time I spent with him. He is such a great person and charming man. I also want to thank my lab members Dr. Sharad Gupta, Mr. Jacob Vasquez, Mr. Vicente Nunez, Ms. Jill Larsen for their supports whenever I needed.

A special thanks to undergraduate researchers who assisted me to carry out projects including but not limiting in microfluidic devices, electrochemical studies, photophysical measurements and organic synthesis. They are Ms. Amy Ferreira, Ms. Connie Hong, Ms. Elizabeth Zielins, Ms. Sangeetha Ramu, Ms. Anam Qureshi, Ms. Krystal Vasquez, Mr. Brent Millare, Mr. Joseph Matthew Clift, Mr. Alex Gerasimenko, Mr. Benjamin Steyer, Mr. Robert Bonderer, Mr. Stephen Bishop, Mr. Andy Chang, Mr. Kenny Chau, Mr. Antonio Contreras, Mr. Taifeng Zhao, Mr. Trevor Vandergrift, Mr. Jason Larkin, Mr. Ricardo Jara Castro, and Mr. Chongguang Lin. A special thanks to Ms. Wardah Bari, Ms. Paulina Perlin and Mr. Daniel Bromberg, who were high school students and worked with me in doping of chromophores in polydimethylsiloxane in their summer breaks. A special thanks to Ms. Borianna Georgieva, a chemistry teacher from Swampscott High, MA for helping me with electrochemical measurements.

A special thanks to my best friends Dr. Prashanthi Vandrangi from UCR, Dr. Yan Liu from Shanghai Jiaotong University, and Dr. Xiaobo Sun from Beihang University for their friendship and support in my life.

Very special thanks to Dr. Robert I. Krieger, a great mentor in my life. Thank him for all the professional advice, sincere suggestion and strong recommendation to help me with my career-starting. A special thanks to Ms. Ana Krieger for giving so much sincere advice to help me land on US life and for No. 1 ‘Mom-made’ food that I have ever had.

I want to thank my parents-in-law, Mr. Guangtian Chen and Ms. Xiuhua Li for all their essential supports throughout my life. I greatly appreciate them visiting me in Riverside and taking care of my baby son and family. During their visiting I focused more on my research since I had supportive parents at home. They helped and they never complained. They are the greatest parents-in-law in the world.

I want to thank my parents, Mr. Changsu Bao and Ms. Youlan Xia, for bringing me to this wonderful world, for growing me up healthy and happily, for their forever supports and love. A special thanks to my grandfather, Mr. Guotong Bao for taking care of me when I was young, educating me to be a lady I am now and encouraging me to pursue my Ph.D. degree. I know I mean a lot to him and he means the same to me. Thanks to my sisters, Ms. Lilin Zhu, Ms. Yuxiao Luo, Ms. Xiaoxiao Bao and my brother, Mr. Fazhe Bao for their great support in my life. They initially taught me what is responsibility and they are my driving force to move forward. Life is so precious especially having all my

dear siblings with me. Thank all the people living in my small village who love me and I love. I will keep on going to be proud of them.

A special thanks to my son Darren B. Chen, the best reward in my life. His smile encourages me to overcome difficulties and to bear hard times. He is my 'Gibbs energy' that pushes me to move forward. He is the love of my life. Finally, I want to thank another love in my life who always supports me with his strength and smile. This one is my husband, Dr. Zhenshan Chen. Thank you, dear, for being there whenever I need you.

With love, life is so good. Thank you all!

ABSTRACT OF THE DISSERTATION

Design and Charge-Transfer Properties of Bio-inspired Electrets

by

Duoduo Bao

Doctor of Philosophy, Graduate Program in Bioengineering
University of California, Riverside, March 2013
Dr. Valentine I. Vullev, Chairperson

In order to develop and demonstrate fundamental strategies for improving the efficiency of photovoltaic devices that are commonly used for solar-energy capture and conversion, we introduced and studied anthranilamides as bioinspired electrets.

Charge transfer processes play a key role in chemical and biological systems. Photoinduced charge transfer represents the central paradigm of light-energy conversion of photosynthesis and photovoltaic devices. The Rehm-Weller equation allows for estimating the driving force of photoinduced charge transfer by employing readily measurable quantities such as the redox potentials and spectroscopic data of electron donors and acceptors. A significant part of my studies focused on the Born solvation term in the Rehm-Weller equation that introduces the electrostatic stabilization of the charge-transfer species by the surrounding media. Cyclic voltammetry, allowed me to demonstrate experimentally the effects of the supporting electrolyte on the redox potentials. These effects were especially pronounced for non-polar solvents. Most importantly, I devised an approach to address the discrepancies that the presence of electrolyte introduces to the charge-transfer analysis. Concurrently, my studies

demonstrated that the Generalized Born model allows for addressing the deficiencies in the charge-transfer analysis involving redox species that are not spherical and that have heterogeneous charge distribution.

The other significant part of my studies focused on anthranilamides as bioinspired electrets that have the potential to accelerate charge separation and suppress the undesired charge recombination. My research provided the first experimental demonstration that the anthranilamides possess intrinsic dipoles. These amides with large intrinsic dipole moments (that is, electrets) can generate electric field, which enhances electron transfer from their N- to their C-termini and impedes it in the backward direction. To test the ability of the electrets to modify the direction of electron transfer, I incorporated an anthranilamide monomer in electron donor-acceptor (DA) dyads. Comparison between the charge-transfer kinetics of electret-acceptor dyads, revealed a faster initial photoinduced charge separation and a slower charge recombination when electron was transferred toward C-terminus. These findings were consistent with the orientation of the intrinsic dipole moment of the anthranilamide monomer. Aside from previous work employing polypeptides, this is the first demonstration of rectification of charge transfer by dipole moments of synthetic bioinspired derivatives.

In summary, the most important contributions from my doctoral work were: (1) developing methods for reliable interpretation of experimental results pertinent to charge-transfer kinetics and thermodynamics; (2) demonstrating rectification of photoinduced charge transfer induced by the anthranilamide intrinsic dipole; and (3) demonstrating that the photoinduced processes result in charges residing on the

anthranilamides (i.e., radical ions) which is essential for attaining hopping mechanism for long-range charge transfer.

Contents

Chapter 1. Introduction: Solar-Energy Conversion and Moving the Focus from Biomimetic to Bioinspired.....	1
Energy consumption	2
Solar energy conversion technology	2
Photoinduced charge transfer	3
Photoinduced charge transfer modified by intrinsic electric field	6
Photoinduced charge transfer rectified by bioinspired electrets	8
Chapter 2. Electrochemical Oxidation of Ferrocene Manifests a Strong Dependence on the Concentration of the Supporting Electrolyte for Solutions of non-Polar Solvents.....	22
Abstract	23
Keywords	24
Introduction	25
Results and Discussion	28
Redox properties of ferrocene	28
Dielectric properties of CH ₂ Cl ₂ electrolyte solutions	29
Correlation between oxidation potential and dielectric constant	30
Redox behavior of Fc in dilute electrolyte solutions	31
Prediction of the oxidation potential of ferrocene for neat solvents	35
Reduction potential of Ph-ANI	38
Implications for charge-transfer studies	39
Conclusions	42
Experimental	43
References	46

Chapter 3. Electrochemical Reduction of Quinones: Interfacing Experiment and Theory for Defining Effective Radii of Redox Moieties	62
Abstract	63
Keywords	63
Introduction	64
Results and Discussion	67
Accounting for solvation in redox processes	67
Quinone reduction	69
Polarity of the electrolyte solutions	72
Correlation between reduction potentials and solvent dielectric properties.....	73
Theoretical values of the effective radii	77
Interfacial properties of the working electrode	78
Generalized Born approach	80
Implications of effective radii for the analysis of charge-transfer systems.....	86
Conclusions	87
Experimental	88
References	92
Chapter 4. Anthranilamides as Bioinspired Molecular Electrets: Experimental Evidence for Permanent Ground-State Electric Dipole Moment	117
Abstract	118
Introduction	119
Results and Discussion	121
Conclusions	134
Experimental	135
Supporting Information	142
References	143

LIST OF TABLES

Chapter 2

Table 2-1. Half-wave oxidation potentials of ferrocene, $E_{\text{Fc}^+/\text{Fc}}^{(1/2)}$, for different solvents in the presence of various concentrations of TBATFB.....	49
Table 2-2. Dielectric constants, ϵ , of CH_2Cl_2 solutions containing TBATFB with different concentration.	50
Table 2-3. Extrapolated half-wave oxidation potentials of ferrocene, $E_{\text{Fc}^+/\text{Fc}}^{(1/2)}$, for neat dichloromethane (CH_2Cl_2), acetonitrile (MeCN) and dimethylformamide (DMF). ^a	51

Chapter 3

Table 3-1. First half-wave reduction potentials of quinones, $E_1^{(1/2)}$, for chloroform electrolyte solutions with different concentrations.....	104
Table 3-2. Effective radii of quinones obtained from electrochemical data and from <i>ab initio</i> calculations.....	106
Table 3-3. Generalized-Born effective radius, $R_{\text{eff}}^{(GB)}$, of a hypothetical singly charged molecular ion (Scheme 3) with different charge distribution.....	107

Chapter 4

Table 4-1. Photophysical properties of the anthranilamide oligomers.....	148
Table 4-2. Linear analysis of $\lg(C(1-\zeta))$ vs. $\lg(C\zeta)$, implementing equation 4-3.....	149
Table 4-3. Measured and calculated molar polarizations, P_2 , of the anthranilamide oligomers.	150

List of Schemes

Chapter 3

Scheme 3-1. Quinones used for this study.....108

Scheme 3-2. Analogues of CoQ₁₀ and VK₁ with truncated aliphatic chains with the corresponding CHELPG charges of the non-hydrogen atoms (in atomic units).
.....109

Scheme 3-3. A hypothetical molecular ion with D₄ symmetry composed of five spheres.....110

Chapter 4

Scheme 4-1. Origin of the intrinsic dipole moment of anthranilamides.....151

Scheme 4-2. Anthranilamide oligomers with highlighted hydrogen-bonded (red) and non-hydrogen-bonded (blue) protons.....152

Scheme 4-3. Anthranilamide trimer, h-AAA-ph, with highlighted protons used for establishing the connectivity patterns in the NMR analysis.....153

LIST OF FIGURES

Chapter 1

- Figure 1-1.** Frontier orbital diagrams of donor-bridges-acceptor systems (DBA), mediating photoinduced charge transfer via tunnelling mechanisms.....18
- Figure 1-2.** Frontier orbital diagrams of donor-bridges-acceptor systems (DBA), mediating photoinduced charge transfer via hopping mechanisms.....19
- Figure 1-3.** Frontier orbital diagrams of donor-bridges-acceptor systems (DBA) with local electric field mediating photoinduced charge transfer via hopping mechanisms.....20
- Figure 1-4.** Anthranilamides and the origin of their intrinsic electric dipole moment ...21

Chapter 2

- Figure 2-1.** Cyclic voltammograms for ferrocene (5 mM) in the presence of various concentrations of supporting electrolyte, TBATFB, for different solvents.....52
- Figure 2-2.** Dependence of the half-wave oxidation potential of ferrocene, $E_{\text{Fc}^+/\text{Fc}}^{(1/2)}$, on the concentration of the supporting electrolyte, C_{TBATFB} , for three different solvents.53
- Figure 2-3.** Solvatochromism of Ph-ANI.....54
- Figure 2-4.** Fluorescence properties of Ph-ANI for dichloromethane with various concentrations of electrolyte, TBATFB.....55
- Figure 2-5.** Dependence of the dielectric constant of the electrolyte solutions, ϵ , on the electrolyte concentration.....56
- Figure 2-6.** Correlation between the half-wave oxidation potential of ferrocene and the inverse dielectric constant of dichloromethane solutions with different concentrations of electrolyte.....57
- Figure 2-7.** Comparison between the experimentally measured and the calculated (from equation 2-4) dependence of the half-wave potential of ferrocene, $E_{\text{Fc}^+/\text{Fc}}^{(1/2)}$, on the concentration of the supporting electrolyte, C_{TBATFB} , for acetonitrile.....58
- Figure 2-8.** Dependence of the half-wave oxidation potential of ferrocene on the concentration of the supporting electrolyte.....59
- Figure 2-9.** Electrochemical properties of Ph-ANI.....60

Figure 2-10. Dependence of the charge-separation energy, ΔG_{CS} , on the dielectric constant of the media.....	61
Chapter 3	
Figure 3-1. Dependence of the electrochemical reduction of quinones on the electrolyte concentration for chloroform media.....	111
Figure 3-2. Solvatochromism of the fluorescence of Ph-ANI observed for solvent media with different polarity.....	112
Figure 3-3. Dependence of the quinone first-wave reduction potentials on the inverted dielectric constant of the electrolyte media.....	113
Figure 3-4. CHELPG atomic charges (in atomic units) for each species computed at the B3LYP/aug-cc-pVTZ level.....	114
Figure 3-5. Optimized structures of CoQ ₁₀ and VK ₁ (neutral and singly reduced) with truncated aliphatic chains.....	115
Figure 3-6. Impedance spectroscopy chloroform solutions of Bu ₄ NPF ₆ with different concentrations.....	116
Chapter 4	
Figure 4-1. Absorption and emission properties of the anthranilamide oligomers.....	154
Figure 4-2. Concentration dependence of the emission properties of the anthranilamide oligomers.....	155
Figure 4-3. Dependence of the density, ρ , and the dielectric properties of anthranilamide solutions in chloroform on the oligomer molar fraction	157
Figure 4-4. ¹ H-NMR spectra of the three anthranilamide oligomers with assignments of the peaks corresponding to the amide protons	158
Figure 4-5. ¹ H- ¹³ C gHMBC spectrum of h-AAA-ph	159
Figure 4-S1. ¹³ C NMR spectra of oligoanthranilamide monomer – h-A-ph	160
Figure 4-S2. ¹³ C NMR spectra of oligoanthranilamide dimer – h-AA-ph	161
Figure 4-S3. ¹³ C NMR spectra of oligoanthranilamide trimer – h-AAA-ph.....	162

LIST OF APPENDIX

Appendix	163
Appendix 1. Rectification of Photoinduced Charge Separation and Charge Recombination Induced by Dipole of Anthranilamide	164
Introduction	165
Results and Discussion	167
Synthesis and basic photophysical properties	167
Redox properties and driving force calculation.	168
Charge-Transfer Kinetics	169
Conclusion	172
Experimental	173
References	182
Appendix 2. Print-and-Peel Fabrication of Microelectrodes	200
Abstract	201
Keywords	201
Introduction	202
Research and Results	203
Experimental	205
References	212

MAIN ABBREVIATIONS AND DEFINITIONS

Aa: anthranilamide, 2-hexanamino-*N*-hexyl-5-(piperidin-1-yl)benzamide

Aa-Py: 2-hexanamino-5-(piperidin-1-yl)-*N*-(pyren-1-ylmethyl)benzamide

BHJ : Bulk heterojunction

BQ: 1,4-benzoquinone

Bu₄NPF₆: tetrabutylammonium hexafluorophosphate

CL4BQ: Tetrachloro-1,4-benzoquinone

CL2NQ: 2,3-dichloro-1,4-naphthoquinone

CT: charge transfer

CS: charge separation

CoQ₁₀: coenzyme Q₁₀

CR: charge recombination

CV: cyclic voltammetry

DBA: donor-bridges-acceptor systems

DCM: dichloromethane, CH₂Cl₂

DMF: dimethylformamide

DSSC: dye-sensitized solar cells

h-A-ph: monoanthranilamide, 2-octanamido-*N*-phenylbenzamide

h-AA-ph: dianthranilamide, 2-octanamido-*N*-(2-(phenylcarbamoyl)phenyl)benzamide

h-AAA-ph: trianthranilamide, 2-octanamido-*N*-(2-((2-(phenylcarbamoyl)phenyl)carbamoyl)phenyl)benzamide

HOMO: highest occupied molecular orbital

LUMO: lowest unoccupied molecular orbital

MeCN: acetonitrile, CH₃CN

MePy: 1-methylpyrene

NMR: nuclear magnet resonance

NQ: 1,4-naphthaquinone

PAP: print-and-peel

Ph-ANI: N-phenyl-4-dimethylamino-1,8-naphthalimide

PhCN: benzonitrile

PRC: photosynthetic reaction center

PVs: photovoltaic devices

Py-Aa: *N*-hexyl-5-(piperidin-1-yl)-2-[2-(pyren-1-yl)acetamino]benzamide

QDSSC: quantum-dot-sensitized solar cells

SCE: saturated calomel electrode

TBATFB: tetrabutylammonium tetrafluoroborate

THF: tetrahydrofuran

TICT: twisted intramolecular charge-transfer

TW: terawatts, $1\text{TW} = 10^{12}\text{ W}$

VK₁: vitamin K₁

Chapter 1

Introduction.

Solar-Energy Conversion and Moving the Focus from Biomimetic to Bioinspired

Energy consumption. Currently, global energy consumption is mainly dependent on fossil fuels as a principal energy source.¹ In the United States, for instance, fossil fuels account for 82% of energy production in 2011.² The world energy consumption rate is projected to double from 13.5 TW (1TW = 10^{12} W) in 2001 to 27 TW by 2050 and to triple to 43 TW by 2100. The estimated fossil energy resources can support a 25- to 30-TW energy consumption rate globally. Consumption of fossil energy at this fast rate, however, will produce global issues such as climate change due to CO₂ emissions, high oil prices and peak oil crisis.³ Those issues have raised increasing demands for exploring alternative energy sources. Solar energy, which has the potential to afford energy-production rates of 600 TW, offers a means of sustaining our growing energy needs in an environmentally benign manner.⁴⁻⁶ The utilization is yet limited due to fundamental issues with the conversion and storage technologies. As a result, currently solar contributes less than 0.2% to the total energy production in the USA (based on data for 2011).²

Solar energy conversion technology. Photovoltaic devices (PVs) provide means for capturing solar light and converting it into electrical energy. Cost-competitive PVs for solar-energy-conversion will require either (1) lowering the material cost and the fabrication cost for existing high-efficiency cells, or (2) increasing the efficiency of PVs made of inexpensive materials.^{5,7-9} Bulk heterojunction (BHJ) solar cells, dye-sensitized solar cells (DSSC), and quantum-dot-sensitized solar cells (QDSSC) are some of the excellent candidates for the latter strategy.^{10-14, 15-17}

Most of the processes that govern the device efficiency occur at the material interfaces of these heterogeneous systems. The formation of charge-transfer (CT) excitons, in which

electrons and holes are electrostatically bound across donor-acceptor interfaces, presents a key issue for organic PVs.¹⁸⁻²⁰ Trapped CT excitons have been observed experimentally²¹⁻²⁷ and predicted theoretically.^{28,29} Long-range CT is essential for moving photogenerated electron and hole away from each other to prevent trapping and charge recombination.^{18,30} An increase in the electron-hole binding energy, for example, increases the probability for charge recombination.^{29,31}

Charge recombination, leading to reducing the photocurrents (or the quantum efficiency), is one of the sources of considerable energy loss in PVs.^{32,33} Meanwhile, large driving forces employed for attaining efficient high-quantum-yield CT, reduce the voltage of the PV cells (i.e., open-circuit voltage, V_{oc}).³⁴ By suppressing the undesired back CT and achieving efficient forward CT at relatively small driving forces, rectifying macromolecules and materials will permit PVs to approach their theoretical limits of efficiency.^{32,33}

Photoinduced charge transfer. Photoinduced CT is the vital process in natural photosynthesis that initiates the transduction of absorbed radiation energy into charge flow.³⁵ The principal component of the light harvesting apparatus of higher plants and numerous microorganisms is the photosynthetic reaction center (PRC) where light energy is converted into charge-separated states and where electron entrainment is initiated.³⁶ The predominant secondary structure of PRC transmembrane proteins is α -helices spanning along the CT pathways.³⁷ The helices provide various modes of electronic

coupling essential for CT, and electrostatic fields generated by helix intrinsic dipoles that influence significantly on charge entrainment.³⁸

Tunneling and hopping are the mechanisms by which electrons transfer from donors to acceptors. In tunneling, or superexchange charge transfer, electrons move via the virtue of weak overlaps of the evanescent components of the donor and acceptor wave functions (Figure 1-1). These overlaps are most significant along covalent bonds. Although the antibonding orbitals are energetically inaccessible for the transferred electrons, they provide spatial passages with lower potential barriers. That is, the electron moves along virtual states that are within the highest occupied molecular orbital (HOMO)–lowest unoccupied molecular orbital (LUMO) gap (or the bandgap) of the molecular chains that connect the donor and the acceptor. This non-adiabatic mechanism of CT is prevalent for biomolecular systems because the redox potentials of the connecting groups are either too large or too low to inject charges into them, i.e., they are electrical insulators. A principal drawback of quantum mechanical tunneling is its distance limitations, i.e., electron-tunneling rates fall off exponentially with the increase in the donor-acceptor distance. As a result, efficient electron tunneling through proteins and other biomolecules is limited to about two nanometers.^{39, 40,41}

If charges have to be transferred farther than this range, multiple short tunneling steps are involved, i.e., the electrons or holes hop along redox active sites situated between the donor and the acceptor (Figure 1-2). Chains of redox cofactors in the PRCs and the respiratory mitochondrion chain provide a means for long-range electron transduction. Similarly, easily oxidizable bases of DNA strands, e.g., guanine, G ($E_{ox} = 1.2$ V vs SCE),

and adenine, A ($E_{ox} = 1.7$ V vs. SCE), provide a means for hole hopping at distances exceeding 4 nm.^{42,43} In electron hopping, an electron from the LUMO of the photoexcited donor is injected into the LUMO of the nearest redox moiety. Then the electron moves along the LUMOs of the moieties bridging the donor and the acceptor to eventually reach the LUMO of the acceptor (Figure 1-2a). In hole hopping, an electron is extracted from the HOMO of the moiety nearest to a photoexcited acceptor and a sequence of short electron transfer steps between neighboring redox sites provide the means for the generated positive charge, i.e., the hole, to migrate toward the donor (Figure 1-2b).

Numerous processes with pronounced efficiency can compete with the photoinduced long-range CT. For example, radiative (e.g., fluorescence) and non-radiative decays of the photoexcited donor or acceptor (also referred to as sensitizers) can suppress the initial photoinduced charge-separation step needed for injecting an electron or a hole in the bridging moieties. Ultimately, the photoinduced multiple steps should store the absorbed energy in the form of long-lived long-range CT states that will allow the electrons to be collected from the LUMO of the reduced acceptor and the holes from the HOMO of the oxidized donor.

Local electric fields, generated by molecular dipoles, have the unexplored potential to control the discreet charge-transfer steps essential for light-energy harvesting. Larger rectification is expected for the hopping, in comparison with tunneling processes, because of the numerous energetically unfavorable steps along the bridge when the electric field is co-directional with the CT. For such systems we expect the elimination of back CT in HUMOs (electron hopping) or LUMOs (hole hopping) from one bridge molecule to

another (Figure 1-3). Based on the direction of local electric field and CT, the local electric field will also increase (co-direction) or decrease (anti-direction) the driving force for photo-induced charge-transfer processes, $\Delta G^{(0)}$.

Herein, my primary research goal is to demonstrate how molecular dipoles can accelerate the desired forward CT and suppress the undesired charge recombination in CT process. To achieve my research goals I resorted to molecular electrets that are systems with co-directional ordered orientation of electric dipoles, i.e., electrets are the electrostatic analogues of magnets.⁴⁴

Photoinduced charge transfer modified by intrinsic electric field. Polypeptide helices are some of the best known natural electrets. The protein α -helices, for example, possess intrinsic dipole moments of about 5 D per residue, generating fields in the order of 10^8 V/m.^{45, 46-50}

Biomimetic systems, based on polypeptide α -helices, presented an excellent paradigm for studying photoinduced CT in relevance to the basic processes of photosynthesis and redox processes mediated by proteins. Due to their large intrinsic dipole moments, polypeptide α -helical biomimetic systems have been used to test the effect of local electric fields on photoinduced charge separation.^{46,51} The local electric fields, generated by the macromolecular dipoles in such electret CT systems, generally lead to a rectification effects. That is, the electrons move faster toward the positive poles of the dipoles than to the negative poles.

Galoppini and Fox were the first to report this effect using polypeptide α -helices, possessing dipole moments of 40 D, and with an electron donor and an acceptor attached to amino acid residues in the helical conformers.^{46,47} The CT toward the positive pole of the helix dipole was 5-27 times faster than the CT toward the negative pole. In a relatively nonpolar solvent tetrahydrofuran (THF), for example, the rate constant of fast CT can be as high as 27 fold of that of slow CT.^{46,47} They also observed no significant difference between CT rates if the structure of polypeptide was denatured, that is, the helix dipoles were eliminated by using protic solvents or guanidinium salt.⁴⁷ A recent report on proline peptides with three different redox residues showed that charges have a field effect similar that of the dipoles.⁵² Reports on electrochemistry and photo-electrochemistry of self-assembled monolayers of polypeptide helices on gold confirmed this dipole effect. Measured currents showed faster heterogeneous CT when the electrons flowed in the direction of the dipoles (i.e., from the negative to the positive poles) than when they flowed against the dipole.^{48,53,54}

Changes in the CT driving force, $-\Delta G^{(0)}$, account for these dipole effects.⁵⁵ Namely, the molecular dipoles stabilize the charge-separated states in which the radical cation is at the negative poles of the dipoles and radical anion is at the positive poles. This orientation makes $\Delta G^{(0)}$ more negative and increases the CT rates for processes occurring in the Marcus normal region.⁵⁶⁻⁵⁸ For oppositely oriented charge-separated states, this effect is reversed, resulting in a decrease in the CT rates.

These important developments unequivocally show that local electric fields from molecular dipoles affect charge transfer and provide a means for controlling its directionality.

Photoinduced charge transfer rectified by bioinspired electrets. Although polypeptide α -helices are natural existing macromolecules with large dipole moment, they are not always the best choice for charge-transfer systems because they exhibit media and temperature sensitivity. Their biological properties restrict their feasibility as materials for large-scale industrial application. More importantly, since they mediate charge transfer via tunneling mechanism, they are not promising electrets for efficient long-range charge transfer over distances exceeding one or two nanometers.⁵⁹

Herein, we took lessons from biology (i.e., protein structural motifs, such as ordered amide and hydrogen bonds) and applied them to synthetic systems to produce feasible candidates for organic electronic materials. Organic polymers, with their large intrinsic dipole moments and abilities to mediate long-range charge transfer along π -conjugated backbones,⁶⁰ present alternative electronic materials for inducing charge-transfer rectification.

As a principal focus of my research, I was involved in the design of the bioinspired macromolecular electrets. We selected anthranilamides, which are composed of aromatic residues linked with amide bonds (Figure 1-4).⁶⁰ We demonstrated that the amide bond dipoles formed between the carbonyl O at the C-terminus and the nitrogen at the N-terminus, along with the hydrogen bond dipole directed from H to O, contributes to the

intrinsic dipole moments of these bioinspired macromolecules.^{60,61} The aromatic moieties that are directly linked by the amide bonds present sites for charge transfer via multiple short electron transfer steps.

The dipole moments in these structures, composed of identical redox moieties, induced the “cascade” electronic configurations essential for directing charge transfer. Such derivatives of identical moieties provide a means for facile extension of charge transfer pathways by increasing the length of the homomeric chains. It is the featured molecular dipoles, introducing asymmetry in the directionality of the charge hopping, which set apart our systems from others with extended π -conjugation.⁶² Altering the media polarity, which screens the dipoles, tunes the $\Delta G^{(0)}$ of the charge-hopping steps.⁶³ It provides a means for exploring the conditions for maximum efficiency of long-range CT at feasibly small $-\Delta G^{(0)}$. Thus, anthranilamides offer an indispensable, straightforward model for mechanistic studies of the effect of molecular dipoles on long-range CT.

With the assistance of Prof. Roger Lake’s group (leading theoreticians in the field of charge transport) we demonstrated theoretically for the first time that the anthranilamide oligomers possess intrinsic dipole moments that amount to 3 – 5 D per residue.⁶⁰ Without any doping groups (either electron withdrawing or donating groups) at the distal positions of the aromatic residues, the addition of each residue increased the axial dipole moment with about 3 D, of which ~2 D resulted from the additional amide bond and ~1 D from the additional hydrogen bond. The effects of doping groups on the intrinsic dipole moments differed by placed positions of the aromatic residues. The addition of electron

withdrawing groups towards the N-terminus contributed to the increasing of total dipole moment of monomer by about 1.5 D in comparison with the anthranilamide monomer. The position of electron donating group also affects the axial and total dipole moments. If attached to the R₁ position (towards N-terminus, Figure 1-4), there is an induced polarization that opposes the direction of the anthranilamide intrinsic dipole moment, which reduces its values. Concurrently, placing the electron donating group at the R₂ positions (towards C-terminus) significantly increases the dipole moment of the anthranilamides. In addition, the bandgaps of anthranilamides were narrowed down by more than 1 eV, due to extension of the p-conjugation by some of the doping groups.

In order to experimentally investigate the electronic properties of these bioinspired systems, I was involved in an extensive evaluation of the dipoles of six amide conjugates, i.e., the principal building blocks of the bioinspired electrets. By employing Debye-Hedestrand relations, we experimentally determined the dipole moments of amides, and set the foundation for our future studies.⁶⁴ We found that in polar solvent, chloroform ($\epsilon = 4.8$), the values of the dipole moments of the six amides were notably larger than the corresponding dipoles obtained theoretically for vacuum, i.e., for gas phase. Therefore, we introduced the media polarization (and the solvated cavity reaction field) in the *ab initio* calculations to account for the solvent effects.⁶⁴ Our final findings showed agreement between theory and experiment; and both experimentally measured and theoretically calculated dipole moments increased with the increase in the media polarity, which manifested a solvent dependence.

I synthesized a series of anthranilamide conjugates, for many of which I developed the synthetic procedures. My research provided the first experimental demonstration that the anthranilamides possess intrinsic dipoles (Chapter 4, *J. Org. Chem.* 2013).⁴⁴ To determine the orientation of the molecular dipoles in these macromolecules we resorted to advanced nuclear magnet resonance (NMR) techniques, with the assistance of collaborators from Boston University and Harvard University. The study of the electronic properties proved that these anthranilamide oligomers are electrets, based on their intrinsic dipole moments as evident from their spectral and dielectric properties. Two dimensional NMR studies provided the means for estimating the direction of the intrinsic electric dipoles of these conjugates. This study sets the foundation for the development of a class of organic materials that are *de novo* designed from biomolecular motifs and possess unexplored electronic properties.

Utilization of electrochemical approaches like cyclic voltammetry allowed me to further investigate the fundamentals of the charge-transfer theory. By electrochemical and photophysical studies, I developed methods for reliable estimation of driving force of photoinduced charge transfer process (Chapters 2, *J. Phys. Chem. A* 2009; Chapter 3, *J. Phys. Chem. B* 2010).^{65, 66}

The estimation of the driving force for photoinduced charge-transfer processes, using the Rehm-Weller equation, requires the employment of redox and spectroscopic quantities describing the participating electron donor and acceptor. While the spectroscopic data are usually obtained from diluted solutions, usually neat solvents; the redox potentials are most frequently obtained from electrochemical measurements

conducted in concentrated electrolyte solutions. To correct for the differences in the media, in which the various types of measurements are conducted, a term, based on the Born equation for solvation energy of ions, is introduced in the Rehm-Weller equation. The Born correction term, however, requires a prior knowledge of the dielectric constants of the electrolyte solutions used for the redox measurements. Because of limited information for such dielectrics, the values for the dielectric constants of electrolyte solutions are approximated to the values of the dielectric constants of the corresponding neat solvents. I examined the validity of this approximation and developed a method for accounting for the discrepancies induced by the presence of electrolyte in the media (Chapter 2, J. Phys. Chem. A 2009).⁶⁵

Based on study of Chapter 2, I experimentally examined the validity of spherical approximation for molecular ions in the Born solvation energy calculation. The experimentally obtained effective radii were up to four-fold smaller than the radii of the solvation cavities that we calculated. To address this discrepancy, we demonstrated for the first time that a generalized Born approach, which represents molecular species as collections of spheres, yields theoretical values that agrees with the experimental findings and demonstrates plausible means for addressing the potential deficiencies in the single-sphere approximation of organic ions (Chapter 3, J. Phys. Chem. B 2010).⁶⁶

In summary, the most important contributions from my doctoral work were: (1) developing methods for reliable interpretation of experimental results pertinent to the interpretation of the charge-transfer kinetics and thermodynamics; (2) demonstrating rectification of photoinduced charge transfer induced by the anthranilamide intrinsic

dipole; and (3) demonstrating that the photoinduced processes result in charges residing on the anthranilamides (i.e., radical ions) which is essential for attaining hopping mechanism for long-range charge transfer.

References:

- (1) Lewis, N. S. *Science* **2007**, *315*, 798-801.
- (2) U. S. Energy Information Administration, *Annual Energy Review 2011 No. DOE/EIA-0384*, 2011.
- (3) Lewis, N. S.; Nocera, D. G. *Proc Natl Acad Sci U S A* **2006**, *103*, 15729-15735.
- (4) Gray, H. B. *Nature Chemistry* **2009**, *1*, 7-7.
- (5) Barnham, K. W. J.; Mazzer, M.; Clive, B. *Nature Materials* **2006**, *5*, 161-164.
- (6) Sorensen, B. *Energy Policy* **1991**, *19*, 386-391.
- (7) Carts-Powell, Y. *Laser Focus World* **2006**, *42*, 119-121,123.
- (8) Miles, R. W. *Vacuum* **2006**, *80*, 1090-1097.
- (9) Carts-Powell, Y. *Laser Focus World* **2006**, *42*, 119.
- (10) Brabec, C. J. *Solar Energy Materials and Solar Cells* **2004**, *83*, 273-292.
- (11) Chen, L. M.; Hong, Z. R.; Li, G.; Yang, Y. *Advanced Materials* **2009**, *21*, 1434-1449.
- (12) Dennler, G.; Scharber, M. C.; Brabec, C. J. *Advanced Materials* **2009**, *21*, 1323-1338.
- (13) Gratzel, M. *Journal of Photochemistry and Photobiology C-Photochemistry Reviews* **2003**, *4*, 145-153.
- (14) Gratzel, M. *Philosophical Transactions of the Royal Society a-Mathematical Physical and Engineering Sciences* **2007**, *365*, 993-1005.
- (15) Zhang, Y. N.; Ouyang, Z.; Stokes, N.; Jia, B. H.; Shi, Z. R.; Gu, M. *Applied Physics Letters* **2012**, *100*.
- (16) Lok, C. *Technology Review* **2005**, *108*, 85-86.
- (17) Overton, G. *Laser Focus World* **2006**, *42*, 44-46.
- (18) Zhu, X. Y.; Yang, Q.; Muntwiler, M. *Acc. Chem. Res.* **2009**, *42*, 1779-1787.

- (19) Blom, P. W. M.; Mihailetchi, V. D.; Koster, L. J. A.; Markov, D. E. *Adv. Mater. (Weinheim, Ger.)* **2007**, *19*, 1551-1566.
- (20) Guenes, S.; Neugebauer, H.; Sariciftci, N. S. *Chem. Rev.* **2007**, *107*, 1324-1338.
- (21) Yang, Q.; Muntwiler, M.; Zhu, X. Y. *Phys. Rev. B Condens. Matter Mater. Phys.* **2009**, *80*, 115214/115211-115214/115218.
- (22) Lalov, I. J.; Warns, C.; Reineker, P. *New J. Phys.* **2008**, *10*, No pp given.
- (23) Muntwiler, M.; Yang, Q.; Zhu, X. Y. *J. Electron Spectrosc. Relat. Phenom.* **2009**, *174*, 116-124.
- (24) Yokoyama, M.; Endo, Y.; Matsubara, A.; Mikawa, H. *Polym. Prepr., Am. Chem. Soc., Div. Polym. Chem.* **1979**, *20*, 399-402.
- (25) Yokoyama, M.; Endo, Y.; Matsubara, A.; Mikawa, H. *J. Chem. Phys.* **1981**, *75*, 3006-3011.
- (26) Yokoyama, M.; Endo, Y.; Mikawa, H. *Chem. Phys. Lett.* **1975**, *34*, 597-600.
- (27) Schmidtke, J. P.; Friend, R. H.; Silva, C. *Phys. Rev. Lett.* **2008**, *100*, 157401/157401-157401/157404.
- (28) Peumans, P.; Forrest, S. R. *Chem. Phys. Lett.* **2004**, *398*, 27-31.
- (29) Albrecht, U.; Baessler, H. *Chem. Phys. Lett.* **1995**, *235*, 389-393.
- (30) Blom, P. W. M.; Mihailetchi, V. D.; Koster, L. J. A.; Markov, D. E. *Adv. Mater.* **2007**, *19*, 1551-1566.
- (31) Albrecht, U.; Baessler, H. *Chem. Phys.* **1995**, *199*, 207-214.
- (32) Huang, S. Y.; Schlichthorl, G.; Nozik, A. J.; Gratzel, M.; Frank, A. J. *Journal of Physical Chemistry B* **1997**, *101*, 2576-2582.
- (33) Wang, Z. S.; Zhou, G. *Journal of Physical Chemistry C* **2009**, *113*, 15417-15421.
- (34) Eberhard, S.; Finazzi, G.; Wollman, F. A. *Annual Review of Genetics* **2008**, *42*, 463-515.
- (35) Fox, M. A. *Photochemistry and Photobiology* **1990**, *52*, 617-627.

- (36) Rabinowitch, E. *Annual Review of Plant Physiology and Plant Molecular Biology* **1952**, *3*, 229-264.
- (37) Krauss, N.; Schubert, W. D.; Klukas, O.; Fromme, P.; Witt, H. T.; Saenger, W. *Nature Structural Biology* **1996**, *3*, 965-973.
- (38) Parson, W. W.; Chu, Z. T.; Warshel, A. *Biochimica Et Biophysica Acta* **1990**, *1017*, 251-272.
- (39) Gray, H. B.; Winkler, J. R. *Proc Natl Acad Sci U S A* **2005**, *102*, 3534-3539.
- (40) Onuchic, J. N.; Beratan, D. N.; Winkler, J. R.; Gray, H. B. *Annual Review of Biophysics and Biomolecular Structure* **1992**, *21*, 349-377.
- (41) Gray, H. B.; Winkler, J. R. *Annual Review of Biochemistry* **1996**, *65*, 537-561.
- (42) Jortner, J.; Bixon, M.; Voityuk, A. A.; Rosch, N. *Journal of Physical Chemistry A* **2002**, *106*, 7599-7606.
- (43) Li, X. Q.; Zhang, H. Y.; Yan, Y. J. *Journal of Physical Chemistry A* **2001**, *105*, 9563-9567.
- (44) Xia, B. B., D.; Upadhyayula, S.; Jones II, G.; Vullev, V. *The Journal of Organic Chemistry* **2013**, *in press*.
- (45) Knorr, A.; Galoppini, E.; Fox, M. A. *Journal of Physical Organic Chemistry* **1997**, *10*, 484-498.
- (46) Galoppini, E.; Fox, M. A. *Journal of the American Chemical Society* **1996**, *118*, 2299-2300.
- (47) Fox, M. A.; Galoppini, E. *Journal of the American Chemical Society* **1997**, *119*, 5277-5285.
- (48) Mandal, H. S.; Kraatz, H. B. *Chemical Physics* **2006**, *326*, 246-251.
- (49) Sek, S.; Misicka, A.; Swiatek, K.; Maicka, E. *Journal of Physical Chemistry B* **2006**, *110*, 19671-19677.
- (50) Shin, Y. G. K.; Newton, M. D.; Isied, S. S. *Journal of the American Chemical Society* **2003**, *125*, 3722-3732.
- (51) Jones, G.; Zhou, X.; Vullev, V. I. *Photochemical & Photobiological Sciences* **2003**, *2*, 1080-1087.

- (52) Gao, J. A.; Muller, P.; Wang, M.; Eckhardt, S.; Lauz, M.; Fromm, K. M.; Giese, B. *Angewandte Chemie-International Edition* **2011**, *50*, 1926-1930.
- (53) Morita, T.; Kimura, S.; Kobayashi, S.; Imanishi, Y. *Journal of the American Chemical Society* **2000**, *122*, 2850-2859.
- (54) Yasutomi, S.; Morita, T.; Imanishi, Y.; Kimura, S. *Science* **2004**, *304*, 1944-1947.
- (55) Shin, Y.-G. K.; Newton, M. D.; Isied, S. S. *Journal of the American Chemical Society* **2003**, *125*, 3722-3732.
- (56) Bolton, J. R.; Archer, M. D. *Adv. Chem. Ser.* **1991**, *228*, 7-23.
- (57) Suppan, P. *Top. Curr. Chem.* **1992**, *163*, 95-130.
- (58) Marcus, R. A.; Sutin, N. *Biochimica Et Biophysica Acta* **1985**, *811*, 265-322.
- (59) Beratan, D. N.; Onuchic, J. N.; Winkler, J. R.; Gray, H. B. *Science* **1992**, *258*, 1740-1741.
- (60) Ashraf, M. K.; Pandey, R. R.; Lake, R. K.; Millare, B.; Gerasimenko, A. A.; Bao, D.; Vullev, V. I. *Biotechnology Progress* **2009**, *25*, 915-922.
- (61) Vullev, V. I. *Journal of Physical Chemistry Letters* **2011**, *2*, 503-508.
- (62) Sikes, H. D.; Smalley, J. F.; Dudek, S. P.; Cook, A. R.; Newton, M. D.; Chidsey, C. E. D.; Feldberg, S. W. *Science* **2001**, *291*, 1519-1523.
- (63) Wan, J. D.; Ferreira, A.; Xia, W.; Chow, C. H.; Takechi, K.; Kamat, P. V.; Jones, G.; Vullev, V. I. *Journal of Photochemistry and Photobiology a-Chemistry* **2008**, *197*, 364-374.
- (64) Upadhyayula, S.; Bao, D.; Millare, B.; Sylvia, S. S.; Habib, K. M. M.; Ashraf, K.; Ferreira, A.; Bishop, S.; Bonderer, R.; Baqai, S.; Jing, X. Y.; Penchev, M.; Ozkan, M.; Ozkan, C. S.; Lake, R. K.; Vullev, V. I. *Journal of Physical Chemistry B* **2011**, *115*, 9473-9490.
- (65) Bao, D.; Millare, B.; Xia, W.; Steyer, B. G.; Gerasimenko, A. A.; Ferreira, A.; Contreras, A.; Vullev, V. I. *Journal of Physical Chemistry A* **2009**, *113*, 1259-1267.
- (66) Bao, D.; Ramu, S.; Contreras, A.; Upadhyayula, S.; Vasquez, J. M.; Beran, G.; Vullev, V. I. *Journal of Physical Chemistry B* **2010**, *114*, 14467-14479.

Figures

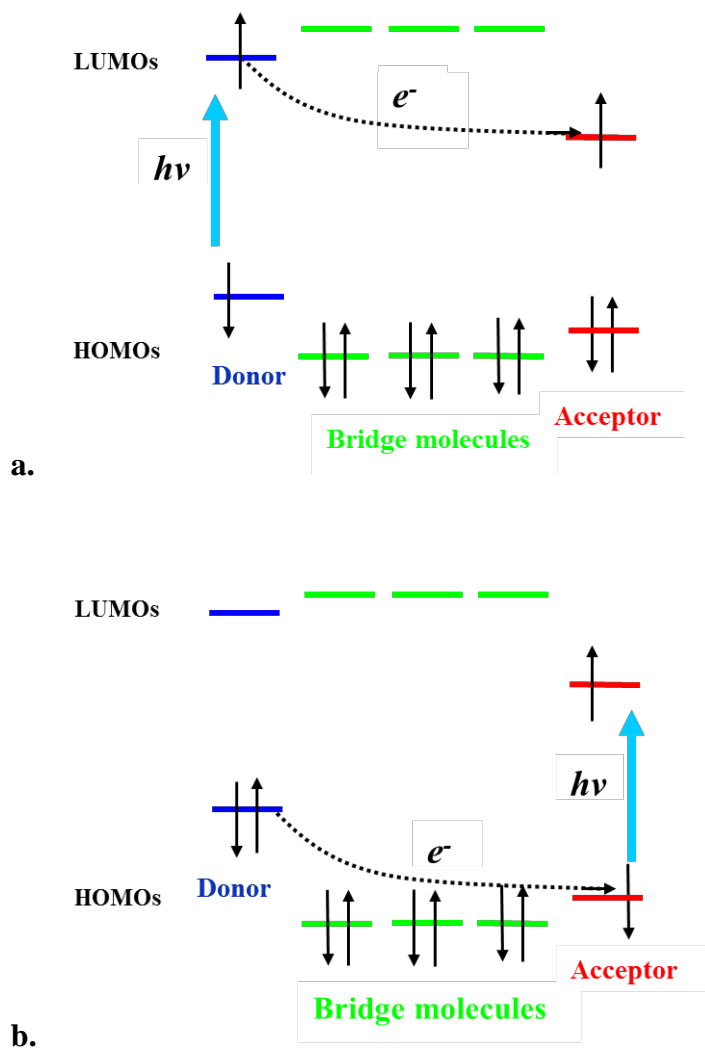


Figure 1-1. Frontier orbital diagrams of donor-bridges-acceptor systems (DBA), mediating photoinduced charge transfer via: **(a)** tunneling with the donor as the principal chromophore; **(b)** tunneling with the acceptor as the principal chromophore. $h\nu$ = photoexcitation of the principal chromophore; LUMO = lowest unoccupied molecular orbitals; HOMO = highest occupied molecular orbitals.

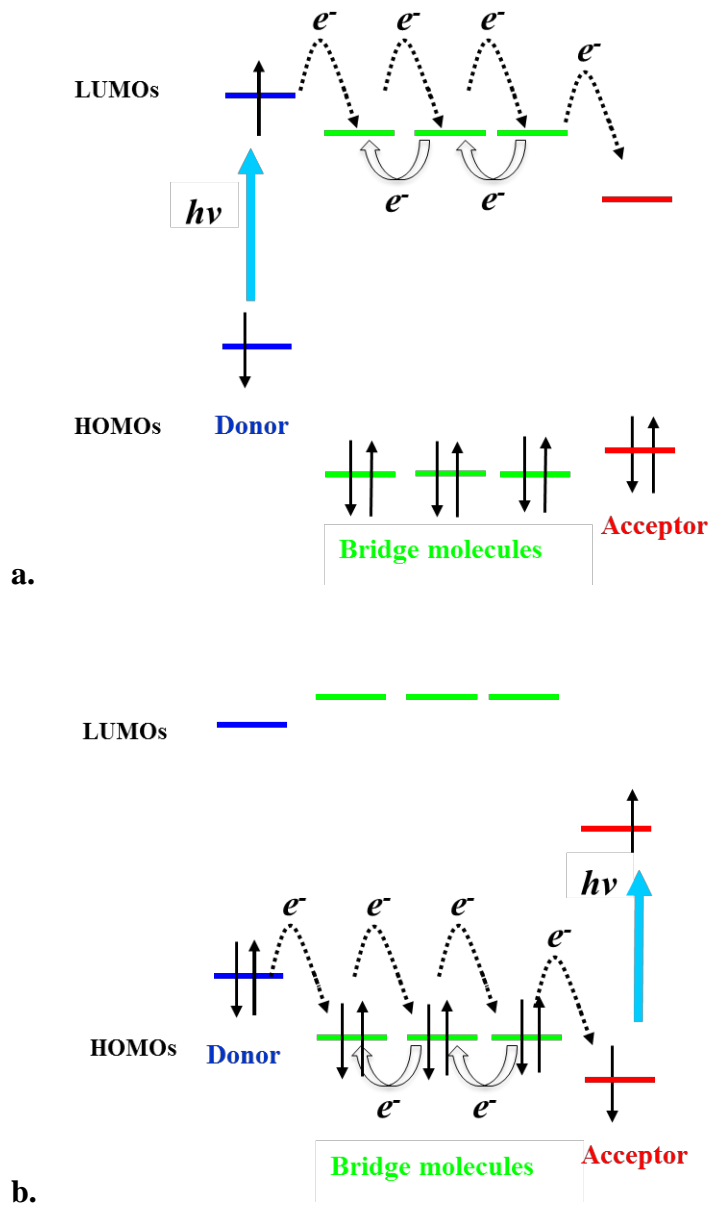


Figure 1-2. Frontier orbital diagrams of donor-bridges-acceptor systems (DBA), mediating photoinduced charge transfer via (a) electron hopping – the donor is the principal chromophore; and (b) hole hopping – the acceptor is the principal chromophore. For hole hopping, an electron from the bridge is transferred to the lower-level singly-occupied orbital (which is the HOMO of the acceptor after the photoexcitation). The consecutive electron transfer steps along the HOMOs of the bridge, followed by electron transfer from the HOMO of the donor, create a total effect of positive-charge (hole) transfer from the acceptor to the donor.

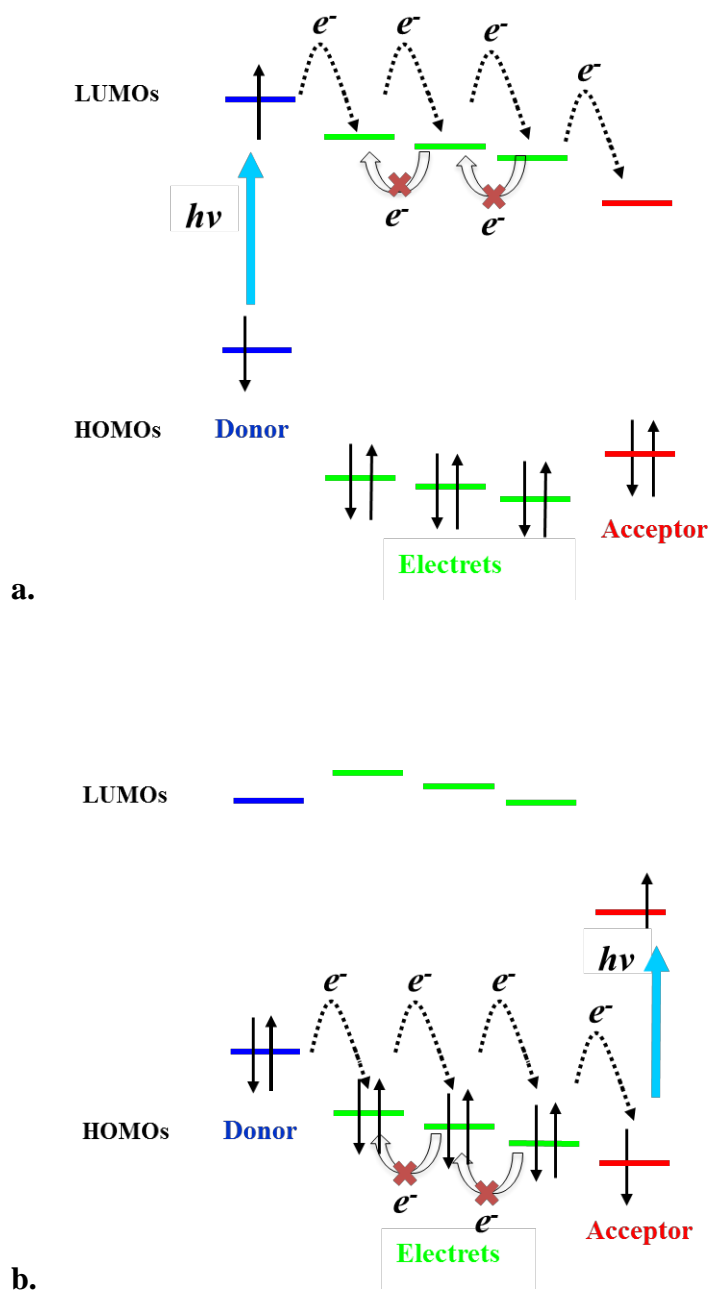


Figure 1-3. Frontier orbital diagrams of donor-bridges-acceptor systems (DBA) with local electric field mediating photoinduced charge transfer via **(a)** electron hopping and **(b)** hole hopping. With intrinsic electric field that are generated by dipoles of bridge molecules, that is, electrets, the back charge transfer processes will be suppressed. These diagrams are based on assumptions for homogeneous effect of the local electric field on the frontier orbitals of the bridging moieties.

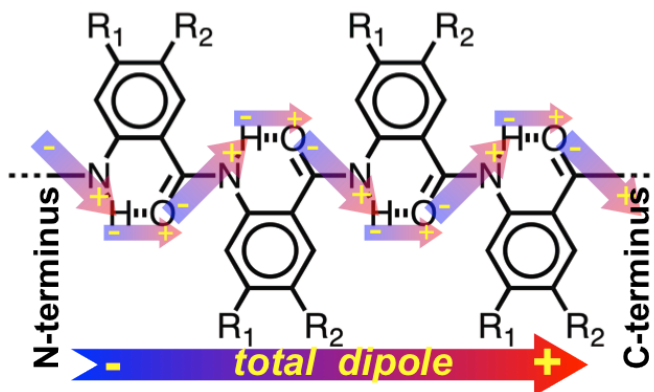


Figure 1-4. Anthranilamides and the origin of their intrinsic electric dipole moment from: (1) the ordered orientation of the amide bonds; and (2) the shift in the electron density from H to O upon hydrogen-bond formation. Unlike protein α -helices, the anthranilamide dipole is oriented from the N- to the C-terminus.

Chapter 2

Electrochemical Oxidation of Ferrocene Manifests a Strong Dependence on the Concentration of the Supporting Electrolyte for Solutions of non-Polar Solvents

Abstract

The estimation of the driving force for photoinduced charge-transfer processes, using the Rehm-Weller equation, requires the employment of redox and spectroscopic quantities describing the participating electron donor and acceptor. While the spectroscopic data are usually obtained from diluted solutions, the redox potentials are most frequently obtained from electrochemical measurements conducted in concentrated electrolyte solutions. To correct for the differences in the media, in which the various types of measurements are conducted, a term, based on the Born equation for solvation energy of ions, is introduced in the Rehm-Weller equation. The Born correction term, however, requires a prior knowledge of the dielectric constants of the electrolyte solutions used for the redox measurements. Because of limited information for such dielectrics, the values for the dielectric constants of electrolyte solutions are approximated to the values of the dielectric constants of the corresponding neat solvents. We examined the validity of this approximation. Using cyclic voltammetry, we recorded the first one-electron oxidation potential of ferrocene for three different solvents in the presence of 1 – 500 mM supporting electrolyte. The dielectric constants for some of the electrolyte solutions were extracted from fluorescence measurements of a dimethylaminonaphthalimide chromophore that exhibits pronounced solvatochromism. The dielectric constants of the concentrated electrolyte solutions correlated well with the corresponding oxidation potentials. The dependence of the oxidation potential of ferrocene on the electrolyte concentration for different solvents revealed that the abovementioned approximation in the Born correction term, indeed, introduces a

significant error in the estimation of the charge-transfer driving force from redox data collected using relatively non-polar solvents.

Keywords: electron transfer, charge transfer, Born equation, Rehm Weller equation, ferrocene, tetrabutylammonium, tetrafluoroborate, dimethylamino-1,8-naphthalimide, solvatochromism, redox potential, oxidation potential, half-wave potential.

Introduction

This article describes electrochemical investigation of the redox properties of ferrocene in the presence of various concentrations of a supporting electrolyte for different organic solvent media. We observed up to half-a-volt shifts in the oxidation potential of ferrocene with the increase in the electrolyte concentration to 500 mM.

The Rehm-Weller equation provides an important relation between measurable quantities that allows for estimation of the driving force (i.e., the change in the Gibbs energy, $\Delta G_{\text{et}}^{(0)}$) of photoinduced electron transfer processes:¹⁻³

$$\Delta G_{\text{et}}^{(0)} = F \left(E_{\text{D}^{z_{\text{D}}+n}/\text{D}^{z_{\text{D}}}}^{(0)} - E_{\text{A}^{z_{\text{A}}}/\text{A}^{z_{\text{A}}-n}}^{(0)} \right) - \mathcal{E}_{00} + \Delta G_{\text{S}} + W \quad (2-1)$$

where $E_{\text{D}^{z_{\text{D}}+n}/\text{D}^{z_{\text{D}}}}^{(0)}$ and $E_{\text{A}^{z_{\text{A}}}/\text{A}^{z_{\text{A}}-n}}^{(0)}$ are the standard oxidation and reduction potentials for the donor and the acceptor, respectively; F is the Faraday constant; \mathcal{E}_{00} is the zero-to-zero energy of the principal chromophore; ΔG_{S} and W are the Born and Coulombic correction terms:

$$\Delta G_{\text{S}} = \frac{nq^2}{8\pi\epsilon_0} \left(\frac{2z_{\text{D}} + n}{r_{\text{D}}} \left(\frac{1}{\epsilon} - \frac{1}{\epsilon_{\text{D}}} \right) - \frac{2z_{\text{A}} - n}{r_{\text{A}}} \left(\frac{1}{\epsilon} - \frac{1}{\epsilon_{\text{A}}} \right) \right) \quad (2-2)$$

$$W = \frac{n(z_{\text{A}} - z_{\text{D}} - n)q^2}{4\pi\epsilon_0\epsilon R_{\text{DA}}} \quad (2-3)$$

where r_{D} and r_{A} are the donor and acceptor radii, respectively; R_{DA} is the center-to-center donor acceptor distance; n is the number of transferred electrons; q is an elementary charge; z_{A} and z_{D} are the charges of the donor and the acceptor, respectively, prior to the electron-transfer process; and ϵ_0 is the electric permittivity of vacuum.

In equation 2-2, while ϵ_D and ϵ_A are the dielectric constants of the solutions, in which the redox potentials of the donor and the acceptor, respectively, were measured, ϵ is the dielectric constant of the media, for which $\Delta G_{\text{et}}^{(0)}$ is calculated and the spectroscopic measurements for estimation of E_{00} are conducted. The Born term, therefore, introduces a correction for the differences in the solvation energies for the charged species,^{4,5} involved in the electron-transfer process, when in media with dielectric constants ϵ , ϵ_D and ϵ_A : i.e., $\Delta G_S/F$ corrects the values of the redox potentials, $E_{D^{z_D+n}/D^{z_D}}^{(0)}$ and $E_{A^{z_A}/A^{z_A-n}}^{(0)}$, measured in media with dielectric constants ϵ_D and ϵ_A , to the expected values for $E_{D^{z_D+n}/D^{z_D}}^{(0)}$ and $E_{A^{z_A}/A^{z_A-n}}^{(0)}$, if they were measured in media with dielectric constant ϵ .

The redox potentials, $E_{D^{z_D+n}/D^{z_D}}^{(0)}$ and $E_{A^{z_A}/A^{z_A-n}}^{(0)}$, are most frequently obtained from electrochemical measurements, which are conducted in concentrated electrolyte solutions. Because data for dielectric properties of electrolyte solutions are scarce, ϵ_D and ϵ_A are approximated with the dielectric constants of the corresponding neat solvents.^{2,6,7} This approximation, although broadly employed, can be a source of a significant error in the estimation of $\Delta G_{\text{et}}^{(0)}$.

Assuming that $\epsilon^{-1} \gg \epsilon_D^{-1}$ and $\epsilon^{-1} \gg \epsilon_A^{-1}$ allows for an alternative approximation for the Born term in equation 2-2 that for a one-electron transfer ($n = 1$) between non-charged donor and acceptor is $\Delta G_S \approx q^2(r_D^{-1} + r_A^{-1})(8\pi\epsilon_0\epsilon)^{-1}$.⁸ This alternative approximation, however, is not universally applicable: it is acceptable solely for charge-transfer studies in relatively non-polar media, for which the redox potentials are determined in relatively polar solvents in the presence of high electrolyte concentration.

Due to the robustness of its reversibility at experimentally accessible potentials, the ferrocenium/ferrocene redox couple, Fc^+/Fc ($\text{Fc} = \text{Fe}(\text{C}_5\text{H}_5)_2$), has been established as one of the standards for calibration of electrochemical measurements and extensively investigated.⁹⁻¹³ The oxidation potential of ferrocene, $E_{\text{Fc}^+/\text{Fc}}^{(0)}$, recorded in the presence of ~ 0.1 M supporting electrolyte, manifests relatively small dependence on the polarity of the neat solvent used for the measurements.^{11,14,15} Furthermore, $E_{\text{Fc}^+/\text{Fc}}^{(0)}$ shows negligible dependence on the chemical composition of the electrolyte and the material of the working electrode used for the voltammetric measurements.¹⁶ Changes in the concentration of the supporting electrolyte, however, cause dramatic shifts in the oxidation potential of ferrocene for dilute solutions.¹⁷⁻¹⁹ These redox properties, which are not limited to ferrocene only, raise questions about the feasibility of the approximation of ϵ_{D} and ϵ_{A} (equation 2-2) to the dielectric constants of the corresponding neat solvents.

Herein we examine the errors that can be potentially introduced in the Born correction term through the abovementioned approximation of ϵ_{D} and ϵ_{A} . We describe a relatively facile approach for estimation of redox potentials for neat solvent media and hence, obtaining the exact, rather than approximate, values for ΔG_{S} .

Using cyclic voltammetry (CV), we investigated the changes in the oxidation potential of ferrocene (Fc) in the presence of various concentrations of tetrabutylammonium tetrafluoroborate (TBATFB) as a supporting electrolyte for three aprotic organic solvents broadly used for electrochemical measurements: dichloromethane (CH_2Cl_2), acetonitrile (MeCN) and N,N-dimethylformamide (DMF). An increase in the electrolyte

concentration shifts the oxidation potential of Fc to more negative values with as much as 0.5 V.

Using the solvatochromic properties of a dimethylaminonaphthalimide fluorophore, we estimated the dielectric constants of CH₂Cl₂ solutions of TBATFB with different concentrations. An increase in the electrolyte concentration to 500 mM, resulted in a 2.7-fold increase in the dielectric constant of the solution in comparison with the dielectric constant of the neat solvent, CH₂Cl₂. The observed shifts in the oxidation potential of Fc correlated well with the dielectric properties of the electrolyte solution for electrolyte concentration exceeding ~ 20 mM.

Results and Discussion

Redox properties of ferrocene. For this series of studies, we chose ferrocene as a redox probe because of its well-defined one-electron oxidation to a ferrocenium ion, Fc⁺.¹¹ Due to the relative stability of Fc⁺, ferrocene exhibits reversible oxidation behavior in voltammetry measurements.¹⁴ Its oxidation potential, $E_{\text{Fc}^+/\text{Fc}}^{(0)}$, therefore, can be reliably approximated to its half-wave potential, $E_{\text{Fc}^+/\text{Fc}}^{(1/2)}$,^{14,16} defined as the midpoint between the values of the potentials corresponding to the anodic and the cathodic peak in the cyclic voltammograms of Fc. We selected three organic solvents, CH₂Cl₂, MeCN and DMF, which are electrochemically inert within the window of potentials used for this study.

For each of the solvent media, an increase in the concentration of the electrolyte from 1 mM to 500 mM resulted in considerable shifts of the anodic peaks to less positive values (Figure 2-1). The cathodic peaks, concurrently, shifted to a lesser extent toward

more positive values. As a result, for all three solvent media, the increase in the TBATFB concentration shifted the oxidation potential of Fc, $E_{\text{Fc}^+/\text{Fc}}^{(1/2)}$, toward more negative values (Figure 2-2 and Table 2-1). This electrolyte-induced effect was most pronounced for the least-polar of the three solvent, CH_2Cl_2 .

Upon the increase in the electrolyte concentration, the oxidation potentials of Fc for the three solvents asymptotically approach values that are within 0.1 from one another (Figure 2-2): i.e., $E_{\text{Fc}^+/\text{Fc}}^{(1/2)}(C_{\text{TBATFB}} \rightarrow \infty)$ is equal to 0.52, 0.44 and 0.43 V vs. SCE for CH_2Cl_2 , MeCN and DMF, respectively. The increase in the electrolyte concentration increases the dielectric constant and hence, decreases the inverse values of the dielectric constants, ϵ^{-1} , of the solutions. (For the Born term in equation 2-1, it is the values of the inverse dielectric constants, ϵ^{-1} , that are important.) Therefore, for relatively large electrolyte concentrations, the absolute difference between the small values of ϵ^{-1} are relatively small, resulting in relatively small differences in $E_{\text{Fc}^+/\text{Fc}}^{(1/2)}$.

Dielectric properties of CH_2Cl_2 electrolyte solutions. We used N-phenyl-4-dimethylamino-1,8-naphthalimide (Ph-ANI) for estimating the dielectric constants of the CH_2Cl_2 solutions of TBATFB. The lowest excited state of Ph-ANI has a charge-transfer character. An increase in the media polarity, therefore, causes red shift in the fluorescence spectrum of Ph-ANI (Figure 2-3). This solvatochromism appeared most pronouncedly for solvents with relatively low to medium polarity: e.g., as the media changed from CH_2Cl_2 ($\epsilon = 8.93$) to benzonitrile (PhCN, $\epsilon = 25.9$), the maximum of the fluorescence spectrum of Ph-ANI shifted almost 13 nm to the red.

The increase in the concentration of the electrolyte in CH₂Cl₂ caused a similar red shift in the fluorescence spectrum of Ph-ANI (Figure 2-4). Relating the spectral maxima for the electrolyte solutions (Figure 2-4b and c) with the spectral maxima for organic solvents with known dielectric constants (Figure 2-3b) allowed us to extract the dielectric constants of the CH₂Cl₂ solutions with various concentrations of TBATFB (Figure 2-5 and Table 2-2).

The increase in the electrolyte concentration causes close to a three-fold increase in the dielectric constant of the CH₂Cl₂ solutions. While for neat CH₂Cl₂, $\epsilon^{-1} = 0.11$, for 500 mM TBATFB solution in CH₂Cl₂, $\epsilon^{-1} = 0.041$. For ferrocene, the Born correction term (equation 2-2) translates this difference in ϵ^{-1} translates into a difference of about 0.2 V between $E_{\text{Fc}^+/\text{Fc}}^{(1/2)}$ for the neat solvent and the electrolyte solution. This finding indicates that for this particular solvent system, approximating ϵ_{D} (or ϵ_{A}) to the dielectric constant of the neat organic solvent, CH₂Cl₂, introduces a non-trivial error.

Correlation between oxidation potential and dielectric constant. The oxidation potential of ferrocene, $E_{\text{Fc}^+/\text{Fc}}^{(1/2)}$, and the dielectric constant of the electrolyte solutions manifest similar trends in their dependence on the concentration of TBATFB (Figure 2-2 and 2-5).

As predicted by the Born equation, $E_{\text{Fc}^+/\text{Fc}}^{(1/2)}$ should manifest linear dependence on the inverse dielectric constant of the media, ϵ^{-1} , and the slope of $E_{\text{Fc}^+/\text{Fc}}^{(1/2)}$ vs. ϵ^{-1} should be equal to $q / (8\pi\epsilon_0 r_{\text{Fc}})$.⁵ An examination of the correlation between $E_{\text{Fc}^+/\text{Fc}}^{(1/2)}$ and ϵ^{-1} , for CH₂Cl₂ electrolyte media, showed two distinct regions (Figure 2-6). For electrolyte

concentrations exceeding 20 mM, the slope of the linear fit yielded a value of 2.6 Å for the radius of ferrocene, r_{Fc} . For electrolyte concentrations smaller than 5 mM, on the other hand, the linear fit produced an unrealistically small value for r_{Fc} . Employment of media with relatively large electrolyte concentration, e.g., $C_{\text{TBATFB}} \geq 20$ mM, for electrochemical measurements, therefore, assures reliable determination of $E_{\text{Fc}^+/\text{Fc}}^{(1/2)}$.

Despite the good correlation between $E_{\text{Fc}^+/\text{Fc}}^{(1/2)}$ and ε^{-1} for the CH_2Cl_2 electrolyte solutions (for $C_{\text{TBATFB}} \geq 20$ mM), these results should be approached with caution. The fluorescence solvatochromism of Ph-ANI allowed us to determine the bulk dielectric constant of the electrolyte CH_2Cl_2 solutions. The electrochemical oxidation, on the other hand, is an interfacial process. At the surface of the working electrode the electrolyte concentration differs from the bulk concentration of the supporting electrolyte. Furthermore, the adsorbed redox species, Fc, are not surrounded only by the electrolyte solution: they are also in contact with the electrode material. Therefore, the dielectric constant of the microenvironment of the ferrocene species, upon their oxidation at the electrode surface, is different from the dielectric constant of the bulk solution determined from the fluorescence measurements. For the described system, however, this difference does not compromise the quality of the correlation between the oxidation potential and the inverse values of the bulk dielectric constant.

Redox behavior of Fc in dilute electrolyte solutions. A decrease in the electrolyte concentration below ~10 mM caused a sharp shift of $E_{\text{Fc}^+/\text{Fc}}^{(1/2)}$ toward more positive values for all three solvent media (Figure 2-2). As a result, a linear correlation analysis, based on

the Born equation, yielded an abnormally large value for r_{Fc} for diluted electrolyte solutions (Figure 2-6).

The concentration of ferrocene for the described CV measurements was 5 mM. As the electrolyte concentration decreases to the lower millimolar range, the amount of ions (e.g., tetrafluoroborates) in the vicinity of the non-charged ferrocene species becomes scarce. To preserve the electroneutrality upon electro-oxidation of Fc, therefore, extra work is required for migrating counterions to the generated ferrocenium cations. This extra energy required for the electro-oxidation translates into considerable positive shifts in the anodic peak of the voltammograms. Upon the reverse sweep of the applied potential, a consequent reduction of the ferrocenium cation requires extra energy for removing the counterions away from the electrogenerated non-charged Fc species, causing a positive shift in the cathodic peak and overall a positive shift in the calculated $E_{\text{Fc}^+/\text{Fc}}^{(1/2)}$.¹⁷ Hence, the dilution of the supporting electrolyte adds an overpotential to the values of the measured half-wave potentials, $E_{\text{Fc}^+/\text{Fc}}^{(1/2)}$, deviating them from the value of the “true” thermodynamic redox potential, $E_{\text{Fc}^+/\text{Fc}}^{(0)}$.

Furthermore, the electrogeneration of ferrocenium, along with the attracted counterions, increases the local concentration of ions in the vicinity of the working electrode, decreasing the resistivity of the solution in that region. (Although this phenomenon is referred as “ohmic polarization,” it should be noted that in the presence of faradaic current, the resistance is current-dependent, especially, for diluted electrolyte solutions: i.e., the solution media in the vicinity of the working and counter electrodes

does not obey Ohm's law.¹⁷⁾ Oldham quantified this effect of ohmic polarization and later other authors confirmed it:¹⁷⁻¹⁹

$$E_{\text{Fc}^+/\text{Fc}}^{(1/2)} = E_{\text{Fc}^+/\text{Fc}}^{(0)} + \frac{k_B T}{nq} \ln \left(\frac{D_{\text{Fc}}}{D_{\text{Fc}^+}} \left(1 + \frac{D_{\text{Fc}} C_{\text{Fc}}}{D_{\text{Fc}^+} C_{\text{TBATFB}}} \right) \right) \quad (2-4)$$

where D_{Fc} and D_{Fc^+} are the diffusion coefficients of the ferrocene and ferrocenium, respectively; C_{Fc} and C_{TBATFB} are the bulk concentrations of the ferrocene and of the electrolyte, respectively; k_B is the Boltzmann constant; T is the temperature; q is an elementary charge; and n is the number of electrons transferred from the ferrocene to the electrode.

Decrease in C_{TBATFB} from 10 to 1 mM produces up to 0.4 V shifts in $E_{\text{Fc}^+/\text{Fc}}^{(1/2)}$ (Figure 2-2). Equation 2-4, however, predicts such tenths-of-a-volt shifts only for C_{Fc} exceeding C_{TBATFB} at least 100 fold:¹⁷ i.e., for electrolyte concentrations smaller than 50 mM for 5 mM Fc solutions (Figure 2-7). As Pendley et al. pointed out, however, equation 2-4 implies two principal assumptions: (1) the rate of the heterogeneous electron transfer is relatively fast and does not depend on the electrolyte concentration; and (2) the ratio between the diffusion coefficients, $RDC = D_{\text{Fc}^+}/D_{\text{Fc}}$, does not depend on the electrolyte concentration.¹⁹ The fast rates recorded for heterogeneous electron-transfer for ferrocene,^{12,13} suggest that the first assumption is acceptable. Therefore, the concentration dependence of the diffusion coefficients may offer a plausible reason for the observed discrepancies at low electrolyte concentrations.

The diffusion coefficient is inversely proportional to the size of the species, r , and to the viscosity of the media, h : from the Stokes-Einstein equation, $D = k_B T / 6\pi hr$. Neither

the solvent (CH_2Cl_2) nor the electrolyte ions have tendency for bonding with the non-charged ferrocene. Changes in the electrolyte concentration, therefore, should not change the effective size of the ferrocene ions. For a range of organic solvents, however, an increase in the concentration of the supporting electrolyte increases the viscosity of the solutions.²⁰⁻²² Therefore, a decrease in C_{TBATFB} can result in a substantial increase in the diffusion coefficient of ferrocene.^{22,23} For ferrocenium ions in dilute solutions, on the other hand, the electrostatic effects can prevail the viscosity-induced modulation of their diffusion properties.^{22,24} A decrease in C_{TBATFB} can impede the mass transport of the charged ferrocenium ions due to a lack of electrostatic screening in diluted electrolyte solutions. The corollary of these effects, indeed, will be a decrease in $D_{\text{Fc}^+}/D_{\text{Fc}}$ with dilution of the supporting electrolyte. Such a decrease in the ratio between the diffusion coefficients, RDC , does make the shifts of $E_{\text{Fc}^+/\text{Fc}}^{(1/2)}$, predicted by equation 2-4, apparent at relatively high concentrations of the supporting electrolyte (Figure 2-7a).

For the calculation of $E_{\text{Fc}^+/\text{Fc}}^{(1/2)}$, using equation 2-4, we introduced constant values for the ratio $D_{\text{Fc}^+}/D_{\text{Fc}}$.²⁵⁻²⁷ Although, such calculations demonstrate the trends expected with the change in the diffusion coefficients, they do not reflect the dependence of RDC on the concentration of the supporting electrolyte: i.e., the ratio $D_{\text{Fc}^+}/D_{\text{Fc}}$ is a constant, rather than concentration dependent, $D_{\text{Fc}^+}(C_{\text{TBATFB}})/D_{\text{Fc}}(C_{\text{TBATFB}})$.

Another deficiency of equation 2-4 representing the relationship between $E_{\text{Fc}^+/\text{Fc}}^{(1/2)}$ and $E_{\text{Fc}^+/\text{Fc}}^{(0)}$, is the lack of a Born correction term for the change in the solvation energy due to the alteration in the dielectric constant of the solutions induced by the changes in the

concentration of the supporting electrolyte. Examination of the calculated results from equation 2-4, however, shows a lack of concentration dependence of $E_{\text{Fc}^+/\text{Fc}}^{(1/2)}$ at relatively large C_{TBATFB} (Figure 2-7b): i.e., according to eq. 4, $E_{\text{Fc}^+/\text{Fc}}^{(0)} \approx E_{\text{Fc}^+/\text{Fc}}^{(1/2)}$ for $C_{\text{Fc}} \ll C_{\text{TBATFB}}$. The experimental data, however, do manifest a C_{TBATFB} dependence of $E_{\text{Fc}^+/\text{Fc}}^{(1/2)}$ even for $C_{\text{TBATFB}} > 50$ mM. As it was discussed in the previous section, this dependence of $E_{\text{Fc}^+/\text{Fc}}^{(1/2)}$ on C_{TBATFB} (i.e., of $E_{\text{Fc}^+/\text{Fc}}^{(1/2)}$ on the dielectric constant of the media) can be readily quantified by using the Born relationship (Figure 2-6). Therefore, the “true” redox potentials, $E_{\text{Fc}^+/\text{Fc}}^{(0)}$ (e.g., for neat solvents), can be readily extracted from the half-wave potentials, $E_{\text{Fc}^+/\text{Fc}}^{(1/2)}$, electrochemically measured at high concentrations of supporting electrolyte, by employing the Born dependence of the solvation energy on the dielectric constants of the solutions.

Prediction of the oxidation potential of ferrocene for neat solvents. Using values of redox potentials, $E_{\text{D}^{2\text{D}^+}/\text{D}^{2\text{D}}}^{(0)}$ and $E_{\text{A}^{2\text{A}^-}/\text{A}^{2\text{A}^-n}}^{(0)}$, for the donor and the acceptor in neat solvents in the Rehm-Weller equation (equation 2-1), will allow for the use of the dielectric constants of the corresponding neat solvent for ϵ_{D} and ϵ_{A} in the Born correction term (equation 2-2). The observed linear dependence of $E_{\text{Fc}^+/\text{Fc}}^{(1/2)}$ on ϵ^{-1} for CH_2Cl_2 with high electrolyte concentration ($20 \text{ mM} \leq C_{\text{TBATFB}} \leq 500 \text{ mM}$) allowed us to extrapolate the values for the oxidation potentials for neat solvents (Table 2-3, fourth column). The oxidation potentials for the neat solvents were extrapolated on the basis of the solvation energy of the electrogenerated ferrocenium cations and did not contain the overpotential

introduced by long-range diffusion of counterions in diluted electrolyte solutions. Therefore, the extrapolated potentials had less-positive values than the values of $E_{\text{Fc}^+/\text{Fc}}^{(1/2)}$ for some of the diluted electrolytes in the same solvents (Table 2-1 and 2-3).

The extrapolation of redox potentials from the linear dependence of $E_{\text{Fc}^+/\text{Fc}}^{(1/2)}$ on ε^{-1} requires prior knowledge of the dielectric constants of the corresponding electrolyte solutions with a broad range of concentrations. Using solvatochromism of fluorescent chromophores presents a facile approach for estimating the dielectric constants of electrolyte solutions. Chromophores that manifest large spectral fluorescence (or absorption) shifts in the dielectric range for electrolyte solutions of interests, however, might not be always readily available. Therefore, we examined an alternative approach for extrapolation of the oxidation potentials to zero electrolyte concentrations that requires solely electrochemical data.

Because of the exponential dependence of the measured dielectric constants on the electrolyte concentration (Figure 2-5), we predicted an exponential dependence of $E_{\text{Fc}^+/\text{Fc}}^{(1/2)}$ on C_{TBATFB} :

$$E_{\text{Fc}^+/\text{Fc}}^{(1/2)}(C_{\text{TBATFB}}) = E_{\infty} + E_{\Delta C} e^{\gamma C_{\text{TBATFB}}} \quad (2-5)$$

where E_{∞} is the oxidation potential at large electrolyte concentration, and for neat solvents, $E_{\text{Fc}^+/\text{Fc}}^{(0)} = E_{\text{Fc}^+/\text{Fc}}^{(1/2)}(0) = E_{\infty} + E_{\Delta C}$; γ is an empirical parameter. Fitting the data within the electrolyte concentration range between 20 and 500 mM to equation 2-5 (Figure 2-8), yielded values for $E_{\text{Fc}^+/\text{Fc}}^{(1/2)}(0)$ equal to 0.69, 0.49 and 0.45 V vs. SCE for neat CH_2Cl_2 , MeCN and DMF, respectively. These values differ with about two-to-four

percents from the values for the same neat solvents obtained from the linear dependence of $E_{\text{Fc}^+/\text{Fc}}^{(1/2)}$ on ε^{-1} (Table 2-3), indicating that the linear (Figure 2-6) and the exponential (Figure 2-8) extrapolation methods allow for obtaining the redox potentials for zero-electrolyte concentration with equal reliability. The latter method involving exponential extrapolation, however, has a significant advantage: it does not require prior knowledge of the dielectric constants of the electrolyte solutions.

The typical working range of electrolyte concentrations in organic solvent for analytical electrochemistry is between about 100 and 200 mM. Comparison between the values of $E_{\text{Fc}^+/\text{Fc}}^{(1/2)}(0)$ for the three solvents with the corresponding measured values for $C_{\text{TBATFB}} = 100$ and 200 mM (Table 2-1), reveals that the extrapolation of the oxidation potential to $C_{\text{TBATFB}} = 0$ is not truly crucial for relatively polar solvents, such as MeCN and DMF. For both, DMF and MeCN, the values of $E_{\text{Fc}^+/\text{Fc}}^{(1/2)}$ for 100 and 200 mM TBATFB are within a difference of 10% or less from the extrapolated values for the corresponding neat solvents.

For a relatively non-polar solvent such as CH_2Cl_2 , however, the extrapolation to $C_{\text{TBATFB}} = 0$ mM proved to be important. The values of $E_{\text{Fc}^+/\text{Fc}}^{(1/2)}$ for 0, 100, 200 and 500 mM TBATFB in CH_2Cl_2 are 0.69, 0.60, 0.55 and 0.52 V vs. SCE, respectively (Figure 2-8 and Table 2-1). These values of $E_{\text{Fc}^+/\text{Fc}}^{(1/2)}$ reveal a considerable dependence of the redox potentials on the electrolyte concentration for relatively non-polar solvents. For such solvents, therefore, extrapolation to zero electrolyte concentration may prove crucial for analyses of charge transfer processes, using equations 2-1 and 2-2. For example, using

the Born equation for calculating the values of the oxidation potential of Fc for DMF from the measured oxidation potentials for 100 and 200 mM electrolyte in CH₂Cl₂, predicts $E_{\text{Fc}^+/\text{Fc}}^{(1/2)}(\text{DMF}) = 0.36$ and 0.31 V vs. SCE, respectively. These predicted values considerably deviate from the determined value of 0.45 V vs. SCE for $E_{\text{Fc}^+/\text{Fc}}^{(1/2)}(\text{DMF})$. Alternatively, using the extrapolated value of 0.69 V vs. SCE for neat CH₂CH₂ in the same calculations, yields $E_{\text{Fc}^+/\text{Fc}}^{(1/2)}(\text{DMF}) = 0.45$ V vs. SCE, which is in excellent agreement with the directly measured oxidation potential.

Reduction potential of Ph-ANI. For a range of applications, dialkylamino-1,8-naphthalimides are acceptably good electron donors²⁸⁻³² and acceptors.^{33,34} The cyclic voltammograms of Ph-ANI (Figure 2-3c) show an irreversible oxidation wave at about 1.1 V vs. SCE and a reversible reduction wave at about -1.4 V vs. SCE (Figure 2-9a). We employed the exponential extrapolation analysis for determination of the half-wave reduction potential of Ph-ANI, $E_{\text{ANI}^+/\text{ANI}}^{(1/2)}$, for neat acetonitrile.

As predicted by equations 2-1 and 2-2, an increase in the media polarity shifts the oxidation potentials of non-charged species, such as ferrocene, toward less positive values (Figure 2-2 and 2-8) because the oxidized forms of the redox couples are charged. On the contrary, increase in the media polarity should shift the reduction potentials of non-charged species toward more positive values because the reduced forms of the redox couples are charged.

The values of $E_{\text{ANI}^+/\text{ANI}}^{(1/2)}$ determined from CV measurements of Ph-ANI for acetonitrile with different concentrations of TBATFB, indeed, showed the expected

trend: the increase in the electrolyte concentration resulted in less negative values for $E_{\text{ANI} / \text{ANI}^{\bullet-}}^{(1/2)}$ (Figure 2-9b). Fitting the half-wave potential vs. electrolyte concentration to an exponential function (Figure 2-9b), allowed us to extrapolate the reduction potential of Ph-ANI for neat acetonitrile: i.e., for $C_{\text{TBATFB}} = 0$ M, $E_{\text{ANI} / \text{ANI}^{\bullet-}}^{(1/2)} = -1.38 \pm 0.004$ V vs. SCE.

Implications for charge-transfer studies. We analyzed a hypothetical system, in which ferrocene is an electron donor and Ph-ANI is an electron acceptor, separated 1 nm (center-to-center distance, R_{DA} , in equation 2-3) from each other. The half-wave redox potentials for acetonitrile (Figure 2-8 and 2-9) allowed us to estimate the energy of the charge-separated state, ΔG_{CS} , of such donor-acceptor system, using equations 2-1 – 2-3, $\Delta G_{\text{CS}} = \Delta G_{\text{et}}^{(0)} + \mathcal{E}_{00}$.

In the calculated values of ΔG_{CS} , a discrepancy of about 0.04 – 0.07 eV became apparent when using data for redox potentials measured in the presence of 100 – 500 mM electrolyte solutions in comparison with ΔG_{CS} calculated from redox potentials extrapolated to zero concentration for neat acetonitrile (Figure 2-10). Such errors, introduced by a direct use of redox potential measured for electrolyte solutions, can prove significant in the estimation of the driving force of photoinduced electron transfer, $\Delta G_{\text{et}}^{(0)}$, for cases where the energy of the charge-separated state, ΔG_{CS} , is comparable with the photoexcitation zero-to-zero energy, E_{00} .

Assuming Ph-ANI is the principal chromophore, E_{00} varies between about 2.6 and 2.8 eV for media with different polarity, due to Ph-ANI solvatochromism. Therefore, for a

relatively non-polar media (e.g., ϵ between about 5 and 10), $\Delta G_{\text{et}}^{(0)}$ will vary between about -0.2 and 0.2 eV. A discrepancy of 0.04 eV, thus, will introduce an error of about 20 % and more. Such discrepancy and errors will become significantly more pronounced for: (1) large electrolyte concentrations; (2) low polarity of the solvents for the electrochemical measurements; and (3) small size of the redox species, i.e., small r_D and r_A in equation 2-2.

Electrolyte solution media for electrochemical measurements should, ideally, be composed of relatively polar solvents should. Instead of the solvent polarity, however, predominantly other factors, such as analyte solubility and electrochemical windows, govern the choices for solution media. For example, acetonitrile is a relatively polar solvent with a broad electrochemical window (spanning between about -2.5 to 2.5 V vs. SCE for 0.1 M TBATFB)³⁵ and hence, it appears to be an excellent choice for redox measurements. Many large-molecular-weight organic conjugates, however, have a limited solubility in acetonitrile. Other solvents, such as benzonitrile or dichloromethane, which are less polar than acetonitrile and have narrower electrochemical windows, may offer the analyte solubility required for the redox measurements.³⁶⁻³⁸

DMF is a relatively polar solvent, but it is not the best choice for relatively extreme oxidation potentials: the electrochemical window for 0.1 M Bu_4NClO_4 in DMF spans between about -2.7 and 1.5 V vs. SCE. Benzonitrile and dichloromethane (with 0.1 M TBATFB and Bu_4NClO_4 , respectively), on the other hand, have electrochemical windows, respectively, spanning from about -1.6 to 2.5 V vs. SCE, and from about -1.9 and 1.7 V vs. SCE.³⁵

A range of aprotic solvents, significantly less polar than acetonitrile and DMF, allow for shifting the electrochemical window. Ethers, such as tetrahydrofuran (THF), for example, allow for studying reduction processes at relatively extreme negative potentials (in addition to providing the required analyte solubility for the redox measurements):³⁹⁻⁴¹ e.g., the electrochemical window for 0.1 M Bu₄NClO₄ in THF spans between about – 3 and 1.2 V vs. SCE.^{35,39}

Non-polar small-molecular-weight solvents tend to have relatively low viscosity. Therefore, for electrochemical studies, requiring large diffusion rates and low-viscosity media, electrolyte solutions composed of non-polar solvents, such as toluene, prove to be the choice.²²

As we demonstrated for ferrocene-Ph-ANI donor-acceptor systems, neglecting the dependence of the measured redox potentials on the electrolyte concentration in acetonitrile can yield sensible errors in the estimation of relatively small driving forces, $\Delta G_{\text{et}}^{(0)}$, of photoinduced charge transfer (i.e., for cases, in which ΔG_{CS} is comparable with E_{00}). Using relatively non-polar solvents for electrochemical measurements, further substantiates such errors in estimation of $\Delta G_{\text{et}}^{(0)}$ that are induced by the dependence of the redox potentials on the concentration of the supporting electrolyte. For dichloromethane, for example, the difference between the measured (for $C_{\text{TBATFB}} \geq 100$ mM) and extrapolated (to $C_{\text{TBATFB}} = 0$ mM) values of the redox potentials can be 100 mV or more (Tables 2-1 and 2-3). For the donor and the acceptor, the effects of the electrolyte concentration on the oxidation and reduction potentials, respectively, manifest opposite trends (Figure 2-8 and 2-9), doubling the error in estimation of $\Delta G_{\text{et}}^{(0)}$ to 0.2 eV or larger.

Using values of redox potentials, which are extrapolated to zero electrolyte concentration (Figure 2-8 and 2-9), offers an approach for eliminating such errors in the estimations of the driving force for charge-transfer processes.

Conclusions

The dependence of the redox potentials on the concentration of the supporting electrolyte is considerably more pronounced for solutions composed of relatively non-polar solvents (such as dichloromethane) than for solutions of relatively polar solvents (such as acetonitrile and dimethylformamide). Therefore, for redox measurements conducted with relatively polar solvents, approximating the dielectric constants, ϵ_D and ϵ_A (equation 2-2), with the values of the dielectric constants for the corresponding neat solvent, will not result in considerable error in the estimation of relatively large charge-transfer driving forces, i.e., for $|\Delta G_{\text{et}}^{(0)}|$ exceeding about 0.5 eV. For relatively small $|\Delta G_{\text{et}}^{(0)}|$, and for electrochemical measurements involving relatively non-polar solvents, such as dichloromethane, chloroform and tetrahydrofuran, however, the values of the redox potentials (recorded at several different electrolyte concentrations) should be extrapolated to zero concentration prior to their use in Rehm-Weller equation (equation 2-1). Such extrapolation will permit the use of the values of the dielectric constants of the corresponding neat solvents for ϵ_D and ϵ_A (equation 2-2). We believe that the described zero-concentration extrapolation method will extend the applicability of the Born term in the Rehm-Weller equation to electrochemical media composed of relatively non-polar solvents and to cases involving relatively small $|\Delta G_{\text{et}}^{(0)}|$.

Experimental

Materials. Ferrocene, tetrabutylammonium tetrafluoroborate, 4-Bromo-1,8-naphthalic anhydride, 3-dimethylaminopropanenitrile, 1,2-dimethoxyethane, acetic acid and aniline were purchased from Aldrich. Anhydrous solvents (dichloromethane, acetonitrile and N,N-dimethylformamide) and spectroscopic-grade solvents (chloroform, dichloromethane, benzonitrile, acetonitrile and dimethylsulfoxide) were purchased from Fisher Scientific. N-phenyl-4-dimethylamino-1,8-naphthalimide (Ph-ANI) was prepared using a two-step synthesis by adopting published procedures.^{42,43}

4-Dimethylamino-1,8-naphthalic anhydride. 4-Bromo-1,8-naphthalic anhydride (1.0 g, 3.5 mmol) was suspended in 4 ml 3-dimethylaminopropanenitrile, purged with argon and heated to reflux. The solid material completely dissolved forming a reddish-brown homogeneous solution. After three hours, the reaction solution was allowed to cool to room temperature, forming yellow precipitate. The precipitate was collected by filtration, washed with MQ water and ethanol, and dried under vacuum at elevated temperature to produce orange solid, 4-dimethylamino-1,8-naphthalic anhydride (0.52 g, 60 % yield). ¹H NMR (300 MHz, DMSO-d₆), δ / ppm: 8.60 (d, 1H), 8.47 (d, 1H), 8.34 (d, 1H), 7.77 (t, 1H), 7.21 (d, 1H), 3.17 (s, 6H).

N-phenyl-4-dimethylamino-1,8-naphthalimide (Ph-ANI). 4-Dimethylamino-1,8-naphthalic anhydride (150 mg, 0.62 mmol) was mixed with 0.34 ml aniline (~ 3.6 mmol) in 3 ml 1,2-dimethoxyethane. The reaction mixture was purged with argon and heated to 90 °C. When the reflux began, 1 ml acetic acid was added to the mixture. After 12 hours of reflux, the reaction was allowed to cool down to room temperature. The cooled

mixture was diluted with 200 ml water and the fine precipitate, which formed, was allowed to coagulate for 12 hours. The precipitate was collected by filtration, washed with MQ water and ethanol, and dried under vacuum at elevated temperature to produce orange-yellow solid, Ph-ANI, with high purity (0.11 g, 57 % yield). (The purity of the product was tested with TLC and HPLC.) ^1H NMR (300 MHz, DMSO- d_6), δ / ppm: 8.56 (d, 1H), 8.42 (d, 1H), 8.36 (d, 1H), 7.80 (t, 1H), 7.50 (m, 3H), 7.34 (d, 2H), 7.23 (d, 1H), 3.11 (s, 6H).

Cyclic voltammetry. The electrochemical measurements were conducted at ambient room temperature (~ 20 °C) using Reference 600 potentiostat-galvanostat (Gamry Instruments, PA, U.S.A.), equipped with a three-electrode cell. Glassy carbon electrode and platinum wire were used for working and counter electrodes, respectively. Saturated calomel electrode (Gamry Instruments) was used for a reference electrode. To prevent contamination, the reference electrode was brought in contact with the sample solutions via two salt bridges. When not in use, the reference electrode is stored submersed in saturated potassium chloride solution. For all samples, the ferrocene concentration was 5 mM. For each sample, at least five scans were recorded at scan rates between 0.1 and 0.5 V/min.

Fluorescence measurements. Steady state emission measurements were conducted with a FluoroLog-3 spectrofluorometer (Horiba-Jobin-Yvon) equipped with double-grating monochromators and a TBX single-photon-counting detector. By adjusting the slitwidths, the signal at all wavelengths was kept under 10^6 CPS to assure that it is within the linear range of the detector. Concurrently, the intensity of the excitation light was also

monitored at a reference detector. At each data point (1 point per nm), the fluorescence intensity (recorded at the signal detector) was divided by the excitation intensity (recorded at the reference detector) in order to correct the spectra for fluctuations in the intensity of the excitation source during the measurements. For all samples, the concentration of Ph-ANI was 10 μ M.

Data analysis. The values for the peak maxima (and minima) from the cyclic voltammograms and from the fluorescence spectra were obtained by fitting the region around the maxima (or the minima) to a Gaussian function. The quality of the fits was monitored by examination of the residuals. All least-square data fits were conducted using Igor Pro, v. 6 (Wavemetrics, Inc.) on MacOS and Windows XP workstations. For each of the cyclic voltammograms, the half-wave potentials were obtained by averaging the potentials of the cathodic and the anodic peaks. For each set of conditions, at least five measurements were conducted. The error limits (Table 2-1) represent the standard deviation obtained for the corresponding set of measurements.

References

- (1) Rehm, D.; Weller, A. *Israel Journal of Chemistry* **1970**, *8*, 259-271.
- (2) Verhoeven, J. W.; van Ramesdonk, H. J.; Groeneveld, M. M.; Benniston, A. C.; Harriman, A. *ChemPhysChem* **2005**, *6*, 2251-2260.
- (3) Braslavsky, S. E.; Acuna, A. U.; Adam, W.; Amat, F.; Armesto, D.; Atvars, T. D. Z.; Bard, A.; Bill, E.; Bjoern, L. O.; Bohne, C.; Bolton, J.; Bonneau, R.; Bouas-Laurent, H.; Braun, A. M.; Dale, R.; Dill, K.; Doepp, D.; Duerr, H.; Fox, M. A.; Gandolfi, T.; Grabowski, Z. R.; Griesbeck, A.; Kutateladze, A.; Litter, M.; Lorimer, J.; Mattay, J.; Michl, J.; Miller, R. J. D.; Moggi, L.; Monti, S.; Nonell, S.; Ogilby, P.; Olbrich, G.; Oliveros, E.; Olivucci, M.; Orellana, G.; Prokorenko, V.; Naqvi, K. R.; Rettig, W.; Rizzi, A.; Rossi, R. A.; San Roman, E.; Scandola, F.; Schneider, S.; Thulstrup, E. W.; Valeur, B.; Verhoeven, J.; Warman, J.; Weiss, R.; Wirz, J.; Zachariasse, K. *Pure and Applied Chemistry* **2007**, *79*, 293-465.
- (4) Born, M. *Zeitschrift fuer Physik* **1920**, *1*, 45-48.
- (5) Rashin, A. A.; Honig, B. *Annals of the New York Academy of Sciences* **1986**, *482*, 143-144.
- (6) Oseki, Y.; Fujitsuka, M.; Cho, D. W.; Sugimoto, A.; Tojo, S.; Majima, T. *Journal of Physical Chemistry B* **2005**, *109*, 19257-19262.
- (7) Tavernier, H. L.; Kalashnikov, M. M.; Fayer, M. D. *Journal of Chemical Physics* **2000**, *113*, 10191-10201.
- (8) Wan, J.; Ferreira, A.; Xia, W.; Chow, C. H.; Takechi, K.; Kamat, P. V.; Jones, G.; Vullev, V. I. *Journal of Photochemistry and Photobiology, A: Chemistry* **2008**, *197*, 364-374.
- (9) Zhang, J.; Bond, A. M. *Analyst* **2005**, *130*, 1132-1147.
- (10) Rogers, E. I.; Silvester, D. S.; Poole, D. L.; Aldous, L.; Hardacre, C.; Compton, R. G. *Journal of Physical Chemistry C* **2008**, *112*, 2729-2735.
- (11) Gritzner, G. *Pure and Applied Chemistry* **1990**, *62*, 1839-1858.
- (12) Bond, A. M.; Henderson, T. L. E.; Mann, D. R.; Mann, T. F.; Thormann, W.; Zoski, C. G. *Analytical Chemistry* **1988**, *60*, 1878-1882.
- (13) Montenegro, M. I.; Pletcher, D. *Journal of Electroanalytical Chemistry and Interfacial Electrochemistry* **1986**, *200*, 371-374.
- (14) Tsierekzos, N. G. *Journal of Solution Chemistry* **2007**, *36*, 289-302.
- (15) Abeed, F. A.; Al-Allaf, T. A. K.; Sulaiman, S. T. *Analyst* **1988**, *113*, 333-336.

- (16) Bond, A. M.; McLennan, E. A.; Stojanovic, R. S.; Thomas, F. G. *Analytical Chemistry* **1987**, *59*, 2853-2860.
- (17) Oldham, K. B. *Journal of Electroanalytical Chemistry and Interfacial Electrochemistry* **1988**, *250*, 1-21.
- (18) Drew, S. M.; Wightman, R. M.; Amatore, C. A. *Journal of Electroanalytical Chemistry and Interfacial Electrochemistry* **1991**, *317*, 117-124.
- (19) Pendley, B. D.; Abruna, H. D.; Norton, J. D.; Benson, W. E.; White, H. S. *Analytical Chemistry* **1991**, *63*, 2766-2771.
- (20) Casteel, J. F.; Angel, J. R.; McNeeley, H. B.; Sears, P. G. *Journal of the Electrochemical Society* **1975**, *122*, 319-324.
- (21) Rebagay, T. V.; Casteel, J. F.; Sears, P. G. *Journal of the Electrochemical Society* **1974**, *121*, 977-982.
- (22) Bento, M. F.; Geraldo, M. D.; Montenegro, M. I. *Analytica Chimica Acta* **1999**, *385*, 365-371.
- (23) Zhou, H.; Dong, S. *Electrochimica Acta* **1997**, *42*, 1801-1807.
- (24) Dong, S.; Zhou, H. *Journal of Electroanalytical Chemistry* **1996**, *403*, 117-123.
- (25) Martin, R. D.; Unwin, P. R. *Analytical Chemistry* **1998**, *70*, 276-284.
- (26) Ikeuchi, H.; Kanakubo, M. *Electrochemistry (Tokyo)* **2001**, *69*, 34-36.
- (27) Jacob, S. R.; Hong, Q.; Coles, B. A.; Compton, R. G. *Journal of Physical Chemistry B* **1999**, *103*, 2963-2969.
- (28) Lockard, J. V.; Wasielewski, M. R. *Journal of Physical Chemistry B* **2007**, *111*, 11638-11641.
- (29) Chernick, E. T.; Mi, Q.; Vega, A. M.; Lockard, J. V.; Ratner, M. A.; Wasielewski, M. R. *Journal of Physical Chemistry B* **2007**, *111*, 6728-6737.
- (30) Chernick, E. T.; Mi, Q.; Kelley, R. F.; Weiss, E. A.; Jones, B. A.; Marks, T. J.; Ratner, M. A.; Wasielewski, M. R. *Journal of the American Chemical Society* **2006**, *128*, 4356-4364.
- (31) Keinan, S.; Ratner, M. A.; Marks, T. J. *Chemical Physics Letters* **2006**, *417*, 293-296.
- (32) Sinks, L. E.; Weiss, E. A.; Giaimo, J. M.; Wasielewski, M. R. *Chemical Physics Letters* **2005**, *404*, 244-249.
- (33) Veale, E. B.; Gunnlaugsson, T. *Journal of Organic Chemistry* **2008**, *73*, 8073-8076.

- (34) Grabchev, I.; Dumas, S.; Chovelon, J.-M.; Nedelcheva, A. *Tetrahedron* **2008**, *64*, 2113-2119.
- (35) Bard, A. J.; Faulkner, L. R. *Electrochemical Methods: Fundamentals and Applications*, 2 ed.; John Wiley & Sons, Inc., 2001.
- (36) Kanato, H.; Takimiya, K.; Otsubo, T.; Aso, Y.; Nakamura, T.; Araki, Y.; Ito, O. *Journal of Organic Chemistry* **2004**, *69*, 7183-7189.
- (37) van Haare, J. A. E. H.; Groenendaal, L.; Peerlings, H. W. I.; Havinga, E. E.; Vekemans, J. A. J. M.; Janssen, R. A. J.; Meijer, E. W. *Chemistry of Materials* **1995**, *7*, 1984-1989.
- (38) Kumagai, A.; Fukumoto, H.; Yamamoto, T. *Journal of Physical Chemistry B* **2007**, *111*, 8020-8026.
- (39) Bennett, B. L.; Robins, K. A.; Tennant, R.; Elwell, K.; Ferri, F.; Bashta, I.; Aguinaldo, G. *Journal of Fluorine Chemistry* **2006**, *127*, 140-145.
- (40) Paolucci, F.; Carano, M.; Ceroni, P.; Mottier, L.; Roffia, S. *Journal of the Electrochemical Society* **1999**, *146*, 3357-3360.
- (41) Paddon, C. A.; Bhatti, F. L.; Donohoe, T. J.; Compton, R. G. *Journal of Physical Organic Chemistry* **2007**, *20*, 115-121.
- (42) Plakidin, V. L.; Vostrova, V. N. *Zhurnal Organicheskoi Khimii* **1983**, *19*, 2591-2600.
- (43) Plakidin, V. L.; Vostrova, V. N. *Zhurnal Organicheskoi Khimii* **1981**, *17*, 1118-1119.

Tables

Table 2-1. Half-wave oxidation potentials of ferrocene, $E_{\text{Fc}^+/\text{Fc}}^{(1/2)}$, for different solvents in the presence of various concentrations of TBATFB.^a

$C_{\text{TBATFB}} / \text{mM}$	solvent		
	CH_2Cl_2	MeCN	DMF
1	1.12 ± 0.02	0.600 ± 0.008	0.487 ± 0.006
2	0.878 ± 0.029	0.561 ± 0.002	0.484 ± 0.004
5	0.754 ± 0.016	0.564 ± 0.003	0.479 ± 0.001
10	0.734 ± 0.006	0.539 ± 0.007	0.476 ± 0.010
20	0.667 ± 0.001	0.481 ± 0.002	0.444 ± 0.001
50	0.630 ± 0.004	0.469 ± 0.002	0.441 ± 0.002
100	0.600 ± 0.003	0.454 ± 0.006	0.436 ± 0.004
200	0.549 ± 0.006	0.445 ± 0.005	0.429 ± 0.003
500	0.521 ± 0.004	0.441 ± 0.003	0.427 ± 0.002

^a The oxidation potentials are reported in V vs. SCE.

Table 2-2. Dielectric constants, ϵ , of CH_2Cl_2 solutions containing TBATFB with different concentration.^a

$C_{\text{TBATFB}} / \text{mM}$	ϵ
0	8.93
1	9.23
2	9.26
5	9.36
10	9.77
20	10.5
50	12.4
100	14.1
200	18.0
500	24.2

^a The dielectric constants are obtained from fluorescence data (Figure 2- 3 and 2-5).

Table 2-3. Extrapolated half-wave oxidation potentials of ferrocene, $E_{\text{Fc}^+/\text{Fc}}^{(1/2)}$, for neat dichloromethane (CH_2Cl_2), acetonitrile (MeCN) and dimethylformamide (DMF).^a

solvent	ϵ	ϵ^{-1}	$E_{\text{Fc}^+/\text{Fc}}^{(1/2)}$ ^b	$E_{\text{Fc}^+/\text{Fc}}^{(1/2)}$ ^c
CH_2Cl_2	8.93	0.112	0.71	0.69
MeCN	36.6	0.0273	0.48	0.49
DMF	38.3	0.0261	0.47	0.45
<i>super polar media</i> ^d	∞	0.000	0.40	—

^a The oxidation potentials are reported in V vs. SCE.

^b Oxidation potentials for neat solvents obtained from the linear correlation between the measured half-wave potential and the inverse dielectric constant for electrolyte solutions, for the range between 20 and 500 mM TBATFB in CH_2Cl_2 (Figure 2-6).

^c Oxidation potentials for neat solvents obtained from the exponential relation between the half-wave potential and electrolyte concentration for the corresponding CH_2Cl_2 , MeCN and DMF solutions (Figure 2-7)

^d Media with high dielectric constant, for which ϵ^{-1} can be approximated to zero.

Figures

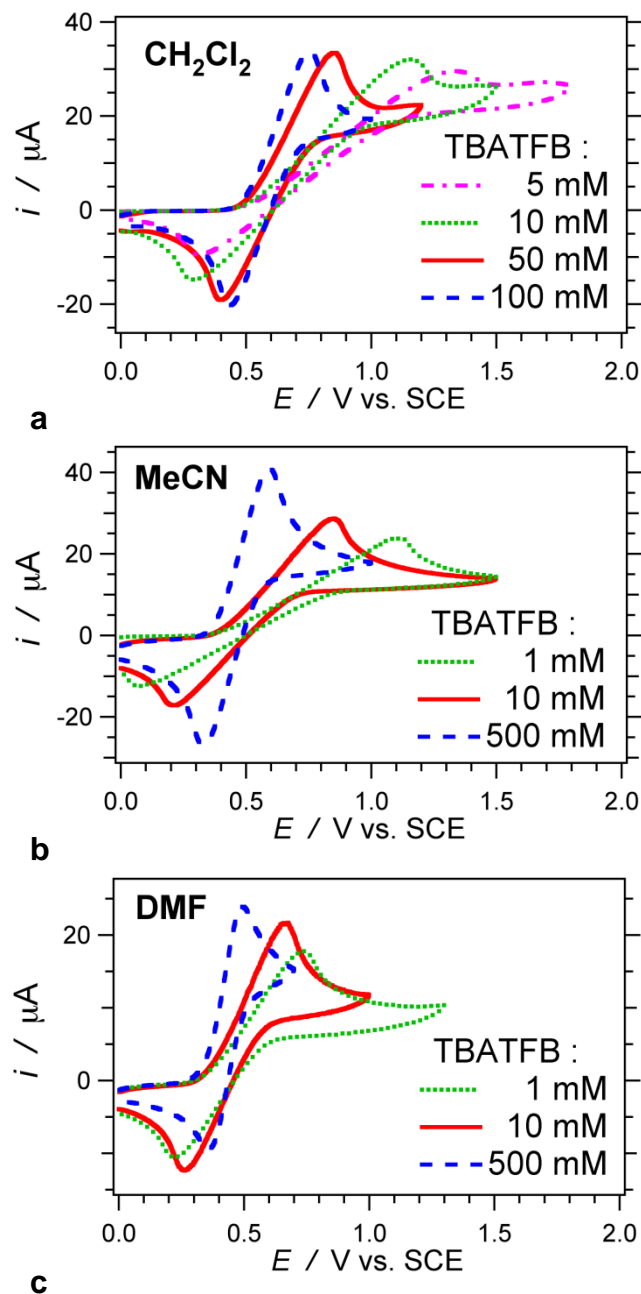


Figure 2-1. Cyclic voltammograms for ferrocene (5 mM) in the presence of various concentrations of supporting electrolyte, TBATFB, for different solvents: (a) dichloromethane, (b) acetonitrile and (c) dimethylformamide. (Scan rates = 50 mV / s)

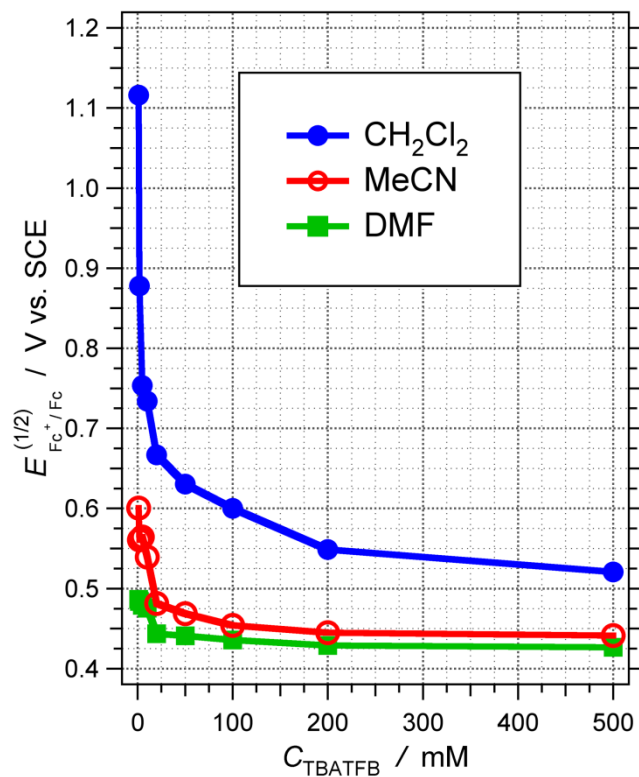


Figure 2-2. Dependence of the half-wave oxidation potential of ferrocene, $E_{\text{Fc}^+/\text{Fc}}^{(1/2)}$, on the concentration of the supporting electrolyte, C_{TBATFB} , for three different solvents.

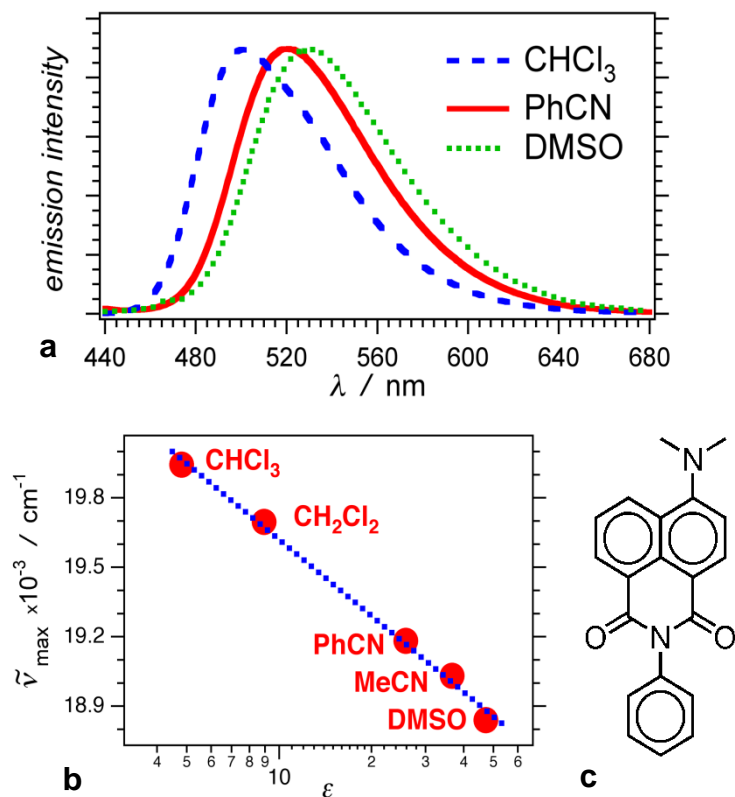


Figure 2-3. Solvatochromism of Ph-ANI. **(a)** Fluorescence spectra of Ph-ANI for different solvents (10 μM Ph-ANI, $\lambda_{\text{ex}} = 410$ nm, intensities normalized at $I_{\text{fl}}^{(\text{max})}$). **(b)** Dependence of the fluorescence maximum on the dielectric constant of the solvent: chloroform (CHCl₃), dichloromethane (CH₂Cl₂), benzonitrile (PhCN), acetonitrile (MeCN) and dimethylsulfoxide (DMSO). **(c)** Structural chemical formula of Ph-ANI.

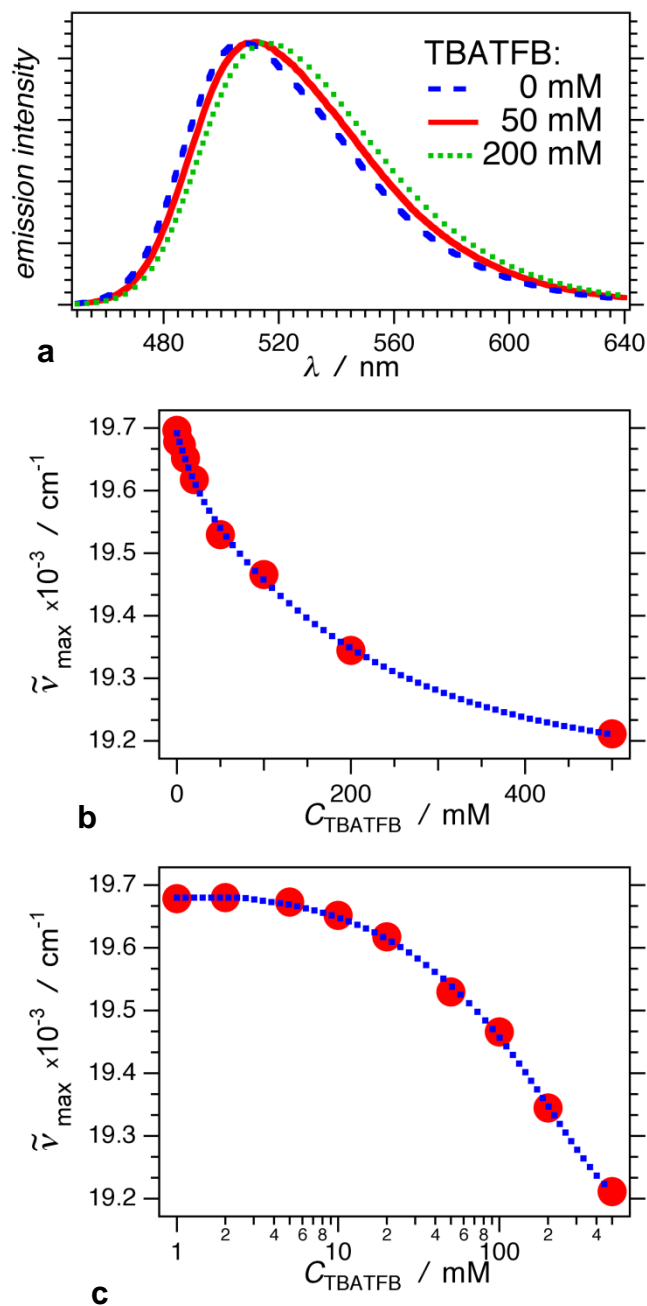


Figure 2-4. Fluorescence properties of Ph-ANI for dichloromethane with various concentrations of electrolyte, TBATFB. **(a)** Fluorescence spectra of Ph-ANI in the presence of various concentrations of TBATFB (10 μM Ph-ANI, $\lambda_{\text{ex}} = 410 \text{ nm}$, intensities normalized at $I_{\text{fl}}^{(\text{max})}$). **(b, c)** Dependence of the fluorescence maximum on the electrolyte concentration, C_{TBATFB} , presented **(b)** linearly and **(c)** logarithmically. The dotted lines represent an exponential fit of the fluorescence maximum vs. TBATFB concentration.

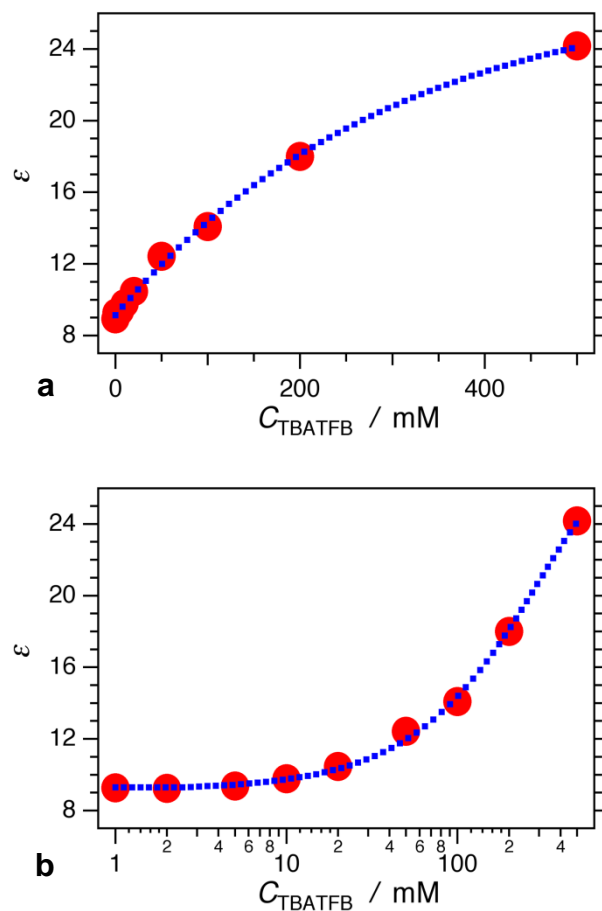


Figure 2-5. Dependence of the dielectric constant of the electrolyte solutions, ϵ , on the electrolyte concentration, C_{TBATFB} , presented (a) linearly and (b) logarithmically. The values of ϵ were obtained from the values of the fluorescence maxima (Figure 2- 4b, c) and the calibration line on Figure 2-3b. The dotted lines represent an exponential fit of the dielectric constant vs. TBATFB concentration.

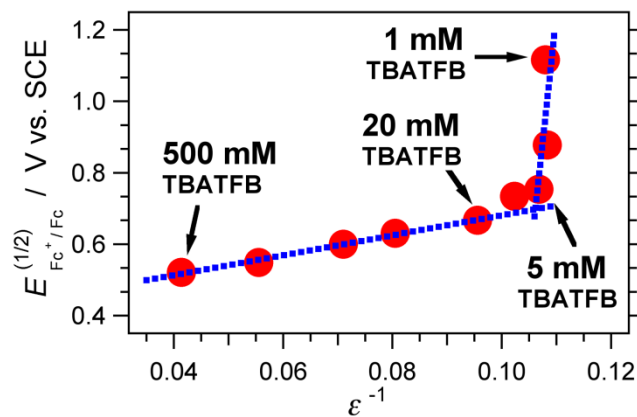


Figure 2-6. Correlation between the half-wave oxidation potential of ferrocene and the inverse dielectric constant of dichloromethane solutions with different concentrations of electrolyte, TBATFB. The correlation coefficient for the region between 20 mM and 500 mM TBATFB is 0.997.

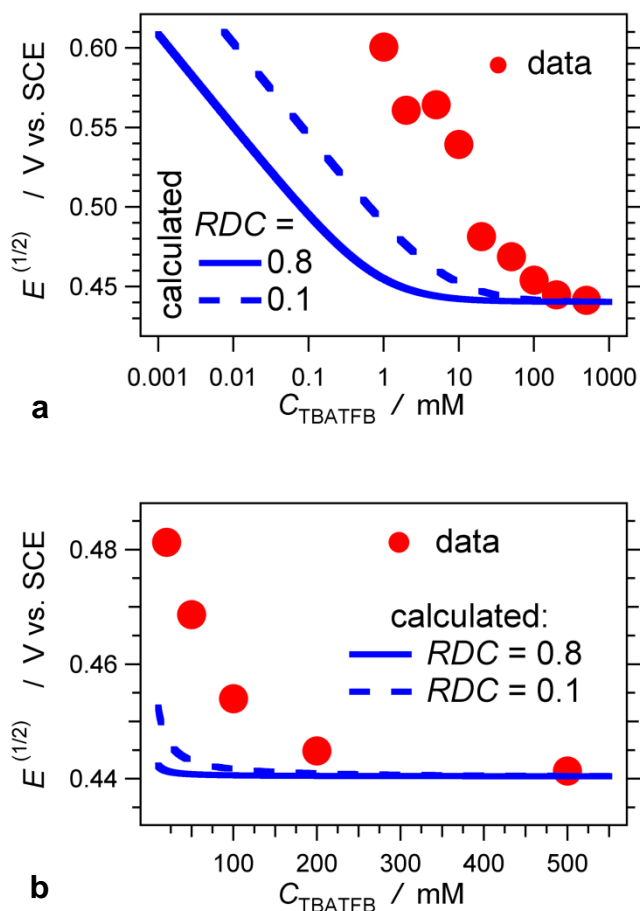


Figure 2-7. Comparison between the experimentally measured and the calculated (from equation 2-4) dependence of the half-wave potential of ferrocene, $E_{\text{Fc}^+/\text{Fc}}^{(1/2)}$, on the concentration of the supporting electrolyte, C_{TBATFB} , for acetonitrile. Calculated dependence for two diffusion coefficient ratios, $RDC = D_{\text{Fc}^+}/D_{\text{Fc}}$, and the measured values represented in (a) a logarithmic concentration scale, and (b) a linear concentration scale. The reported values for D_{Fc^+} and D_{Fc} in concentrated electrolyte solution in MeCN are about 2.1×10^{-5} and 2.6×10^{-5} $\text{cm}^2 \text{s}^{-1}$, respectively, for which $RDC = 0.8$. The RDC value of 0.1 is hypothetical for demonstrating the dependence of $E_{\text{Fc}^+/\text{Fc}}^{(1/2)}$ on C_{TBATFB} .

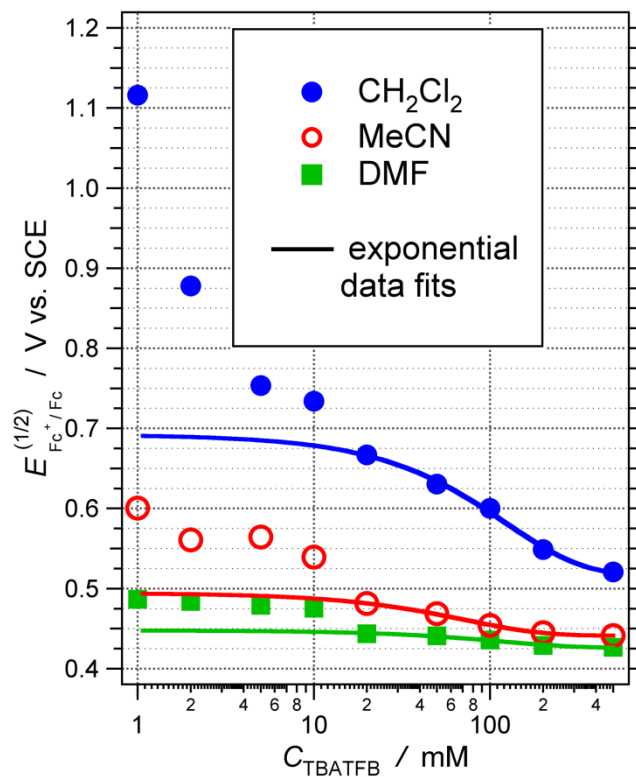
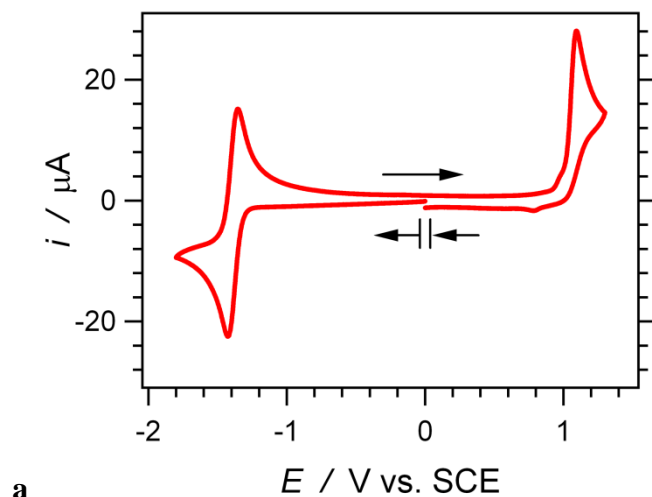
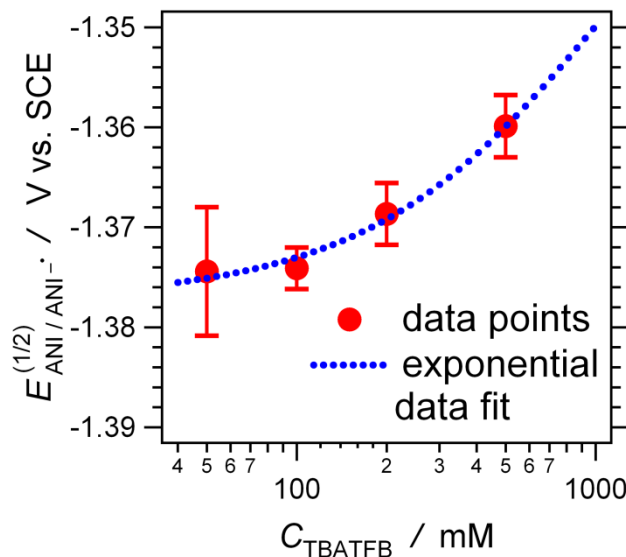


Figure 2-8. Dependence of the half-wave oxidation potential of ferrocene on the concentration of the supporting electrolyte. The exponential data fits were performed for the concentration region between 20 mM and 500 mM TBATFB.



a



b

Figure 2-9. Electrochemical properties of Ph-ANI. **(a)** Cyclic voltammogram of Ph-ANI (5 mM) for acetonitrile in the presence of 100 mM TBATFB, recorded at scan rate 50 mV / s. The arrows indicate the direction of the scan with the initial and the final point. **(b)** Dependence of the half-wave reduction potential of Ph-ANI for acetonitrile, $E_{\text{ANI}/\text{ANI}^{\bullet-}}^{(1/2)}$, on the electrolyte concentration, C_{TBATFB} , with a monoexponential data fit for extrapolation of the value of $E_{\text{ANI}/\text{ANI}^{\bullet-}}^{(1/2)}$ for neat solvent, i.e., for $C_{\text{TBATFB}}=0$.

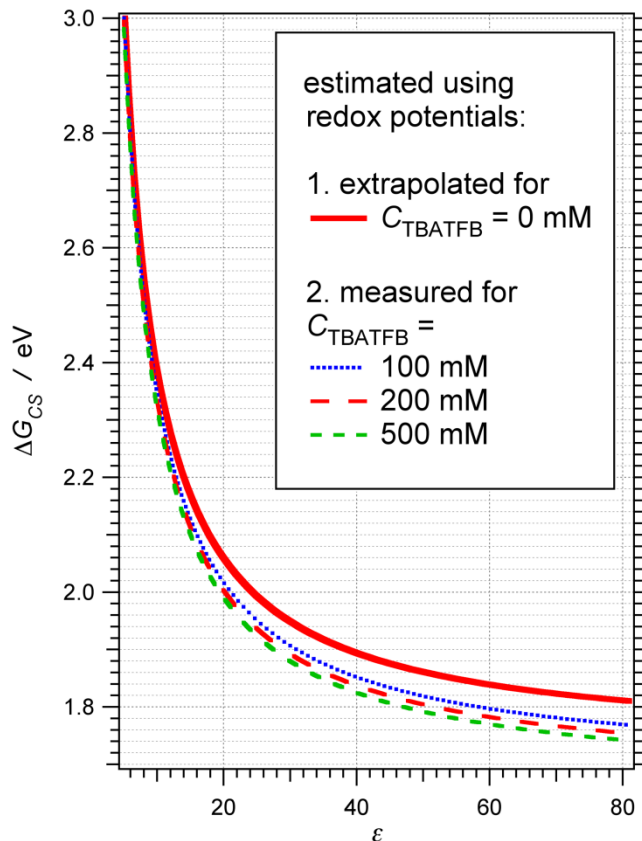


Figure 2-10. Dependence of the charge-separation energy, ΔG_{CS} , on the dielectric constant of the media, ϵ , calculated using equations 2-1 – 2-3 for a charge-transfer system, in which ferrocene is an electron donor and Ph-ANI is an electron acceptor: $\Delta G_{CS} = \Delta G_{et}^{(0)} + \mathcal{E}_{00}$; $r_D = 2.6 \text{ \AA}$, $r_A = 3.0 \text{ \AA}$ and $R_{DA} = 10 \text{ \AA}$. For the oxidation potentials of the donor, $E_{D^{2D^{+n}}/D^{2D}}^{(0)} \approx E_{Fc^+/Fc}^{(1/2)}$, and for the reduction potential of the acceptor, $E_{A^{2A}/A^{2A-n}}^{(0)} \approx E_{ANI^+/ANI}^{(1/2)}$, we used the values of the half-wave potentials: (1) measured for acetonitrile electrolyte solutions, 100, 200 and 500 mM TBATFB; or (2) extrapolated to $C_{TBATFB} = 0 \text{ mM}$ for neat acetonitrile. All ΔG_{CS} vs. ϵ curves have the same shape. Because we adopted $\epsilon_D = \epsilon_A = 36.6$ (i.e., for neat acetonitrile, $C_{TBATFB} = 0$) for all calculations, the direct use of half-wave redox potentials in equation 2-1 for measurements for acetonitrile electrolyte solutions underestimates ΔG_{CS} with about 0.04, 0.06 and 0.07 eV for 100, 200 and 500 mM TBATFB.

Chapter 3

Electrochemical Reduction of Quinones: Interfacing Experiment and Theory for Defining Effective Radii of Redox Moieties

Abstract

Using cyclic voltammetry, we examined the dependence of the reduction potentials of six quinones on the concentration of the supporting electrolyte. An increase in the electrolyte concentration, resulting in an increase in the solution polarity, caused positive shifts of the reduction potentials. We ascribed the observed changes in the potentials to the dependence of the solvation energy of the quinones and their anions on the media polarity. Analysis of the reduction potentials, using the Born solvation-energy equation, yielded unfeasibly small values for the effective radii of the quinone species: i.e., the experimentally obtained effective radii were up to four-fold smaller than the radii of the solvation cavities that we calculated for the quinones. The non-spherical shapes of the quinones, along with the uneven charge-density distribution in their anions, encompassed the underlying reasons for the discrepancies between the obtained experimental and theoretical values for the radii of these redox species. The generalized Born approach, which does not treat the solvated species as single spheres, provided means for addressing this discrepancy and yielded effective radii that were relatively close to the measured values.

Keywords: solvation, polarity, solvatochromism, cyclic voltammetry, impedance spectroscopy, charge transfer, electron transfer, Rehm Weller equation

Introduction

This article describes an electrochemistry study of benzo- and naphthaquinones. Our findings reveal a pronounced dependence of the quinone reduction potentials on the concentration of the supporting electrolyte. An increase in the electrolyte concentration causes a positive shift in the values of the measured reduction potentials of the quinones. We ascribe the observed positive shifts to the electrolyte-induced increase in the media polarity. The Born solvation energy, estimated via the widely used spherical approximation for molecular ions, fails to quantify the observed trends. As an alternative, a generalized Born approach,^{1,2} which represents molecular species as collections of spheres, yields results that agrees with the experimental findings and demonstrates plausible means for addressing the potential deficiencies with the single-sphere approximation of organic ions.

Electron transfer processes play a key role in chemical and biological systems.³⁻²³ Photoinduced electron transfer represents the central paradigm of light-energy conversion, e.g., of photosynthesis²⁴⁻³¹ and of photovoltaics.³²⁻³⁹ Rehm-Weller equation allows for estimation of the thermodynamic driving force, i.e., the change in the Gibbs energy, $\Delta G_{\text{et}}^{(0)}$, of photoinduced charge-transfer processes, by employing readily measurable quantities such as the redox potentials of electron donors and acceptors.⁴⁰⁻⁴²

A significant portion of the values of measured standard redox potentials (essential for estimation of $\Delta G_{\text{et}}^{(0)}$) encompasses a contribution of the solvation of the charged species involved in the electron-transfer processes. The Born equation for the electrostatic component of the solvation energy, ΔG_S , of spherical ions with radius R and charge Z , in

medium with dielectric constant ϵ , is $\Delta G_S = -Z^2 e^2 (8\epsilon\epsilon_0 R)^{-1} (1 - \epsilon^{-1})$.^{43,44} The Born expression allows for quantification of the solvation contribution to the redox potentials and it is introduced as a correction term in the Rhem-Weller equation in order to relate thermodynamic data acquired for media with different polarities.⁴²

Assuming a spherical shape for the ionic species, however, presents an important approximation in the Born solvation-energy expression. For metal ions and for a range of chelates, such a single-sphere approximation is acceptable. Very few organic molecules and protein co-factors, however, have shapes that resemble spheres. Therefore, for estimation of the energetics of electron-transfer systems comprising non-spherical redox species, the assignment of the values of effective radii involves non-trivial assumptions.

Experimentally obtained molecular volumes provide means for estimation of effective radii, assuming spherical shape of the solute species. For example, molecular volumes, obtained from mass-density, sound-velocity or refractivity measurements allow for estimation of “average” effective radii.⁴⁵⁻⁵⁷ Diffusivity characteristics of molecules and their ions yield values for their effective Stokes radii,⁵⁸⁻⁷⁴ which represent their mass-transport properties.⁷⁵ Alternatively, from x-ray or NMR structural data, the radius of a spherical solvation cavity can be ascribed to the distance from the center of mass of the solvated molecule to its most distal van der Waals boundary.⁷⁶⁻⁷⁸ For moieties with highly irregular shapes, however, this approach provides dimensions that are an overestimation of the effective radii reflecting their redox and charge-transfer behavior observed experimentally. Fitting such molecular species into ellipsoid cavities, allows for representing the effective radii as averages of the three ellipsoid axes.⁷⁹ Even this

approach of averaging the length, width and height of such molecular moieties can overestimate the effective radii for molecular ions with localized charges.⁸⁰⁻⁸³

Although reaction-field theory allows for analytical and numerical solutions for the solvation energies of species with, respectively, ellipsoid and arbitrary shapes,⁸⁴⁻⁸⁹ the significant increase in the number of parameters appears to prevent their use for analysis of charge-transfer systems. The commodity of representing the molecular dimensions with a single parameter – an effective radius – underlines the need for relating this parameter with the structural features of the molecular ions.

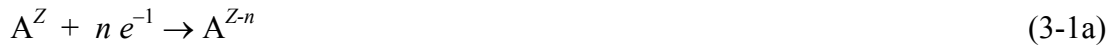
Herein, we examine the relation between the effective radii of quinone derivatives (obtained electrochemically) and their molecular dimensions. Using cyclic voltammetry, we examined the solvation-induced trends in the redox properties of six quinones (Scheme 3-1). Varying the concentration of the supporting electrolyte allowed for inducing changes in the media polarity.⁴² An increase in the solution polarity, indeed, caused positive shifts in the reduction potentials of the quinones. We ascribed the observed effects to the dependence of the quinone solvation energy on the media polarity. The long aliphatic chains attached to the quinone rings did not provide notable contribution to the solvation stabilization of the quinones: i.e., the dependence of the reduction potentials of coenzyme Q₁₀ and vitamin K₁ on the media polarity was similar to the media-polarity dependence for 1,4-benzoquinone and 1,4-naphthaquinone, respectively (Scheme 3-1).

Adopting the single-sphere approximation for the Born solvation energy (equation 3-2) failed to feasibly quantify the trends in the reduction properties of the quinones

induced by the variations in the media polarity. Via applying the Born relation to the redox data (equations 3-1b and 3-2b), we obtained effective radii for all six quinones that were unfeasibly small. The thus experimentally obtained effective radii were up to four-fold smaller than the theoretical values for the radii that we obtained from *ab initio* calculations of the corresponding molecular volumes. Alternatively, a generalized Born approach, which does not treat the charged molecular species as spherical entities,^{1,2,90-95} manifested a good agreement with the experimental findings. Further examination revealed that the charge localization was the principle underlying reason for the observed discrepancy between theory and experiment.

Results and Discussion

Accounting for solvation in redox processes. The solvation-energy dependence of the redox potential, $E^{(0)}$, of an n -electron reduction of species, A, with a charge Z , is:



$$E^{(0)} = E^{(0,ns)} + \frac{\Delta G_S^{(0)}}{nF} \quad (3-1b)$$

where $E^{(0,ns)}$ is the standard redox potential in the absence of solvation; F is the Faraday constant; and $\Delta G_S^{(0)}$ represents the change in the solvation of species A upon the alteration of their charge:

$$\Delta G_S^{(0)} = \frac{e^2}{8\pi\epsilon_0} \left(\frac{(Z-n)^2}{R_{Red}} - \frac{Z^2}{R_{Ox}} \right) \left(1 - \frac{1}{\epsilon} \right) = \frac{\Xi_{Red} - \Xi_{Ox}}{8\pi\epsilon_0} \left(1 - \frac{1}{\epsilon} \right) \quad (3-2a)$$

where e is an elementary charge; ϵ_0 is the dielectric permittivity of vacuum; and R_{Red} and R_{Ox} are defined as the radii of the cavities that accommodate, respectively, the reduced, A^{Z-n} , and the oxidized, A^Z , species. The charge-to-size ratios, Ξ_{Red} and Ξ_{Ox} , for the reduced and the oxidized species, respectively, have units of charge square over distance. Assuming negligible change in the size of A^Z upon reduction, i.e., $R = R_{Red} \approx R_{Ox}$, allows for simplifying the solvation-energy correction term for the redox potential, $E^{(0)}$:

$$\Delta G_s^{(0)} \approx \frac{(n - 2Z)ne^2}{8\pi\epsilon_0 R} \left(1 - \frac{1}{\epsilon}\right) \quad (3-2b)$$

□ These expressions (equations 3-1b and 3-2b) depict two important trends for the redox properties of non-charged species (equation 3-1a): (1) an increase in the media polarity results in negative shifts in the oxidation potentials and positive shifts in the reduction potentials; and (2) the redox potentials of smaller species are more susceptible to changes in the media polarity. The former trend is readily explained by the fact that polar media stabilizes charged species. For reduction of electro-neutral species, the oxidized form is charged. An increase in the media polarity, therefore, drives the redox equilibrium toward the oxidized form and increases the reducing potency of the species, and hence, results in negative shifts in the standard redox potential. Similar argument stands for the reduction potentials of electro-neutral species, for which the reduced form is negatively charged (equation 3-1a). The latter trend reflects the electrostatic requirement for increased electric-field density, generated by fewer media dipoles, to stabilize a charge confined in

a smaller solvation cavity: i.e., a decrease in R requires an increase in ϵ to achieve the same electrostatic “screening” of the confined charge.

We have previously demonstrated the dependence of the redox potentials of ferrocene and of an aminonaphthalimide derivative on the media polarity.⁴² The oxidation potential of ferrocene shifted toward more negative values upon an increase in the electrolyte concentration and in the polarity of the organic solvents used.⁴² Concurrently, the reduction potential of the aminonaphthalimide shifted toward more positive values as the media polarity increased.⁴²

Quinone reduction. Due to their large electron affinities,⁹⁶⁻⁹⁹ quinones represent a widely preferred choice for electron acceptors in synthetic charge-transfer systems.¹⁰⁰⁻¹⁰⁹ Furthermore, derivatives of quinones have key importance for biological redox processes, such as photosynthesis and cellular respiration.¹¹⁰⁻¹¹⁵ For example, two plastoquinones – derivatives of 2,3-dimethyl-1,4-benzoquinone with long aliphatic chains – are a part of the electron-transfer chain of Photosystem II and one of them, Q_B, provides means for transmembrane proton transport via double reduction/oxidation.¹¹⁶⁻¹²¹ Similar quinones mediate the same functions in the bacterial photosynthetic reaction center.¹²²⁻¹²⁶ Ubiquinones, also known as coenzyme Q, – derivatives 2,3-dimethoxy-5-methyl-1,4-benzoquinone, also with long aliphatic chains – are a key component of the respiratory electron-transport chain.¹²⁷⁻¹³² Among them, coenzyme Q₁₀ is the most abundant quinone in the human mitochondria and it has significant health implications.¹³³⁻¹⁴¹ (The subscript 10 refers to the number of isoprenylene units in the aliphatic chain (Scheme 3-1).)

Photosynthesis and respiration are not the only biological processes that take advantage of the redox properties of quinones. For example, a group of lipophilic vitamins, denoted as vitamin K – derivatives of 2-methyl-1,4-naphthaquinone with long aliphatic chains (Scheme 3-1) – are essential for posttranslational carboxylation of glutamates in certain proteins involved in the blood coagulation cascade¹⁴²⁻¹⁴⁵ and in mineralization of tissues such as bone and dentin.¹⁴⁶⁻¹⁵⁰

The two one-electron reduction steps of quinones are characterized with standard redox potentials $E_1^{(0)}$ and $E_2^{(0)}$:



Accordingly, the cyclic voltammograms revealed two distinct reduction steps for the investigated quinones (Figure 3-1a).^{79,151-153} Because of the reversibility of the investigated electrochemical reduction steps, we used the half-wave potentials instead of the corresponding standard reduction potentials for our analysis: i.e., $E_i^{(1/2)} \approx E_i^{(0)}$.

The choice of solvent and electrolyte for the electrochemical measurements was driven by two factors essential for this study: (1) no hydrogen-bonding capabilities; and (2) low media dielectric constants. The redox properties of quinones are sensitive to protonation of the phenolate oxygens of Q^- and Q^{2-} (equation 3-3).^{151,152} Therefore, using a solvent and an electrolyte that cannot form hydrogen bonds or chelate oxygens ensured that the observed changes in the redox properties did not result specific interactions involving the quinone oxygens.

Media polarity, γ , is inversely proportional to the negative value of its dielectric constant, ϵ , i.e., $\gamma = (n^{-2} - \epsilon^{-1})$; where n is the index of refraction and n^2 , hence, is viewed as the dynamic dielectric constant of non-magnetic media. The differences between the refractive indexes of the used electrolyte solutions, however, are negligible (Table 3-1). For this study, therefore, the dielectric properties of the solutions account for their polarities.

The Born solvation energy has a similar dependence as γ on the dielectric properties of the media: i.e., $\Delta G_S \propto 1 - \epsilon^{-1}$ (equation 3-2).^{43,44} A solvent with a relatively small dielectric constant ought to exhibit relatively large changes not only in ϵ , but also in ϵ^{-1} upon addition of electrolyte. Therefore, the use of electrolyte solutions in non-polar solvent allows for exploration of a relatively broad range of ϵ^{-1} and ΔG_S .

Based on the above two considerations, i.e., no hydrogen bonding and low polarity, we chose chloroform solutions of tetrabutylammonium hexafluorophosphate (Bu_4NPF_6) with different concentrations. Use of chloroform, however, posed a limitation due to its relatively narrow redox window. The Faradaic currents, resultant from the reduction of chloroform, became apparent at potentials more negative than about -1.5 V vs. SCE (Figure 3-1a). Therefore, in this study we focused predominantly on the first one-electron reduction of the quinone species, i.e., on $E_1^{(1/2)}$ (equation 3-3a).

The reduction potentials of all six quinones manifested dependence on the electrolyte concentration, $C_{\text{Bu}_4\text{NPF}_6}$ (Figure 3-1b, c, d). Exponential fits allowed us to extrapolate the reduction potentials for the neat solvent, i.e., for $C_{\text{Bu}_4\text{NPF}_6} = 0$ (Table 3-1).⁴² As we have demonstrated, the use of such extrapolated values for the redox potentials in the Rehm-

Weller equation proves immensely convenient for estimation of the charge-transfer driving forces by considering solely the dielectric properties of the neat solvents (rather than of the electrolyte solution) for the Born correction term.⁴²

Polarity of the electrolyte solutions. We ascribed the observed electrolyte-concentration dependence of the reduction potentials to the variations of the dielectric properties of the chloroform solutions. An increase in the concentration of the supporting electrolyte, increases the dielectric constant of the chloroform solutions,¹⁵⁴ and hence, of $\Delta G_s^{(0)}$, causing positive shifts in the values of $E^{(0)}$ (equations 3-1b and 3-2).

The fluorescence solvatochromism of *N*-phenyl-4-dimethylamino-1,8-naphthalimide (Ph-ANI), which can be readily prepared in two synthetic step,^{42,155,156} allowed us to determine the dielectric constants of the electrolyte solutions.⁴² For non-polar solvents (such as tetrachloromethane and hexane, which do not have a permanent molecular dipole moment), the fluorescence spectra of Ph-ANI revealed two overlapping bands (Figure 3-2a). For relatively polar solvents, however, the Ph-ANI fluorescence spectra exhibited a single band, which shifted to the red with an increase in the media polarity (Figure 3-2a).

The observed spectral behavior of Ph-ANI was consistent with the formation of an twisted intramolecular charge-transfer (TICT) excited state,¹⁵⁷⁻¹⁶⁰ involving the electron-donating dimethylamine group attached to the electron-withdrawing naphthalimide.^{161,162} For dialkylamine aromatic chromophores, two opposing effects determine the dihedral angle of the arylamine C-N bond. While the conjugation of the amine free electron pair

with the aromatic π -system stabilizes the planar conformation, the steric hindrance between the alkyls and the aromatic ring drives toward twisted conformation. Upon excitation, the move of an electron to an orbital with antibonding character decreases the strength of the amine-aryl π -conjugation increasing the preference for the twisted conformation. Although the π -conjugation polarizes the dialkylamine aromatic moieties, the charge-transfer character of the twisted states results in increased polarization and pronounced solvatochromism.

For non-polar media, while the blue-shifted fluorescence of Ph-ANI was ascribed to the decay from an excited state with conformation close to the conformation of the ground state, the red-shifted fluorescence was ascribed to a radiative transition from a TICT state (Figure 3-2a). An increase in the media polarity stabilized the polar TICT state, causing the observed red shift of the fluorescence. Furthermore, such polarity-induced lowering of the energy of the charge-transfer state made the TICT conformer the predominant source for the radiative decay, resulting in the single-band fluorescence spectra observed for relatively polar solvents (Figure 3-2a).

The TICT fluorescence of Ph-ANI manifested a strong dependence on the dielectric properties of the media (Figure 3-2b).^{42,161} This dependence allowed us to estimate the dielectric constants of the chloroform Bu_4NPF_6 solutions (Figure 3-2c, d). Our findings revealed about four-fold increase in the dielectric constant with an increase in the electrolyte concentration, $C_{\text{Bu}_4\text{NPF}_6}$, from 0 to 300 mM (Figure 3-2d, Table 3-1). The measured refractive index, however, showed only 0.05% – 0.1% decrease with the addition of the electrolyte.

Correlation between reduction potentials and solvent dielectric properties. The difference between the reduction potentials, measured for $C_{\text{Bu}_4\text{NPF}_6} = 100$ mM and for $C_{\text{Bu}_4\text{NPF}_6} = 300$ mM, demonstrated the extent of dependence of the redox properties of the quinones on the electrolyte concentration (Table 3-1). The reduction of 1,4-benzoquinone (BQ) manifested strongest dependence on the amount of electrolyte in the media (Table 3-1), which was consistent with its smallest molecular size in comparison with the other quinones (Scheme 3-1): i.e., the smallest effective cavity radius, R (equation 3-2b).

The reduction potentials of the largest quinones, coenzyme Q₁₀ (CoQ₁₀) and vitamin K₁ (VK₁) (Scheme 3-1), however, did not manifest the smallest dependence on the electrolyte concentration (Table 3-1). Hence, the aliphatic chains attached to the quinone rings did not contribute significantly to the effective radii, R_{Ox} , R_{Red} or R , of the species (equation 3-2).

We observed the smallest dependence of $E_1^{(1/2)}$ on $C_{\text{Bu}_4\text{NPF}_6}$ for the two chlorinated quinones, 2,3-dichloro-1,4-naphthaquinone (CL2NQ) and 2,3,5,6-tetrachloro-1,4-benzoquinone (CL4BQ) (Table 3-1). The redox behavior of both chlorinated species manifested almost the same dependence on $C_{\text{Bu}_4\text{NPF}_6}$, implying that the addition of four chlorines to BQ (i.e., to yield CL4BQ) has a charge-stabilization effect similar to the addition of two chlorines and four carbons (i.e., to yield CL2NQ). The chlorine substituents, indeed, had more dramatic effect than the alkyl and methoxy substituents of CoQ₁₀ and VK₁ (Scheme 3-1). The larger size of the third-period chlorine, in comparison with the size of the second-period elements, carbon and oxygen, provides a plausible explanation for these trends. Furthermore, unlike the chlorine substituents, the alkyls do

not contribute efficiently toward expanding the π -conjugation of the quinones and delocalizing the negative charges of their molecular ions.

The Born solvation-energy expression reveals the dependence of the redox potentials on the media dielectric constant (equation 3-1b and 3-2a). For the first one-electron reduction step of the quinones (i.e., $Z = 0$ and $n = 1$), the dependence of the oxidation potential on the reciprocal dielectric constant is:

$$E_1^{(1/2)} = E_1^{(1/2,ns)} + \frac{e^2}{8F\pi\epsilon_0 R_{eff}} \left(1 - \frac{1}{\epsilon}\right) \quad (3-4)$$

Plots of half-wave reduction potentials vs. $(1 - \epsilon^{-1})$, indeed, revealed linear correlations (Figure 3-3). The slopes of these linear fits yielded the effective radii, $R_{eff} = R_{Red}$ (equation 3-2a, 3-4), of the quinone radical anions (equation 3-3a). The obtained values for R_{eff} , however, were unfeasibly small for spherical cavities that could accommodate the reduced quinones (Table 3-2). Nevertheless, it should be noted that the values of R_{eff} represented effective radii, which, although correlated to the size of the molecular ions, are not necessarily true radii.

Previous reports about solvent dependence of the reduction of quinones failed to correlate the measured potentials, $E_1^{(0)}$, with the reciprocal values of the dielectric constant of the media, ϵ^{-1} , which is directly proportional to the Born solvation energy.¹⁶³ The reported quinone reduction potentials, however, manifested linear correlation with the electrophilicity of the used solvents, empirically expressed as a Gutmann Acceptor Number:¹⁶⁴⁻¹⁶⁹ i.e., an increase in the solvent electrophilicity stabilized the negatively charged semiquinones, causing the observed positive shifts of their reduction

potentials.¹⁶³ We ascribe the reported failure to directly correlate the solvation energy with the shifts in the reduction potentials to: (1) the use of ferrocene oxidation as an internal standard, while the redox properties of ferrocene strongly depend on the media polarity;⁴² and (2) the use of the dielectric values of the neat organic solvents for the electrolyte solutions employed for the electrochemical measurements, while, especially for non-polar solvents, dissolved electrolytes increase the dielectric permittivity of the media.⁴²

The values that we obtained for the effective radii, R_{eff} , of the reduced quinones exhibited several trends. The effective sizes of the reduced 1,4-naphthaquinone (NQ) and VK₁ were identical (Table 3-2), suggesting that the addition of the alkyl chains to the naphthaquinone ring system did not notably perturb the electrostatic interactions of the generated molecular ions with the dielectric media. The effective size of the CoQ₁₀^{•-} ion only slightly exceeds the size of BQ^{•-}. This slight size increase could be ascribed to the two π -conjugating methoxy substituents in CoQ₁₀, rather than to the methyl and the long aliphatic chains (Scheme 3-1).

These findings have a key implication on the manner of defining the size parameter, R , in the Born solvation-energy terms. According to the electrostatic model, the effective radius corresponds to the size of a spherical cavity around the charged species.⁴⁴ Functional groups, such as aliphatic chains, on which the charges do not reside, did not contribute to the cavity size of the molecular ions. For the spherical approximation, therefore, such electronically non-conjugated substituents appear as a part of the solution media, rather than as a part of the molecular ion encapsulated in the solute cavity.

Viewing molecular components as a part of the surrounding media, however, places challenges on the dielectric-continuum approach for the Born solvation-energy treatment: i.e., it requires an introduction either of separate terms for the solution and for the molecular dielectric constants, or of a correction factor for the solution dielectric constant.

Theoretical values of the effective radii. From *ab initio* calculations, we estimated the effective radii of the spherical cavities for BQ, CL4BQ, NQ and CL2NQ. For CoQ₁₀ and VK₁, we conducted the *ab initio* calculations on analogous structures with truncated aliphatic chains (Scheme 3-2). We used Monte Carlo integration of the density within a 0.001 electrons/bohr³ cutoff for determining the molecular volumes of the quinones. From the volumes, the spherical radii were calculated. We applied an empirical correction to the calculated radii that predict reasonable solute cavity sizes for implicit solvent modeling.¹⁷⁰

These calculated cavity radii, $R_{sph}^{(Q)}$ and $R_{sph}^{(Q^{\bullet})}$, for the quinones and their anions, respectively, exceed the electrochemically measured effective radii by a factor of 1.5 to 4.9 (Table 3-2). This discrepancy was more pronounced for BQ and NQ than for the chloroquinones, CL4BQ and CL2NQ, which agrees well with the notion for charge localization. While the negative charges of the radical anions were localized predominantly on the two oxygens of BQ^{•-} and NQ^{•-}; in CL4BQ^{•-} and CL2NQ^{•-} the charges were also distributed over the peripheral chlorines (Figure 3-4).

For CoQ₁₀ and VK₁, the sizes of the solute cavities strongly depend on the conformation of the flexible aliphatic and methoxy chains. Geometry optimization

calculations produced conformations for CoQ₁₀ and VK₁, in which the flexible chains folded over the aromatic rings (Figure 3-5). While intramolecular van der Waals interactions can explain the preference for such folded conformation in vacuum, the abundance of the extended conformers for favorable solution media should not be overlooked. Therefore, the interpretation of solute-cavity radii for moieties with flexible side chains should be approached with caution.

Possible sources for the discrepancy between the experimentally obtained effective radii, and the physically realistic molecular dimensions (confirmed with the radii of the solvation cavities of the quinones) include the assumptions for: (1) the single-sphere approximation of the shape of the molecular anions; (2) homogeneous charge-density distribution throughout the molecular volume; and (3) the correlation of the interfacial electrochemical thermodynamics with the bulk dielectric properties of the supporting electrolyte.

Interfacial properties of the working electrode. To examine the environment of the interfacial redox processes, we employed impedance spectroscopy (IS). IS allowed us to characterize the capacitance of the double-layer on the working electrode for different electrolyte concentrations and for different applied potentials. For the IS data analysis, we modeled the double layer as a capacitor with a shunt resistor, R_{Sh} , and a series resistor, R_{Ser} (Figure 3-6a).¹⁷¹ For the range of electrolyte concentration that we used for the cyclic voltammetry measurements, i.e., for $C_{\text{Bu}_4\text{NPF}_6}$ between 100 and 300 mM, the IS data revealed a negligible correlation between the double-layer capacitance, C_{DL} , and $C_{\text{Bu}_4\text{NPF}_6}$

(Figure 3- 6c). The values of C_{DL} , however, did manifest dependence on the potential of the working electrode (Figure 3-6c).

The observed lack of concentration dependence of the double-layer capacitance is consistent with the Gouy-Chapman-Stern model for surfaces submersed in concentrated electrolyte solutions.¹⁷¹⁻¹⁷³ At such high $C_{\text{Bu}_4\text{NPF}_6}$, the capacitance of the compact Stern layer has the predominant contribution to the reactance component of the measured impedance. The gradual potential-induced changes of C_{DL} , although not depicted by the Helmholtz approximation for the Stern-layer capacitance, are consistent with alterations in the composition of the compact layer induced by charging and discharging of the working electrode.¹⁷⁴

While the thickness and the composition of the diffuse layer depend strongly on the ionic charge and concentration, the compact layer is concentration independent.¹⁷¹ Furthermore, the Debye length, characteristic of the thickness of the diffuse layer, ranges between about 0.2 and 0.7 nm for the electrolyte concentrations we used. Such short Debye lengths are smaller than the size of the electrolyte ions, making it meaningless to define a true diffuse layer. Therefore, beyond the compact layer, the quinone species at the electrode interface experience environment comparable to the bulk electrolyte solutions. As a result, $E_1^{(1/2)}$ exhibited a pronounced dependence on $C_{\text{Bu}_4\text{NPF}_6}$, while C_{DL} was concentration independent.

We have previously demonstrated the dependence of the redox potentials of other species on the dielectric properties of the electrolyte solutions.⁴² Using similar analysis, we have estimated the effective radius of ferrocenium to be about 2.6 Å,⁴² which was in

an agreement with the crystallographic radius, 2.7 Å, and the hydrodynamic radius, 3.2 Å, of ferrocene.¹⁷⁵⁻¹⁷⁷ Apparently, such electrochemical analysis manifested the potential for yielding plausible results for the effective dimensions of redox species. Therefore, the principal reasons for the discrepancies observed for the investigated quinones should be sought in their structural features. Two important structural differences, however, set apart the quinones from ferrocene: (1) quinone molecules are planar, while the ferrocene chelate has a shape that can be approximated to a cylinder or a sphere; and (2) the charges of the quinone anions are localized predominantly on the peripheral oxygens (Figure 3-4), while the charge of the ferrocenium cation resides on the relatively large orbitals of the ferric ion, distributed around the center of the chelate.

Generalized Born approach. To address the discrepancies between the measured and calculated quinone radii, we explored the generalized Born (GB) approach. The GB approach, rather than attempt to fit a molecule and its ions into a single sphere, treats the molecular species as a collection of spheres.^{1,2,90-95} Representing each of the reduced and oxidized molecules as a collection of N atoms with atomic radii, r_i , and atomic charges, z_i , transforms their charge-to-size ratios, Ξ (equation 3-2a), into the corresponding GB forms:^{1,2}

$$\Xi^{(GB)} = e^2 \sum_{i=1}^N \sum_{j=1}^N \frac{z_i z_j}{f_{ij}} \quad (3-5a)$$

where $\sum_{i=1}^N z_i = Z - n$ and $\sum_{i=1}^N z_i = Z$ represent the total charge of the reduced and the

oxidized species, respectively, and the GB parameter, f_{ij} , represents the corrected interatomic distance:¹

$$f_{ij} = \sqrt{d_{ij}^2 + \alpha_i \alpha_j \exp\left(-\frac{d_{ij}^2}{4\alpha_i \alpha_j}\right)} \quad (3-5b)$$

where d_{ij} is the center-to-center distance between atoms i and j ; and a_i is the Born radius of atom i . For cases of non-overlapping spheres, a_i can be expressed analytically:¹

$$\alpha_i^{-1} = r_i^{-1} - \sum_{\substack{j=1 \\ j \neq i}}^N \frac{r_j}{2(d_{ij}^2 - r_j^2)} - \sum_{\substack{j=1 \\ j \neq i}}^N \frac{1}{4d_{ij}} \lg \frac{d_{ij} - r_j}{d_{ij} + r_j} \quad (3-5c)$$

where for r_i , we assumed the covalent radii, which we extracted from the atomic coordinates for the minimized structures of the quinones (Figure 3-4).¹⁷⁸ It should be noted, that although the oxidized form of the quinones is not charged, i.e., $Z = 0$, the partial charges on the different atoms in the electro-neutral molecules, i.e., $z_i \neq 0$ (Figure 3-4, top row), result in non-zero values for their GB charge-to-size ratio, $\Xi_{Ox}^{(GB)}$ (equation 3-5a).

Apparently, the Born atomic radii, a_i , are larger than the corresponding covalent or van der Waals radii, r_i . As revealed by equation 3-5c, this difference between a_i , and r_i is less pronounced for atoms located at the periphery of the molecule.

The classical Born expressions revealed that the slopes of the linear correlations between the measured reduction potentials, $E_1^{(1/2)}$, and the inverted dielectric constants of the media, $1 - \epsilon^{-1}$ (Figure 3-3), should yield the difference between the charge-to-size ratios, $\Xi_{Red}^{(GB)} - \Xi_{Ox}^{(GB)}$ (equation 3-2a). This difference, $\Xi_{Red}^{(GB)} - \Xi_{Ox}^{(GB)}$, encompasses information about the measured effective radii, R_{eff} , of the electrochemically analyzed species (equations 3-2b, 3-4). As we demonstrated, the thus obtained values of R_{eff} from

the experimental data, however, proved physically unfeasible to accommodate the spherical approximation adopted by the classical Born approach (Table 3-2).

Adopting physically feasible molecular geometries and charge distributions, the generalized Born approach allowed for estimation of the charge-to-size ratios, $\Xi_{Red}^{(GB)}$ and $\Xi_{Ox}^{(GB)}$, of the reduced and oxidized components of redox couples (equation 3-5). Concurrently, for the treatment of the experimental findings involving one-electron reduction, $n = 1$, of non-charged species, $Z = 0$, we equated the difference between the charge-to-size ratios with e^2 / R_{eff} (equations 3-2, 3-4). As a corollary, it permitted to extract from the generalized Born approach values for the effective radii, $R_{eff}^{(GB)}$, expected to be observed for one-electron reduction of the investigated redox species:

$$R_{eff}^{(GB)} = \frac{e^2}{\Xi_{Red}^{(GB)} - \Xi_{Ox}^{(GB)}} \quad (3-6)$$

A comparison between the experimental R_{eff} (equation 3-4) and the predicted $R_{eff}^{(GB)}$ (equation 3-6) values, allowed us to test if the GB approach adequately addresses the discrepancy issues with the single-sphere approximation of the quinone ions.

In order to employ this GB approach, using *ab initio* calculations, we estimated the atomic charges and coordinates for the relaxed structures of four of the quinones and their anions. Molecular structures for the neutral and anionic versions of the four benzo- and naphthaquinones were optimized using the B3LYP density functional and the aug-cc-pVTZ basis set. Atomic point charges were determined using the CHELPG method, which determines a set of atomic charges that reproduce the molecular electrostatic potential at a large number of grid points around the molecule. The negative charges of

the quinone radical-ions were localized around the periphery of the molecules, predominantly on the oxygen atoms (Figure 3-4).

The calculated $R_{eff}^{(GB)}$ (equations 3-5, 3-6) manifested a closer agreement with the effective radii, R_{eff} , obtained from the redox-potential analysis than the effective radii of the solvation spheres, R_{sph} , with R_{eff} (Table 3-2). The relative discrepancies between $R_{eff}^{(GB)}$ and R_{eff} , (i.e., $\Delta gb = \left| R_{eff} - R_{eff}^{(GB)} \right| R_{eff}^{-1}$) are 2 to 35 fold smaller than the relative discrepancies between $R_{sph}^{(Q^{\cdot-})}$ and R_{eff} , (i.e., $\Delta sph = \left| R_{eff} - R_{sph}^{(Q^{\cdot-})} \right| R_{eff}^{-1}$), as illustrated by the $\Delta sph / \Delta gb$ ratios (Table 3-2). This finding suggested that it was most probably the spherical approximation of the molecular shapes that led to the observed discrepancy between the experimentally estimated effective radii and the feasible molecular dimensions.

The larger size of the CoQ10 and VK1 quinones makes B3LYP/aug-cc-pVTZ calculations too computationally expensive. Given the aforementioned ambiguity about the behavior of the long, flexible aliphatic chain in solution and the need to reduce the computational cost, we (1) truncated the chain to only six carbon atoms (Scheme 3-2) and (2) used the smaller 6-31+G(d) basis set to compute both the optimal geometry and CHELPG atomic charges. A series of control calculations determined that these two approximations have a relatively small impact on the predicted effective radii. First, using the 6-31+G(d) basis set for BQ and BQ $^{\cdot-}$, for example, yielded $R_{eff}^{(GB)}$ values that differed with less than 1% from each other. Second, semiempirical AM1 geometry optimizations followed by B3LYP/aug-cc-pVDZ CHELPG atomic charge predictions on VK $_1$ with the

truncated and complete aliphatic chains (Scheme 3-1) produced effective radii that differ by less than 10% from each other.

Compared to the other four quinones, CoQ₁₀ and VK₁ manifested the much larger discrepancies between $R_{eff}^{(GB)}$ and R_{eff} : i.e., the largest Δgb (Table 3-2). Our aforementioned control calculations suggest that these discrepancies are not due to the use of a smaller basis set or chain truncation in the calculations. Rather, we believe they arise from the flexible nature of the aliphatic chains. The effective GB radii, $R_{eff}^{(GB)}$, strongly depend on the Born radii, a_i , of the comprising atomic spheres (equation 3-5c). A decrease in a_i of the atoms, on which the negative charges of the singly-reduced quinones reside, results in a decrease in $R_{eff}^{(GB)}$. Gas-phase *ab initio* calculations yielded folded conformations of CoQ₁₀ and VK₁ (Figure 3-5). Extended conformers (which are expected for solution media), however, provide an increase in the interatomic distances, d_{ij} , leading to a decrease in a_i (equation 3-5c), and hence, a decrease in $R_{eff}^{(GB)}$. Therefore, the folded conformations underline a potential reason for the overestimated values of $R_{eff}^{(GB)}$ for CoQ₁₀ and VK₁.

To further examine the role of the molecular shape and of the charge distribution on the effective radii of molecular ions, we employed the GB approach to a singly-charged hypothetical molecule composed of five spheres arranged in a square, i.e., D₄ symmetry (Scheme 3-3). Setting the diameter for each of the five spheres to 1 Å, yielded the dimensions of the hypothetical molecule: i.e., 2.4 × 2.4 × 1 Å (Scheme 3-3), which could fit into a spherical cavity with a radius 1.5 Å. We applied the GB analysis to the

hypothetical species, in which the charge was localized on one of the five spheres, or equally distributed between two, three, four and five spheres with different configurations (Table 3-3).

The size of the hypothetical molecular ion was the same for all charge distributions, and hence, it should occupy the same solvent cavity. The GB effective radius, $R_{eff}^{(GB)}$, however, manifested a strong dependence on the patterns in which the charge was distributed among the five spheres (Table 3-3). For all cases, the values of the effective radii were 1.3- to 2.3-fold smaller than the 1.5-Å radius of the solvation spherical cavity that could accommodate the molecule (Table 3-3). For the cases of charge distribution over two of the five spheres, the effective radii of the hypothetical molecular anions were smaller when the two spheres carrying the charge were closer together. A similar trend was observed for the charge that was distributed over three and even over four spheres: i.e., the values of $R_{GB}^{(eff)}$ were smaller when the charged spheres were next to one another (Table 3-3). These findings demonstrated that: (1) non-spherical charged species have effective radii smaller than the radii of the spheres, in which they could fit; and (2) localization of the charges within the molecular entities leads to a decrease in the values of the effective radii of their ions.

The generalized Born approach is still an approximation. Defining atoms or functional groups as spheres, with homogeneous distribution of charge densities, presents a potentially crucial pitfall. For covalently bonded atoms, charge-density distribution does not necessarily have spherical symmetry. Furthermore, defining the boundaries of the electronic clouds that encompass the ionic charges (and hence, defining the effective

ionic radii) is somewhat arbitrary. Nevertheless, the generalized Born approach presents a significant improvement over the single-sphere approximation. It has the potential ability to relate experimentally measurable quantities with physically feasible dimensions of charged molecular species.

Implications of effective radii for the analysis of charge-transfer systems. For semi-classical analyses of charge transfer processes, information about the radii of the participating electron donors and acceptors is crucial. The effective radii are essential for estimating not only of the driving force of the process, via the Rehm-Weller equation,⁴⁰⁻⁴² but also of the outer-sphere reorganization energy.¹⁷⁹⁻¹⁸¹ Semi-classical dielectric-continuum approaches, which were developed and confirmed for spherically-symmetrical ions, have proven immensely indispensable for a wide range of charge-transfer studies and have demonstrated predictive capabilities.³

For organic moieties that are not spherically shaped, the estimation of the effective radii from experimental or from computational data is somewhat arbitrary. For example, for moieties that have elongated and/or flat shapes, such as quaterthiophenes and quinones, the effective diameters can be equated with the average of their length, width and height, in order to analyze charge-transfer kinetics.

As we demonstrated with the GB approach for the hypothetical ionic species (Scheme 3-3, Table 3-3), such effective radii, obtained from averaging of the three dimensions of the molecular ions, are plausible when the charges are evenly distributed over the whole molecular volume. Indeed, the average for $2.4 \times 2.4 \times 1 \text{ \AA}$ species is about 1.9 \AA , the half

of which agrees well with the 1-Å effective radii calculated for the cases of charge distribution over four of five spheres (Table 3-3).

Charges localized within relatively small volumes at the periphery of the molecular ions, however, present potentials for significant discrepancies in the estimation of their effective radii directly from their molecular dimensions. Recently we reported, for example, charge-transfer behavior of an acridinium-thiophene dyad suggesting that the effective radius of the acridinium cation (comprising three condensed six-member rings) was smaller than the thiophene radical-cation (comprising a single five-member ring).⁸⁰ The localization of the acridinium positive charge on its nitrogen heteroatom can provide an explanation for the observed trend.^{82,83}

Quinones presented another example for effective-radius discrepancies resultant from charge localization in non-spherically shaped species. The generalized Born approach, however, presented trends that tend to account for the charge localization in the estimation of the quinone effective radii (Table 3-2).

Conclusions

The values of the effective radii of charged organic moieties have a key importance for the estimation of the energetics of charge-transfer processes. The dielectric continuum treatment involving effective radii, is important for estimation not only of the Born solvation term in the Rehm-Weller equation, but also of the outer-sphere component of the reorganization energy. Therefore, the relation between the “true” molecular dimensions and the effective radii for the broadly used spherical approximation is crucial

for semi-classical analysis of charge-transfer systems. The generalized Born approach allowed us to relate experimentally obtained effective radii of quinone derivatives with their structural and charge-distribution characteristics. We believe that such approaches, deviating from the single-sphere approximation, have the potential to provide means for analysis of redox processes involving moieties with irregular shapes and uneven charge-density distributions.

Experimental

Materials. 1,4-Benzoquinone, 1,4-naphthoquinone, 2,3-dichloro-1,4-naphthoquinone, tetrachloro-1,4-benzoquinone, vitamin K₁, coenzyme Q₁₀, tetrabutylammoniumhexafluorophosphate, 4-Bromo-1,8-naphthalic anhydride, 3-dimethylaminopropanenitrile, 1,2-dimethoxyethane, acetic acid and aniline were purchased from Sigma-Aldrich. Anhydrous solvents, chloroform and acetonitrile; spectroscopic-grade solvents, n-hexane, tetrachloromethane, chloroform, dichloromethane, benzonitrile and dimethyl sulfoxide were purchased from Fisher Scientific. N-phenyl-4-dimethylamino-1,8-naphthalimide (Ph-ANI) was prepared from 4-Bromo-1,8-naphthalic anhydride, 3-dimethylaminopropanenitrile and aniline via a two-step synthesis, as we have previously reported.⁴²

Cyclic voltammetry. The electrochemical measurements were conducted using Reference 600TM Potentiostat/Galvanostat/ZRA (Gamry Instruments, PA, U.S.A.), equipped with a three-electrode cell. Glassy carbon electrode and platinum wire were used for working and counter electrodes, respectively. Saturated calomel electrode (Gamry Instruments) was used for a reference electrode. To prevent contamination, the

reference electrode was brought in contact with the sample solutions via two salt bridges. To prevent drastic potential drops between the aqueous electrode media and the chloroform solutions, the solution between the two salt bridges was 100 mM tetrabutylammonium hexafluorophosphate in anhydrous acetonitrile. When not in use, the reference electrode is stored submersed in saturated potassium chloride solution. For all samples, the quinones concentration was 2 mM. For each sample, the solution was purged with pure argon gas for 30 min and at least five scans were recorded at 50 mV / s scan rate.^{18,42,182}

Impedance spectroscopy. Impedance measurements were conducted using a Reference 600TM Potentiostat/Galvanostat/ZRA (Gamry Instruments, PA, U.S.A.). The measurements were carried out by setting the AC voltage amplitude to 0.1 V, while the applied DC potential ranged from -0.8 V to 0.8 V vs. SCE. Prior to the conductivity measurements, the working electrode surface was polished with alumina (0.05 microns grade, Buehler Ltd., U.S.A.) and thereafter cleaned in ethanol (200 proof, Fisher Scientific, U.S.A.) in an ultrasonic bath and dried by air. The impedance spectra of the double layer on the working electrode for different electrolyte concentrations were recorded at frequency from 1 kHz to 1 MHz and fitted by Randles Model.

Fluorescence spectroscopy. Steady state emission measurements were conducted using a FluoroLog-3 spectrofluorometer (Horiba-Jobin-Yvon) equipped with double-grating monochromators and a TBX single-photon-counting detector.^{42,101,183-185} By adjusting the slit widths, the signal at all wavelengths was kept under 10^6 CPS to assure

that it is within the linear range of the detector. For all samples, the concentration of Ph-ANI was 10 μM .

Refractive index measurements. The refractive indices for the varying electrolyte concentrations were measured at 21°C using Spectronic Instruments Refractometer model 334610. The reported values are averages of four individual readings. Different concentrations of electrolytes were prepared by mixing anhydrous chloroform with tetrabutylammonium hexafluorophosphate and sealed in dry sample vials until use.

Data analysis. The values for the peak maxima (and minima) from the cyclic voltammograms and from the fluorescence spectra were obtained by fitting the region around the maxima (or the minima) to a Gaussian function. The fluorescence spectra of Ph-ANI were deconvoluted by fitting them to sums of Gaussian functions.^{186,187} The quality of the fits was monitored by examination of the residuals. All least-square data fits and the deconvolutions of fluorescence spectra were conducted using Igor Pro, v. 6 (Wavemetrics, Inc.) on MacOS and Windows XP workstations.¹⁸⁸⁻¹⁹¹

Ab initio calculations. Density functional theory (DFT) calculations were performed using the B3LYP density functional.^{192,193} For the anions, spin-unrestricted DFT was used. Initial results were obtained in the aug-cc-pVDZ basis.¹⁹⁴ For the generalized Born geometries and point charges, these were refined with the larger aug-cc-pVTZ basis set. For the truncated CoQ₁₀ and VK₁ (Scheme 3-2), a reduced basis set, 6-31+G(d), was used. All calculations were performed using GAUSSIAN 03.¹⁹⁵

Spherical radii for the molecules were computed in a two-step procedure. First, the molecular volume inside a 0.001 electrons/Bohr³ density contour was estimated using

Monte Carlo integration, using 10,000 integration points. Each integration was repeated 100 times, and the resulting standard deviation for the calculated volumes was approximately 0.5%. Second, the spherical radius was estimated from the mean volume according to the scheme of Wong and co-workers.¹⁷⁰ In this scheme, the volume is scaled by a factor of 4/3. Then, the corresponding spherical radius is computed and increased by 0.5 angstroms. This empirical adjustment typically provides improved cavity sizes for implicit solvent models.¹⁷⁰ The standard deviation in the predicted spherical radii over the 100 runs per molecule is less than 0.01 Angstroms.

For the generalized Born model, the neutral and anionic species for each of the four molecules were optimized separately. For each optimized structure, atomic charges were computed using the CHELPG scheme,¹⁹⁶ which fits charges to reproduce the molecular electrostatic potential at a series of grid points surrounding the molecule.

GB calculations. The GB calculations (equations 3-5 and 3-6) were conducted using macros written for Igor Pro, v. 6 (Wavemetrics, Inc.), run on MacOS. The charges atomic charges were obtained from the ab initio calculations (Figure 3-4) or estimated for equal-distribution over the charged spheres of the hypothetical species (Table 3-3). The atomic radii, r_i , were estimated from the atomic coordinates of the minimized structures (Figure 3-4). In order to employ equation 3-5c, the radius of each atom, r_i , represents the maximum radius of a sphere (centered at the coordinates of the corresponding atom) that can fit within the molecular structure without overlapping with the spheres representing the neighboring atoms.

References

- (1) Bashford, D.; Case, D. A. *Annu. Rev. Phys. Chem.* **2000**, *51*, 129-152.
- (2) Still, W. C.; Tempczyk, A.; Hawley, R. C.; Hendrickson, T. *J. Am. Chem. Soc.* **1990**, *112*, 6127-6129.
- (3) Marcus, R. A.; Sutin, N. *Biochimica et Biophysica Acta, Reviews on Bioenergetics* **1985**, *811*, 265-322.
- (4) Gust, D.; Moore, T. A.; Moore, A. L. *Acc. Chem. Res.* **2009**, *42*, 1890-1898.
- (5) Wasielewski, M. R. *Acc. Chem. Res.* **2009**, *42*, 1910-1921.
- (6) Schuster, D. I.; Megiatto, J. D., Jr. *Nat. Chem.* **2009**, *1*, 182-183.
- (7) Hambourger, M.; Moore, G. F.; Kramer, D. M.; Gust, D.; Moore, A. L.; Moore, T. A. *Chem. Soc. Rev.* **2009**, *38*, 25-35.
- (8) van der Est, A. *Wiley Encycl. Chem. Biol.* **2009**, *3*, 676-682.
- (9) Chen, F.; Tao, N. J. *Acc. Chem. Res.* **2009**, *42*, 429-438.
- (10) Rosokha, S. V.; Kochi, J. K. *Acc. Chem. Res.* **2008**, *41*, 641-653.
- (11) Piera, J.; Backvall, J. E. *Angew. Chem., Int. Ed.* **2008**, *47*, 3506-3523.
- (12) Wasielewski, M. R. *J. Org. Chem.* **2006**, *71*, 5051-5066.
- (13) Schuster, D. I.; Li, K.; Guldi, D. M. *C. R. Chim.* **2006**, *9*, 892-908.
- (14) Seibert, M.; Wasielewski, M. R. *Adv. Photosynth. Respir.* **2005**, *20*, 269-274.
- (15) Jones, G., II; Zhou, X.; Vullev, V. I. *Photochem. Photobiol. Sci.* **2003**, *2*, 1080-1087.
- (16) Vullev, V. I.; Jones, G., II *Res. Chem. Intermed.* **2002**, *28*, 795-815.
- (17) Bracher, P. J.; Schuster, D. I. *Dev. Fullerene Sci.* **2002**, *4*, 163-212.
- (18) Jones, G., II; Vullev, V. I. *Org. Lett.* **2002**, *4*, 4001-4004.
- (19) Lukas, A. S.; Wasielewski, M. R. *Electron Transfer Chem.* **2001**, *5*, 48-96.

- (20) Jones, G., II; Vullev, V.; Braswell, E. H.; Zhu, D. *J. Am. Chem. Soc.* **2000**, *122*, 388-389.
- (21) Jones, G., II; Lu, L. N.; Vullev, V.; Gosztola, D.; Greenfield, S.; Wasielewski, M. *Bioorg. Med. Chem. Lett.* **1995**, *5*, 2385-2390.
- (22) Newton, M. D. *Chem. Rev.* **1991**, *91*, 767-792.
- (23) Wasielewski, M. R.; Niemczyk, M. P.; Svec, W. A.; Pewitt, E. B. *Springer Ser. Chem. Phys.* **1985**, *42*, 242-249.
- (24) Siegbahn, P. E. M. *Acc. Chem. Res.* **2009**, *42*, 1871-1880.
- (25) Davidson, V. L. *Acc. Chem. Res.* **2008**, *41*, 730-738.
- (26) Rosenberg, E.; Koren, O.; Reshef, L.; Efrony, R.; Zilber-Rosenberg, I. *Nat. Rev. Microbiol.* **2007**, *5*, 355-362.
- (27) Rascher, U.; Nedbal, L. *Curr. Opin. Plant Biol.* **2006**, *9*, 671-678.
- (28) Iverson, T. M. *Curr. Opin. Chem. Biol.* **2006**, *10*, 91-100.
- (29) Chergui, M. *Science* **2006**, *313*, 1246-1247.
- (30) Szacilowski, K.; Macyk, W.; Drzewiecka-Matuszek, A.; Brindell, M.; Stochel, G. *Chem. Rev.* **2005**, *105*, 2647-2694.
- (31) Fagnoni, M.; Albini, A. *Acc. Chem. Res.* **2005**, *38*, 713-721.
- (32) Gratzel, M. *Acc. Chem. Res.* **2009**, *42*, 1788-1798.
- (33) Kaneko, M. *Springer Ser. Mater. Sci.* **2009**, *111*, 199-215.
- (34) Heremans, P.; Cheyns, D.; Rand, B. P. *Acc. Chem. Res.* **2009**, *42*, 1740-1747.
- (35) Sirimanne, P. M.; Perera, V. P. S. *Phys. Status Solidi B* **2008**, *245*, 1828-1833.
- (36) Andrews, D. L. *J. Nanophotonics* **2008**, *2*, No pp given.
- (37) Gratzel, M. *Philos. Trans. R. Soc., A* **2007**, *365*, 993-1005.
- (38) Blom, P. W. M.; Mihailitchi, V. D.; Koster, L. J. A.; Markov, D. E. *Adv. Mater.* **2007**, *19*, 1551-1566.

- (39) Graetzel, M. C. R. *Chim.* **2006**, *9*, 578-583.
- (40) Rehm, D.; Weller, A. *Israel Journal of Chemistry* **1970**, *8*, 259-271.
- (41) Braslavsky, S. E.; Acuna, A. U.; Adam, W.; Amat, F.; Armesto, D.; Atvars, T. D. Z.; Bard, A.; Bill, E.; Bjoern, L. O.; Bohne, C.; Bolton, J.; Bonneau, R.; Bouas-Laurent, H.; Braun, A. M.; Dale, R.; Dill, K.; Doepp, D.; Duerr, H.; Fox, M. A.; Gandolfi, T.; Grabowski, Z. R.; Griesbeck, A.; Kutateladze, A.; Litter, M.; Lorimer, J.; Mattay, J.; Michl, J.; Miller, R. J. D.; Moggi, L.; Monti, S.; Nonell, S.; Ogilby, P.; Olbrich, G.; Oliveros, E.; Olivucci, M.; Orellana, G.; Prokorenko, V.; Naqvi, K. R.; Rettig, W.; Rizzi, A.; Rossi, R. A.; San Roman, E.; Scandola, F.; Schneider, S.; Thulstrup, E. W.; Valeur, B.; Verhoeven, J.; Warman, J.; Weiss, R.; Wirz, J.; Zachariasse, K. *Pure and Applied Chemistry* **2007**, *79*, 293-465.
- (42) Bao, D.; Millare, B.; Xia, W.; Steyer, B. G.; Gerasimenko, A. A.; Ferreira, A.; Contreras, A.; Vullev, V. I. *J. Phys. Chem. A* **2009**, *113*, 1259-1267.
- (43) Born, M. *Zeitschrift fuer Physik* **1920**, *1*, 45-48.
- (44) Rashin, A. A.; Honig, B. *Annals of the New York Academy of Sciences* **1986**, *482*, 143-144.
- (45) Sinha, B.; Roy, P. K.; Sarkar, B. K.; Brahman, D.; Roy, M. N. *J. Chem. Thermodyn.* **2010**, *42*, 380-386.
- (46) Yadava, S. S.; Yadav, A.; Kushwaha, N.; Yadav, N. *Indian J. Chem., Sect. A Inorg., Bio-inorg., Phys., Theor. Anal. Chem.* **2009**, *48A*, 650-657.
- (47) Jakli, G. *J. Chem. Eng. Data* **2009**, *54*, 2656-2665.
- (48) Cibulka, I.; Hnedkovsky, L.; Sedlbauer, J. *J. Chem. Thermodyn.* **2009**, *42*, 198-207.
- (49) Tjahjono, M.; Garland, M. *J. Solution Chem.* **2007**, *36*, 221-236.
- (50) Mallick, B. C.; Kishore, N. *J. Solution Chem.* **2006**, *35*, 1441-1451.
- (51) Pandey, J. D.; Dey, R.; Datt Bhatt, B. *J. Mol. Liq.* **2004**, *111*, 67-71.
- (52) Raos, N. *Croat. Chem. Acta* **2003**, *76*, 81-85.
- (53) Elkashef, H. *Opt. Mater. (Amsterdam)* **1997**, *8*, 175-183.

- (54) Aminabhavi, T. M.; Aralaguppi, M. I.; Harogoppad, S. B.; Balundgi, R. H. *Indian J. Technol.* **1993**, *31*, 27-31.
- (55) Aminabhavi, T. M.; Aralaguppi, M. I.; Harogoppad, S. B.; Balundgi, R. H. *Indian J. Technol.* **1993**, *31*, 32-36.
- (56) Aminabhavi, T. M.; Aralaguppi, M. I. *Indian J. Technol.* **1993**, *31*, 801-807.
- (57) Swaddle, T. W.; Mak, M. K. S. *Can. J. Chem.* **1983**, *61*, 473-480.
- (58) Tsierkezos, N. G.; Philippopoulos, A. I. *Fluid Phase Equilib.* **2009**, *277*, 20-28.
- (59) Kuznetsova, E. M. *Russ. J. Phys. Chem.* **2005**, *79*, 1165-1168.
- (60) Ue, M. *J. Electrochem. Soc.* **1996**, *143*, L270-L272.
- (61) Crouch, E.; Persson, A.; Chang, D.; Heuser, J. *J. Biol. Chem.* **1994**, *269*, 17311-17319.
- (62) Lim, S. K.; Burba, M. E.; Albrecht, A. C. *Chem. Phys. Lett.* **1993**, *216*, 405-408.
- (63) Shimada, E.; Matsumura, G. *J. Chromatogr.* **1992**, *627*, 43-50.
- (64) Schiller, R. *Radiat. Phys. Chem.* **1991**, *37*, 549-550.
- (65) Kapinus, E. I.; Dilung, I. I. *Chem. Phys. Lett.* **1990**, *174*, 75-79.
- (66) Pau, P. C. F.; Berg, J. O.; McMillan, W. G. *J. Phys. Chem.* **1990**, *94*, 2671-2679.
- (67) Heyrovska, R. *Chem. Phys. Lett.* **1989**, *163*, 207-211.
- (68) Ribela, M. T.; Bartolini, P. *Anal Biochem* **1988**, *174*, 693-697.
- (69) Ibuki, K.; Nakahara, M. *J. Phys. Chem.* **1986**, *90*, 6362-6365.
- (70) Fawcett, W. R.; Jaworski, J. S. *J. Phys. Chem.* **1983**, *87*, 2972-2976.
- (71) Gill, D. S. *Electrochim. Acta* **1977**, *22*, 491-492.
- (72) Nakagawa, S.; Takehara, Z.; Yoshizawa, S. *Electrochim. Acta* **1973**, *18*, 1043-1044.
- (73) Waldmann-Meyer, H. *Biochim. Biophys. Acta, Gen. Subj.* **1972**, *261*, 148-160.
- (74) Rodbard, D.; Chrambach, A. *Anal. Biochem.* **1971**, *40*, 95-134.

- (75) Bousfield, W. R. *Phil. Trans.* **1906**, *206*, 101-159.
- (76) Zhan, C.-G.; Chipman, D. M. *J. Chem. Phys.* **1998**, *109*, 10543-10558.
- (77) Medina-Llanos, C.; Ågren, H.; Mikkelsen, K. V.; Jensen, H. J. A. *J. Chem. Phys.* **1989**, *90*, 6422-6435.
- (78) McCreery, J. H.; Christoffersen, R. E.; Hall, G. G. *J. Am. Chem. Soc.* **1976**, *98*, 7191-7197.
- (79) Rüssel, C.; Jaenicke, W. *J. Electroanal. Chem. Interfacial Electrochem.* **1984**, *180*, 205-217.
- (80) Hu, J.; Xia, B.; Bao, D.; Ferreira, A.; Wan, J.; Jones, G.; Vullev, V. I. *J. Phys. Chem. A* **2009**, *113*, 3096-3107.
- (81) Jones, G., II; Yan, D.; Hu, J.; Wan, J.; Xia, B.; Vullev, V. I. *J. Phys. Chem. B* **2007**, *111*, 6921-6929.
- (82) Seiffert, W.; Limbach, H. H.; Zanker, V.; Mantsch, H. *Tetrahedron* **1970**, *26*, 2663-2675.
- (83) Nishimoto, K.; Nakatsukasa, K.; Fujishiro, R.; Kato, S. *Theor. Chim. Acta* **1969**, *14*, 80-90.
- (84) Karelson, M. M.; Zerner, M. C. *J. Phys. Chem.* **1992**, *96*, 6949-6957.
- (85) Rinaldi, D.; Rivail, J. L.; Rguini, N. *J. Comput. Chem.* **1992**, *13*, 675-680.
- (86) Harrison, S. W.; Nolte, H. J.; Beveridge, D. L. *J. Phys. Chem.* **1976**, *80*, 2580-2585.
- (87) Huron, M. J.; Claverie, P. *J. Phys. Chem.* **1972**, *76*, 2123-2133.
- (88) Lee, B.; Richards, F. M. *J. Mol. Biol.* **1971**, *55*, 379-400.
- (89) Kirkwood, J. G.; Westheimer, F. H. *J. Chem. Phys.* **1938**, *6*, 506-512.
- (90) Banks, J. L.; Beard, H. S.; Cao, Y.; Cho, A. E.; Damm, W.; Farid, R.; Felts, A. K.; Halgren, T. A.; Mainz, D. T.; Maple, J. R.; Murphy, R.; Philipp, D. M.; Repasky, M. P.; Zhang, L. Y.; Berne, B. J.; Friesner, R. A.; Gallicchio, E.; Levy, R. M. *J. Comput. Chem.* **2005**, *26*, 1752-1780.

- (91) Chen, J.; Brooks, C. L., III; Khandogin, J. *Curr. Opin. Struct. Biol.* **2008**, *18*, 140-148.
- (92) Constanciel, R.; Contreras, R. *Theor. Chim. Acta* **1984**, *65*, 1-11.
- (93) Feig, M.; Brooks, C. L. *Curr. Opin. Struct. Biol.* **2004**, *14*, 217-224.
- (94) Felts, A. K.; Gallicchio, E.; Wallqvist, A.; Levy, R. M. *Proteins Struct., Funct., Genet.* **2002**, *48*, 404-422.
- (95) Hawkins, G. D.; Cramer, C. J.; Truhlar, D. G. *J. Phys. Chem.* **1996**, *100*, 19824-19839.
- (96) Heinis, T.; Chowdhury, S.; Scott, S. L.; Kebarle, P. *J. Am. Chem. Soc.* **1988**, *110*, 400-407.
- (97) Kebarle, P.; Chowdhury, S. *Chem. Rev.* **1987**, *87*, 513-534.
- (98) Jaworski, J. S. *Chem. Phys. Lett.* **1986**, *127*, 133-135.
- (99) Peover, M. E. *Nature* **1962**, *193*, 475-476.
- (100) Freguia, S.; Tsujimura, S.; Kano, K. *Electrochim. Acta* **2009**, *55*, 813-818.
- (101) Wan, J.; Ferreira, A.; Xia, W.; Chow, C. H.; Takechi, K.; Kamat, P. V.; Jones, G.; Vullev, V. I. *J. Photochem. Photobiol., A* **2008**, *197*, 364-374.
- (102) Sumida, J. P.; Liddell, P. A.; Lin, S.; Macpherson, A. N.; Seely, G. R.; Moore, A. L.; Moore, T. A.; Gust, D. *J. Phys. Chem. A* **1998**, *102*, 5512-5519.
- (103) Kuciauskas, D.; Liddell, P. A.; Hung, S.-C.; Lin, S.; Stone, S.; Seely, G. R.; Moore, A. L.; Moore, T. A.; Gust, D. *J. Phys. Chem. B* **1997**, *101*, 429-440.
- (104) Macpherson, A. N.; Liddell, P. A.; Lin, S.; Noss, L.; Seely, G. R.; DeGraziano, J. M.; Moore, A. L.; Moore, T. A.; Gust, D. *J. Am. Chem. Soc.* **1995**, *117*, 7202-7212.
- (105) Sakata, Y.; Tsue, H.; O'Neil, M. P.; Wiederrecht, G. P.; Wasielewski, M. R. *J. Am. Chem. Soc.* **1994**, *116*, 6904-6909.
- (106) Wasielewski, M. R.; Gaines, G. L., III; Wiederrecht, G. P.; Svec, W. A.; Niemczyk, M. P. *J. Am. Chem. Soc.* **1993**, *115*, 10442-10443.
- (107) Johnson, D. G.; Niemczyk, M. P.; Minsek, D. W.; Wiederrecht, G. P.; Svec, W. A.; Gaines, G. L., III; Wasielewski, M. R. *J. Am. Chem. Soc.* **1993**, *115*, 5692-5701.

- (108) Wasielewski, M. R.; O'Neil, M. P.; Gosztola, D.; Niemczyk, M. P.; Svec, W. A. *Pure Appl. Chem.* **1992**, *64*, 1319-1325.
- (109) Seta, P.; Bienvenue, E.; Moore, A. L.; Mathis, P.; Bensasson, R. V.; Liddell, P.; Pessiki, P. J.; Joy, A.; Moore, T. A.; Gust, D. *Nature* **1985**, *316*, 653-655.
- (110) Roessler, M. M.; King, M. S.; Robinson, A. J.; Armstrong, F. A. *Proc. Natl. Acad. Sci. U. S. A., Early Ed.* **2010**, 1-6, 6 pp.
- (111) Hirst, J. *Biochem. J.* **2010**, *425*, 327-339.
- (112) Uchimiya, M.; Stone, A. T. *Chemosphere* **2009**, *77*, 451-458.
- (113) Nabedryk, E.; Breton, J. *Biochim. Biophys. Acta, Bioenerg.* **2008**, *1777*, 1229-1248.
- (114) Savitsky, A.; Moebius, K. *Helv. Chim. Acta* **2006**, *89*, 2544-2589.
- (115) Wraight, C. A. *Biophys. Struct. Aspects Bioenerg.* **2005**, 273-313.
- (116) Semenov, A.; Cherepanov, D.; Mamedov, M. *Photosynth. Res.* **2008**, *98*, 121-130.
- (117) Renger, G.; Renger, T. *Photosynth. Res.* **2008**, *98*, 53-80.
- (118) Kirchhoff, H. *Biochem. Soc. Trans.* **2008**, *36*, 967-970.
- (119) DeRuyter, Y. S.; Fromme, P. *Cyanobacteria* **2008**, 217-269.
- (120) Lichtenthaler, H. K. *Photosynth. Res.* **2007**, *92*, 163-179.
- (121) Xiong, L.; Seibert, M.; Gusev, A. V.; Wasielewski, M. R.; Hemann, C.; Hille, C. R.; Sayre, R. T. *J. Phys. Chem. B* **2004**, *108*, 16904-16911.
- (122) Gunner, M. R.; Madeo, J.; Zhu, Z. *J. Bioenerg. Biomembr.* **2008**, *40*, 509-519.
- (123) Wraight, C. A. *Photosynth. Mech. Eff., Proc. Int. Congr. Photosynth., 11th* **1998**, *2*, 693-698.
- (124) Laible, P. D.; Zhang, Y.; Morris, A. L.; Snyder, S. W.; Ainsworth, C.; Greenfield, S. R.; Wasielewski, M. R.; Parot, P.; Schoepp, B.; Schiffer, M.; Hanson, D. K.; Thurnauer, M. C. *Photosynth. Res.* **1997**, *52*, 93-103.
- (125) Breton, J.; Nabedryk, E. *Biochim. Biophys. Acta, Bioenerg.* **1996**, *1275*, 84-90.

- (126) Shinkarev, V. P.; Wraight, C. A. *Photosynth. React. Cent.* **1993**, *1*, 193-255.
- (127) Lenaz, G.; Genova, M. L. *Int. J. Biochem. Cell Biol.* **2009**, *41*, 1750-1772.
- (128) Lenaz, G.; Genova, M. L. *Biochim. Biophys. Acta, Bioenerg.* **2009**, *1787*, 563-573.
- (129) Genova, M. L.; Baracca, A.; Biondi, A.; Casalena, G.; Faccioli, M.; Falasca, A. I.; Formiggini, G.; Sgarbi, G.; Solaini, G.; Lenaz, G. *Biochim. Biophys. Acta, Bioenerg.* **2008**, *1777*, 740-746.
- (130) Lenaz, G.; Fato, R.; Formiggini, G.; Genova, M. L. *Mitochondrion* **2007**, *7*, S8-S33.
- (131) Zhu, L.; Wang, B.; Tan, J.; Luo, M. *Int. J. Cancer Res.* **2006**, *2*, 290-298.
- (132) Genova, M. L.; Bianchi, C.; Lenaz, G. *BioFactors* **2005**, *25*, 5-20.
- (133) Quinzii, C. M.; Lopez, L. C.; Naini, A.; DiMauro, S.; Hirano, M. *BioFactors* **2008**, *32*, 113-118.
- (134) Spindler, M.; Beal, M. F.; Henschcliffe, C. *Neuropsychiatr. Dis. Treat.* **2009**, *5*, 597-610.
- (135) Kumar, A.; Kaur, H.; Devi, P.; Mohan, V. *Pharmacol. Ther.* **2009**, *124*, 259-268.
- (136) DiMauro, S.; Rustin, P. *Biochim. Biophys. Acta, Mol. Basis Dis.* **2009**, *1792*, 1159-1167.
- (137) Schneider, C. B.; Storch, A. *Agro Food Ind. Hi-Tech* **2008**, *19*, 11-13.
- (138) Henschcliffe, C.; Beal, M. F. *Nat. Clin. Pract. Neurol.* **2008**, *4*, 600-609.
- (139) Hargreaves, I. P.; Lane, A.; Sleiman, P. M. A. *Neurosci. Lett.* **2008**, *447*, 17-19.
- (140) Chaturvedi, R. K.; Beal, M. F. *Ann. N. Y. Acad. Sci.* **2008**, *1147*, 395-412.
- (141) Littarru, G. P.; Tiano, L. *Mol. Biotechnol.* **2007**, *37*, 31-37.
- (142) Li, W.; Schulman, S.; Dutton, R. J.; Boyd, D.; Beckwith, J.; Rapoport, T. A. *Nature* **2010**, *463*, 507-512.
- (143) Wallin, R.; Wajih, N.; Hutson, S. M. *Vitam. Horm.* **2008**, *78*, 227-246.

- (144) Berkner, K. L. *Vitam. Horm.* **2008**, 78, 131-156.
- (145) Benzakour, O. *Thromb. Haemostasis* **2008**, 100, 527-529.
- (146) Booth, S. L. *Annu. Rev. Nutr.* **2009**, 29, 89-110.
- (147) Rubinacci, A. *Am. J. Physiol.* **2009**, 297, C1336-C1338.
- (148) Krueger, T.; Westenfeld, R.; Schurgers, L. J.; Brandenburg, V. M. *Int. J. Artif. Organs* **2009**, 32, 67-74.
- (149) Gorter de Vries, I.; Wisse, E.; Williamson, M. K.; Price, P. A. *Calcif. Tissue Int.* **1991**, 49, 355-358.
- (150) Price, P. A.; Fraser, J. D.; Metz-Virca, G. *Proc. Natl. Acad. Sci. U. S. A.* **1987**, 84, 8335-8339.
- (151) Hui, Y.; Chng, E. L. K.; Chng, C. Y. L.; Poh, H. L.; Webster, R. D. *J. Am. Chem. Soc.* **2009**, 131, 1523-1534.
- (152) Quan, M.; Sanchez, D.; Wasylkiw, M. F.; Smith, D. K. *J. Am. Chem. Soc.* **2007**, 129, 12847-12856.
- (153) Rüssel, C.; Jaenicke, W. *J. Electroanal. Chem. Interfacial Electrochem.* **1986**, 199, 139-151.
- (154) Gestblom, B.; Svorstøl, I.; Songstad, J. *J. Phys. Chem.* **1986**, 90, 4684-4686.
- (155) Plakidin, V. L.; Vostrova, V. N. *Zhurnal Organicheskoi Khimii* **1981**, 17, 1118-1119.
- (156) Plakidin, V. L.; Vostrova, V. N. *Zhurnal Organicheskoi Khimii* **1983**, 19, 2591-2600.
- (157) Grabowski, Z. R.; Rotkiewicz, K.; Rettig, W. *Chem. Rev.* **2003**, 103, 3899-4031.
- (158) Rettig, W. *Top. Curr. Chem.* **1994**, 169, 253-299.
- (159) Rettig, W. *Angew. Chem.* **1986**, 98, 969-986.
- (160) Grabowski, Z. R.; Dobkowski, J. *Pure Appl. Chem.* **1983**, 55, 245-252.
- (161) Knyazhanskii, M. I.; Metelitsa, A. V.; Alekseev, Y. E.; Pyshchev, A. I.; Kovaleva, T. V.; Sudareva, T. P.; Uzhinov, B. M. *Russ. J. Org. Chem.* **2000**, 36, 1192-1197.

- (162) Alekseev, Y. E.; Knyazhanskii, M. I.; Metelitsa, A. V.; Sudareva, T. P.; Zhdanov, Y. A. *Dokl. Akad. Nauk* **2000**, *370*, 190-192.
- (163) Jaworski, J. S.; Lesniewska, E.; Kalinowski, M. K. *J. Electroanal. Chem. Interfacial Electrochem.* **1979**, *105*, 329-334.
- (164) Gutmann, V. *Electrochim. Acta* **1976**, *21*, 661-670.
- (165) Mayer, U.; Gutmann, V.; Gerger, W. *Monatsh. Chem.* **1975**, *106*, 1235-1257.
- (166) Gutmann, V.; Wychera, E. *Inorg. Nucl. Chem. Lett.* **1966**, *2*, 257-260.
- (167) Shraydeh, B. F.; Zatar, N. *Monatsh. Chem.* **1994**, *125*, 655-659.
- (168) Toma, H. E.; Takasugi, M. S. *J. Solution Chem.* **1989**, *18*, 575-583.
- (169) Erlich, R. H.; Popov, A. I. *J. Amer. Chem. Soc.* **1971**, *93*, 5620-5623.
- (170) Wong, M. W.; Wiberg, K. B.; Frisch, M. J. *J. Comput. Chem.* **1995**, *16*, 385-394.
- (171) Bard, A. J.; Faulkner, L. R. *Electrochemical Methods: Fundamentals and Applications*; 2nd ed., 2001.
- (172) Henderson, D.; Boda, D. *Phys. Chem. Chem. Phys.* **2009**, *11*, 3822-3830.
- (173) Chatteraj, D. K. *J. Indian Chem. Soc.* **2009**, *86*, 1009-1017.
- (174) Hahn, M.; Baertschi, M.; Barbieri, O.; Sauter, J. C.; Kotz, R.; Gallay, R. *Electrochim. Solid-State Lett.* **2003**, *7*, A33-A36.
- (175) Laoire, C. O.; Plichta, E.; Hendrickson, M.; Mukerjee, S.; Abraham, K. M. *Electrochim. Acta* **2009**, *54*, 6560-6564.
- (176) Shotwell, J. B.; Flowers, R. A., II *Electroanalysis* **2000**, *12*, 223-226.
- (177) Armstrong, N. R.; Quinn, R. K.; Vanderborgh, N. E. *Anal. Chem.* **1974**, *46*, 1759-1764.
- (178) Pyykkö, P.; Atsumi, M. *Chem.--Eur. J.* **2009**, *15*, 186-197.
- (179) Ayala, R.; Sprik, M. *J. Phys. Chem. B* **2008**, *112*, 257-269.
- (180) Liu, Y.-P.; Newton, M. D. *J. Phys. Chem.* **1994**, *98*, 7162-7169.

- (181) Brunschwig, B. S.; Ehrenson, S.; Sutin, N. *J. Phys. Chem.* **1986**, *90*, 3657-3668.
- (182) Vullev, V. I.; Jones, G. *Tetrahedron Lett.* **2002**, *43*, 8611-8615.
- (183) Thomas, M.; Wan, J.; Vullev, V. I. *AIP Conf. Proc.* **2009**, *1140*, 120-126.
- (184) Vasquez, J. M.; Vu, A.; Schultz, J. S.; Vullev, V. I. *Biotechnol. Prog.* **2009**, *25*, 906-914.
- (185) Wan, J.; Thomas, M. S.; Guthrie, S.; Vullev, V. I. *Ann Biomed Eng* **2009**, *37*, 1190-1205.
- (186) Jones, G., II; Vullev, V. I. *Photochem. Photobiol. Sci.* **2002**, *1*, 925-933.
- (187) Jones, G., II; Vullev, V. I. *J. Phys. Chem. A* **2002**, *106*, 8213-8222.
- (188) Vullev, V. I.; Wan, J.; Heinrich, V.; Landsman, P.; Bower, P. E.; Xia, B.; Millare, B.; Jones, G., II *J. Am. Chem. Soc.* **2006**, *128*, 16062-16072.
- (189) Hong, C.; Bao, D.; Thomas, M. S.; Clift, J. M.; Vullev, V. I. *Langmuir* **2008**, *24*, 8439-8442.
- (190) Millare, B.; Thomas, M.; Ferreira, A.; Xu, H.; Holesinger, M.; Vullev, V. I. *Langmuir* **2008**, *24*, 13218-13224.
- (191) Thomas, M. S.; Clift, J. M.; Millare, B.; Vullev, V. I. *Langmuir* **2010**, *26*, 2951-2957.
- (192) Becke, A. D. *J. Chem. Phys.* **1993**, *98*, 5648-5652.
- (193) Lee, C.; Yang, W.; Parr, R. G. *Phys. Rev. B Condens. Matter* **1988**, *37*, 785-789.
- (194) Dunning, T. H., Jr. *J. Chem. Phys.* **1989**, *90*, 1007-1023.
- (195) Frisch, M. J.; Trucks, G. W.; Schlegel, H. B.; Scuseria, G. E.; Robb, M. A.; Cheeseman, J. R.; Montgomery Jr., J. A.; Vreven, T.; Kudin, K. N.; Burant, J. C.; Millam, J. M.; Iyengar, S. S.; Tomasi, J.; Barone, V.; Mennucci, B.; Cossi, M.; Scalmani, G.; Rega, N.; Petersson, G. A.; Nakatsuji, H.; Hada, M.; Ehara, M.; Toyota, K.; Fukuda, R.; Hasegawa, J.; Ishida, M.; Nakajima, T.; Honda, Y.; Kitao, O.; Nakai, H.; Klene, M.; Li, X.; Knox, J. E.; Hratchian, H. P.; Cross, J. B.; Bakken, V.; Adamo, C.; Jaramillo, J.; Gomperts, R.; Stratmann, R. E.; Yazyev, O.; Austin, A. J.; Cammi, R.; Pomelli, C.; Ochterski, J. W.; Ayala, P. Y.; Morokuma, K.; Voth, G. A.; Salvador, P.; Dannenberg, J. J.; Zakrzewski, V. G.; Dapprich, S.; Daniels, A. D.; Strain, M. C.; Farkas, O.; Malick, D.

K.; Rabuck, A. D.; Raghavachari, K.; Foresman, J. B.; Ortiz, J. V.; Cui, Q.; Baboul, A. G.; Clifford, S.; Cioslowski, J.; Stefanov, B. B.; Liu, G.; Liashenko, A.; Piskorz, P.; Komaromi, I.; Martin, R. L.; Fox, D. J.; Keith, T.; Al-Laham, M. A.; Peng, C. Y.; Nanayakkara, A.; Challacombe, M.; Gill, P. M. W.; Johnson, B.; Chen, W.; Wong, M. W.; Gonzalez, C.; Pople, J. A.; Gaussian, Inc., Wallingford CT: 2004.

(196) Breneman, C. M.; Wiberg, K. B. *J. Comput. Chem.* **1990**, *11*, 361-373.

Tables

Table 3-1. First half-wave reduction potentials of quinones, $E_1^{(1/2)}$, for chloroform electrolyte solutions with different concentrations.^a

Quinone	Concentration of Bu ₄ NPF ₆					
	0 mM ^b	100 mM	150 mM	200 mM	250 mM	300 mM
	($\varepsilon = 4.77$)	($\varepsilon = 11.8$) ^c	($\varepsilon = 13.6$) ^c	($\varepsilon = 15.9$) ^c	($\varepsilon = 16.5$) ^c	($\varepsilon = 17.1$) ^c
	($n = 1.447$)	($n = 1.448$)	($n = 1.448$)	($n = 1.447$)	($n = 1.446$)	($n = 1.446$)
	($\gamma = 0.268$) ^d	($\gamma = 0.392$) ^d	($\gamma = 0.404$) ^d	($\gamma = 0.415$) ^d	($\gamma = 0.417$) ^d	($\gamma = 0.420$) ^d
BQ	-1.24±0.26	-0.559±0.021	-0.454±0.014	-0.391±0.012	-0.387±0.009	-0.357±0.011
CL4BQ	-0.341±0.226	0.062±0.025	0.105±0.009	0.125±0.006	0.138±0.008	0.130±0.017
CoQ ₁₀	-1.17±0.30	-0.749±0.009	-0.700±0.019	-0.616±0.008	-0.605±0.004	-0.604±0.005
NQ	-0.857±0.397	-0.725±0.045	-0.622±0.043	-0.673±0.024	-0.590±0.017	-0.570±0.010
CL2NQ	-0.413±0.160	-0.350±0.010	-0.358±0.005	-0.308±0.007	-0.313±0.004	-0.302±0.010
VK ₁	-0.995±0.258	-0.846±0.055	-0.949±0.061	-0.766±0.018	-0.779±0.039	-0.738±0.013

- ^a The values of $E_1^{(1/2)}$, in V vs. SCE, for 100 to 300 mM Bu_4NPF_6 were obtained from cyclic voltammetry data (Figure 3-1). The error bars represent 90% confidence level from two-sided Student t -analysis.
- ^b The values of $E_1^{(1/2)}$ for neat chloroform, i.e., 0 mM Bu_4NPF_6 , were obtained from monoexponential extrapolation to 0 (Figure 3-1d). The error bars represent a single standard deviation as yielded from the least-square fits.
- ^c The dielectric constants for the electrolyte solutions were extracted from fluorescence solvatochromism data (Figure 3-2).
- ^d $\gamma = n^{-2} - \epsilon^{-1}$.

Table 3-2. Effective radii of quinones obtained from electrochemical data and from *ab initio* calculations.

Quinone	$R_{eff} / \text{\AA}$ ^a	$R_{eff}^{(GB)} / \text{\AA}$ ^b	$R_{sph}^{(Q)} / \text{\AA}$ ^c	$R_{sph}^{(Q^{\cdot-})} / \text{\AA}$ ^d	Δgb ^e	Δsph ^f	$\Delta sph/\Delta gb$
BQ	0.935	1.67	3.99	4.06	0.786	3.34	4.25
CL4BQ	2.53	2.47	4.58	4.63	0.0237	0.830	35.0
CoQ ₁₀	1.09	2.59 ^g	5.31 ^g	5.35 ^g	1.38	3.91	2.84
NQ	1.44	2.00	4.43	4.50	0.389	2.13	5.46
CL2NQ	3.35	2.44	4.68	4.73	0.272	0.412	1.52
VK ₁	1.38	2.44 ^g	5.26 ^g	5.32 ^g	0.768	2.86	3.72

^a Effective radii, R_{eff} , of the singly-reduced quinone ions from electrochemical data, assuming spherical approximation (equation 3-4, Figure 3-3).

^b Effective sizes for one-electron reduction, $R_{eff}^{(GB)}$, calculated using generalized Born approach (equation 3-6). Atoms were approximated to spheres with homogeneously-distributed partial charges. The atomic radii and atomic charges were obtained from *ab initio* calculated structures (Figure 3-4).

^c Effective radii, $R_{sph}^{(Q)}$, of the non-charged quinone molecules from *ab initio* calculations, assuming spherical approximation. The standard deviations did not exceed 0.7 pm.

^d Effective radii, $R_{sph}^{(Q^{\cdot-})}$, of the singly-reduced quinone ions from *ab initio* calculations, assuming spherical approximation. The standard deviations did not exceed 0.7 pm.















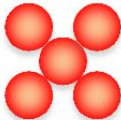

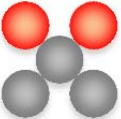

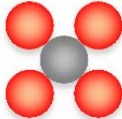
^e Δgb represents the relative difference between the experimentally measured effective radii and the calculated GB effective radii: $\Delta gb = \frac{|R_{eff} - R_{eff}^{(GB)}|}{R_{eff}}$.

^f Δsph represents the relative difference between the experimentally measured effective radii and the calculated radii of the solute spherical cavities for the anions: $\Delta sph = \frac{|R_{eff} - R_{sph}^{(Q^{\cdot-})}|}{R_{eff}}$.

^g These values were obtained from *ab initio* calculations, employing a reduced basis set on structures with truncated aliphatic chains: i.e., CoQ₁₀ and VK₁ containing only one isoprenylene unit attached to their rings (Scheme 3-2, Figure 3-5).

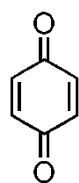
Table 3-3. Generalized-Born effective radius, $R_{eff}^{(GB)}$, of a hypothetical singly charged molecular ion (Scheme 3-3) with different charge distribution.

□

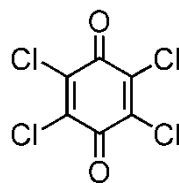
				
$z_i = 1.0$	$z_i = 0.50$	$z_i = 0.33$	$z_i = 0.25$	$z_i = 0.20$
				
$z_i = 0.0$	$z_i = 0.0$	$z_i = 0.0$	$z_i = 0.0$	$z_i = 0.0$
				
$R_{eff}^{(GB)} = 0.64 \text{ \AA}$	$R_{eff}^{(GB)} = 0.90 \text{ \AA}$	$R_{eff}^{(GB)} = 0.99 \text{ \AA}$	$R_{eff}^{(GB)} = 1.1 \text{ \AA}$	$R_{eff}^{(GB)} = 0.99 \text{ \AA}$
				
$R_{eff}^{(GB)} = 0.87 \text{ \AA}$	$R_{eff}^{(GB)} = 0.88 \text{ \AA}$	$R_{eff}^{(GB)} = 1.0 \text{ \AA}$	$R_{eff}^{(GB)} = 1.2 \text{ \AA}$	

Schemes

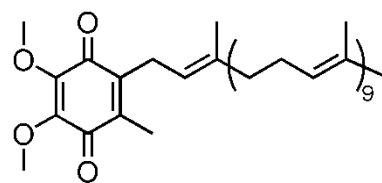
Scheme 3-1. Quinones used for this study.



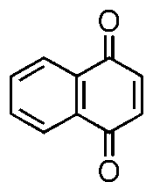
BQ



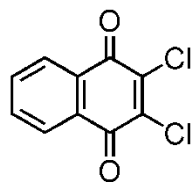
CL4BQ



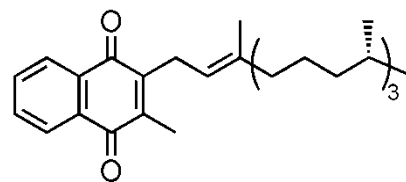
CoQ₁₀



NQ

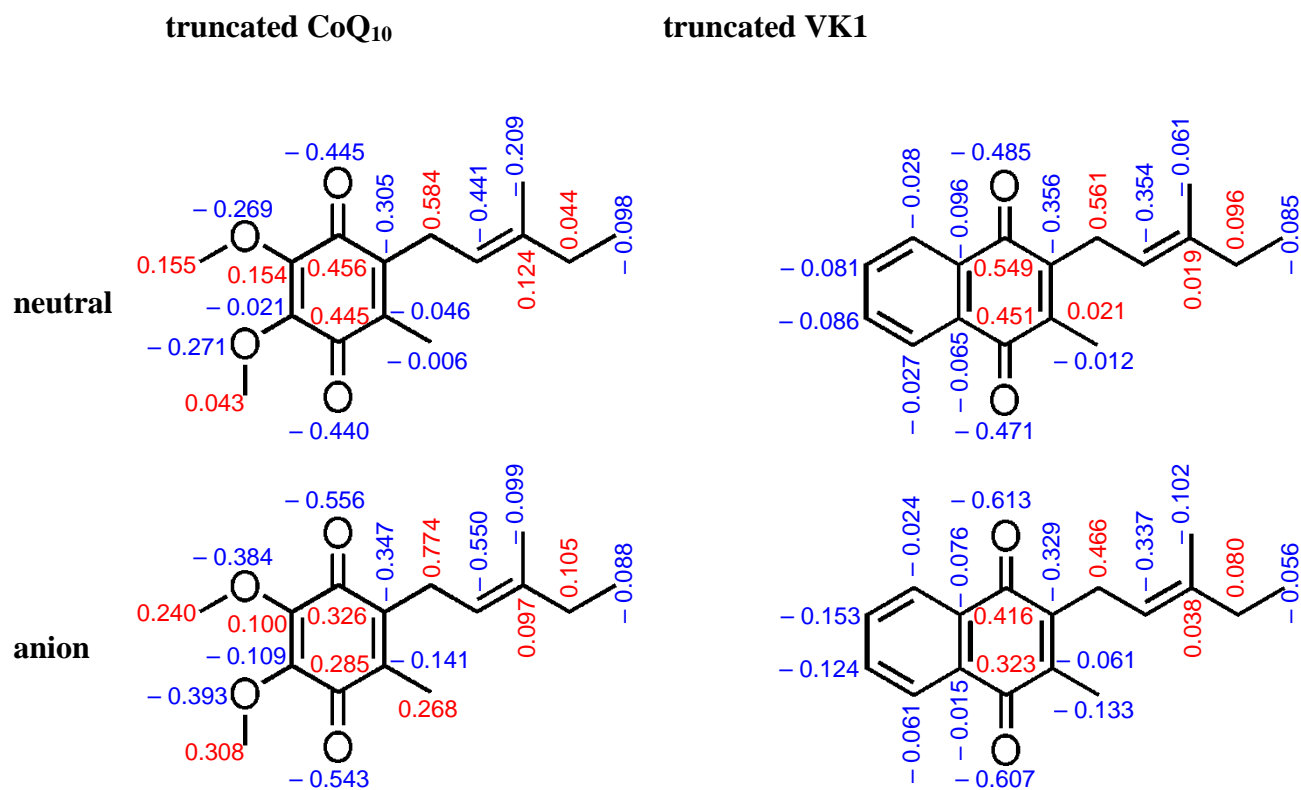


CL2NQ

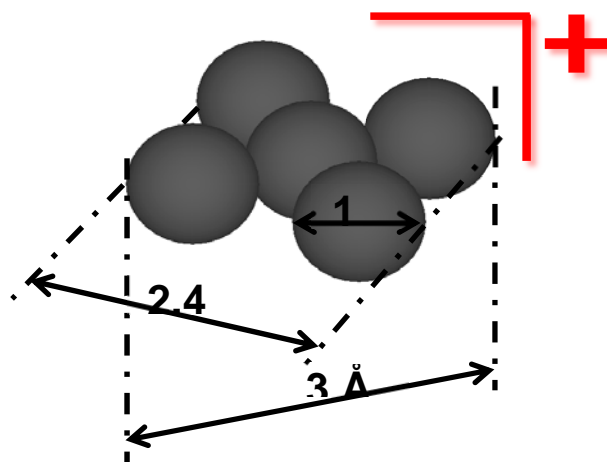


VK₁

Scheme 3-2. Analogues of CoQ₁₀ and VK₁ with truncated aliphatic chains with the corresponding CHELPG charges of the non-hydrogen atoms (in atomic units).



Scheme 3-3. A hypothetical molecular ion with D_4 symmetry composed of five spheres.



Figures

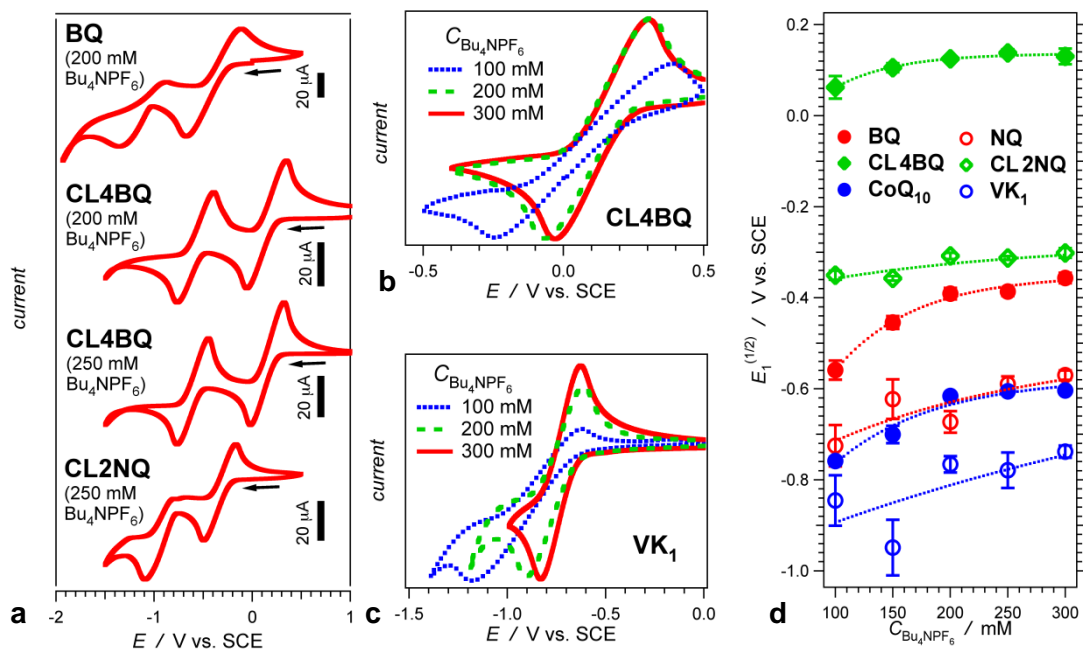


Figure 3-1. Dependence of the electrochemical reduction of quinones on the electrolyte concentration for chloroform media (quinone concentration = 2 mM; scan rate = 50 mV / s). **(a)** Cyclic voltammograms of three quinones for two different electrolyte concentrations. **(b, c)** Cyclic voltammograms displaying the first reduction waves of two quinones for three different electrolyte concentrations. The cathodic peaks are normalized for visualizing the trends. **(d)** Dependence of the quinone first-wave reduction potentials on the electrolyte concentration.

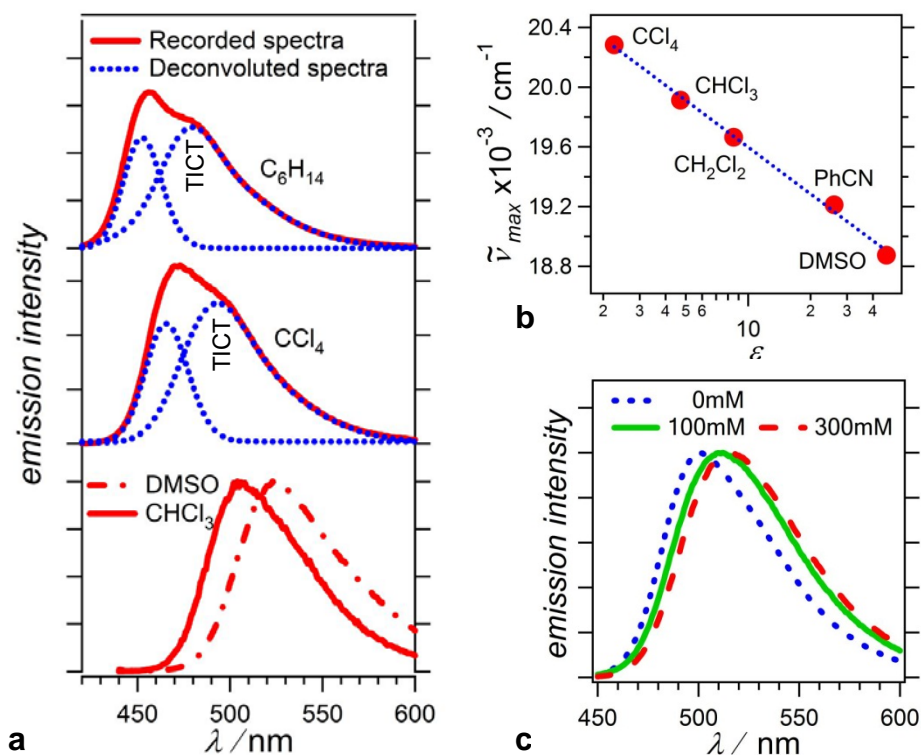


Figure 3-2. Solvatochromism of the fluorescence of Ph-ANI observed for solvent media with different polarity: dimethylsulfoxide (DMSO), benzonitrile (PhCN), dichloromethane (CH_2Cl_2), chloroform (CHCl_3), tetrachloromethane (CCl_4), and hexane (C_6H_{14}). **(a)** Fluorescence spectra of Ph-ANI ($10 \mu\text{M}$) for solvents with different polarity ($\lambda_{\text{ex}} = 410 \text{ nm}$; intensities normalized at $\lambda_{\text{em}}^{(\text{max})}$). The shoulders of the spectral bands, collected for the non-polar solvents (CCl_4 and C_6H_{14}), suggested for multiple components, and hence, were deconvoluted. The broad red-shifted components, obtained from the deconvolution, were ascribed to the radiative deactivation of the TICT state.¹⁵⁷⁻¹⁶⁰ Similar deconvolution algorithms did not yield multiple components for the Ph-ANI spectra recorded for the rest of the solvents. **(b)** Dependence of the spectral maxima on the dielectric constant of the solvents for solvents with similar indexes of refraction: i.e., $n_{\text{CCl}_4} = 1.46$; $n_{\text{CHCl}_3} = 1.45$; $n_{\text{CH}_2\text{Cl}_2} = 1.42$; $n_{\text{PhCN}} = 1.53$; and $n_{\text{DMSO}} = 1.48$. For CCl_4 , the maximum of the red-shifted TICT band was used. **(c)** Fluorescence spectra of Ph-ANI recorded for chloroform solutions with different concentrations of Bu_4NPF_6 . From the concentration dependence of the fluorescence maxima and the calibration curve, shown on (b), the dielectric constants of the electrolyte solutions were extracted.⁴²

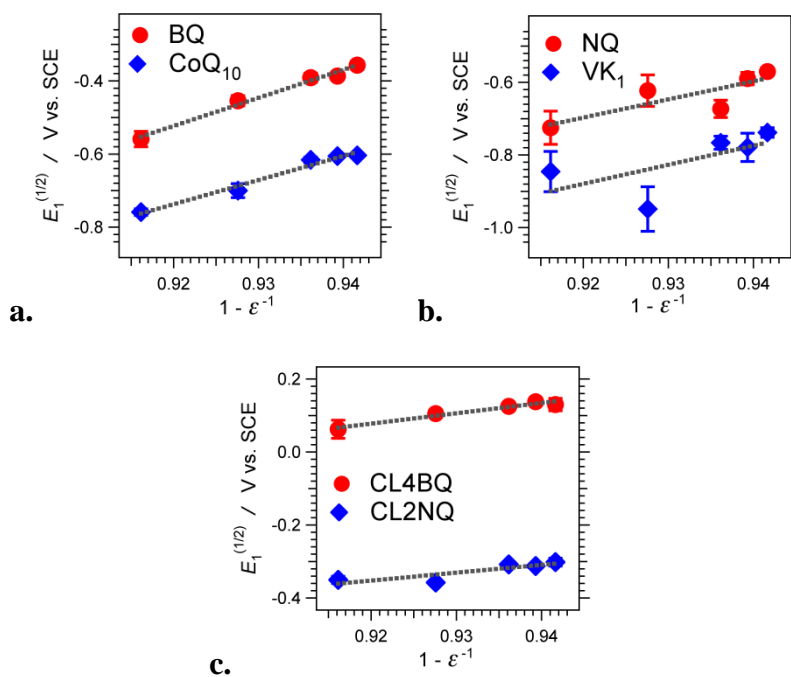


Figure 3-3. Dependence of the quinone first-wave reduction potentials on the inverted dielectric constant of the electrolyte media. The dotted lines represent least-square linear fits with the following correlation coefficients, R : **(a)** for BQ, $R = 0.993$; and for CoQ₁₀, $R = 0.987$; **(b)** for NQ, $R = 0.825$; and for VK₁, $R = 0.650$; and **(c)** for CL4BQ, $R = 0.976$; and for CL2NQ, $R = 0.875$.

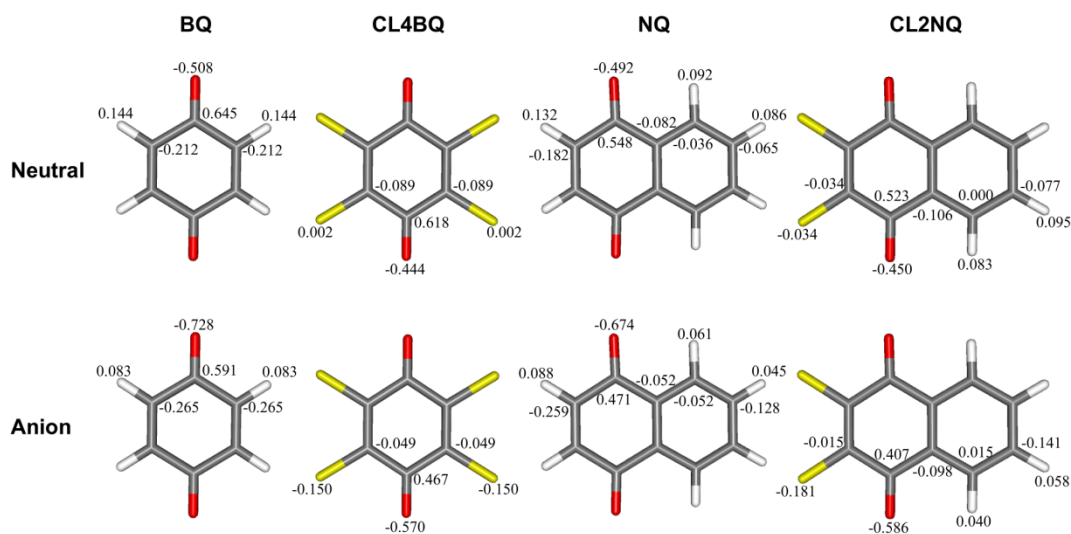


Figure 3-4. CHELPG atomic charges (in atomic units) for each species computed at the B3LYP/aug-cc-pVTZ level. Each molecule exhibits a horizontal mirror plane, and the unlabeled charges are determined by symmetry. Gray atoms correspond carbon, white to hydrogen, red to oxygen, and yellow to chlorine.

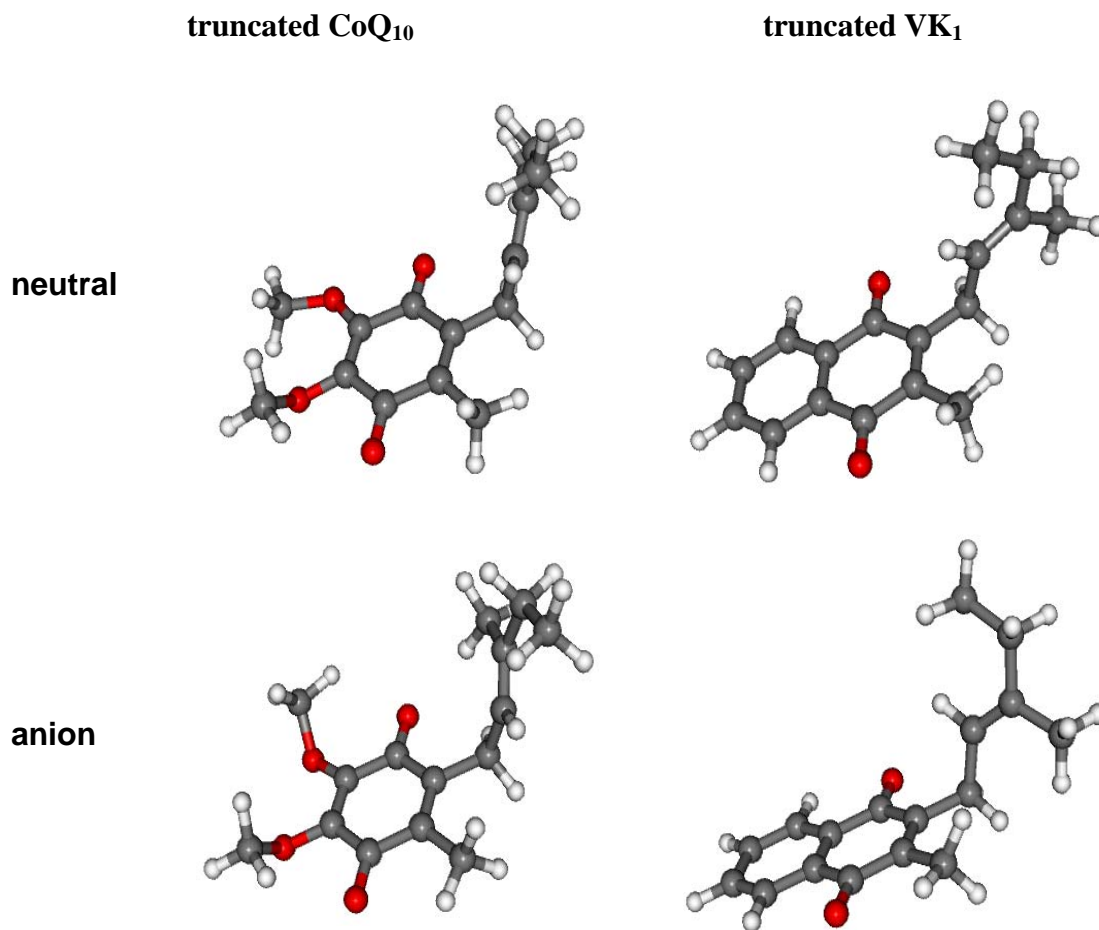


Figure 3-5. Optimized structures of CoQ₁₀ and VK₁ (neutral and singly reduced) with truncated aliphatic chains. For all structures, the geometry optimization produced conformers with aliphatic and methoxy chains folded orthogonally to the ring planes. For the truncated CoQ₁₀, all three flexible chains (the aliphatic and the two methoxy substituents) were folded toward the same side of the ring plane.

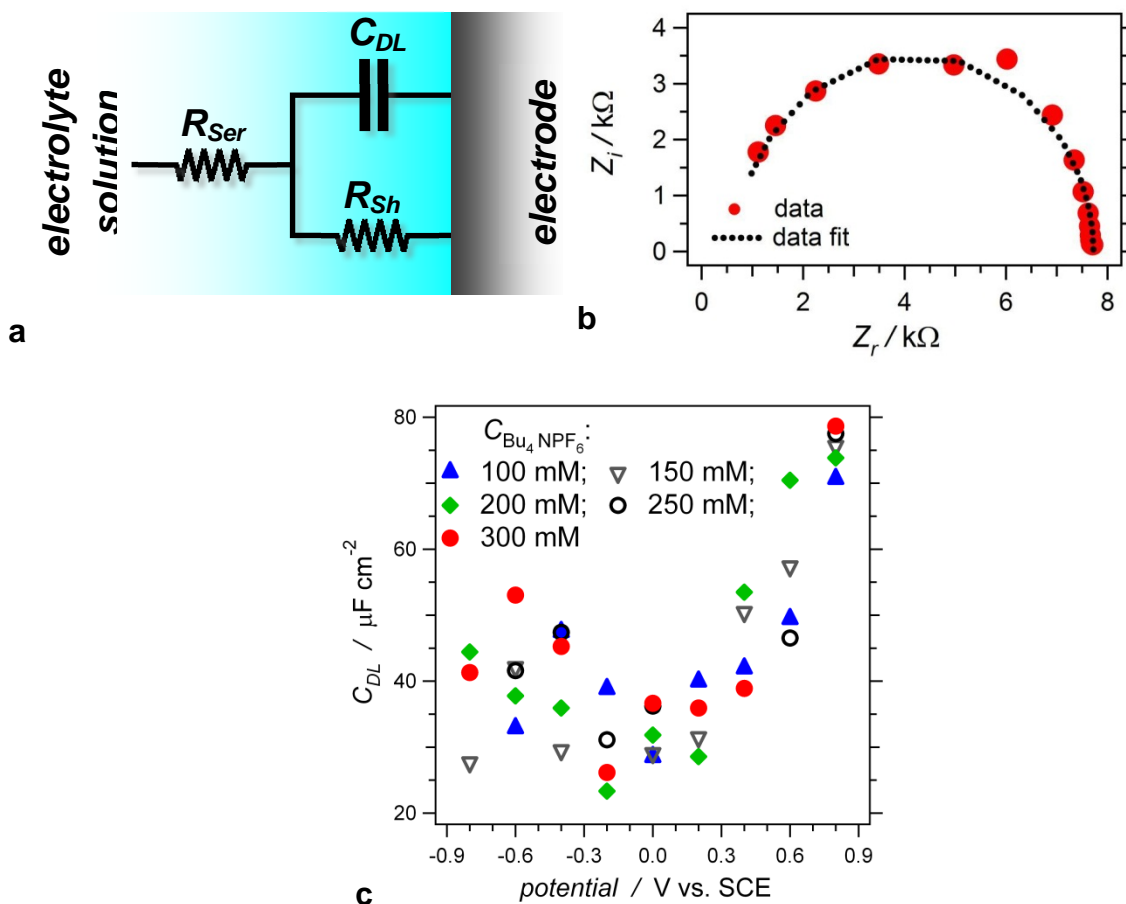


Figure 3-6. Impedance spectroscopy chloroform solutions of Bu_4NPF_6 with different concentrations. **(a)** Circuit representation of the electrical properties of the double layer on the working electrode in the absence of Faradaically active species: C_{DL} = double-layer capacitance; R_{Sh} = shunt resistance; and R_{Ser} = series resistance. **(b)** Nyquist plot of 150 mM Bu_4PF_6 at 0.6 V vs. SCE. Z_r and Z_i are the real and imaginary components, respectively, of the impedance. The dotted line represents the Randles Model fit: i.e., using the circuit model shown on (a). **(c)** Dependence of the double-layer capacitance on the applied potential for different electrolyte concentrations.

Chapter 4

Anthranilamides as Bioinspired Molecular Electrets: Experimental Evidence for Permanent Ground-State Electric Dipole Moment

Abstract

As electrostatic equivalents of magnets, organic electrets offer unparalleled properties for impacting energy-conversion and electronic applications. While biological systems have evolved to efficiently utilize protein alpha helices as molecular electrets, the synthetic counterparts of these conjugates still remain largely unexplored. This article describes a study of the electronic properties of anthranilamide oligomers, which proved to be electrets based on their intrinsic dipole moments as evident from their spectral and dielectric properties. NMR studies provided the means for estimating the direction of the intrinsic electric dipoles of these conjugates. This study sets the foundation for the development of a class of organic materials that are *de novo* designed from biomolecular motifs and possess unexplored electronic properties.

Introduction

Electrets are materials and macromolecules with ordered electric dipoles, i.e., electrets are the electrostatic analogues of magnets.^{1,2} Due to the substantial electric-field gradients that their dipoles generate, electrets have an enormous potential for unprecedented applications in energy conversion, electronics and photocatalysis applications.³⁻⁵

Protein helices present an important class of natural electrets. The ordered co-directional orientation of the amide and the hydrogen bonds in these protein conformers results in permanent electric dipoles amounting to about five Debyes per residue.^{6,7} For example, electric fields from protein α -helices stabilize weakly solvated ions in the interiors of the potassium, KcsA, and chloride, ClC, ion channels, permitting them to function efficiently.^{8,9}

Employing polypeptide helices, derivatized with an electron donor and acceptor, Galoppini and Fox demonstrated for the first time the preferential directionality of the photoinduced electron transfer toward the positive pole of the dipole.^{10,11} This charge-transfer rectification was ascribed to the stabilization of the charge-transfer states, in which the electrons were transduced toward the positive poles of the helix dipoles.⁷ Employing this approach to gold interfaces coated with polypeptide helices provided a means for controlling the directionality of photocurrent.¹²

The studies described above share the corresponding electronic properties of helical peptides as the common theme for rectifying charge transfer. Indeed, these biomimetic polypeptide conjugates have proven immensely instrumental for bringing the concept of electrets to charge transfer. Such polypeptides, however, pose some challenging

limitations: (1) the conformational integrity of polypeptide α -helices is often compromised when taken out of their natural environment, thus, limiting the scopes of their applications;¹³ and (2) polypeptides composed of natural α -amino acids are wide-band-gap materials with an optical band gap of approximately 5.6 eV, which limits the distance of efficient charge transfer to less than two nanometers. Charge transfer through such polypeptides is attained solely via electron tunneling.¹⁴⁻¹⁸ Hopping mechanism, involving multiple discreet electron-transfer steps along precisely arranged cofactors or redox residues, such as tryptophan, is essential for extending the charge-transfer distances beyond the intrinsic limits of the protein backbone chains.¹⁹

To address these issues, we undertook a bioinspired approach to attain organic electrets, which have the structural and functional advantages over their biological counterparts, and do not suffer the disadvantages of the biological macromolecules.^{4,20} Similar to protein α -helices, we aimed at ordered amide and hydrogen bonds to generate intrinsic electric dipoles along the backbones of the bioinspired conjugates. Unlike proteins, however, our goal was to place aromatic moieties as a part of the macromolecular backbones, in order to attain extended π -conjugation and hence pathways for long-range efficient charge transfer. Anthranilamides proved to be excellent candidates for this bioinspired approach (Scheme 4-1).²⁰

Anthranilamide oligomers are known structures existing in extended conformations stabilized by intramolecular hydrogen bonding.^{21,22} In fact, anthranilic acid, i.e., *o*-aminobenzoic acid, is vitamin L₁. To date, the electronic properties of anthranilamides oligomers and their derivatives have not been investigated. Recently, using *ab initio*

calculations, we demonstrated for the first time that these anthranilamide oligomers have intrinsic dipole moments. The vectorial sum of the dipoles from the amide bonds, along with the dipoles generated from the shift in the electron density upon the formation of hydrogen bonds, resulted in total electric ground-state dipole moments of about three Debyes per residue (Scheme 4-1).²⁰ Unlike in protein α -helices, the intrinsic dipoles of the anthranilamide oligomers were oriented from their N- to their C-termini (Scheme 4-1).²⁰

Herein, we experimentally demonstrate that anthranilamides possess intrinsic dipole moments. We used relatively small conjugates, i.e., monomer, dimer and trimer, for this investigation (Scheme 4-2). Even in organic solvents, such as chloroform, in which these anthranilamide conjugates had pronounced solubility, they exhibited a strong propensity for aggregation. This self-assembly, however, was not electrostatically driven and the aggregates themselves had intrinsic dipoles as it became evident from dielectric studies of their solutions: i.e., at least partial co-directional arrangement of the anthranilamides within the aggregates. Analysis of ¹H chemical shifts, as determined using NMR spectroscopy, allowed us to determine that the direction of the intrinsic dipole was from the N- to the C-termini of the anthranilamides, which confirmed our theoretical findings.

Results and Discussion

We prepared monoanthranilamide (h-A-ph), dianthranilamide (h-AA-ph) and trianthranilamide (h-AAA-ph) derivatives, in which the C-termini were capped with phenyl and the N-termini with heptyl groups (Scheme 4-2). For these studies, the solvent

of choice was chloroform. It provided the needed sample solubility and concurrently, it was non-polar enough to ensure that the effects from the permanent dipoles were readily detectable.²³

Previously reported structural data indicate that anthranilamides have a preference for an extended conformation. X-ray and NMR studies demonstrated that anthranilamide oligomers assume an extended conformation with a coplanar arrangement of the aromatic rings.^{21,22} Hydrogen bonding between amides attached to the same aromatic ring supports this coplanar extended conformation (Scheme 4-1).^{21,22} Such coplanar conformations, supported by hydrogen-bond networks, are not unusual for polymers of aromatic amides and esters in organic solvents.²⁴⁻²⁷ Furthermore, structure relaxation of a range of anthranilamide oligomers, using computational methods, constantly led to coplanar extended conformations supported by hydrogen bonds between amides attached to the same aromatic residue (Scheme 4-1).²⁰

The UV/visible emission spectra of all three conjugates exhibited two peaks, the intensity of which was concentration dependent (Figure 4-1). A decrease in the concentration of these conjugates in chloroform caused a decrease in the intensity of the red-shifted band, and an increase in the intensity of the high-energy peaks. These findings were an indication for aggregation of the anthranilamides in the investigated concentration range. The emission peak at about 400 nm was due to fluorescence from the monomeric forms of the anthranilamide oligomers; and the broad band at around 520 nm was ascribed to the emission of their aggregated forms. Especially for h-AAA-ph, the intensity decrease in the aggregate emission band was less substantial than the increase in

the fluorescence intensity of the 400-nm monomer emission. This finding suggested that the aggregation of the anthranilamides caused a decrease in their emission quantum yields.

Possible origins of the low-energy emission band include: (1) the formation of ground-state aggregates and their direct excitation; and (2) excited-state aggregation (excimer formation), where photoexcited molecule aggregates with a ground-state molecule, were possible origins of the aggregate emission. Close examination of the absorption spectra showed a slight increase in the extinction coefficient as the concentrations increased; a case, which was most pronounced for h-AA-ph (Figure 4-1a, c). These small spectral changes, however, cannot be conclusive for claiming or ruling out ground-state aggregation.

To address this issue, we resorted to time-resolved emission spectroscopy. The emission-decay curves, measured at the 520-nm aggregate bands, for each of the three oligomers showed a rise within the excitation pulse, followed by immediate nanosecond decay (Figure 4-1d). The lack of a slow post-excitation rise (characteristic for excimer formation), along with the fast emission decay kinetics, was indicative that the low-energy bands resulted primarily from ground-state aggregates.^{34,35}

Addition of electrolyte and the use of a solvent media with higher polarity did not prevent the aggregation of the oligomers. Thus, electrostatic interactions (between the anthranilamide dipoles) were not the principal driving force for the aggregate formation. Due to the abundance of aromatic moieties in each of the oligomers, the aggregation could be plausibly ascribed to π - π stacking.

The concentration dependence of the fluorescence properties of the anthranilamides provided a means for evaluating their aggregation behavior.³⁷⁻⁴⁰ Deconvolution of the fluorescence spectra (Figure 4-2a) allowed us to estimate the relative contribution to the emission from the monomer and the aggregate bands, i.e., R_m and R_a , respectively:

$$R_m = \frac{S_m}{S_m + S_a} \quad (4-1a)$$

$$R_a = \frac{S_a}{S_m + S_a} \quad (4-1b)$$

where S_m and S_a represent the integrated emission under the monomer and aggregate bands, respectively, i.e., $S = \int F(\tilde{\nu})d\tilde{\nu}$, and $F(\tilde{\nu})$ is the fluorescence intensity at wavenumber $\tilde{\nu}$.^{38,41,42}

As expected, an increase in the total concentration, C , of the anthranilamides, A , caused a decrease in S_m and an increase in S_a (Figure 4-2b). For h-A-ph, this change in the ratios, S , between the aggregate and monomer fluorescence bands occurred at $C < 10^{-4}$ M. For h-AA-ph and h-AAA-ph, the largest changes in S_m and S_a occurred in the sub- μ M concentration range (Figure 4-2b).

The aggregation led to fluorescence quenching, and the emission quantum yields, Φ , of the aggregates were about 2 to 20 times smaller than Φ of the monomeric forms of the anthranilamides (Table 4-1). Therefore, R_m and R_a , as defined in equation 4-1, did not directly represent the equilibrium concentrations $[A]$ and $[A_n]$ of the anthranilamide monomers and aggregates, respectively. Considering that $S_m \propto \Phi_m[A]$ and $S_a \propto \Phi_a[A_n]$, along with $C = [A] + n[A_n]$, yields:

$$[A] = \frac{\phi R_m}{1-(1-\phi)R_m} C = \xi C \quad (4-2)$$

where $\phi = \Phi_a / \Phi_m$, and ξ is the fraction of the anthranilamides that are in the form of monomers, i.e., $\xi = [A] / C$ (Figure 4-2c). Substituting equation 4-2 in the expression for the equilibrium constant, $K = [A_n] / [A]^n$, representing the aggregation process, $n A \rightleftharpoons A_n$, yields:

$$\lg(C - (1 - \xi)) = n \lg(C\xi) + \lg(nK) \quad (4-3)$$

The slopes of the linear fits of $\lg(C(1-\xi))$ vs. $\lg(C\xi)$ provided a means for estimating of the state of aggregation, n , for the different anthranilamides (Figure 4-2d). For each of the anthranilamides, however, autocorrelation analysis revealed that a single linear fit over the whole concentration range did not yield statistically significant representations of the prelateship between $\lg(C(1-\xi))$ and $\lg(C\xi)$. The Durbin-Watson statistics (d) was smaller than 1 for all fits covering the full concentration ranges (Table 4-2),⁴³⁻⁴⁶ indicating for possible positive autocorrelations that were not accounted for by the linear model, equation 4-3. As an alternative, linear fits limited to the concentration ranges, where the biggest changes in R_m and R_a occurred, provided excellent linear correlations with $d \approx 2$ (Table 4-2).

The slopes of the linear fits, limited to the low μM and sub- μM ranges, were about 1.7, 4.1 and 2.2 for h-A-ph, h-AA-ph, and h-AAA-ph, respectively (Table 4-2). Therefore, the observed concentration-dependent changes in the fluorescence of h-A-ph and h-AAA-ph corresponded to the formation of predominantly dimers, and of h-AA-ph – tetramers. The linear fits in the concentration ranges extending to 10 mM yielded slopes of about unity, $n \approx 1$ (Table 4-2). Assuming that any aggregation, including between a monomer and an

aggregate and between two aggregates, would affect the emission properties of the anthranilamides, the unity slopes for $C > 10^{-4}$ M indicated that no detectable aggregation took place in that concentration range.

The zero-to-zero energies (E_{00}),⁴⁷ extracted from the absorption and the emission spectra, correspond to the optical gaps between their highest occupied molecular orbitals (HOMOs) and their lowest unoccupied molecular orbitals (LUMOs), i.e., the optical HOMO-LUMO gaps of the anthranilamide conjugates (Table 4-1). The optical gaps, however, do not quantitatively represent the HOMO-LUMO energy differences. Instead, the optical HOMO-LUMO gaps of the anthranilamides characterize the direct transitions between the ground and the lowest singlet excited states; i.e., transitions that do not involve nuclear reorganization, and that are between closed-shell ground states and states with singly-occupied molecular orbitals. Conversely, the calculated HOMO-LUMO gaps (ΔE) represent the theoretically estimated differences between the HOMOs and LUMOs of the ground states of the anthranilamides.²⁰

For the anthranilamides, E_{00} was between 0.6 and 1.3 eV smaller than ΔE (Table 4-1). Two considerations could account for the differences between E_{00} and ΔE . (1) Optically-determined HOMO-LUMO gaps tend to be underestimated due to the charge-charge stabilization between the electron in LUMO and the hole in the HOMO. (2) Density functional theory (DFT), which we used for calculating ΔE ,²⁰ cannot provide feasible predictive power for the energies of unoccupied orbitals, such as LUMOs. That is, DFT can provide estimates of trends in the energies of the LUMOs within series of analogous molecules, but the absolute values of these estimates should be approached with caution.

A noticeable feature for these oligomers was the lack of considerable spectral shifts when the number of anthranilamide residues increased. While the molar extinction coefficients extrapolated to zero concentration, ϵ_0 , increased substantially with the number of residues, the shifts in the spectral maxima did not exceed 25 nm (Table 4-1). In fact, the spectral maxima of h-AA-ph and h-AAA-ph were practically identical. These observations indicated that the excited states, involved in the optical transitions, were localized.⁴⁸

To experimentally test for permanent ground-state electric dipole moments, we used the Hedestrand approach employed with the Debye solvation theory, as we have previously described.^{23,49-54} Linear analysis of the concentration dependence of the dielectric constant and the density of diluted solutions of polar solutes in relatively non-polar solvents, provides the means for estimating the molecular dipole moments of the solutes (Figure 4-3).^{23,54,55}

In the mM concentration range, required for this set of studies, the anthranilamides existed as aggregates. Nevertheless, an increase in the concentration of the anthranilamides caused an increase in the dielectric constant of the chloroform solutions as determined at different frequencies from capacitance measurements with a three-terminal cell (Figure 4-3b, c).⁵⁴ Because only small fraction of the anthranilamides existed as monomers at concentrations exceeding about 0.5 mM (Figure 4-2c), the observed increase in the dielectric constant was ascribed to permanent dipole moments of the aggregates. That is, the aggregation did not cancel the permanent dipoles of these conjugates, indicating that they assembled, at least partially, in a co-directional manner.

Using the Hedestrand approach, we extracted the molar polarizations, P_{2H} (per mole oligomer), from the experimental measurements that revealed the effect of the dipole moments on the dielectric properties of the solutions (Table 4-3). For comparison, we calculated the orientation polarization, $P_{2\mu}$, from the theoretically determined values of the dipole moments, μ_0 , of similar anthranilamide oligomers in gas phase (Table 4-3).²⁰ The magnitude of the measured polarization, P_{2H} , indeed, increased with an increase in the oligomer size, and theoretically predicted $P_{2\mu}$ followed the same trend.

Although a fraction of the anthranilamides existed as monomers in the mM concentration range of the dielectric measurements (Figure 4-2c),⁵⁶ we could not ascribe the experimentally obtained polarizations, P_{2H} , solely to the dipoles of the non-aggregated oligomer molecules that were free in solution. Assuming that the oligomer aggregates did not have ground-state dipoles and considering the fractions of the monomers, ζ , we estimated that the measured polarizations, P_{2H} , should result in dipole values of 38 D, 22 D, and 34 D for h-A-ph, h-AA-ph, and h-AAA-ph, respectively, which were unfeasibly large, exceeding about 3 to 9 times the theoretically determined dipoles, μ_0 (Table 4-3). Conversely, assuming that the dipoles of the monomeric anthranilamide derivatives had values close to the theoretically estimated values of μ_0 , we estimated that the non-aggregated oligomers contributed about 1.4%, 11% and 8.5% of the measured polarizations, P_{2H} , of A-ph, h-AA-ph, and h-AAA-ph, respectively. Therefore, it was the dipole moments of the aggregates that predominantly contributed to the experimentally determined polarizations, P_{2H} .

For h-A-ph, the experimentally obtained value of P_{2H} was slightly higher than $P_{2\mu}$ (Table 4-3). In the mM concentration range of the dielectric measurements only about 2% of h-A-ph existed as a monomer (Figure 4-2c), and indeed it was the aggregate that contributed to the dielectric properties of the solutions. Considering the dimerization behavior of h-A-ph (Table 4-2), we estimated that the permanent dipole moment of its aggregate was 7.5 D. Assuming that each anthranilamide molecule contributes about 4.5 D to the aggregate total dipoles (Table 4-3), the maximum dipole expected for these dimers was 9 D. That is, the experimentally obtained value was about 83% of the theoretically expected maximum value for the dimers, indicating that h-A-ph has a strong preference for aggregating in a co-directional manner.

This propensity for co-directional self-assembly of h-A-ph could be ascribed to the asymmetry in the terminal capping groups. Upon dimerization the C-terminal phenyl would have stronger aggregation propensity with another aromatic moiety, due to π - π stacking, for example, rather than for the N-terminal heptyl. Similarly, the N-terminal heptyl group would have a stronger propensity for aggregating with another alkyl, rather than with an aromatic moiety.

Considering that h-AA-ph exhibited an aggregation behavior leading to tetramers (Figure 4-2d, Table 4-2), from the measured polarization we estimated the dipole moment of its aggregate to be in the order of 13 D. Based on the calculated μ_0 , the maximum possible value of the dipole of h-AA-ph tetramers was about 30 D. Similarly, the estimated value from the experimentally measured polarization for the dipole of the h-AAA-ph dimer was about 9.9 D, which was about half of the maximum possible value of

20 D for this aggregate, based on the theoretical estimate for μ_0 (Table 4-3). These findings indicated that h-AA-ph and h-AAA-ph also had propensity for aggregating in a co-directional manner that, however, was not as pronounced as the propensity exhibited by h-A-ph. The reason for this decrease in the preference of h-AA-ph and h-AAA-ph toward co-directional aggregation could be ascribed to the increase in their size. The larger number of aromatic rings in the longer oligomers would provide a means for more interactions between aromatic moieties, decreasing the relative contribution of the N-terminal heptyls toward the aggregation interactions, and hence decreasing the preference for the N-termini to aggregate with the N-termini of the other molecules, and the C-termini with C-termini.

Trends in the deshielding of the amide protons, $H^{(N)}$, as observed from their NMR chemical shifts, provided a means for estimation of the orientation of the anthranilamide dipoles. The C-terminal amide protons, H_a , which were not hydrogen-bonded, exhibited chemical shifts in the “aromatic” region, i.e., about 8 ppm (Figure 4-4). The hydrogen bonding of the rest of the amide protons, H_b , H_c , and H_d , caused deshielding and a downfield shift in their signals, placing them in the “acid” region between 10.5 and 12.5 ppm (Figure 4-4).

Although at the concentrations we used for the NMR studies the anthranilamides existed as aggregates, each of the amide protons exhibited a single peak with a narrow Lorentzian shape. Two-dimensional (2D) NMR experiments utilizing intramolecular couplings revealed that each of these different singlets exhibited different correlation patterns, indicating that each of the peaks corresponded to only one amide proton. These

findings suggested that the same amide proton, from the different molecules in an aggregate, had identical microenvironment.

To examine the effect of the anthranilamide intrinsic dipoles, we compared the chemical shifts of amide protons that belonged to the same molecule and that had identical bonding environment (i.e., identical within about one-residue radius comparable with the intramolecular NMR coupling effects we measured). The hydrogen-bonded amide protons, H_b and H_c of h-AAA-ph, were the choice for this comparison (Scheme 4-2). Both protons were in the middle of the oligomer, and each one of them was surrounded by three aromatic moieties with identical bonding pattern and orientation (Scheme 4-2). Despite their close similarity, H_b and H_c had distinctly different chemical shifts as evident from the three singlets separated from one another in the 11-13-ppm region (Figure 4-4). The difference in their chemical shifts could be ascribed to: (1) effects from the permanent electric dipole moments; and (2) differences in the microenvironments within the aggregates. The latter is not plausible because non-specific aggregation is very unlikely to provide unique microenvironment for the same proton from different molecules in an aggregate. Therefore, it would be the intramolecular effects, along with the permanent electric dipoles, that govern the observed NMR chemical shifts.

To avoid ambiguities due to aggregation, we used only intramolecular correlations to assign the chemical shifts of the hydrogen-bonded amide protons, H_b , H_c , and H_d . Gradient-selected heteronuclear multiple bond correlation (gHMBC) allows for detecting

^1H - ^{13}C coupling through several bonds, including through heteroatoms, such as the amide nitrogens.^{58,59}

For acceptable signal-to-noise ratio, we carried the HMBC and the other 2D NMR measurements at about 50 mM sample concentrations. The chemical shifts of all protons except H_a , did not exhibit concentration dependence in the range from about 1 to 50 mM. The shift of the non-hydrogen bonded proton, H_a , however, moved downfield by about 0.45 ppm as the concentration increased to 50 mM (Figure 4-4, 4-5). Changes in the state of aggregation should affect the chemical shifts of all protons.^{34,38} H_a was the most labile proton in h-AAA-ph, making it sensitive to changes in the activity of traces of water in the deuterated chloroform upon increasing the molar fraction of the anthranilamide. Therefore, this downfield shift of the signal from H_a is not an indication for changes in the state of aggregation. This observation, along with the fluorescence concentration-dependence trends (Figure 4-1c), implied that the aggregation occurred in the μM and sub- μM range.

The signal from the most downfield-shifted aliphatic protons, H_e and $\text{H}_{e'}$ at 2.4 ppm (Scheme 4-3), correlated with only one peak in the carbonyl carbon region on the HMBC spectra (Figure 4-5a). This correlation allowed the assignment of the N-terminal carbonyl carbon C_d (Figure 4-5a). Concurrently, the N-terminal carbonyl carbon correlated with only one of the amide proton signals, at 11.2 ppm, which thus we assigned to H_d , (Scheme 4-2, 4-3)

To assign the chemical shifts of H_b and H_c of h-AAA-ph, we majorly resorted also to gHMBC (Figure 4-5). In the HMBC spectrum of h-AAA-ph, we compared the

correlation peaks of the assigned terminal amide protons with the aromatic carbons in the region around 115 – 130 ppm (Figure 4-5a). The C-terminal amide proton, H_a , which was not hydrogen bonded, exhibited correlation peak with a maximum that spread between 120.9 and 121.4 ppm of the carbon shifts (Figure 4-5e). Concurrently, the N-terminal amide proton, H_d , exhibited two overlapping correlation peaks with maxima spreading between 120.5 and 121.0 ppm, and between 121.4 and 122.0 ppm (Figure 4-5d).

We examined the correlation peaks from the other two amide protons for patterns of connectivity with carbons that were about three bonds away from the H_a and H_d . The correlation peak that corresponded to the amide ^1H at 11.96 ppm, had a maximum that extended between 121.9 and 122.7 ppm (Figure 4-5c). Hence, this proton had some cross-correlation overlap with H_d , i.e., the 11.96-ppm proton and H_d could be coupled to the same carbon. Concurrently, the 11.96-ppm amide proton had no cross-correlation with H_a , i.e., no common carbon to which both of them would be coupled (Figure 4-5c, e). Therefore, we assigned the proton at 11.96 ppm to H_c (Scheme 4-2, Figure 4-4). The amide proton at 12.25 ppm had a correlation peak with a maximum intensity that spread widely between 121.1 to 122.4 ppm over the carbon shift region (Figure 4-5b). This proton had cross-correlation with both H_a and with the proton at 11.96 ppm that we assigned to H_c . Conversely, due to the close overlap of the aromatic carbon peaks, we could not readily rule out cross-correlation between the 12.25-ppm proton and H_d . The lack of cross-correlation between the 11.96-ppm proton and H_a , however, made it implausible to assign the 11.96-ppm peak to H_b . Therefore, considering all possible

coupling patterns, we assigned the peak at 11.96 ppm to H_c, and the peak at 12.25 ppm to H_b (Figure 4-4).

Because everything in the bonding patterns of H_b and H_c was identical within nearest residue range, we could ascribe the difference between the chemical shifts of these two protons to effects from the local electric field generated by the anthranilamide dipole (Scheme 4-1). As observed for polypeptide α -helices, positive polarization from the dipole electric field lowers the pK_a of protic groups, i.e., increases their acidity and causes a downfield shift in the signals from their protons.⁶⁰ For h-AAA-ph, H_b is the most downfield shifted proton, i.e., about 0.3 ppm downfield from H_c. This difference in the chemical shifts indicated for more positive electric-field potential around H_b than around H_c. Because of the identity in the bonding microenvironment around these two protons, the anthranilamide dipole moment was the most plausible source for the difference in the electric potentials around H_b and H_c. Considering that the downfield shift in the H_b signal was consistent with a more positive potential than the potential around H_c, we could assign the direction of the anthranilamide dipole moment to be from the N- to the C-terminus: i.e., the negative pole of the dipole was oriented toward the N-terminus and the positive pole – toward the C-terminus, consistent with the findings from our *ab initio* theoretical findings.²⁰

Conclusions

Anthranilamides possess intrinsic dipole moments and manifest a large propensity for self-assembly. The estimated dielectric properties of solutions of these conjugates, along

with the lack of pronounced dependence of their spectral wavelength features on their molecular size, indicated for co-directional arrangements of these oligomers within their aggregates. NMR data elucidated that the orientation of the intrinsic dipoles is from the N- to the C-termini of the trianthranilamide oligomer. These findings demonstrate the anthranilamides as organic molecular electrets.

Experimental

Materials. Palladium (10%) on activated carbon powder was purchased from Sigma-Aldrich, 2-amino-N-phenylbenzamide (95 %), octanoyl chloride (99 %), pyridine (99.5+%), 2-nitrobenzoyl chloride (97 %), and all other reagents, including spectroscopic grade and anhydrous solvents dichloromethane (>99.8%) and N,N-Dimethylformamide (DMF, 99.8%) were used as supplied by commercial vendors.

Synthesis. The anthranilamide oligomers were synthesized from the C- to the N-termini by consequential addition of 2-nitrobenzoyl chloride and reduction of the nitro groups to amines, preparing it for the next coupling step.²¹ We started with 2-amino-N-phenylbenzamide as a phenyl-capped N-terminus.

General information. Proton (¹H) NMR spectra were recorded at 400 MHz at ambient temperature using CDCl₃ as solvent unless otherwise stated. Chemical shifts are reported in parts per million relative to CDCl₃ (¹H, δ 7.24; ¹³C, δ 77.23). Data for ¹H NMR are reported as follows: chemical shift, integration, multiplicity (s = singlet, d = doublet, t = triplet, q = quartet, m = multiplet), integration and coupling constants. High-resolution mass-spectra were obtained on a Q-TOF mass spectrometer.⁶¹ Analytical thin layer

chromatography was performed using 0.25 mm silica gel 60-F plates. Flash chromatography was performed using 60Å, 32-63 μm silica gel. Yields refer to chromatographically and spectroscopically pure materials, unless otherwise stated.⁶² All reactions were carried out in oven-dried glassware under an argon atmosphere unless otherwise noted.

The purity of the anthranilamide oligomers was examined using TLC (normal phase), HPLC-MS (reverse phase) and melting point. For the HPLC tests, the mobile phase, 10% to 98% acetonitrile in water (+0.1 % trifluoroacetic acid), was applied as linear gradients between 0.5 and 2 ml min⁻², at flow rate 0.9 ml min⁻¹. The stationary phase in the column was 3 μm C8(2), 100 Å, packed in a 30×3.00 mm column (Phenomenex Luna[®]). Melting points were recorded using an electrothermal capillary melting point apparatus and are uncorrected. Combustion elemental analysis for carbon, hydrogen and nitrogen was conducted by Atlantic Microlab, Inc. (Norcross, GA). The samples were dried *in vacuo* for two to four hours prior to the analysis. The weight percentages for carbon, hydrogen and nitrogen were reported. The expected values for the weight percentages were calculated from the empirical formulas using the known atomic weights.⁶³

2-octanamido-N-phenylbenzamide (h-A-Ph). To an ice-chilled 10 ml CH₂Cl₂ solution of 2-amino-N-phenylbenzamide (200 mg, 0.94 mmol) and pyridine (190 mg, 0.20 ml, 2.4 mmol) was added octanoyl chloride (310 mg, 1.9 mmol). The mixture was stirred at 0°C to room temperature for 2 h. The reaction mixture was diluted with 50 ml CH₂Cl₂, then washed with 1N HCl (50 ml × 2), saturated NaHCO₃ (70 ml), and brine (50 ml). The organic layer was dried over Na₂SO₄, and concentrated *in vacuo* to afford white powder.

Purification *via* flash chromatography on silica gel (100% CH₂Cl₂ to 1% MeOH in CH₂Cl₂) afforded 300 mg (0.88 mmol, 94%) of h-A-Ph (CAS# 881768-10-1), white solid: m.p. 115-118 °C. Elemental analysis, expected for C₂₁H₂₆N₂O₂: C, 74.52%; H, 7.74%; N, 8.28%; measured: C, 74.52%; H, 7.74%; N, 8.30%. ¹H NMR (400 MHz, CDCl₃) δ 10.65 (1 H, s), 8.55 (1 H, d, *J* = 8.4 Hz), 8.04 (1 H, s), 7.57 (3 H, t, *J* = 8.4 Hz), 7.45 (1 H, t, *J* = 8.4 Hz), 7.39 (2 H, t, *J* = 7.6 Hz), 7.19 (1 H, td, *J* = 7.6, 1.2 Hz), 7.08 (1 H, t, *J* = 7.6 Hz), 2.36 (2 H, t, *J* = 7.2 Hz), 1.70 (2 H, m), 1.40-1.20 (8 H, m), 0.84 (3 H, t, 7.2 Hz) ppm; ¹³C NMR (100 MHz, CDCl₃) δ 172.69, 167.56, 139.41, 137.73, 132.73, 129.41, 127.09, 125.27, 122.99, 122.19, 121.65, 120.92, 38.63, 31.90, 29.43, 29.23, 25.70, 22.82, 14.28 ppm. HRMS *m/z* calculated for C₂₁H₂₆N₂O₂Na (M+Na) 361.1892, found 361.1891 (M+Na).

2-nitro-N-(2-(phenylcarbamoyl)phenyl)benzamide. To an ice-chilled 100 ml CH₂Cl₂ solution of 2-amino-N-phenylbenzamide (5.0 g, 24 mmol) and pyridine (4.7 g, 4.8 ml, 59 mmol) was added 2-nitrobenzoyl chloride (8.7 g, 47 mmol). The mixture was stirred at 0°C to room temperature for 2 h. The reaction mixture was diluted with 500 ml CH₂Cl₂, then washed with 1N HCl (300 ml × 2), saturated NaHCO₃ (300 ml), and brine (300 ml). The organic layer was dried over Na₂SO₄, and concentrated *in vacuo* to afford white solid (8.1 g, 22 mmol, 95 %). ¹H NMR (400 MHz, CDCl₃) δ 11.30 (1 H, s), 8.71 (1 H, d, *J* = 8.4 Hz), 8.04 (1 H, d, *J* = 8.0 Hz), 7.93 (1 H, s), 7.66 (3 H, m), 7.57 (2 H, m), 7.50 (2 H, t, *J* = 8.0 Hz), 7.36 (2 H, td, *J* = 8, 1.2 Hz), 7.19 (3 H, m) ppm.

2-octanamido-N-(2-(phenylcarbamoyl)phenyl)benzamide (h-AA-Ph). A 45 ml DMF solution of 2-nitro-N-(2-(phenylcarbamoyl)phenyl)benzamide (5.0 g, 14 mmol) was

hydrogenated in the presence of 10% Pd/C (0.44 g) at 1 atm room temperature for 18 h. The reaction mixture was filtered through Celite. 300 ml CH₂Cl₂ was added to the filtrate which was washed with saturated NaHCO₃ (100 ml), and brine (100 ml). The organic layer was dried over Na₂SO₄, then concentrated in *vacuo* to afford 2-amino-N-(2-(phenylcarbamoyl)phenyl)benzamide as brown solid (3.7 g). This compound was used in the next step without any further purification.

To a 10 ml DMF solution of 2-amino-N-(2-(phenylcarbamoyl)phenyl)benzamide (1.0 g) and pyridine (0.6 ml, 7.4 mmol) was added 20 ml CH₂Cl₂ solution octanoyl chloride (1.0 g, 6.0 mmol). The mixture was stirred at room temperature for 2 h. The reaction mixture was diluted with 100 ml CH₂Cl₂, then washed with 1N HCl (50 ml × 2), saturated NaHCO₃ (70 ml), and brine (50 ml). The organic layer was dried over Na₂SO₄, and concentrated *in vacuo* to afford white powder. Purification *via* flash chromatography on silica gel (100% CH₂Cl₂ to 5% MeOH in CH₂Cl₂) afforded 1.2 g (2.6 mmol, 70 % overall yield for the two steps) of h-AA-Ph, white solid: m.p. 169-171 °C. Elemental analysis, expected for C₂₈H₃₁N₃O₃: C, 73.50%; H, 6.83%; N, 9.18%; measured: C, 72.60%; H, 6.64%; N, 9.00%. ¹H NMR (400 MHz, CDCl₃) δ 11.81 (1 H, s), 11.20 (1 H, s), 8.66 (2 H, dd, *J* = 8.0, 8.8 Hz), 7.98 (1 H, s), 7.80 (1 H, d, *J* = 8.0 Hz), 7.67 (1 H, d, *J* = 7.6 Hz), 7.57 (3 H, m), 7.49 (1 H, t, *J* = 7.6 Hz), 7.39 (2 H, t, *J* = 8.0 Hz), 7.22 (3 H, m), 2.40 (2 H, t, *J* = 8.0 Hz), 1.72 (2 H, m), 1.40-1.20 (8 H, m), 0.84 (3 H, t, *J* = 6.4 Hz) ppm; ¹³C NMR (100 MHz, CDCl₃) δ 172.42, 168.08, 167.50, 140.72, 139.47, 137.28, 133.37, 133.15, 129.46, 127.50, 127.05, 125.62, 123.91, 123.32, 122.50, 121.99, 121.65,

121.14, 120.23, 38.88, 31.90, 29.41, 29.22, 25.79, 22.82, 14.28 ppm. HRMS m/z calculated for $C_{28}H_{31}N_3O_3Na$ (M+Na) 480.2263, found 480.2284 (M+Na).

2-octanamido-N-(2-((2-(phenylcarbamoyl)phenyl)carbamoyl)phenyl)benzamide (h-AAA-Ph). To 25 ml DMF solution of 2-amino-N-(2-(phenylcarbamoyl)phenyl)benzamide (2.5 g, 7.5 mmol) and pyridine (1.5 ml, 19 mmol) was added 15 ml DMF solution of 2-nitrobenzoyl chloride (2.8 g, 15 mmol). The mixture was stirred at room temperature for 3 h. Large amount of white solid precipitated out. The solid was collected by filtration, and then washed with 1N HCl, saturated $NaHCO_3$, and water. The dried solid, 2-nitro-N-(2-((2-(phenylcarbamoyl)phenyl)carbamoyl)phenyl)benzamide (2.2 g), was used directly for the next step without further purification.

DMF solution (50 ml) of 2-nitro-N-(2-((2-(phenylcarbamoyl)phenyl)carbamoyl)phenyl)benzamide (2.2 g, 4.6 mmol) was hydrogenated in the presence of 10% Pd/C (0.5 g) at 1 atm room temperature for 48 h. The reaction mixture was filtered through Celite. 500 ml CH_2Cl_2 was added to the filtrate, which was washed with saturated $NaHCO_3$ (200 ml), and brine (200 ml). The organic layer was dried over Na_2SO_4 , then concentrated in *vacuo* to afford 2-amino-N-(2-((2-(phenylcarbamoyl)phenyl)carbamoyl)phenyl)benzamide as brown solid (0.8 g). This compound was used in the next step without any further purification.

To a 15 ml DMF solution of 2-amino-N-(2-((2-(phenylcarbamoyl)phenyl)carbamoyl)phenyl)benzamide (0.5 g, 1.1 mmol) and pyridine (0.2 g, 0.2 ml, 2.7 mmol) was added octanoyl chloride (0.36 g, 2.2 mmol). The mixture was stirred at room temperature for 3 h. The reaction mixture was diluted with 150 ml CH_2Cl_2 , and washed with 1N HCl (70

ml \times 2), saturated NaHCO₃ (100 ml), and brine (70 ml). The organic layer was dried over Na₂SO₄, and concentrated *in vacuo* to afford white powder. Purification *via* flash chromatography on silica gel (100% CH₂Cl₂ to 10% MeOH in CH₂Cl₂) afforded 0.48 g (0.8 mmol, 18% overall yield for the three steps) of h-AAA-Ph, white solid: m.p. 198-200 °C. Elemental analysis, expected for C₃₅H₃₆N₄O₄: C, 72.90%; H, 6.29%; N, 9.72%; measured: C, 72.87%; H, 6.23%; N, 9.77%. ¹H NMR (400 MHz, CDCl₃) δ 12.23 (1 H, s), 11.93 (1 H, s), 11.19 (1 H, s), 8.66 (2 H, m), 8.04 (1 H, s), 7.87 (2 H, t, J = 9.2 Hz), 7.65 (1 H, d, J = 8.0 Hz), 7.57 (4 H, m), 7.45 (1 H, t, J = 8.0 Hz), 7.28 (2 H, t, J = 7.6 Hz), 7.20 (4 H, m), 2.39 (2 H, t, J = 8.0 Hz), 1.71 (2 H, m, J = 7.6 Hz), 1.40-1.20 (8 H, m), 0.84 (3 H, t, 6.4 Hz) ppm; ¹³C NMR (100 MHz, CDCl₃) δ 172.5, 168.0, 167.9, 167.6, 140.6, 140.1, 139.1, 137.4, 133.3, 133.1, 133.0, 132.7, 129.5, 127.8, 127.3, 127.2, 125.6, 124.3, 124.0, 123.2, 122.5, 122.1, 122.0, 121.7, 121.3, 120.8, 38.8, 31.9, 29.4, 29.2, 25.7, 22.8, 14.3 ppm. HRMS m/z calculated for C₃₅H₃₇N₄O₄(M+H) 577.2815, found 577.2819 (M+H).

Absorption and emission UV/visible spectroscopy. Steady-state UV/visible absorption spectra were recorded in a transmission mode. Steady-state and time-resolved emission measurements were conducted using a spectrofluorometer with double-grating monochromators and a single-photon-counting detector.^{64,65} For steady-state emission measurement, a long-pass glass filter was placed on the emission pathway to prevent the appearance of Rayleigh scattered excitation light at $2 \times \lambda_{ex}$.^{39,40,66} For time-resolved emission measurements, a NanoLED was used for an excitation source (λ_{ex} = 278 nm; half-height pulse width, $W_{1/2}$ = 1 ns). For recording the profile of the excitation pulse (i.e.,

the instrument response function), we used deionized water as a scatterer, setting $\lambda_{em} = \lambda_{ex} = 278$ nm. The fluorescence decays of anthranilamides were recorded at two emission maxima, high-energy bands ($\lambda_{em} = 400$ nm for all three anthranilamides), and red-shifted bands ($\lambda_{em} = 545$ nm for h-A-ph, $\lambda_{em} = 520$ nm for h-AA-ph and h-AAA-ph).

The fluorescence quantum yields, Φ , for different contraptions of the anthranilamide oligomers in chloroform were determined by comparing the integrated emission intensities of the samples with the integrated fluorescence of a reference sample with a known fluorescence quantum yield, Φ_0 .^{36,64,67} Extrapolations to zero and to infinity concentrations yielded, respectively, the estimates for the quantum yields of the monomeric and aggregated forms of the oligomers. For references, we used solutions of coumarin 151 in ethanol ($\Phi_0 = 0.49$) and phenanthrene in ethanol ($\Phi_0 = 0.13$).⁶⁸⁻⁷²

Dielectric measurements. We followed procedures as described previously to calculate the dielectric values.²³ Three-terminal capacitance sample cell connected to an ultrahigh precision Wheatstone bridge, incorporated into a precision meter via connecting cables with up to of 4-m length were used to collect capacitance data. The three-terminal sample cell electrodes were separated to 400 μm , and filled with 1.5 ml of freshly prepared sample solution. The capacitance measurements were carried at frequencies ranging from 10^4 Hz to 10^6 Hz. The capacitance of the neat solvent and of air was measured in an empty dry cell as controls.²³

The experimentally determined dielectric values presented in the tables and figures correspond to averages of at least five repeats, where the error bars represent plus/minus one standard deviation.

Density measurements. The densities of freshly prepared anthranilamide solutions were measured with a calibrated portable density meter, recorded at 21 °C (\pm 0.5 °C). Before and after each measurement, the densitometer was washed several times with neat solvent, nitrogen dried, and washed with the corresponding sample solution.

Acknowledgments: This work was supported by the National Science Foundation (CBET 0935995 and CBET 0923408); the Riverside Public Utilities; and the American Public Power Association. We thank Dr. Shugeng Cao (Harvard Medical School), Dr. Yu Chen and Dr. Xiang Liu (Boston University) for helpful discussions.

Supporting Information. Copies of ^{13}C NMR spectra of h-A-ph (Figure 4-S1), h-AA-ph (Figure 4-S2), and h-AAA-ph (Figure 4-S3).

References

- (1) Kepler, R. G. *Annual Review of Physical Chemistry* **1978**, *29*, 497-518.
- (2) Erhard, D. P.; Lovera, D.; von Salis-Soglio, C.; Giesa, R.; Altstaedt, V.; Schmidt, H.-W. *Advances in Polymer Science* **2010**, *228*, 155-207.
- (3) Suzuki, Y. *IEEJ Transactions on Electrical and Electronic Engineering* **2011**, *6*, 101-111.
- (4) Vullev, V. I. *J. Phys. Chem. Lett.* **2011**, *2*, 503–508.
- (5) Garcia, H. *J Phys Chem Lett* **2011**, *2*, 520-521.
- (6) Hol, W. G. J.; Van Duijnen, P. T.; Berendsen, H. J. C. *Nature* **1978**, *273*, 443-446.
- (7) Shin, Y.-G. K.; Newton, M. D.; Isied, S. S. *J. Am. Chem. Soc.* **2003**, *125*, 3722-3732.
- (8) Doyle, D. A.; Cabral, J. M.; Pfuetzner, R. A.; Kuo, A. L.; Gulbis, J. M.; Cohen, S. L.; Chait, B. T.; MacKinnon, R. *Science* **1998**, *280*, 69-77.
- (9) Dutzler, R.; Campbell, E. B.; Cadene, M.; Chait, B. T.; MacKinnon, R. *Nature* **2002**, *415*, 287-294.
- (10) Galoppini, E.; Fox, M. A. *J. Am. Chem. Soc.* **1996**, *118*, 2299-2300.
- (11) Fox, M. A.; Galoppini, E. *J. Am. Chem. Soc.* **1997**, *119*, 5277-5285.
- (12) Yasutomi, S.; Morita, T.; Imanishi, Y.; Kimura, S. *Science* **2004**, *304*, 1944-1947.
- (13) Jones, G., II; Zhou, X.; Vullev, V. I. *Photochem. Photobiol. Sci.* **2003**, *2*, 1080-1087.
- (14) Gray, H. B.; Winkler, J. R. *Proc. Nat. Acad. Sci. U. S. A.* **2005**, *102*, 3534-3539.
- (15) Beratan, D. N.; Onuchic, J. N.; Winkler, J. R.; Gray, H. B. *Science* **1992**, *258*, 1740-1741.
- (16) Vullev, V. I.; Jones, G., II *Res. Chem. Intermed.* **2002**, *28*, 795-815.
- (17) Jones, G., II; Vullev, V.; Braswell, E. H.; Zhu, D. *J. Am. Chem. Soc.* **2000**, *122*, 388-389.

- (18) Jones, G., II; Lu, L. N.; Vullev, V.; Gosztola, D.; Greenfield, S.; Wasielewski, M. *Bioorg. Med. Chem. Lett.* **1995**, *5*, 2385-2390.
- (19) Shih, C.; Museth, A. K.; Abrahamsson, M.; Blanco-Rodriguez, A. M.; Di Bilio, A. J.; Sudhamsu, J.; Crane, B. R.; Ronayne, K. L.; Towrie, M.; Vlcek, A., Jr.; Richards, J. H.; Winkler, J. R.; Gray, H. B. *Science* **2008**, *320*, 1760-1762.
- (20) Ashraf, M. K.; Pandey, R. R.; Lake, R. K.; Millare, B.; Gerasimenko, A. A.; Bao, D.; Vullev, V. I. *Biotechnol. Progr.* **2009**, *25*, 915-922.
- (21) Hamuro, Y.; Geib, S. J.; Hamilton, A. D. *J. Am. Chem. Soc.* **1996**, *118*, 7529-7541.
- (22) Hamuro, Y.; Hamilton, A. D. *Bioorg. Medic. Chem.* **2001**, *9*, 2355-2363.
- (23) Upadhyayula, S.; Bao, D.; Millare, B.; Sylvia, S. S.; Habib, K. M. M.; Ashraf, K.; Ferreira, A.; Bishop, S.; Bonderer, R.; Baqai, S.; Jing, X.; Penchev, M.; Ozkan, M.; Ozkan, C. S.; Lake, R. K.; Vullev, V. I. *J. Phys. Chem. B* **2011**, *115*, 9473-9490.
- (24) Gong, B. *Accounts of Chemical Research* **2008**, *41*, 1376-1386.
- (25) Zhu, J.; Wang, X.-Z.; Chen, Y.-Q.; Jiang, X.-K.; Chen, X.-Z.; Li, Z.-T. *J. Org. Chem.* **2004**, *69*, 6221-6227.
- (26) Colombo, S.; Coluccini, C.; Caricato, M.; Gargiulli, C.; Gattuso, G.; Pasini, D. *Tetrahedron* **2010**, *66*, 4206-4211.
- (27) Coluccini, C.; Mazzanti, A.; Pasini, D. *Org. Biomol. Chem.* **2010**, *8*, 1807-1815.
- (28) Wan, J.; Thomas, M. S.; Guthrie, S.; Vullev, V. I. *Ann. Biomed. Eng.* **2009**, *37*, 1190-1205.
- (29) Upadhyayula, S.; Quinata, T.; Bishop, S.; Gupta, S.; Johnson, N. R.; Bahmani, B.; Bozhilov, K.; Stubbs, J.; Jreij, P.; Nallagatla, P.; Vullev, V. I. *Langmuir* **2012**, *28*, 5059-5069.
- (30) Ghazinejad, M.; Kyle, J. R.; Guo, S.; Pleskot, D.; Bao, D.; Vullev, V. I.; Ozkan, M.; Ozkan, C. S. *Adv. Funct. Mater.* **2012**, *22*, 4519-4525.
- (31) Lu, H.; Bao, D.; Penchev, M.; Ghazinejad, M.; Vullev, V. I.; Ozkan, C. S.; Ozkan, M. *Adv. Sci. Lett.* **2010**, *3*, 101-109.
- (32) Thomas, M. S.; Clift, J. M.; Millare, B.; Vullev, V. I. *Langmuir* **2010**, *26*, 2951-2957.

- (33) Mayers, B. T.; Vezenov, D. V.; Vullev, V. I.; Whitesides, G. M. *Anal. Chem.* **2005**, *77*, 1310-1316.
- (34) Jones, G., II; Vullev, V. I. *J. Phys. Chem. A* **2001**, *105*, 6402-6406.
- (35) Vullev, V. I.; Jiang, H.; Jones, G., II *Topics in Fluorescence Spectroscopy* **2005**, *10*, 211-239.
- (36) Valeur, B. *Molecular Fluorescence, Principles and Applications*; WILEY-VCH, 2002.
- (37) Vasquez, J. M.; Vu, A.; Schultz, J. S.; Vullev, V. I. *Biotechnol. Progr.* **2009**, *25*, 906-914.
- (38) Jones, G., II; Vullev, V. I. *Org. Lett.* **2001**, *3*, 2457-2460.
- (39) Jones, G., II; Vullev, V. I. *J. Phys. Chem. A* **2002**, *106*, 8213-8222.
- (40) Jones, G., II; Vullev, V. I. *Photochem. Photobiolog. Sci.* **2002**, *1*, 925-933.
- (41) Jones, G., II; Vullev, V. I. *Org. Lett.* **2002**, *4*, 4001-4004.
- (42) Vullev, V. I.; Jones, G. *Tetrahedr. Lett.* **2002**, *43*, 8611-8615.
- (43) Eaton, D. F. *Pure Appl. Chem.* **1990**, *62*, 1631-1648.
- (44) Hisamatsu, H.; Maekawa, K. *J. Econometrics* **1994**, *61*, 367-382.
- (45) Rutledge, D. N.; Barros, A. S. *Anal. Chim. Acta* **2002**, *454*, 277-295.
- (46) Xia, B.; Upadhyayula, S.; Nuñez, V.; Landsman, P.; Lam, S.; Malik, H.; Gupta, S.; Sarshar, M.; Hu, J.; Anvari, B.; Jones, G.; Vullev, V. I. *J. Clin. Microbiol.* **2011**, *49*, 2966-2975.
- (47) Bao, D.; Millare, B.; Xia, W.; Steyer, B. G.; Gerasimenko, A. A.; Ferreira, A.; Contreras, A.; Vullev, V. I. *J. Phys. Chem. A* **2009**, *113*, 1259-1267.
- (48) Bao, D.; Ramu, S.; Contreras, A.; Upadhyayula, S.; Vasquez, J. M.; Beran, G.; Vullev, V. I. *J. Phys. Chem. B* **2010**, *114*, 14467-14479.
- (49) Hedestrand, G. *Z. Physik. Chem.* **1929**, *2*, 428-444.
- (50) Debye, P. J. W. *Polar Molecules*; Dover Publications, Inc., NY, 1945.
- (51) Böttcher, C. J. F. *Theory of Electric Polarization*; 2nd ed.; Elsevier Scientific Publishing Company, 1973; Vol. I, Dielectrics Static Fields.
- (52) Böttcher, C. J. F.; Bordewijk, P. *Theory of Electric Polarization*; Elsevier Scientific Publishing Company, 1978; Vol. II, Dielectrics in Time-Dependent Fields.

- (53) Hill, N. E.; Vaughan, W. E.; Price, A. H.; Davies, M. *Dielectric Properties and Molecular Behavior (The Van Nostrand Series in Physical Chemistry)*; Van Nostrand Reinhold Company Ltd., 1969.
- (54) Breitung, E. M.; Vaughan, W. E.; McMahon, R. J. *Rev. Sci. Instrum.* **2000**, *71*, 224-227.
- (55) Tjahjono, M.; Davis, T.; Garland, M. *Rev. Sci. Instrum.* **2007**, *78*, 023902/023901-023902/023906.
- (56) Hong, C.; Bao, D.; Thomas, M. S.; Clift, J. M.; Vullev, V. I. *Langmuir* **2008**, *24*, 8439-8442.
- (57) Hu, J.; Xia, B.; Bao, D.; Ferreira, A.; Wan, J.; Jones, G.; Vullev, V. I. *J. Phys. Chem. A* **2009**, *113*, 3096-3107.
- (58) Araya-Maturana, R.; Pessoa-Mahana, H.; Weiss-Lopez, B. *Natural Product Communications* **2008**, *3*, 445-450.
- (59) Martins, J. C.; Biesemans, M.; Willem, R. *Progress in Nuclear Magnetic Resonance Spectroscopy* **2000**, *36*, 271-322.
- (60) Lockhart, D. J.; Kim, P. S. *Science* **1993**, *260*, 198-202.
- (61) Wu, J.; Becerril, J.; Lian, Y. J.; Davies, H. M. L.; Porco, J. A.; Panek, J. S. *Angew. Chem. Int. Ed.* **2011**, *50*, 5938-5942.
- (62) Jones, G., II; Yan, D.; Hu, J.; Wan, J.; Xia, B.; Vullev, V. I. *J. Phys. Chem. B* **2007**, *111*, 6921-6929.
- (63) Wieser, M. E.; Coplen, T. B. *Pure Appl. Chem.* **2011**, *83*, 359-396.
- (64) Wan, J.; Ferreira, A.; Xia, W.; Chow, C. H.; Takechi, K.; Kamat, P. V.; Jones, G.; Vullev, V. I. *J. Photochem. Photobiol. A* **2008**, *197*, 364-374.
- (65) Bahmani, B.; Gupta, S.; Upadhyayula, S.; Vullev, V. I.; Anvari, B. *J. Biomed. Optics* **2011**, *16*, 051303/051301-051303/051310.
- (66) Vullev, V. I.; Wan, J.; Heinrich, V.; Landsman, P.; Bower, P. E.; Xia, B.; Millare, B.; Jones, G., II *J. Am. Chem. Soc.* **2006**, *128*, 16062-16072.
- (67) Demas, J. N.; Crosby, G. A. *J. Phys. Chem.* **1971**, *75*, 991-1024.
- (68) Nad, S.; Pal, H. *J. Phys. Chem. A* **2001**, *105*, 1097-1106.
- (69) Thomas, M. S.; Nuñez, V.; Upadhyayula, S.; Zielins, E. R.; Bao, D.; Vasquez, J. M.; Bahmani, B.; Vullev, V. I. *Langmuir* **2010**, *26*, 9756-9765.

- (70) Montalti, M.; Credi, A.; Prodi, L.; Gandolfi, M. T. *Handbook of Photochemistry*; 3rd ed.; CRC Press, 2006.
- (71) Brouwer, A. M. *Pure Appl. Chem.* **2011**, *83*, 2213-2228.
- (72) Dawson, W. R.; Windsor, M. W. *J. Phys. Chem.* **1968**, *72*, 3251-3260.

Tables

Table 4-1. Photophysical properties of the anthranilamide oligomers.^a

	$\lambda_{abs} / \text{nm}$	$\varepsilon / \text{M}^{-1} \text{cm}^{-1}$ ^b	λ_{em} / nm	τ / ns ^c	$\Phi_m (\times 10^2)$ ^d	$\Phi_a (\times 10^2)$ ^d	E_{00} / eV ^e	$\Delta E / \text{eV}$ ^f
h-A-ph	305; 260	4,300	390; 545	0.594	10 ± 1	0.45 ± 0.14	3.6	4.9
h-AA-ph	320; 262	11,000	400; 520	1.27	0.94 ± 0.08	0.51 ± 0.04	3.5	4.3
h-AAA-ph	325; 260	24,000	400; 520	1.36	1.7 ± 0.7	0.54 ± 0.22	3.5	4.1

^a Experimental data from UV/visible absorption and emission measurements of chloroform solutions of anthranilamides.

^b Extinction coefficients, extrapolated to zero concentration, from nonlinear fits of the absorption at the low-energy maxima (305 nm for h-A-ph; 320 nm for h-AA-ph and h-AAA-ph) vs. concentration.

^c Lifetimes from time-correlated single-photon-counting measurements, samples excited at 278 nm and emission monitored at the low-energy aggregate bands (545 nm for h-A-ph and 520 nm for h-AA-ph and h-AAA-ph).

^d Φ_m and Φ_a are the emission quantum yields of monomeric and aggregated forms of the anthranilamide conjugates, respectively, obtained from extrapolation to zero and infinity concentrations.

^e Zero-to-zero energies were estimated from the cross-points of normalized absorption and emission spectra at lowest attainable concentrations.

^f Theoretically calculated HOMO-LUMO gaps, i.e., molecular “band gaps,” from reference 16.

Table 4-2. Linear analysis of $\lg(C(1-\zeta))$ vs. $\lg(C\zeta)$, implementing equation 4-3.

	<i>Fitting range</i> ^a	<i>n</i> ^b	<i>d</i> ^c	<i>Accept H₀?</i> ^d
h-A-ph	0.5 μ M – 10 mM	1.29 ± 0.14	0.823	no
	0.5 μ M – 25 μ M	1.65 ± 0.39	2.08	yes
	25 μ M – 10 mM	1.02 ± 0.16	2.36	yes
h-AA-ph	0.1 μ M – 10 mM	1.27 ± 0.12	0.406	no
	0.1 μ M – 1 μ M	4.10 ± 0.89	1.95	yes
	1 μ M – 10 mM	1.05 ± 0.07	2.01	yes
h-AAA-ph	0.1 μ M – 10 mM	1.30 ± 0.11	1.02	inconclusive
	0.1 μ M – 25 μ M	2.16 ± 0.42	2.15	yes
	25 μ M – 10 mM	1.10 ± 0.12	1.92	yes

^a Concentration ranges of the linear fits: (1) the whole concentration range; (2) the range of low concentrations, and (3) the range of the high concentrations.

^b State of aggregation from the slopes of the linear fits (equation 4-3).

^c Durbin-Watson statistics: $d = \sum_{i=1}^{n-1} (\delta_{i+1} - \delta_i)^2 / \sum_{i=1}^n \delta_i^2$, where δ_i are the residuals from the data fits.

^d Results from testing of the null hypothesis, H_0 : no autocorrelation between the residuals from the data fits. The testing of H_0 involved comparison of d with the upper and lower critical limits, $d_{U,\alpha}$ and $d_{L,\alpha}$, respectively, for $\alpha = 0.05$. If $d_{U,0.5} < d < (4 - d_{U,0.5})$, H_0 was accepted. If $d < d_{L,0.5}$ or $d > (4 - d_{L,0.5})$, the counter hypothesis was accepted. If $d_{L,0.5} \leq d \leq d_{U,0.5}$ or $(4 - d_{U,0.5}) \leq d \leq (4 - d_{L,0.5})$, the test was inconclusive.

Table 4-3. Measured and calculated molar polarizations, P_2 , of the anthranilamide oligomers.

	$P_{2H} / \text{cm}^3 \text{mol}^{-1}$ ^a	μ_0 / D ^b	$P_{2\mu}^{(0)} / \text{cm}^3 \text{mol}^{-1}$ ^c
h-A-ph	580 ± 90	4.5	421
h-AA-ph	800 ± 50	7.5	1,170
h-AAA-ph	1,020 ± 310	10	2,080

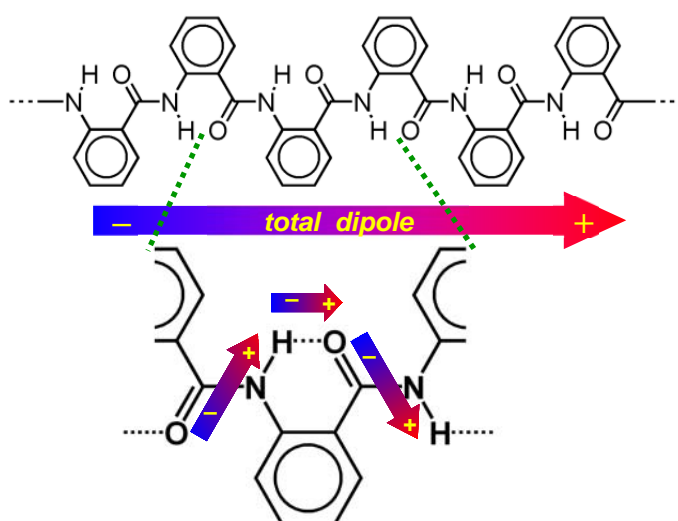
^a Experimental estimated polarizations, using Hedestrand (H) approach, from dielectric and density data for chloroform solutions of anthranilamides. The values are reported per mole of oligomer.

^b Theoretically calculated dipole moments for gas phase from reference 16.

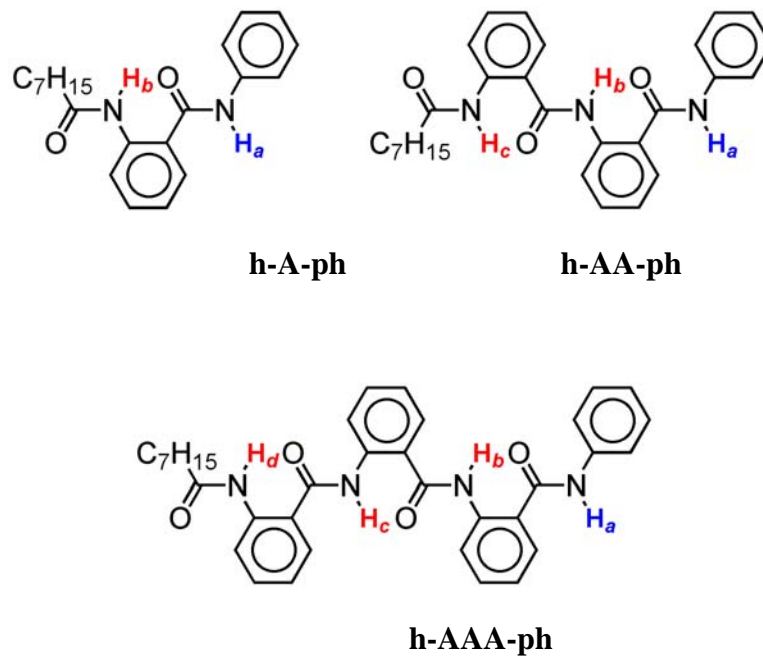
^c Theoretically obtained orientation polarization, $P\mu$, from the calculated dipole moments: $P_{2\mu}^{(0)} = \mu_0^2 N_A / 9 \epsilon_0 k_B T$.¹⁸

Schemes

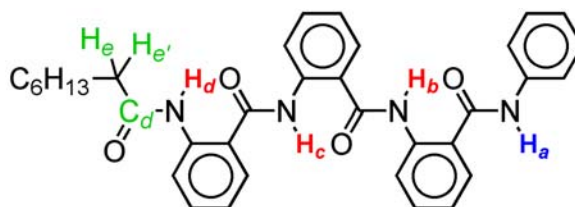
Scheme 4-1. Origin of the intrinsic dipole moment of anthranilamides.



Scheme 4-2. Anthranilamide oligomers with highlighted hydrogen-bonded (red) and non-hydrogen-bonded (blue) protons.



Scheme 4-3. Anthranilamide trimer, h-AAA-ph, with highlighted protons used for establishing the connectivity patterns in the NMR analysis.



Figures

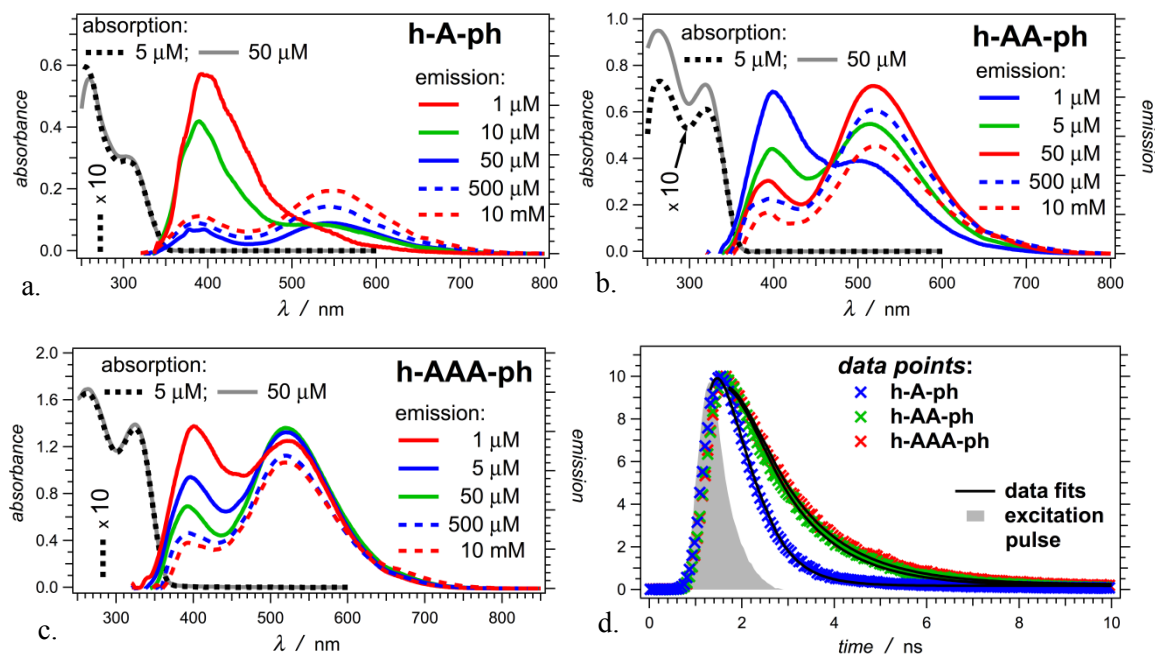
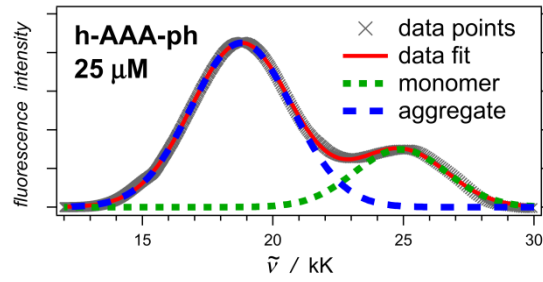
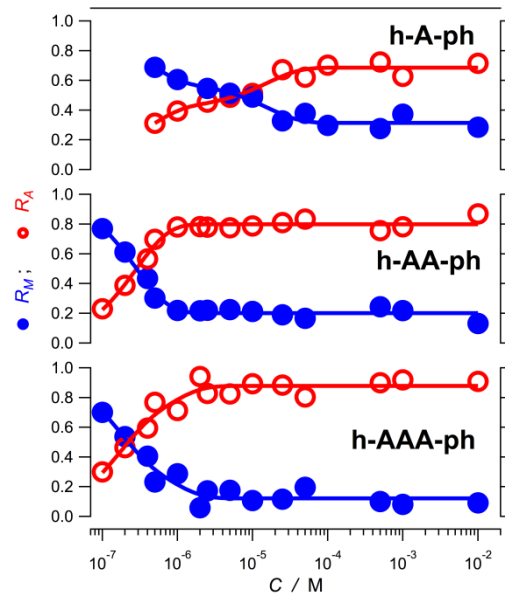


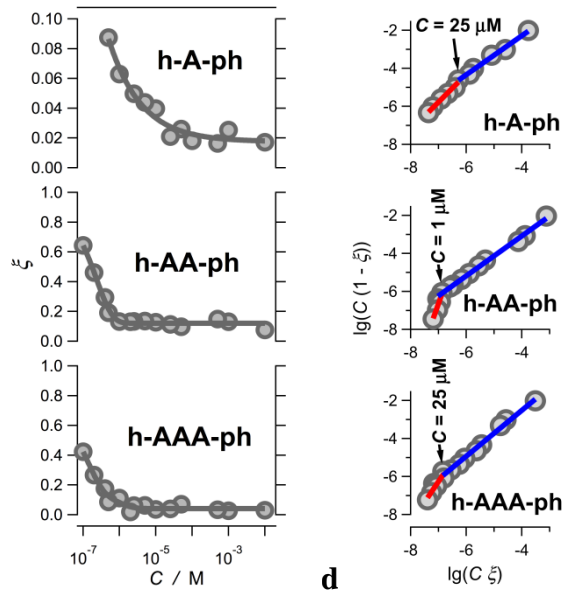
Figure 4-1. Absorption and emission properties of the anthranilamide oligomers. **(a-c)** Steady-state absorption and emission spectra (chloroform solutions; $\lambda_{ex} = 305 \text{ nm}$). The absorption spectra for 5 mM concentrations were scaled up by a factor of 10 for comparison with the absorption spectra for 50 mM concentrations. **(d)** Time-resolved emission decays recorded at the low-energy bands, i.e., at 545 nm for h-A-ph, at 520 nm for h-AA-ph and h-AAA-ph ($\lambda_{ex} = 278 \text{ nm}$, half-height pulse width = 1 ns).



a



b



c

d

Figure 4-2. Concentration dependence of the emission properties of the anthranilamide oligomers. **(a)** A representative example of deconvolution of a fluorescence spectrum using a sum of two Gaussian functions. To plot the spectrum versus energy, i.e., vs. wavenumber, $\tilde{\nu}$, instead of vs. wavelength, λ , we converted the fluorescence intensity accordingly, $F_{\tilde{\nu}}(\tilde{\nu}) = \lambda^2 F_{\lambda}(\lambda)$. **(b)** Concentration dependence of the fractions of the monomer, R_m , and aggregate, R_a , emission (equation 4-1). **(c)** Concentration dependence of the monomer fractions, ξ (equation 4-2). **(d)** Linear analysis of $\lg(C(1-\xi))$ vs. $\lg(C\xi)$ (equation 4-3). The gray circles designate the data points; and the red and blue lines – the linear data fits at low and high concentrations, respectively.

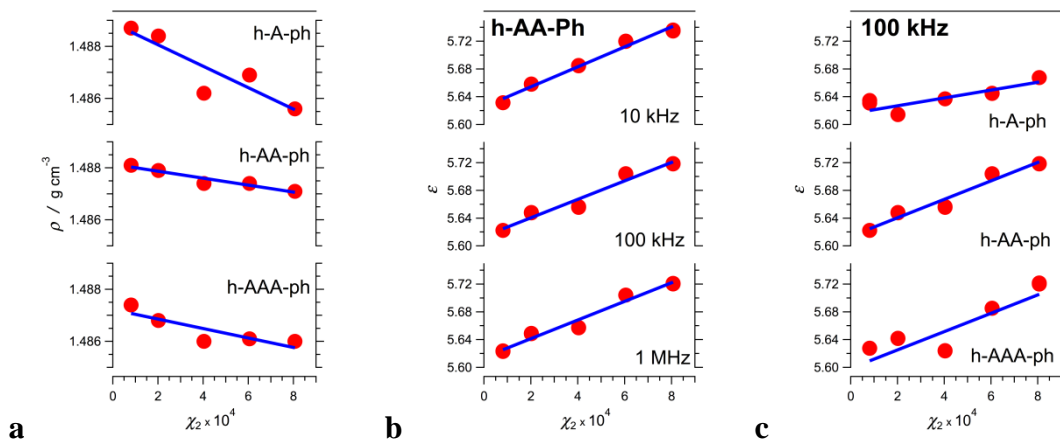


Figure 4-3. Dependence of (a) the density, ρ , and (b, c) the dielectric properties of anthranilamide solutions in chloroform on the oligomer molar fraction, χ_2 . (b) Dielectric constant, ϵ , of h-AA-ph solutions extracted from capacitance measurements at different frequencies. (c) ϵ of solutions of the three oligomers extracted from capacitance measurements at 100 kHz.

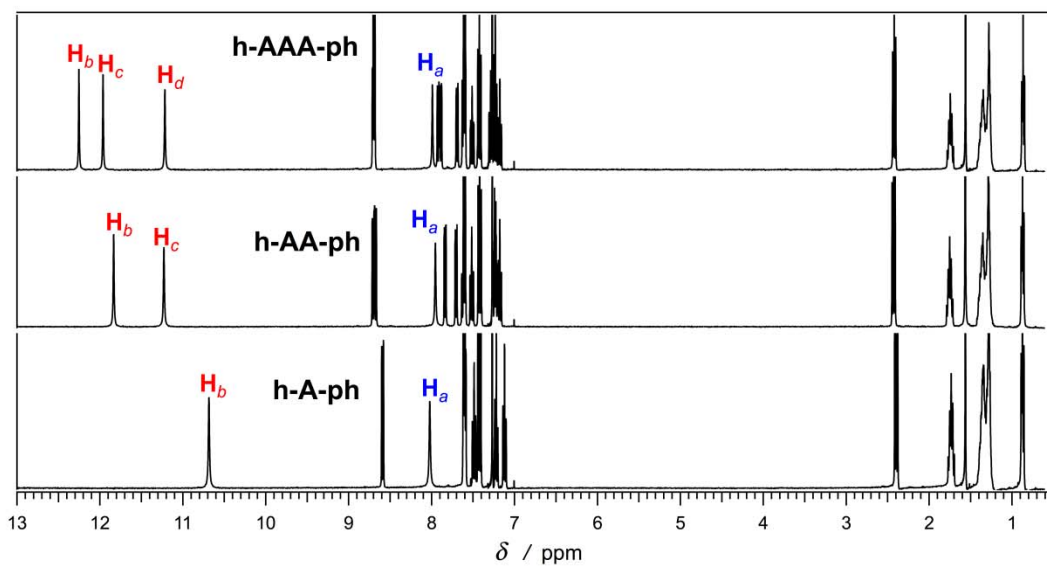


Figure 4-4. ¹H-NMR spectra of the three anthranilamide oligomers with assignments of the peaks corresponding to the amide protons. (50 mM in CDCl₃; 400 MHz)

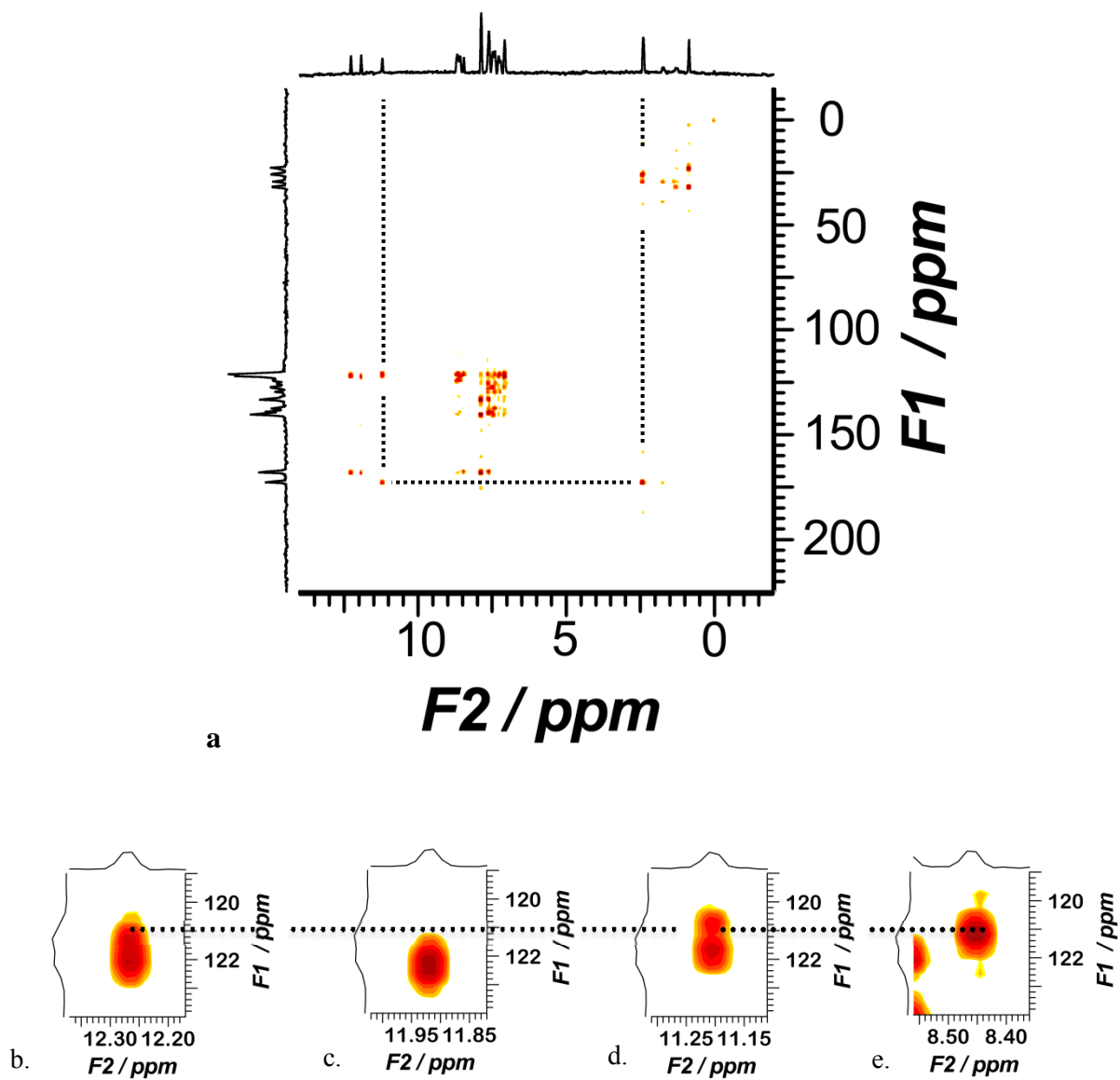


Figure 4-5. ^1H - ^{13}C gHMBC spectrum of h-AAA-ph (2 mM in CDCl_3 ; 400 MHz). (a) The full spectral range with 2J correlations (indicated with the gray lines) between $^1\text{H}_e$ / $^1\text{H}_e'$ and $^{13}\text{C}_d$ and between $^{13}\text{C}_d$ and $^1\text{H}_d$ (Scheme 4-3). (b-e) Zoomed 3J correlation peaks between the amide protons and the carbons three bonds away. The peaks at: (b) 12.3 ppm; (c) 11.9 ppm; (d) 11.2 ppm; and (e) 8.45 ppm.

Supporting Figures

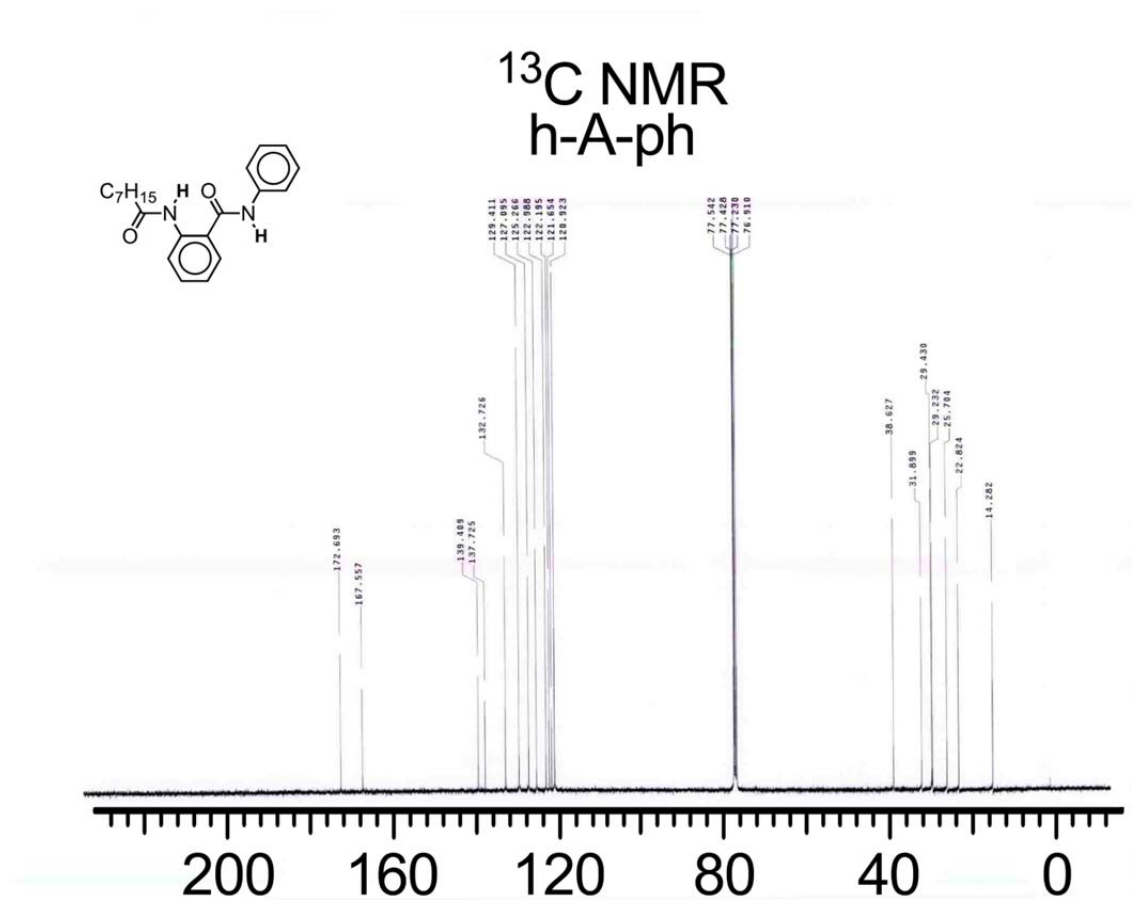


Figure 4-S1. ^{13}C NMR spectra of oligoanthranilamide monomer – h-A-ph

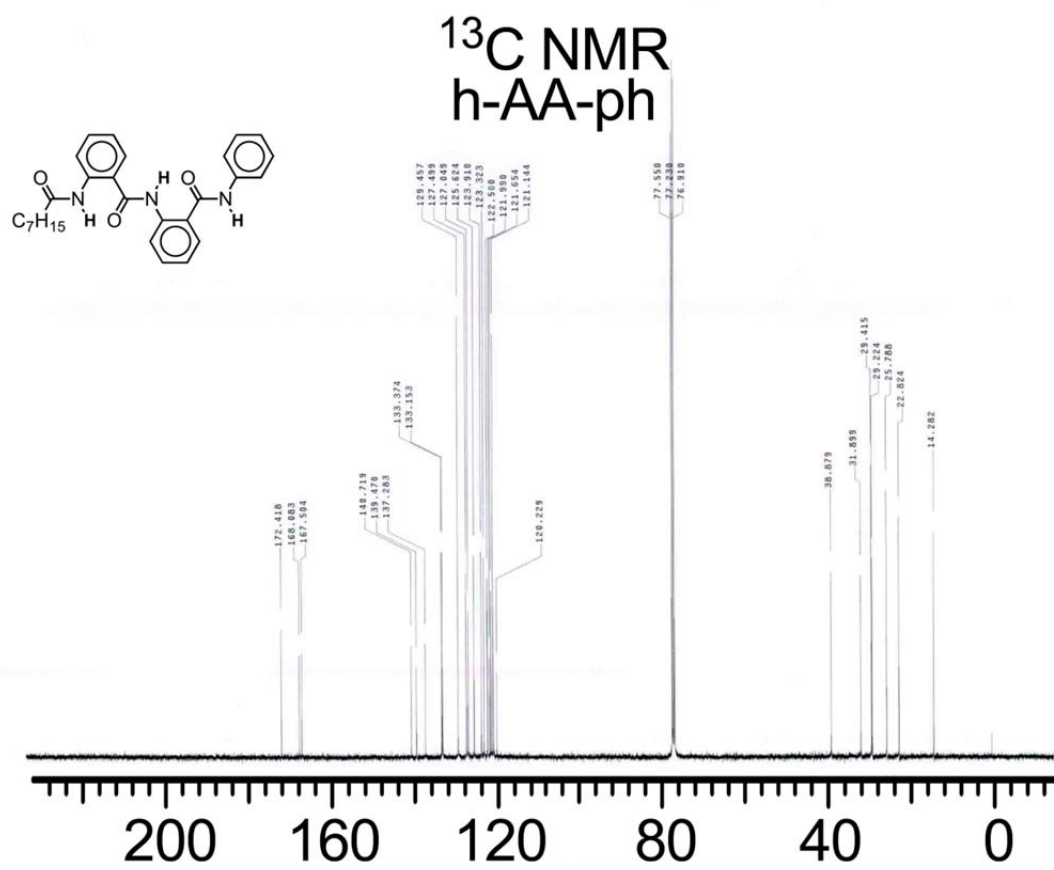


Figure 4-S2. ^{13}C NMR spectra of oligoanthranilamide dimer – h-AA-ph

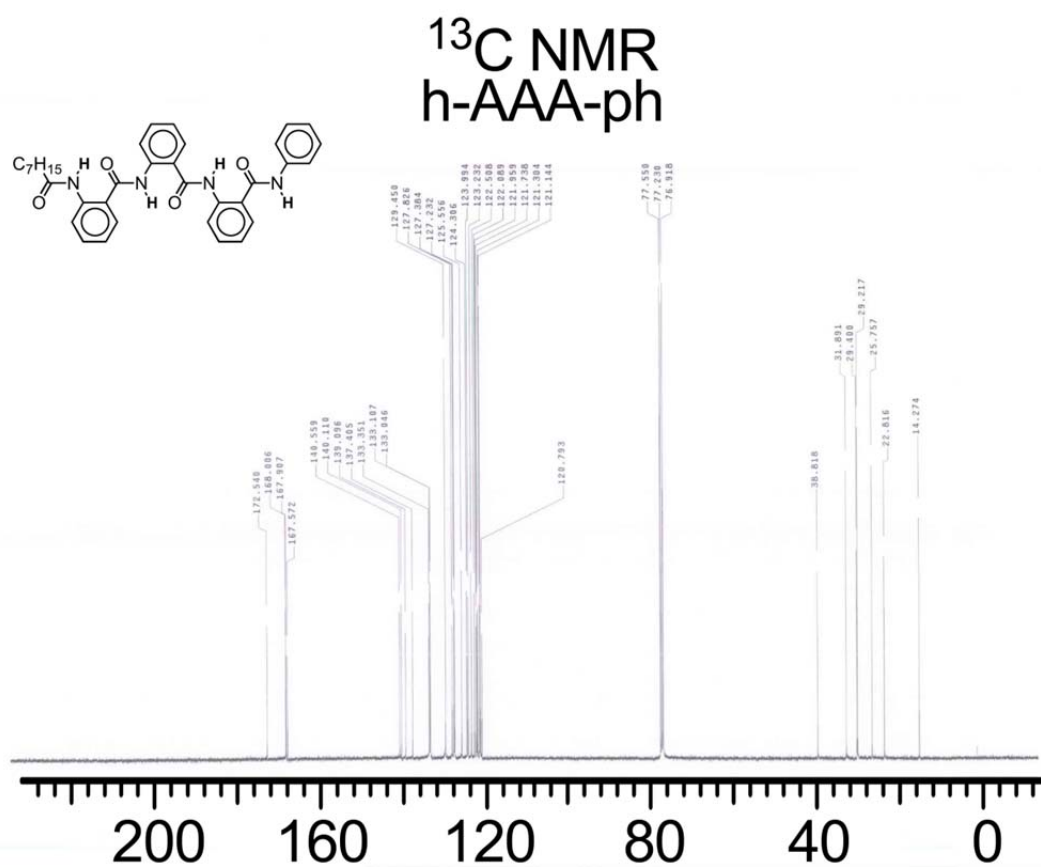


Figure 4-S3. ^{13}C NMR spectra of oligoanthranilamide trimer – h-AAA-ph

Appendix

Appendix 1.

Rectification of Photoinduced Charge Separation and Charge Recombination Induced by Dipole of Anthranilamide

Introduction

Local fields from ions, interfacial polarization, and molecular dipoles substantially affect charge transfer (CT),¹⁻⁶ providing an important means for increasing the efficiency of forward CT and suppressing undesired charge recombination. To elucidate the structure-function relations that govern these effects, and to establish rules for predicting them, it is essential to undertake a physical-chemistry approach for examining their mechanistic features at a molecular level.

Since the first reports on the effect that dipoles of polypeptide α -helices have on electron transfer (ET),^{1,7,8} the dipole effects on ET have been studied almost exclusively for polypeptides with similar structures.^{2,5,9-14} Unless the ET pathways involve redox residues or cofactors with sufficient electronic coupling between them, proteins mediate ET via tunneling mechanism, limiting its efficiency to about 2 nm.^{15,16} Hopping mechanisms, which involve multiple charge-transfer steps along a sequence of redox moieties, allow for overcoming this distance limitation.^{13,17,18} In such pathways, differences in the redox properties of neighboring moieties ensure the ET directionality, i.e., electrons will “hop” to moieties with less negative reduction potentials; and positive charges, or *holes* (h^+), will “hop” to moieties with less positive oxidation potentials. In such a scheme, the back charge transfer occurs via a single tunneling step of the electron to the h^+ site, which will be less efficient, the farther the charges migrate from each other. Local electric fields (from molecular dipoles) can induce the redox differences to attain the same directionality in charge hopping along a sequence of identical moieties.

My research focused on the effects of the dipoles of polar molecular structures on their charge-transfer reactivity. I demonstrated, for the first time, the charge-transfer rectification effects of intrinsic molecular dipoles of bioinspired electret. Our *de novo* designed anthranilamides (Aa), are composed of aromatic residues linked with amide bonds (Scheme A1-1).¹⁹ The ordered orientation of the amide and hydrogen bonds generates the intrinsic molecular electric dipoles.¹⁹ (Hence, we refer to these structures as “bioinspired molecular electrets.”^{19,20} Electrets are systems with co-directionally ordered electric dipoles, i.e., they are the electrostatic analogues of magnets.²¹⁻²⁴)

To test the ability of the electrets to modify the direction of electron transfer, I incorporated an anthranilamide monomer in electron donor-acceptor (DA) dyads: *N*-hexyl-5-(piperidin-1-yl)-2-[2-(pyren-1-yl)acetamino]benzamide (Py-Aa) and 2-hexanamino-5-(piperidin-1-yl)-*N*-(pyren-1-ylmethyl)benzamide (Aa-Py) (Scheme A1-2, 3, 4 and 5). For controls, we prepared and used compounds that contained only the donor, 2-hexanamino-*N*-hexyl-5-(piperidin-1-yl)benzamide (Aa), or only the acceptor 1-methylpyrene (MePy) by themselves (Scheme A1-2, 3 and 6). When the pyrene moiety, the electron acceptor, was attached to the N-terminus of the electret monomer, i.e., Py-Aa, the electron has to move against the dipole orientation; and when the pyrene is at the C-terminus, Aa-Py, the electron moves along the orientation of the molecular dipole. (The dipole direction is defined from its negative to its positive pole.)

We used time-resolved spectroscopy for following the deactivation of the lowest excited state of the electron donor, i.e., the anthranilamide, Aa. The deactivation of the donor singlet-excited state, ¹Aa*, was accompanied by growth of the radical ion

transients, indicative of photo induced charge separation, i.e., of electron injection from the photoexcited donor, Aa, into the acceptor, Py. The consequent decay of the radical ions was ascribed to charge recombination. Comparison between the charge-transfer kinetics of the two electret-pyrene dyads, revealed a faster initial photoinduced charge transfer process and a slower charge recombination that were consistent with orientation of the intrinsic dipole moment of the anthranilamide monomer. Aside from previous work employing polypeptides, this is the first demonstration of rectification of charge transfer by dipole moments of synthetic bioinspired derivatives.

Results and Discussion

Synthesis and basic photophysical properties. I synthesize anthranilamide oligomers from their C- to their N-termini by adding each residue as a derivative of 2-nitrobenzoic acid (Scheme A1-3, 4 and 5).^{25,26} Consequent reduction of the nitro group to amine prepared it for the next coupling step (Scheme A1-3 and 4).

This study focused on 5-piperidinyl derivatives of anthranilamides (Scheme A1-2). The piperidinyl group has a dual role: (1) makes the Aa moiety a relatively good electron donor ($E_{OX} = 0.7$ vs. SCE in CH_3CN); and (2) prevents aggregation. 5-piperidinylanthranilamide has a relatively weak broad absorption at 350 nm ($\epsilon_{350\text{nm}} = 5 \times 10^3 \text{ M}^{-1} \text{ cm}^{-1}$), which extends to ~410 nm. The red edge of the 1-alkylpyrene absorption is at ~350 nm. Therefore, for the CT studies of Py/Aa derivatives (Scheme A1-2), we selectively excited the Aa moieties around 380 – 400 nm (Figure A1-1). The

time-resolved emission measurements of these two dyads and Aa itself in DCM also revealed the fast CT processes in dyads (Figure A1-1c). For Aa, the lifetime in DCM is about 18 nanoseconds, for dyads, however; both have decays that are similar with our instrumental laser pulse (~1 ns). Thus, we use ultra-fast femtosecond system to investigate charge separation and charge recombination processes that happen in picoseconds.

The experimentally estimated excitation energy, E_{00} , of the anthranilamide oligomers showed negligible dependence on their concentration and length (Figure A1-2). The absorption and emission spectra of Aa_n showed no concentration dependence (Figure A1-2a), and negligible dependence on the length, n (Figure A1-2b). For example, the difference in the emission maxima for monomer and trimer was about 2 nm and difference in E_{00} was less than 0.1 eV. These trends suggest for relatively localized excited states, an important feature of Aa_n , the nature of which we will further investigate.

Redox properties and driving force calculation. The Rehm-Weller equation provides an important relation between measurable quantities that allows for estimation of the driving force (i.e., the change in the Gibbs energy, $\Delta G_{et}^{(0)}$) of photoinduced electron transfer processes:²⁷⁻²⁹

Based on the experimental methods described in Chapter 2 and 3, I extrapolated the redox potentials of anthranilamides monomer (Aa, electron donor in the dyads) and 1-methylpyrene (MePy, electron acceptor in the dyads) to $C_{TBABF4} = 0$ mM in relatively

non-polar solvents. I also calculated the effective radii of each of the moieties (Figure A1-3, 4 and Table A1-3). For Aa in CH_2Cl_2 ($\epsilon=8.93$), the oxidized potential $E_{\text{ox}}^{(1/2)}$ is 0.97 V vs *SCE* with effective radius of 0.26 nm (Figure A1-3); for MePy, the reduction potential at neat THF ($\epsilon=7.58$), $E_{\text{red}}^{(1/2)}$ is -2.30 V vs *SCE* with effective radius of 0.3 nm (Figure A1-4 and Table A1-3). Since we have examined the dielectric difference between electrochemical and spectroscopic measurements, $\Delta G_{\text{et}}^{(0)}$ for charge transfer studies in DCM (relatively nonpolar, $\epsilon = 8.93$), and acetonitrile (relatively polar, $\epsilon = 36.6$) is -0.1 eV and -0.32 eV, respectively (Table A1-4).

Charge-Transfer Kinetics. The experimental measured dipole moment for Aa monomer is approximately 5.6 ± 2.0 D by dielectric constant and density measurements. To test how strongly the molecular dipoles affect the initial ET step, I examined donor-acceptor dimers composed of a pyrene (Py) and a single Aa moiety ($n=1$, Scheme A1-2). In Py-Aa, the electron acceptor is attached at the N-terminus, i.e., at the negative side of the Aa dipole; and in Aa-Py, the acceptor is at the C-terminus, or at the positive side of the dipole.

The red-shifted spectrum of Aa (in comparison with Py) allowed us to selectively photoexcite the anthranilamide and to observe the photoinduced CT processes, using transient absorption spectroscopy (Figure A1-2). The initial excitation led to the formation of the anthranilamide singlet-excited state transient, $^1\text{Aa}^*$, characterized by broad absorption with peaks at about 410 nm and 710 nm (Figure A1-5a). The decay of $^1\text{Aa}^*$ was accompanied by a rise of spectral peaks at 500 nm and 580 nm, which were

ascribed to the charge-transfer radical ions, $\text{Py}^{\bullet-}$ and $\text{Aa}^{\bullet+}$, respectively (Figure A1-5).^{30,31} From the transient decay of $^1\text{Aa}^*$, and from the rise of $\text{Py}^{\bullet-}$ and $\text{Aa}^{\bullet+}$, we extracted the rate constants of the photoinduced charge-separation (CS). The decays of $\text{Py}^{\bullet-}$ and $\text{Aa}^{\bullet+}$ yielded the rate constants of charge recombination (CR).

For CH_2Cl_2 , the rate constant of CS for Aa-Py was about four times larger than the CS rate constant for Py-Aa (Table A1-4). This finding was in accordance with the predicted dipole effect on ET kinetics. The dipole orientation stabilized the $\text{Aa}^{\bullet+}\text{-Py}^{\bullet-}$ charge-transfer state, making its CS $\Delta G^{(0)}$ more negative, and destabilized the $\text{Py}^{\bullet-}\text{-Aa}^{\bullet+}$ state, making the CS $\Delta G^{(0)}$ less negative. Because of the small $-\Delta G^{(0)}$ values (i.e., $\Delta G^{(0)} = -0.10$ eV, as estimated for CH_2Cl_2), we assume that the CS processes were in the Marcus normal region, and the dipole-induced negative shifts in $\Delta G^{(0)}$ increased the observed CS rate for Aa-Py.

The use of acetonitrile increased all CS rates, which was consistent with stabilization of the charged CT states by solvation with the more polar solvent. This more polar solvent also decreased the difference between the CS rates for Aa-Py and Py-Aa (Table A1-4). We ascribe this finding to solvent screening of the Aa molecular dipole decreasing its effect on the CS kinetics.

Addition of an electrolyte had a similar effect of decreasing the difference between the CS rates for Aa-Py and Py-Aa (Table A1-4), which was ascribed to screening of the molecular dipole by the free ions in the solution. The increased ionic strength of the CH_2Cl_2 solutions, however, decreased the CS rates for both dyads. The electrolyte ions

most likely stabilize the charged CT states, making $\Delta G^{(0)}$ more negative for both dyads. A prevalent increase in the reorganization energy, λ , due to movement of relatively large ions in the CH_2Cl_2 electrolyte solution, however, would lead to smaller CT rates if the negative shifts in $\Delta G^{(0)}$ are smaller than the increase in λ .

Because $\Delta G^{(0)}$ for the charge recombination (CR) was in the order of -2.8 eV, we could assume that CR is in the Marcus inverted region. This assumption agreed with the observed faster CR rates for acetonitrile than for CH_2Cl_2 (Table A1-4). Namely, the stabilization by the more polar solvent, acetonitrile, would bring the CT states closer to the ground states of the dyads making $\Delta G^{(0)}$ for CR less negative, and the rates of CR larger (because of the inverted region).

The trends in the dipole effect on CR, however, did not agree with this notion of dipole-induced stabilization and destabilization of the charged CT states. The dipole stabilization of the $\text{Aa}^{\bullet+}\text{-Py}^{\bullet-}$ should make $\Delta G^{(0)}$ less negative and its CR rate faster than the CR for $\text{Py}^{\bullet-}\text{-Aa}^{\bullet+}$ (assuming the inverted region), which was contrary of what we repeatedly observed (Table A1-4). Our working hypothesis for the experimentally observed trends is that dipole-induced conformational gating leads to different CR rates for the two dyads. Unlike Py, which is non-polar, the charged reduced pyrene, $\text{Py}^{\bullet-}$, can interact with the Aa dipole. Therefore, the Aa dipole may cause different orientation of $\text{Py}^{\bullet-}$ around the flexible methylene linker for $\text{Py}^{\bullet-}\text{-Aa}^{\bullet+}$ and $\text{Aa}^{\bullet+}\text{-Py}^{\bullet-}$, which will affect the donor-acceptor electronic coupling and the observed CR rates. Studies using media

with different viscosity will allow us to extract such contribution of the molecular dynamics on the CR and CS kinetics.

Another hypothesis states that the asymmetry in the radical cation, $Aa^{\bullet+}$, leads to the observed differences between the CR rates for the two dyads. The amide bonds (generating the molecular dipoles) and the aromatic moiety (hosting radical cation) are in the same solvation cavity. Thus, polar solvents will not completely screen the dipole effect on $Aa^{\bullet+}$ itself. This feature will result in a relatively small solvent-polarity dependence of the difference between the CR rates for $Py^{\bullet-}-Aa^{\bullet+}$ and $Aa^{\bullet+}-Py^{\bullet-}$. Although our preliminary results seem to suggest for the validity of this hypothesis (Table A1-4), examination of the CT kinetics for a much wider range of media polarity is needed before we can draw any statistically significant conclusions. To further examine the asymmetry of the $Aa^{\bullet+}$ radical ion, we can resort to experimental CT studies with the 4-piperidinyl derivatives of Aa, i.e., $-R_1 = -NC_5H_{10}$ (Scheme A1-1), which we prepared using the same Aa procedure (Scheme A1-3).

Conclusion

Our preliminary results provide encouraging demonstration that the effects of the Aa dipoles on the CT kinetics are significant. Furthermore, transient absorption revealed that positive charges can reside on Aa in the form of radical cations, which is essential for attaining hole-hopping mechanism for charge transfer through Aa_n conjugates. The

anthranilamides offer a wealth of mechanistic information about gaining new venues for forming long-range, long-lived CT states.

Experimental

Materials. 5-fluoro-2-nitrobenzoic acid (98 %), 1-pyrenemethylamine hydrochloride (95 %), piperidine (99.5%), 1-pyrenemethylamine hydrochloride (95%), 1-pyreneacetic acid (97%), hexanoic anhydride (97%) were purchased from TCI. Tin(II) chloride dihydrate (SnCl_2 , 98+%), *N, N'*-Diisopropylcarbodiimide (DIC, 99%), *N*-hydroxysuccinimide (NHS, 98%), *N,N*-diisopropylethylamine (DIPEA, 99.5%), 1-[bis(dimethylamino)methylene]-1*H*-1,2,3-triazolo[4,5-*b*]pyridinium-3-oxid hexafluorophosphate (HATU, 97%), 2-chloro-1,3-dimethylimidazolidinium hexafluorophosphate (HoAt, 98+%), triethylamine (99%), hexylamine (99%), were purchased from Sigma-Aldrich. All other reagents, including HPLC grade, spectroscopic grade and anhydrous solvents like dichloromethane (DCM, >99.8%) and *N,N*-dimethylformamide (DMF, 99.8%) were used as supplied by commercial vendors.

General information. Proton (^1H) NMR spectra were recorded at 400 MHz at ambient temperature using CDCl_3 as solvent unless otherwise stated. Chemical shifts are reported in parts per million relative to CDCl_3 (^1H , δ 7.27). Data for ^1H NMR are reported as follows: chemical shift, integration, multiplicity (s = singlet, d = doublet, t = triplet, q = quartet, m = multiplet), integration and coupling constants. High resolution mass-spectra

were obtained on a Q-TOF mass spectrometer.³² Analytical thin layer chromatography was performed using 0.25 mm silica gel 60-F plates. Flash chromatography was performed using 60Å, 32-63 μm silica gel. Yields refer to chromatographically and spectroscopically pure materials, unless otherwise stated. All reactions were carried out in oven-dried glassware under an argon or nitrogen atmosphere unless otherwise noted.

2-nitro-5-(piperidin-1-yl)benzoic acid (Scheme A1-3). 2-nitro-5-fluoro-benzoic acid (1.85g, 10 mmol) was added into a 25 mL flask and piperidine (12 ml, 12 mmol) was added. The mixture was refluxed at 108°C for 4 h. The reaction mixture was diluted with 100 mL CH₂Cl₂, then washed with 1N HCl (100 ml × 3) and brine (100 ml × 3). The organic layer was dried over Na₂SO₄, then concentrated in vacuo to afford yellow powder (1.65g, 6.6 mmol, 66%). 2-nitro-5-(piperidinyl)benzoic acid, yellow solid: ¹H-NMR (400 MHz, CDCl₃) δ 8.28 (1 H, d), 6.94 (1 H, s), 6.84 (1 H, d), 3.48 (4 H, s), 1.72 (6 H, s) ppm; HRMS m/z calculated for C₁₃H₁₅N₂O₆ (M+HCOO)- 295.0928, found 295.0936 (M+HCOO)-.

N-hexyl-2-nitro-5-(piperidin-1-yl)benzamide. To an ice-chilled 15 ml DMF solution of 2-nitro-5-(piperidinyl)benzoic acid (1.0 g, 4 mmol) and NHS (695mg, 6 mmol) was added DIC (1.24mL, 8mmol). The mixture was stirred at 0°C for 2 h. Hexylamine (1.2mL, 8mmol) was drop-wise added into reaction mixture. The mixture was stirred at 0°C for 0.5 h. The reaction mixture was poured into 100 mL 1N HCl to afford yellow precipitate. The whole solution was filtered and yellow precipitate was collected and dissolved in 50 mL CH₂Cl₂ and was dried over Na₂SO₄, then concentrated in *vacuo* to

afford yellow solid. The product was used for next step reaction without any further purification.

2-hexanamino-5-(piperidin-1-yl)-N-(pyren-1-ylmethyl)benzamide (Aa-Py)

(Scheme A1-4). To 10 ml DMF solution of 2-nitro-5-(piperidin-1-yl)benzoic acid (536mg, 2.1 mmol), 1-pyrenemethylamine hydrochloride (268mg, 1mmol) and HoAt (292mg, 2.1 mmol), added DIPEA (708 μ l, 3.15 mmol) and HATU (1.22g, 2.1 mmol) in 4 ml DMF solution. Let reaction mixture react at room temperature for 3 h, and the mixture solution was poured into DI water. There was yellow precipitate coming out. Filter mixture solution and collect yellow parts. Crude yellow product was dissolved by DCM and was dried over Na₂SO₄, then concentrated in vacuo to afford yellow powder (N-(pyrenyl)acethyl-2-nitro-5-(piperidin-1-yl)benzamide, 318mg). The powder was directly used in next step without any further purification. To 25 ml ethanol solution of N-(pyrenyl)acethyl-2-nitro-5-(piperidin-1-yl)benzamide (318mg, crude product) and Tin(II) chloride dihydrate (460mg, 2 mmol), the mixture was refluxed overnight. After conversion completed, the ethanol in reaction mixture was evaporated via *vacuo* to afford colorless jelly product. The product was instantly purged with Argon gas and then dissolved in 4 ml DMF at room temperature. Hexanoic anhydride (787 μ l, 3.4mmol) and Et₃N (474 μ l, 3.4 mmol) were added into reaction mixture, let it still for 4 h. The reaction was filtered and the filtrate was collected and extracted by 50 ml ethyl acetate with saturated NaHCO₃ (100 ml \times 2). The organic layer was dried over Na₂SO₄, then concentrated in vacuo to afford oily product. Purification *via* flash chromatography on silica gel (100% hexanes to 50% ethyl acetate in hexanes) afforded 200mg white powder

(0.37 mmol, 18% overall yield for two steps). $^1\text{H-NMR}$ (400 MHz, CDCl_3): 10.55 (1H, s), 8.21 (1H,d), 8.10 (9H, m), 7.02(1H, d), 6.97 (1H, s), 6.69 (1H, s), 5.34 (2H, d), 2.97 (4H, m), 2.33 (4H, m), 1.62 (5H, m), 1.34 (6H, m), 0.89 (3H, t). HRMS m/z calculated for $\text{C}_{35}\text{H}_{38}\text{N}_3\text{O}_2$ (M+H) $^+$ 532.2959, found 532.2979 (M+H) $^+$.

***N*-hexyl-5-(piperidin-1-yl)-2-[2-(pyren-1-yl)acetamino]benzamide (Py-Aa)**

(Scheme A1-5). To 6 ml ethanol solution of *N*-hexyl-2-nitro-5-(piperidin-1-yl)benzamide (645mg, 1.9 mmol) and Tin(II) chloride dihydrate (1.31g, 5.7 mmol), the mixture was refluxed for 2 h. After conversion completed, the ethanol in reaction mixture was evaporated via *vacuo* to afford colorless jelly product. The product was instantly purged with Argon gas and then dissolved in 10 ml DMF at room temperature. 1-pyreneacetic acid (260mg, 1 mmol), HoAt (136mg, 1 mmol), and HATU (570mg, 1.5 mmol) in 6 ml DMF solution were added to reaction mixture, DIPEA (496 μl , 3 mmol) was drop-wise added lastly. Let reaction mixture react at room temperature for 3 h. The mixture solution was extracted by ethyl acetate with saturated NaHCO_3 (100 ml \times 2), 1 N HCl (100 ml \times 2). The organic layer was dried over Na_2SO_4 , then concentrated in *vacuo* to afford oily product. Purification *via* flash chromatography on silica gel (100% hexanes to 50% ethyl acetate in hexanes) afforded 50mg white powder (0.1 mmol, 10% overall yield for two steps). $^1\text{H-NMR}$ (400 MHz, CDCl_3): 10.30 (1H, s), 8.20 (10H, m), 6.99 (1H, d), 6.79 (1H, s), 5.81 (1H, s), 4.44 (2H, s), 3.04 (4H, t), 2.81 (2H, t), 1.59 (8H,m), 1.17 (8H, m), 0.92 (3H, t). HRMS m/z calculated for $\text{C}_{36}\text{H}_{41}\text{N}_3\text{O}_2$ (M+H) $^+$ 547.3193, found 547.3214 (M+H) $^+$.

2-hexanamino-N-hexyl-5-(piperidin-1-yl)benzamide (Aa) (Scheme A1-6). To 5 ml ethanol solution of N-hexyl-2-nitro-5-(piperidin-1-yl)benzamide (600mg, 1.8 mmol) and Tin(II) chloride dihydrate (2.25g, 9 mmol), the mixture was refluxed for 2 h. After conversion completed, the ethanol in reaction mixture was evaporated via *vacuo* to afford colorless jelly product. The product was instantly purged with Argon gas and then dissolved in 10 ml DMF at room temperature. Hexanoic anhydride (856 μ l, 4mmol) and Et₃N (577 μ l, 4 mmol) were added into reaction mixture, let it stir for 4 h. The reaction was filtered and the filtrate was collected and extracted by 50 ml ethyl acetate with saturated NaHCO₃ (100 ml \times 2). The organic layer was dried over Na₂SO₄, then concentrated in *vacuo* to afford oily product. Purification *via* flash chromatography on silica gel (100% hexanes to 25% ethyl acetate in hexanes) afforded 300mg white powder (0.7 mmol, 42% overall yield for two steps). ¹H-NMR (400 MHz, CDCl₃): 10.48 (1H, s), 8.43 (1H, d), 7.06 (1H, d), 7.01 (1H, s), 6.15 (1H, s), 3.43 (2H, m), 3.12 (4H, t), 2.37 (2H, t), 1.75 (8H, m), 1.60 (5H, m), 1.36 (12H, s), 0.91 (6H, t). HRMS m/z calculated for C₂₄H₄₀N₃O₂ (M+H)⁺, 402.3115, found 402.3126 (M+H)⁺.

Cyclic voltammetry. The electrochemical measurements were conducted using Reference 600TM Potentiostat/Galvanostat/ZRA (Gamry Instruments, PA, U.S.A.), equipped with a three-electrode cell. Glassy carbon electrode and platinum wire were used for working and counter electrodes, respectively. Saturated calomel electrode (Gamry Instruments) was used for a reference electrode. To prevent contamination, the reference electrode was brought in contact with the sample solutions via two salt bridges. To prevent drastic potential drops between the aqueous electrode media and the

chloroform solutions, the solution between the two salt bridges was 100 mM Tetrabutylammonium tetrafluoroborate (TBABF₄) in anhydrous acetonitrile. When not in use, the reference electrode is stored submerged in saturated potassium chloride solution. (Ag/AgCl electrode was also sometimes used for a reference electrode) For all samples, the sample concentration was 3 mM. For each sample, the solution was purged with pure argon or nitrogen gas for 30 min and at least five scans were recorded at 100 mV / s scan rate.³³⁻³⁵

UV/visible absorption and fluorescence emission spectroscopy. Steady-state UV/visible absorption spectra were recorded in a transmission mode recorded using a JASCO V-670 spectrophotometer (Tokyo, Japan). Steady-state and time-resolved emission measurements were conducted using a spectrofluorometer with double-grating monochromators and a TBX single-photon-counting detector.³⁶ For steady-state emission measurement, by adjusting the slit widths, the signal at all wavelengths was kept under 10⁶ CPS to assure that it is within the linear range of the detector. For time-resolved emission measurements, a NanoLED was used for an excitation source ($\lambda_{\text{ex}} = 406$ nm; half-height pulse width, $W_{1/2} = 1$ ns). For recording the profile of the excitation pulse (i.e., the instrument response function), we used bovine serum albumin in deionized water as a scatterer, setting $\lambda_{\text{em}} = \lambda_{\text{ex}} = 406$ nm. The fluorescence decays of electret and dimers were recorded at electret's emission maxima, $\lambda_{\text{em}} = 460$ nm.

Transient absorption spectroscopy. The transient-absorption spectra were recorded in transmission mode using a Helios pump-probe spectrometer (Ultrafast Systems, LLC, Florida) equipped with a delay stage allowing maximum probe delays of 3.2 ns at 7 fs

temporal step resolution, and whit white-light generators providing UV/visible spectral range from 350 to 800 nm.

The laser source for the Helios was a SpitFire Pro 35F regenerative amplifier yielding (Spectra Physics / Newport) generating 800-nm pulses (38 fs, 3.5 mJ, 55 nm bandwidth) 1 kHz. The amplifier was pumped with an Empower 30 Q-switched laser ran at 20 W and a MaiTai SP oscillator provided the seed beam.

For the pump, 500 mW of the amplifier output was sent into an optical parametric amplifier, OPA-800CU (Newport), equipped with a signal second and forth harmonic generators. The signal was tuned at 1,600 nm and the output of 400 nm was sent to the Helios spectrometer, passed through a chopper (cutting every other pump pulse) and converged on the sample surface (about 2 mm beam diameter). For the probe, 10 mW of the amplifier output were reflected several meters back and forth over the table (to compensate for the pump delay in the OPA), and introduced into the Helios, passed through the delay stage, the white-light generator and focused on the sample surfaces to be completely overlapped by the pump beam.

Samples in solvents were freshly prepared and completely purged with Argon gas before measurement. The optical length was 2 mm and a stir bar was used for stirring measuring samples to prevent photo bleaching during process. For charge transfer studies, excitation wavelength was set at $\lambda_{\text{ex}} = 385$ nm, which only excited electron donor. From recorded Raman-scattering repose of non-coated cover slips, the transient absorption spectra for the stacked samples were corrected for the pulse chirp using Surface Xplorer

(Ultrafast Systems, LLC). The transient kinetics was analyzed using Surface Explorer and Igor Pro.

Dielectric measurements. We followed procedures as described previously to calculate the dielectric values.³⁷ Three-terminal capacitance sample cell connected to an ultrahigh precision Wheatstone bridge, incorporated into a precision meter via connecting cables with up to of 4-m length were used to collect capacitance data. The three-terminal sample cell electrodes were separated to 400 μm , and filled with 1.5mL of freshly prepared sample solution. The capacitance measurements were carried at frequencies ranging from 10^4 Hz to 10^6 Hz. The capacitance of the neat solvent and of air was measured in an empty dry cell as controls.³⁷

The experimentally determined dielectric values presented in the tables and figures correspond to averages of at least five repeats, where the error bars represent plus/minus one standard deviation.

Density measurements. The densities of freshly prepared electret and 1-methylpyrene for chloroform solutions were measured with a calibrated portable density meter, recorded at 21 °C (± 0.5 °C). Before and after each measurement, the densitometer was washed several times with neat solvent, nitrogen dried, and washed with the corresponding sample solution.

Data analysis. The values for the peak maxima (and minima) from the cyclic voltammograms and from the fluorescence spectra were obtained by fitting the region around the maxima (or the minima) to a Gaussian function. The quality of the fits was monitored by examination of the residuals. All least-square data fits of fluorescence

spectra were conducted using Igor Pro, v. 6 (Wavemetrics, Inc.) on MacOS and Windows XP workstations.

References

- (1) Galoppini, E.; Fox, M. A. *Journal of the American Chemical Society* **1996**, *118*, 2299-2300.
- (2) Yasutomi, S.; Morita, T.; Imanishi, Y.; Kimura, S. *Science* **2004**, *304*, 1944-1947.
- (3) Gergel-Hackett, N.; Aguilar, I.; Richter, C. A. *Journal of Physical Chemistry C* **2010**, *114*, 21708-21714.
- (4) Albero, J.; Martinez-Ferrero, E.; Iacopino, D.; Vidal-Ferran, A.; Palomares, E. *Physical Chemistry Chemical Physics* **2010**, *12*, 13047-13051.
- (5) Gao, J. A.; Muller, P.; Wang, M.; Eckhardt, S.; Lauz, M.; Fromm, K. M.; Giese, B. *Angewandte Chemie-International Edition* **2011**, *50*, 1926-1930.
- (6) Wang, Y. F.; Li, Y.; Zhou, Z. J.; Li, Z. R.; Wu, D.; Huang, J. G.; Gu, F. L. *Chemphyschem* **2012**, *13*, 756-761.
- (7) Fox, M. A.; Galoppini, E. *Journal of the American Chemical Society* **1997**, *119*, 5277-5285.
- (8) Knorr, A.; Galoppini, E.; Fox, M. A. *Journal of Physical Organic Chemistry* **1997**, *10*, 484-498.
- (9) Morita, T.; Kimura, S.; Kobayashi, S.; Imanishi, Y. *Journal of the American Chemical Society* **2000**, *122*, 2850-2859.
- (10) Kise, K. J.; Bowler, B. E. *Inorganic Chemistry* **2003**, *42*, 3891-3897.
- (11) Mandal, H. S.; Kraatz, H. B. *Chemical Physics* **2006**, *326*, 246-251.
- (12) Kapetanaki, S. M.; Ramsey, M.; Gindt, Y. M.; Schelvis, J. P. M. *Journal of the American Chemical Society* **2004**, *126*, 6214-6215.
- (13) Giese, B.; Wang, M.; Gao, J.; Stoltz, M.; Muller, P.; Graber, M. *Journal of Organic Chemistry* **2009**, *74*, 3621-3625.
- (14) Chaudhry, B. R.; Wilton-Ely, J. D. E. T.; Tabor, A. B.; Caruana, D. J. *Physical Chemistry Chemical Physics* **2010**, *12*, 9996-9998.
- (15) Gray, H. B.; Winkler, J. R. *Quarterly Reviews of Biophysics* **2003**, *36*, 341-372.

- (16) Gray, H. B.; Winkler, J. R. *Proc. Natl. Acad. Sci. U. S. A.* **2005**, *102*, 3534-3539.
- (17) Shih, C.; Museth, A. K.; Abrahamsson, M.; Blanco-Rodriguez, A. M.; Di Bilio, A. J.; Sudhamsu, J.; Crane, B. R.; Ronayne, K. L.; Towrie, M.; Vlcek, A., Jr.; Richards, J. H.; Winkler, J. R.; Gray, H. B. *Science* **2008**, *320*, 1760-1762.
- (18) Wittekindt, C.; Schwarz, M.; Friedrich, T.; Koslowski, T. *J. Am. Chem. Soc.* **2009**, *131*, 8134-8140.
- (19) Ashraf, M. K.; Pandey, R. R.; Lake, R. K.; Millare, B.; Gerasimenko, A. A.; Bao, D.; Vullev, V. I. *Biotechnol. Prog.* **2009**, *25*, 915-922.
- (20) Vullev, V. I. *J. Phys. Chem. Lett.* **2011**, *2*, 503-508.
- (21) Sessler, G. M. *Topics in Applied Physics* **1980**, *33*, 13-80.
- (22) Gerhard-Multhaupt, R.; Gross, B.; Sessler, G. M. *Topics in Applied Physics* **1987**, *33*, 383-431.
- (23) Bauer, S.; Bauer-Gogonea, S.; Dansachmuller, M.; Graz, I.; Leonhartsberger, H.; Salhofer, H.; Schwoediauer, R. *Proceedings - IEEE Ultrasonics Symposium* **2003**, 370-376.
- (24) Goel, M. *Current Science* **2003**, *85*, 443-453.
- (25) Hamuro, Y.; Geib, S. J.; Hamilton, A. D. *Journal of the American Chemical Society* **1996**, *118*, 7529-7541.
- (26) Jiang, C.; Yang, L.; Wu, W.-T.; Guo, Q.-L.; You, Q.-D. *Bioorg. Med. Chem.* **2011**, *19*, 5612-5627.
- (27) Rehm, D.; Weller, A. *Israel Journal of Chemistry* **1970**, *8*, 259-271.
- (28) Verhoeven, J. W.; van Ramesdonk, H. J.; Groeneveld, M. M.; Benniston, A. C.; Harriman, A. *ChemPhysChem* **2005**, *6*, 2251-2260.
- (29) Braslavsky, S. E.; Acuna, A. U.; Adam, W.; Amat, F.; Armesto, D.; Atvars, T. D. Z.; Bard, A.; Bill, E.; Bjoern, L. O.; Bohne, C.; Bolton, J.; Bonneau, R.; Bouas-Laurent, H.; Braun, A. M.; Dale, R.; Dill, K.; Doepp, D.; Duerr, H.; Fox, M. A.; Gandolfi, T.; Grabowski, Z. R.; Griesbeck, A.; Kutateladze, A.; Litter, M.; Lorimer, J.; Mattay, J.; Michl, J.; Miller, R. J. D.; Moggi, L.; Monti, S.; Nonell, S.; Ogilby, P.; Olbrich, G.; Oliveros, E.; Olivucci, M.; Orellana, G.; Prokorenko, V.; Naqvi, K. R.; Rettig, W.; Rizzi, A.; Rossi, R. A.; San Roman, E.; Scandola, F.; Schneider, S.; Thulstrup, E. W.; Valeur,

- B.; Verhoeven, J.; Warman, J.; Weiss, R.; Wirz, J.; Zachariasse, K. *Pure and Applied Chemistry* **2007**, *79*, 293-465.
- (30) Getoff, N.; Solar, S.; Richter, U. B.; Haenel, M. W. *Radiation Physics and Chemistry* **2003**, *66*, 207-214.
- (31) Zhang, G. H.; Thomas, J. K. *Journal of Physical Chemistry* **1994**, *98*, 11714-11718.
- (32) Wu, J.; Becerril, J.; Lian, Y. J.; Davies, H. M. L.; Porco, J. A.; Panek, J. S. *Angewandte Chemie-International Edition* **2011**, *50*, 5938-5942.
- (33) Jones, G., II; Vullev, V. I. *Org. Lett.* **2002**, *4*, 4001-4004.
- (34) Vullev, V. I.; Jones, G. *Tetrahedron Lett.* **2002**, *43*, 8611-8615.
- (35) Bao, D.; Millare, B.; Xia, W.; Steyer, B. G.; Gerasimenko, A. A.; Ferreira, A.; Contreras, A.; Vullev, V. I. *J. Phys. Chem. A* **2009**, *113*, 1259-1267.
- (36) Xia, B.; Upadhyayula, S.; Nuñez, V.; Landsman, P.; Lam, S.; Malik, H.; Gupta, S.; Sarshar, M.; Hu, J.; Anvari, B.; Jones, G.; Vullev, V. I. *J. Clin. Microbiol.* **2011**, *49*, 2966-2975.
- (37) Upadhyayula, S.; Bao, D.; Millare, B.; Sylvia, S. S.; Habib, K. M. M.; Ashraf, K.; Ferreira, A.; Bishop, S.; Bonderer, R.; Baqai, S.; Jing, X.; Penchev, M.; Ozkan, M.; Ozkan, C. S.; Lake, R. K.; Vullev, V. I. *J. Phys. Chem. B* **2011**, *115*, 9473-9490.

Tables

Table A1-1. Dielectric constants of electrolyte TBABF₄ with various concentrations in THF.

C_{TBABF₄} in THF (mM)	v_{max} x 10⁻³ (cm⁻¹)	ε
0	19.54 ± 0.006	7.54
100	19.43 ± 0.006	11.88
200	19.32 ± 0.005	16.67
300	19.26 ± 0.007	19.26
400	19.22 ± 0.007	20.80
500	19.19 ± 0.004	22.26

Table A1-2. Values for each terms needed for ΔG_{et} calculations.

Redox Moieties	$E_{\text{ox}}^{1/2}$ (V vs SCE)	$E_{\text{red}}^{1/2}$ (V vs SCE)	E_{00} (eV)	R_{eff} (Å)	R_{DA} (Å)
Electron Donor: Aa	0.97 in neat DCM		3.04	2.60	
Electron Acceptor: MePy		-2.30 in neat THF		3.09	10.0

Table A1-3. Estimated Photoinduced Charge-transfer Driving Forces, $\Delta G_{et}^{(0)}$, and the Corresponding Born Correction and Columbic Terms, ΔG_s and W , respectively.

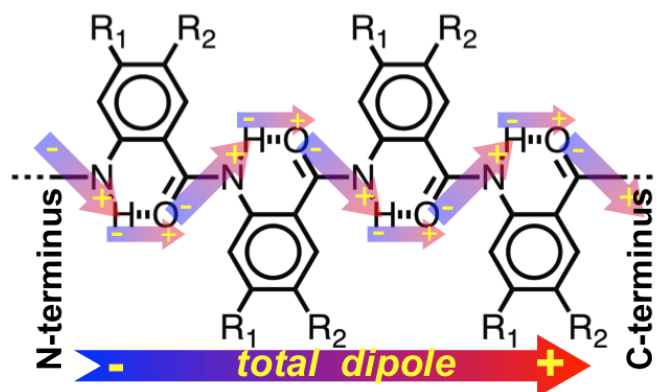
Terms	DCM ($\epsilon = 8.93$)	MeCN ($\epsilon = 36.6$)
Borns term, ΔG_s (eV)	-0.05	-0.48
Columbic term, W (eV)	-0.28	-0.07
Driving force, $\Delta G_{et}^{(0)}$ (eV)	-0.10	-0.32

Table A1-4. Charge separation, $k_{CS} \times 10^9 / \text{s}^{-1}$, and charge-recombination, $k_{CR} \times 10^9 / \text{s}^{-1}$, rate constants for Py-Aa and Aa-Py obtained from transient-absorption data for different solvents.

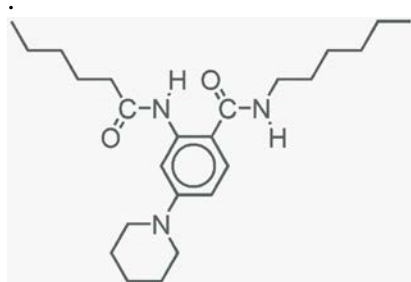
solvent	Py-Aa		Aa-Py	
	k_{CS}	k_{CR}	k_{CS}	k_{CS}
CH ₂ Cl ₂	3.6	0.98	16	0.29
CH ₂ Cl ₂ +0.2M (C ₄ H ₉) ₄ NBF ₄	2.8	0.94	7.5	0.29
CH ₃ CN	60	4.1	90	1.8

Schemes

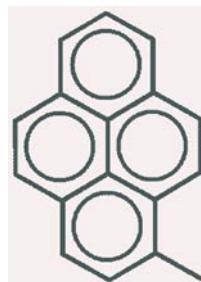
Scheme A1-1. Design of bioinspired electrets. Anthranilamides and the origin of their intrinsic electric dipole moment from: (1) the ordered orientation of the amide bonds; and (2) the shift in the electron density from H to O upon hydrogen-bond formation.



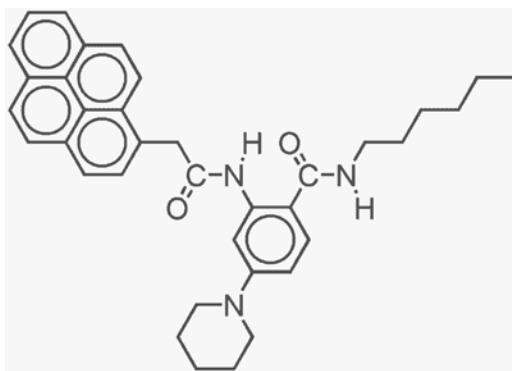
Scheme A1-2. Charge transfer system built on dimer of anthranilamides and 1-methylpyrene.



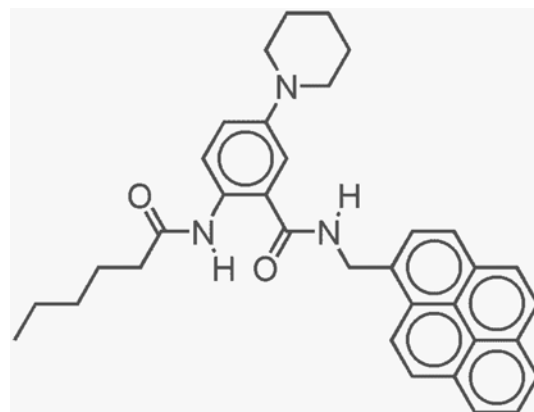
2-hexanamino-*N*-hexyl-5-(piperidin-1-yl)benzamide (Aa)



1-Methylpyrene (MePy)

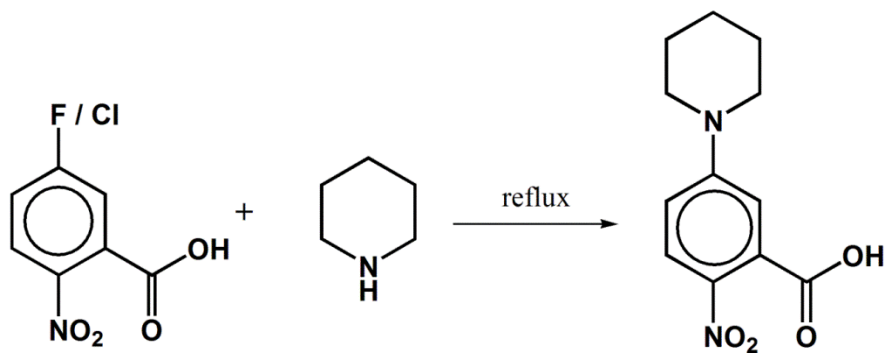


N-hexyl-5-(piperidin-1-yl)-2-[2-(pyren-1-yl)acetamido]benzamide (Py-Aa)

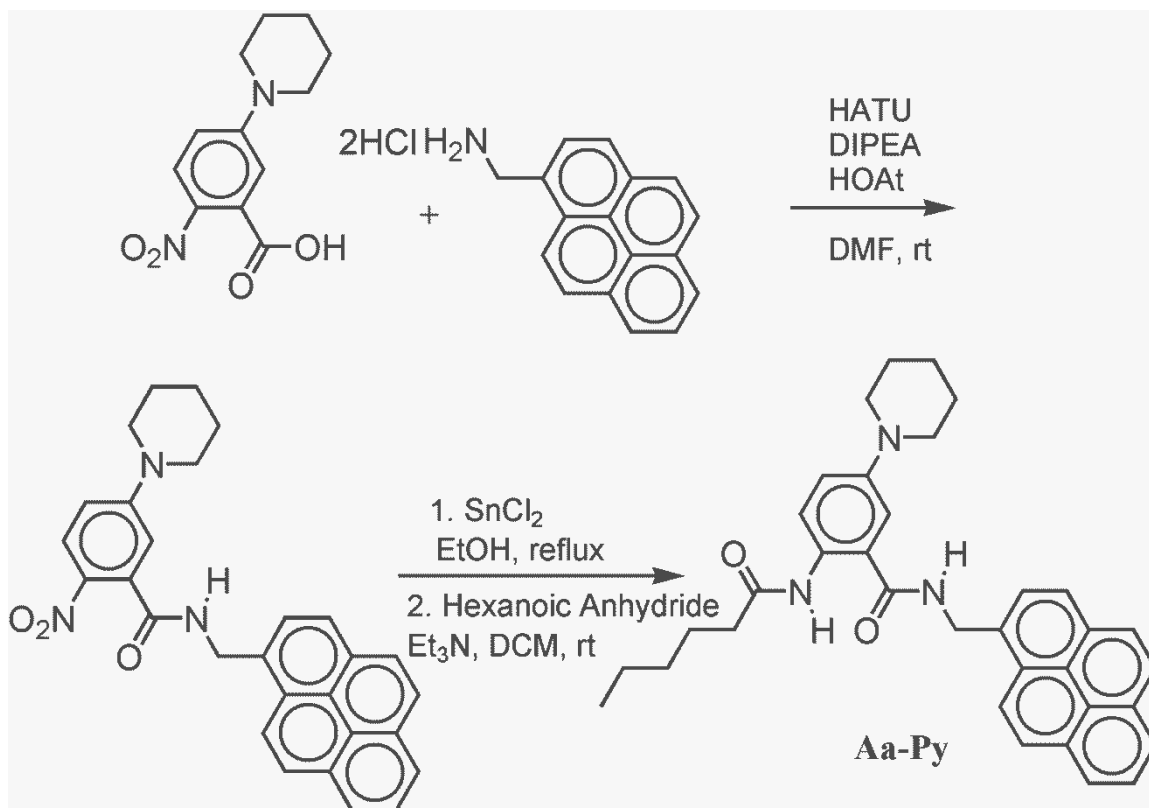


2-hexanamino-5-(piperidin-1-yl)-*N*-(pyren-1-ylmethyl)benzamide (Aa-Py)

Scheme A1-3. Synthesis procedure of 5- piperidin-1-yl- 2-nitrobenzoic acid.

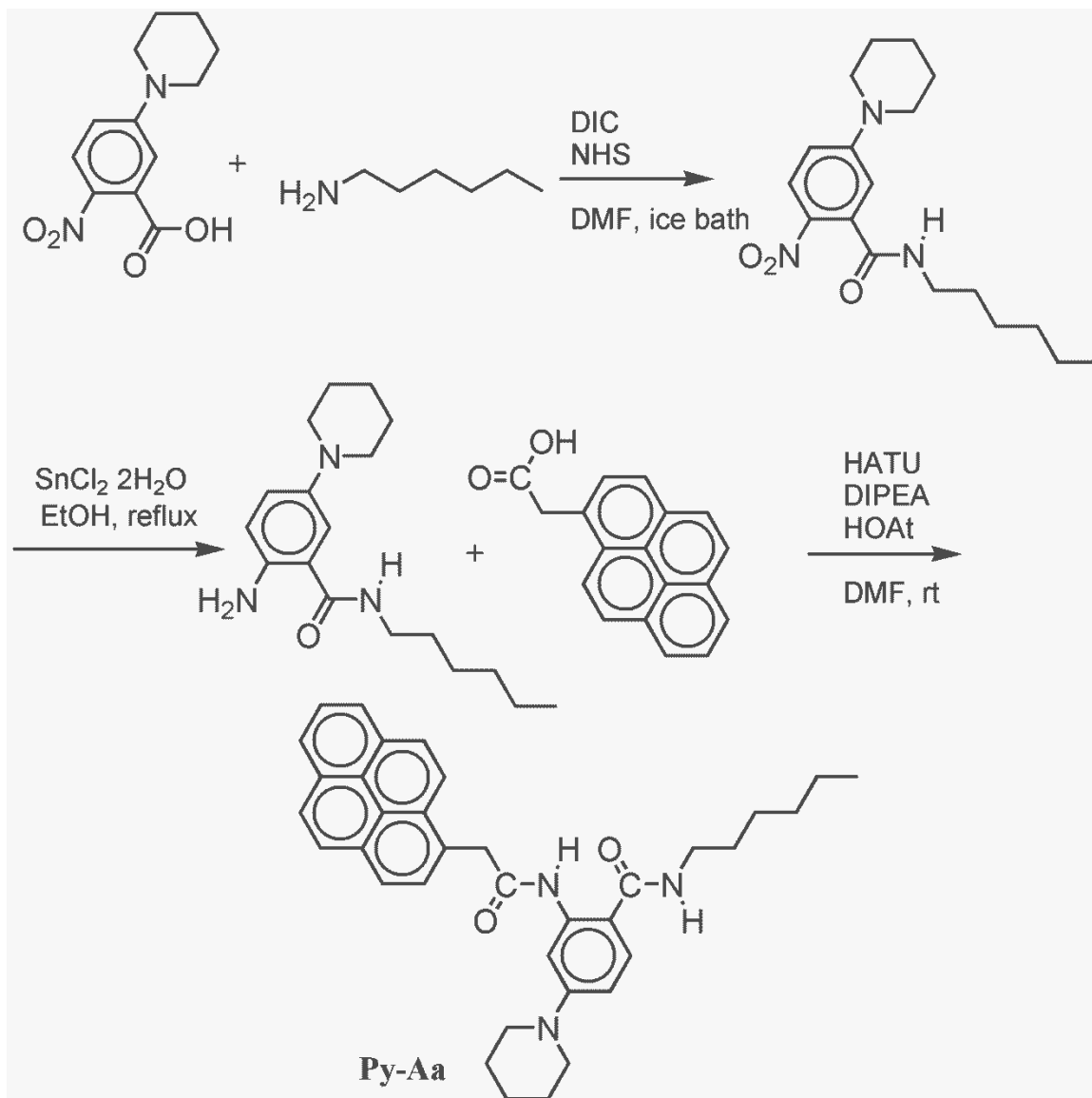


Scheme A1-4. Synthesis procedure of electron donor-acceptor conjugate: 2-hexanamino-5-(piperidin-1-yl)-*N*-(pyren-1-ylmethyl)benzamide (Aa-Py).

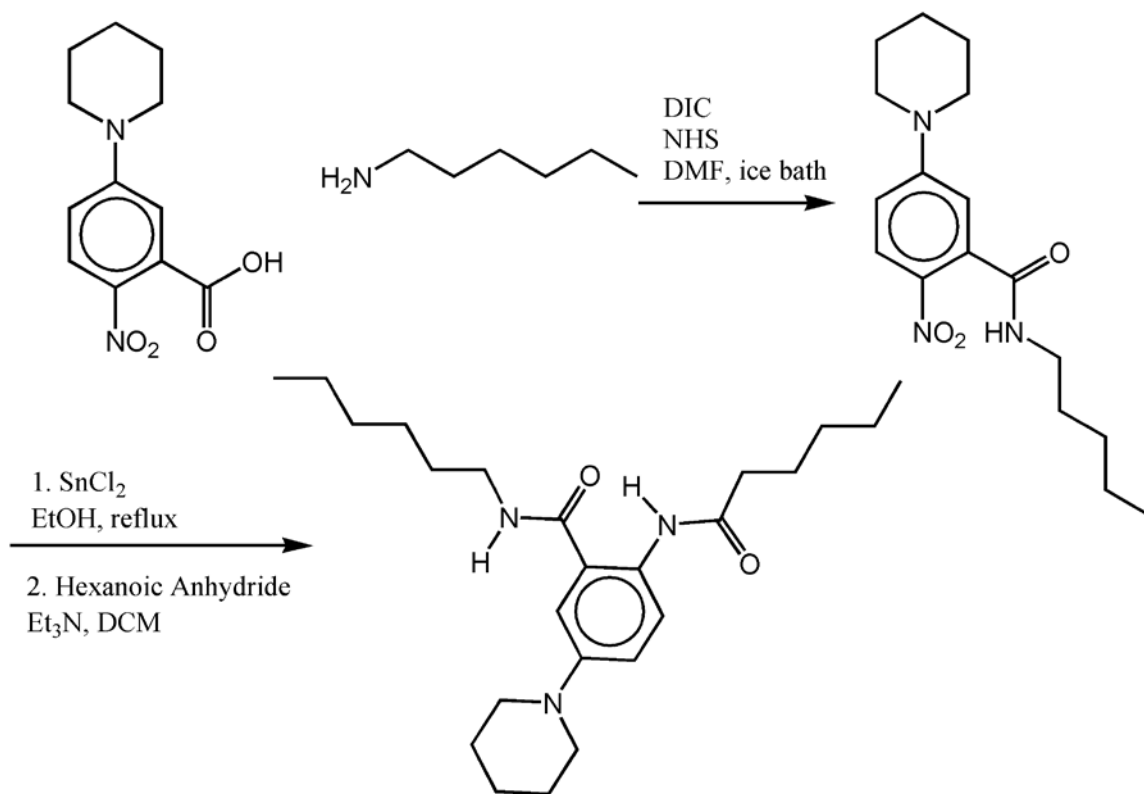


HATU: *N*-[(Dimethylamino)-1*H*-1,2,3-triazolo-[4,5-*b*]pyridin-1-ylmethylene]-*N*-methylmethanaminium hexafluorophosphate *N*-oxide; HoAt: 2-Chloro-1,3-dimethylimidazolidinium hexafluorophosphate; DIPEA: *N,N*-Diisopropylethylamine

Scheme A1-5. Synthesis procedure of electron donor-acceptor conjugate: *N*-hexyl-5-(piperidin-1-yl)-2-[2-(pyren-1-yl)acetamino]benzamide (Py-Aa).



Scheme A1-6. Synthesis procedure of 2-hexanamino-*N*-hexyl-5-(piperidin-1-yl)benzamide (Aa).



DIC: *N, N'*- Diisopropylcarbodiimide; NHS: *N*-Hydroxysuccinimide; SnCl_2 : Tin(II) chloride; Et_3N : triethylamine

Figures

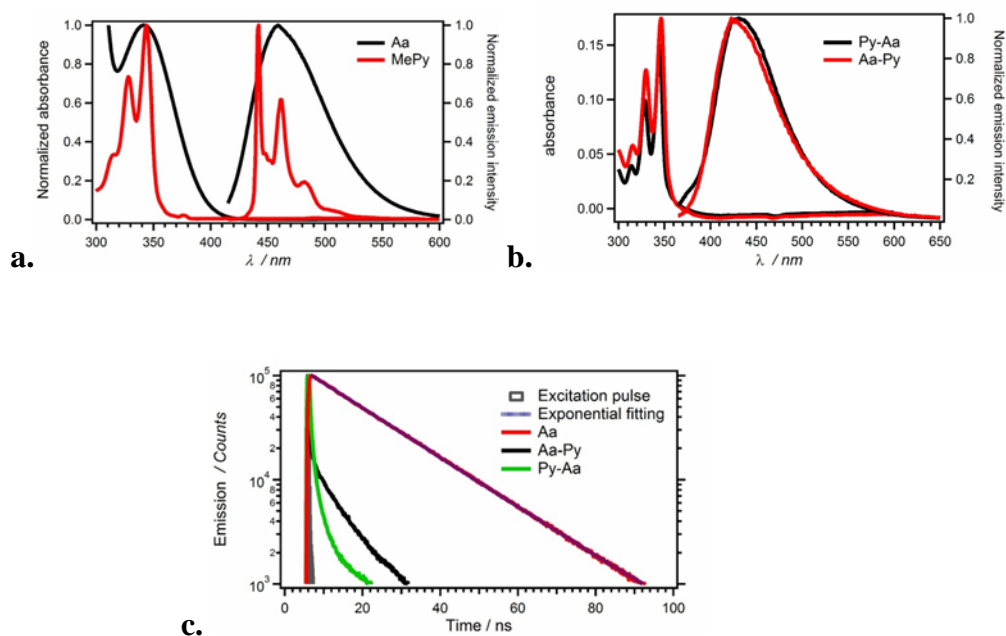


Figure A1-1. Absorption and fluorescence emission spectra of charge transfer systems. **(a, b).** Normalized absorption and emission spectra of Aa ($\lambda_{\text{ex}} = 405\text{nm}$), MePy ($\lambda_{\text{ex}} = 340\text{nm}$), and Aa-Py, ($\lambda_{\text{ex}} = 405\text{nm}$) in CH₂Cl₂. **(c).** Fluorescence decay of Aa, Py-Aa, and Aa-Py in CH₂Cl₂. For lifetime of Aa, $\tau = 18.2 \pm 0.1 \text{ ns}$. For Py-Aa, and Aa-Py the decays are close to excitation pulse.

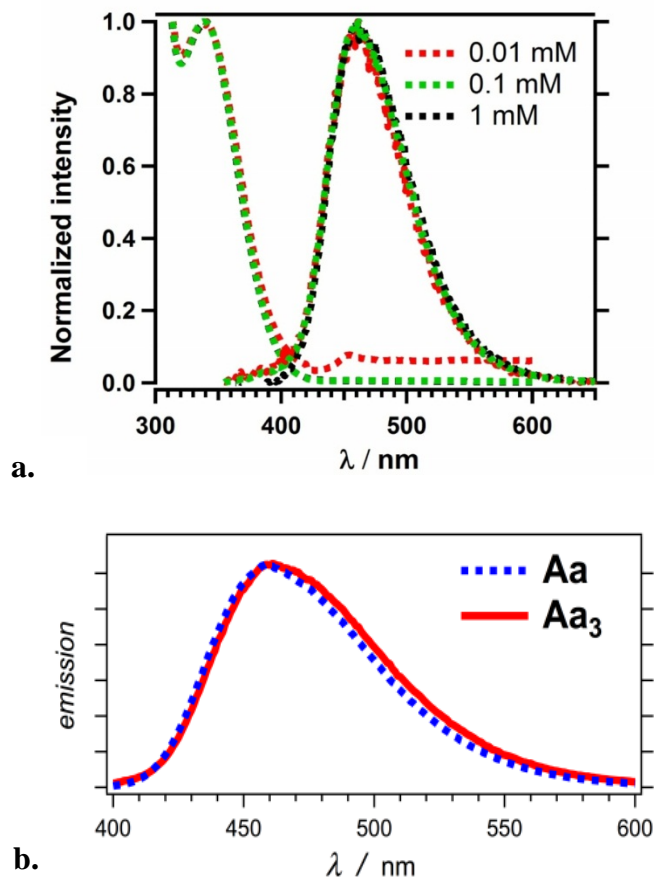


Figure A2-2. Photophysical properties of Aa. **(a).** The aggregation study of electret in chloroform with 1 mM, 0.1 mM and 0.01 mM concentrations. From absorption and emission spectra, we can calculate the zero-to-zero energy, $E_{00} = 3.04$ eV. **(b).** Normalized emission spectra of Aa and Aa₃ (50 μ M in CH₂Cl₂, $\lambda_{\text{ex}} = 350$ nm).

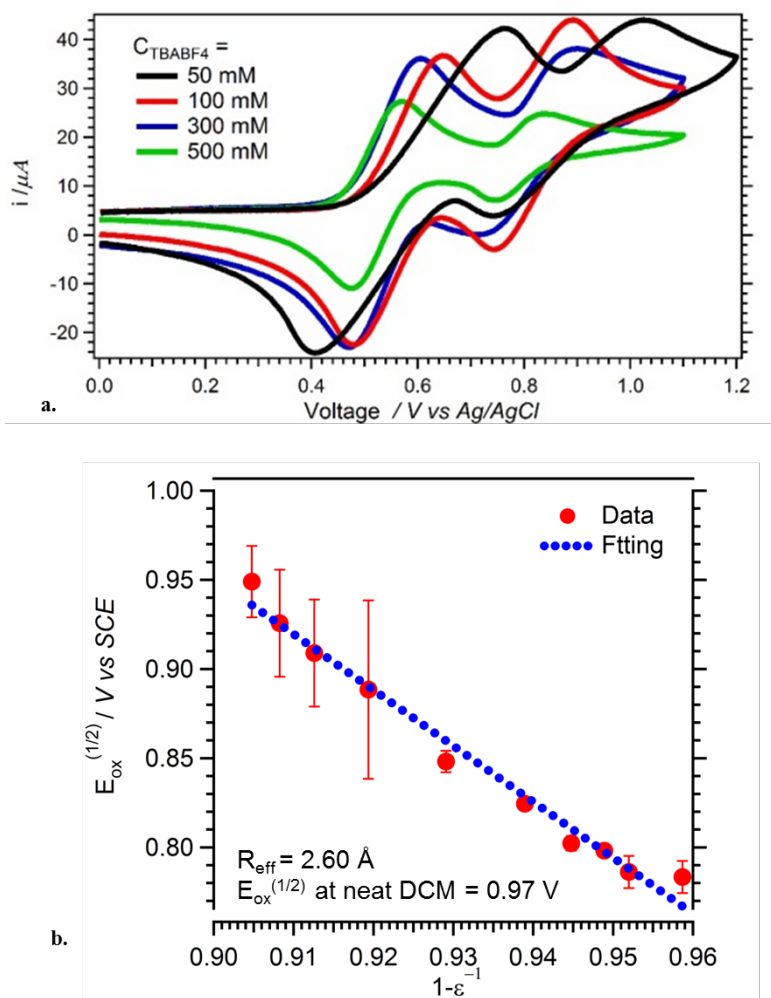


Figure A1-3. Calculations of half-wave oxidation potential of Aa for neat DCM and effective radius of Aa. (a) Cyclic voltammograms of Aa (3 mM) in the presence of various concentrations of the supporting electrolyte, TBABF₄, in DCM. (Scan rate = 100 mV/s). (b) Dependence of Aa half-wave oxidation potentials on the inverted dielectric constant of the electrolyte media. The dotted lines represent least-squares linear fits with the following correlation coefficients, $R=0.99$. By employing equation x, we can calculated reduction potential at neat solvent and effective radius.

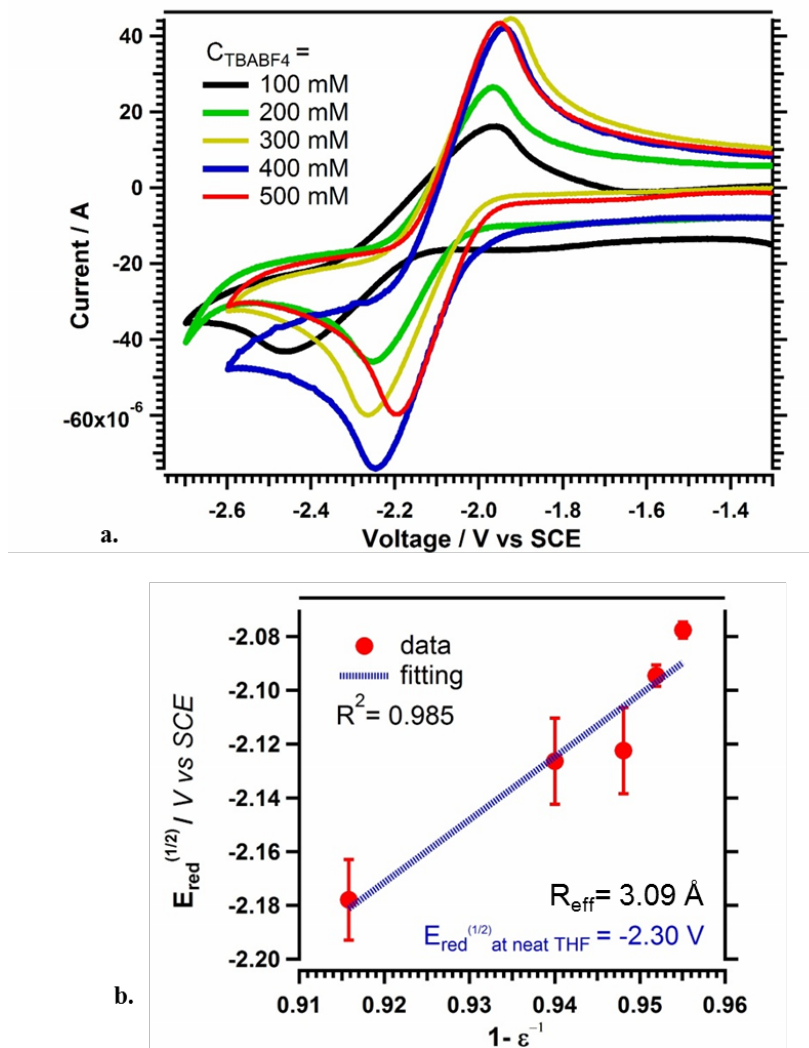


Figure A1-4. Calculations of half-wave reduction potential of 1-Methylpyrene (MePy) for neat THF and effective radius of MePy. **(a)** Cyclic voltammograms of 1-Methylpyrene (3 mM) in the presence of various concentrations of the supporting electrolyte, TBABF₄, in THF. (Scan rate = 100 mV/s). **(b)** Dependence of MePy half-wave reduction potentials on the inverted dielectric constant of the electrolyte media. The dotted lines represent least-squares linear fits with the following correlation coefficients, $R=0.985$.

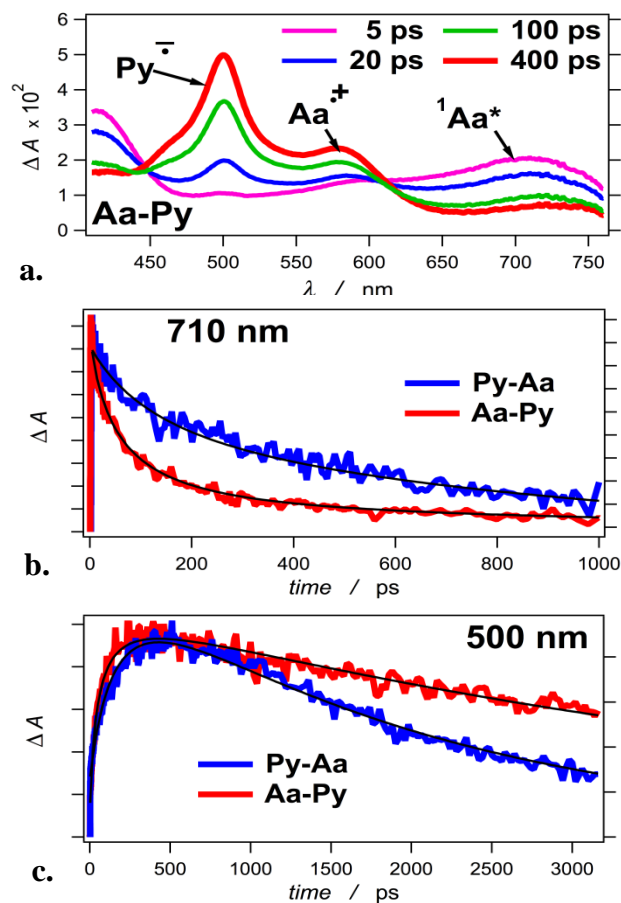


Figure A1-5. Transient absorption (TA) dynamics of Aa-Py and Py-Aa in CH_2Cl_2 : (a) TA spectra of Aa-Py; (b) decays of $^1\text{Aa}^*$, recorded at 710 nm; (c) rise and decays of $\text{Py}^{\bullet-}$, recorded at 500 nm. ($\lambda_{ex} = 390$ nm; 40 fs pulse)

Appendix 2.

Print-and-Peel Fabrication of Microelectrodes

Abstract

We describe a facile and expedient approach for fabrication of arrays of microelectrodes on smooth substrates. A sequence of print-and-peel procedures allowed for microfabrication of impedance-spectroscopy microsensors using office equipment and relatively simple wet chemistry. Microfluidic assemblies with reversibly adhered elastomer components allowed for transferring patterns of metallic silver, deposited via Tollen's reaction, onto the substrate surfaces. Electroplating of the silver patterns afforded an array of micrometer-thick copper electrodes. Capacitance sensors were assembled by placing nonlithographically fabricated flow chambers over the microelectrode arrays. Triangular waveform impedance measurements showed a linear response of these print-and-peel fabricated devices to the dielectric constant of the samples injected in their flow chambers.

Keywords: nonlithographic, impedance spectroscopy, triangular waveform, capacitance, dielectric.

Introduction

This letter describes a facile approach for fabrication of arrays of microelectrodes on smooth substrates. Microfluidic assemblies with reversibly adhered components allow for transferring patterns of conducting materials onto the substrate surface. Using this microfabrication approach, we prepared capacitance sensors and characterized their performance.

Nonlithographic, or “*print-and-peel*” (PAP), fabrication allows for facile and expedient prototyping of microfluidic devices.¹⁻³ Unlike other fabrication techniques, PAP consists of direct printing of the masters, using regular office equipment, and attaching three dimensional (3D) elements to their surfaces.¹ Due to its simplicity and low cost, PAP offers valuable venues for research and development in environment where microfabrication facilities are not readily available.

Impedance spectroscopy (IS) is an invaluable analytical tool for investigating a broad variety of systems, such as complex liquids and biological samples.⁴⁻⁶ Electric interfaces are essential for microfluidic IS devices. A range of techniques, such as photolithography,⁷ sputtering⁸ and microtransfer printing⁹ are employed for fabrication of microelectrodes for IS sensors. These fabrication methods, however, require specialized equipment and/or clean-room environment.

Research and Results

Herein, we demonstrate the utilization of PAP for microfabrication of IS sensors using an office printer and relatively simple wet chemistry. Direct printing of the computer-aided-design (CAD) pattern of microelectrodes to a polyester transparency film produced

a master, to which we attached three-dimensional elements for the inlet and outlet channels (Scheme A2-1,*i*). For microchannels with improved contour smoothness, we utilized a solid-ink printer, instead of LaserJets, which we previously used for PAP fabrication of microfluidic devices.¹ Casting polydimethylsiloxane (PDMS) over the master (Scheme A2-1,*ii*) produced elastomer components with negative-relief imprints (Scheme A2-1,*iii*). Reversible adhesion of the PDMS components to glass surfaces formed microfluidic assemblies (Scheme A2-1,*iv*). Aqueous solutions of a reducing agent, dextrose, and silver ions, consequently flown through the microchannels, resulted in deposition of silver metal onto the channel walls. To assure continuous coverage with conductive material, the procedure of passing Ag^+ solution through microchannels pre-wet with dextrose mixture was repeated 3-5 times (Figure A2-1a).

Detachment of the PDMS components left patterns of electro-conducting silver layers on the glass surfaces (Scheme A2-1,*v*, Figure A2-1a). The silver patterns, however, were rough and prone to mechanical scratching (Figure A2-1c). Therefore, using electroplating, we deposited $\sim 10 \mu\text{m}$ thick copper layers over the silver patterns, producing microelectrodes with improved mechanical stability (Scheme A2-1,*vi*, Figure A2-1b, c).

In the middle of the generated patterns, the copper strips formed arrays of five parallel electrodes, which we utilized for impedance measurements. Electrical connections between every other electrode resulted in a “multilayer” capacitor, the characteristics of which were dependent on the dielectric properties of the surrounding media.

Placing water and other electroconductive samples directly on the electrodes resulted in considerable contribution from the resistance to the measured impedance. To prevent direct electrical contact between the microelectrodes and the samples, we coated the electrode arrays with $70 (\pm 10)$ μm PDMS layers (Scheme A2-1,*vii*). Over the coated electrodes we placed PDMS flow chambers, fabricated using PAP techniques (Scheme A2-1,*viii*). We prepared capacitance flow cells with 1 and 1.5 mm center-to-center electrode separation that corresponds, respectively, to about 450 and 950 μm separation between the edges of neighboring electrodes.

We modeled each cell as two capacitors connected in parallel with total capacitance, $C = C_C + C_S = C_C + \alpha\varepsilon$. C_S accounts for capacitance resulting from the penetration of the electric field through the sample flow chamber. Hence, C_S is linearly dependent on the dielectric constant, ε , of the sample. C_C accounts for the capacitance of the rest of the device and remains constant. Using impedance spectroscopy, we determined that $C_C = 3.4$ and 0.34 pF for cells with 1 and 1.5 mm center-to-center electrode separation, respectively.

Triangular waveform (TW) dielectric measurements (i.e., application of TW voltage bias to the capacitance cells) yield current signals that were superposition of two waves: (1) a triangular waveform resultant from the resistance component of the impedance; and (2) a rectangular waveform (RW) resultant from the capacitance component of the impedance.^{10,11} The height, h , of RW is expected to be linearly proportional to the capacitance, C , of the cell, and hence, to the dielectric constant, ε , of the sample. (The

height, h , represents peak-to-peak current difference: i.e., h is twice the value of the wave amplitude.)

Using TW technique, we characterized the performance of PAP fabricated capacitance sensors. Measurements of air, dimethyl sulfoxide (DMSO) and water (i.e., fluids that do not swell PDMS)¹² produced current waves that we deconvoluted into TW and RW components (Figure A2-2a, b). We observed a linear correlation between h and ε (Figure A2-2c), supporting the plausibility of the representation of the cells as two parallelly wired capacitors.

The described PAP technique offers a facile and inexpensive alternative for fabrication of components for electrical interfaces of microfluidic devices. In addition to silver and copper, the procedure can be readily expanded to utilize electroless deposition of other conducting and semi-conducting materials, followed by electroplating of a wide range of metals.

Experimental

Materials. Pre-polymer of PDMS (Sylgard 184 silicone elastomer base kit) was purchased from Dow Corning Corporation. Microscope glass slides (75×25×1mm) and polyethylene tubing (ID 0.38 mm, OD 1.09 mm) were purchased from Fisher Scientific. Polyethylene line cords (0.64 mm diameter) and hot glue were purchased from a hardware distributor. Transparency films for a solid-ink printer were obtained from Xerox. Silver nitrate and dextrose were purchased from Sigma-Aldrich. Potassium hydroxide, ammonium hydroxide, sulfuric acid and hydrochloric acid were obtained from Fisher Scientific.

Print-and-peel fabrication. The CAD patterns of the microelectrodes were created using Adobe Illustrator. Using a solid-ink printer (Xerox Phaser 8550), the designed patterns were printed on overhead transparency films to form positive-relief masters. Upon immobilization of the masters to the bottoms of polystyrene Petri dishes, three-dimensional (3D) elements (posts of polyethylene line cords for the inlet and outlet channels) were glued to the circles at the termini of the patterned lines (Scheme A2-1,*i*).

PDMS prepolymer was vigorously mixed with the curing agent for at least five minutes and degassed under vacuum. The resultant mixture was poured over the printed masters with the 3D posts attached to them (Scheme A2-1,*ii*) and allowed to cure for a few hours at 40 °C. The cured PDMS slabs were detached from the master and the posts were removed from the slabs. The elastomer microfluidic components were cut from the PDMS slabs and cleaned with adhesive tape (Scheme A2-1,*iii*). Tollen's reaction was used for generating silver patterns on glass surfaces.

A drop of aqueous solution of ammonium hydroxide (20%) was added to 1 mL aqueous solution of silver nitrate (0.10 M), resulting in the formation of a brown precipitate. Upon vigorous shaking the solution became clear. 0.5 mL aqueous solution of potassium hydroxide (0.80 M) was added to the silver nitrate mixture resulting in a dark brown precipitate. Ammonium hydroxide solution was added dropwise until the precipitate dissolved. (Excess of NH_3 should be avoided.)

For the silver deposition, a reducing reagent is required. For this purpose we prepared an aqueous solution of dextrose (0.25 M).

The surfaces of glass slides were cleaned and scratched with sand paper to increase the adhesion area for the silver. The surfaces of the PDMS microfluidic components (with the negative-relief patterns) were cleaned with an adhesion tape and without any further treatment, pressed against the glass surfaces resulting in reversible adhesion between the PDMS and the glass. The PDMS-glass assemblies were kept under vacuum at 60 °C for several hours prior to use (Scheme A2-1,*iv*).

Using a syringe pump (Harvard Apparatus Pico Plus), dextrose solution was flown through each channel at a rate of 1 $\mu\text{L}/\text{min}$. Immediately after the dextrose solution reached the outlets of the channels, the inlet tubing was disconnected. Tubing primed with the silver nitrate alkaline solution was connected to the same inlet. The silver nitrate solution was flown through the same channels (at rate of 1 $\mu\text{L}/\text{min}$) causing formation of dark depositions onto the channels walls. To assure the deposition of continuous silver layers, the procedure of consecutive runs of dextrose and silver nitrate solutions was repeated several times. At certain occasions, the PDMS components had to be detached from the glass slides and cleaned. The glass slides were rinsed with MilliQ water and blown dry with nitrogen. The PDMS components were cleaned with adhesive tape, realigned with the silver patterns and reversibly readhered to the glass slides for more dextrose/silver nitrate treatments. Repeating the silver-deposition procedure for about three to five times resulted in continuous and electroconducting patterns (Scheme A2-1,*v*). Misalignments during the readhesion of the PDMS component to the glass with partially deposited silver pattern, resulted in thin layers of silver along the edges of the patterned strips (Figure A2-1a).

For the copper electrodeposition, the silver patterns were connected to copper tape coated with silver paint to assure a good electrical connection. The copper tape was covered with nonconducting tape leaving only the silver patterns exposed. Each of the glass slides with exposed silver patterns, along with copper plates, were wedged into a plate holder (with the silver patterns facing the copper plates). The slides and the plates were immersed into a bath containing copper sulfate (0.25 M), sulfuric acid (0.015 M) and hydrochloric acid (0.0014 M). The silver patterns on the slides were wired as cathodes and the copper plates as anodes. The current was set based on the area of the silver patterns, exposed to the solution (11.25 mA/cm^2 at thickness deposition rate of 10 nm/s). When the electrodeposition was completed, the slides with the formed copper strips on them were taken out of the bath, washed with copious amounts of D.I. water and blow-dry with nitrogen.

The arrays of copper microelectrodes were covered with PDMS prepolymer (mixed with curing agent and degassed). The slides were immobilized vertically, allowing the extra prepolymer mixture to flow off their surfaces. Curing of the remaining prepolymer at 50 °C produced ~70- μm -thick PDMS coatings covering the copper microelectrodes (Scheme A2-1,vii). The thickness of the PDMS coatings was determined from profilometry measurements across edges of spots where we peeled off the polymer.

PDMS flow chambers were fabricated using PAP approach. Masters for elliptic chambers were prepared from hot glue. Polyethylene posts were placed at the opposite ends of the chamber for inlets and outlets. PDMS prepolymer (mixed with curing agent

and degassed) was cast over the chamber masters and allowed to cure under ambient conditions.

The PDMS-coated glass slides (with microelectrode arrays) and the rectangular elastomer slabs (with the chamber cavities imprinted onto their surfaces) were treated with oxygen plasma (40 mBar, 50 W RF power) for 40 seconds using a capacitively-coupled-discharge system (FEMTO, Diener Electronics). The elliptic chambers of the plasma treated elastomer slabs were aligned to span across the PDMS coated microelectrodes and the polymer surfaces were pressed against each other to form capacitance flow cells (Scheme A2-1,viii). To assure the permanent adhesion between the PDMS surfaces, the capacitance cell assemblies were kept at 120 °C under vacuum for about 12 hours.

Profilometry. A bench-top surface profilometer (Dektak 8, Veeco Systems), with 12.5- μm radius stylus, was employed for the analysis of the silver and copper deposition onto the glass substrates. Each of the electrode strip patterns was placed perpendicularly to the direction of movement of the stylus in order to obtain transverse measurements. Several 2-mm scans separated 0.5-1 mm along the strip were performed for each sample.

Impedance measurements. Impedance spectroscopy (using sinusoidal current/voltage, I/V , wave forms) allowed us to characterize the intrinsic capacitance, C_C , of the cells.

Triangular-waveform (TW) measurements were employed for measurements involving relatively polar samples. TW measurements allow for facile deconvolution of the capacitance component of the impedance from the current signal and hence, for fast

dielectric measurements.^{10,11} For the measurements, liquids that do not cause PDMS to swell were chosen.¹²

Impedance measurements were conducted using a Reference 600™ Potentiostat/Galvanostat/ ZRA (Gamry Instruments, PA, U.S.A.). The microelectrode capacitance cells were wired to the instrument through probes clipped to the copper tapes electrically connected to the electrodes.

Air and organic solvents (perfluoromethyldecalin, decamethyl-cyclopentasiloxane and DMSO) were injected in the flow chambers and the impedance spectra were recorded at frequency from 100 Hz to 1 MHz.

The values for the capacitance were extracted from frequency regions, throughout which the measured phase was $-p/2$. (Negative-90-degree phase indicates that the capacitance is the principal component of the measured impedance. An increase in the solvent polarity or frequency resulted in change in the phase.) Linear fits of the measured capacitance vs. the dielectric constants of the samples, for each cell, yielded the intrinsic cell capacitance, C_C .

The voltage triangular waveform (10 MHz, 10 V) was supplied by a 30-MHz Synthesized wave function generator (DS345, Stanford Research Systems). The applied voltage bias and the current signal were measured using a 500-MHz digital oscilloscope (54616C, Hewlett Packard) connected to a PC via a GPIB interface. 1 MW termination, connected in parallel with the capacitance cell, was used for monitoring the voltage wave applied to the cell. 50 W termination, connected in sequence with cell (i.e., between the cell and the ground), was used for recording the signal from the current passing through

the capacitance cell. The voltage response signal (recorded with the oscilloscope) was divided by 50 W to yield the values for the current waves.

The recorded waves (current vs. time) for each sample measurement were fit to a function, composed of weighed sum of in-phase triangular and rectangular waveforms (TW and RW, respectively). The RW function was composed of sequential monoexponential decays and rises with identical time constants. The obtained time constants were orders-of-magnitude smaller than the inverted frequency (i.e., 10^{-5} s) resulting in rectangularly-appearing waveform (Figure A2- 2b). The pre-exponential parameters, obtained from the deconvolution data fits, were ascribed to the heights of the waves, h .

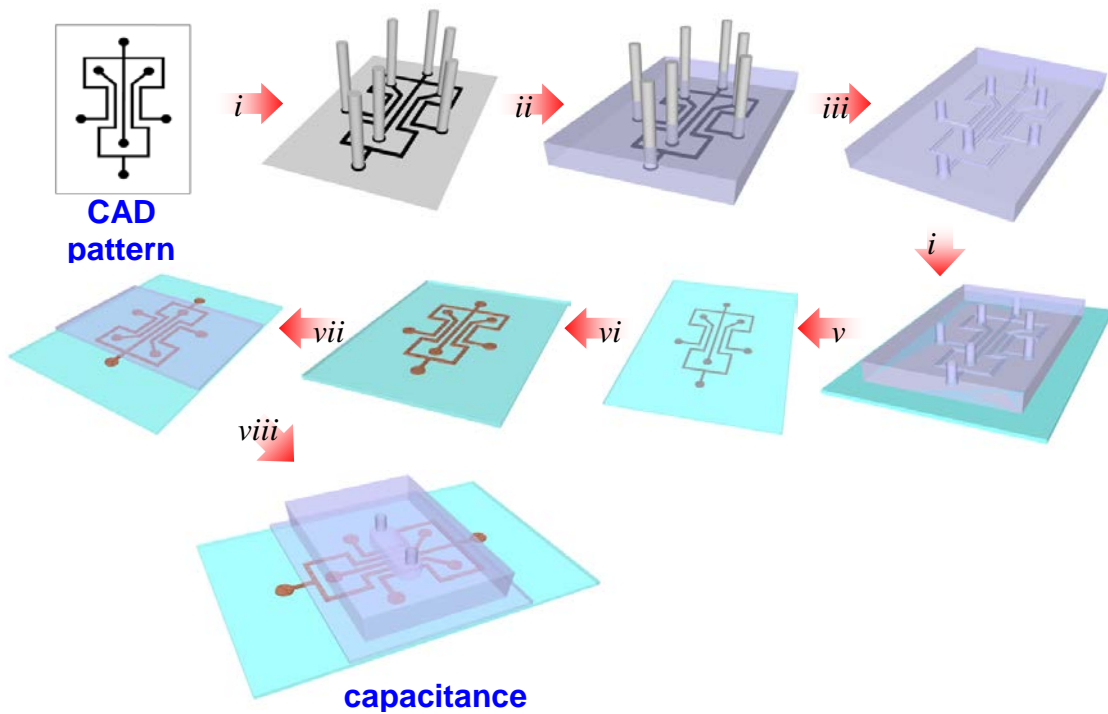
Acknowledgments. This work was funded by U.C. Energy Institute, NSF support for C.H. (REU) and U.S. Department of Education support for M.S.T. (GAANN).

References

- (1) Vullev, V. I.; Wan, J.; Heinrich, V.; Landsman, P.; Bower, P. E.; Xia, B.; Millare, B.; Jones, G., II *Journal of the American Chemical Society* **2006**, *128*, 16062-16072.
- (2) Grimes, A.; Breslauer, D. N.; Long, M.; Pegan, J.; Lee, L. P.; Khine, M. *Lab on a Chip* **2008**, *8*, 170-172.
- (3) Coltro, W. K. T.; Piccin, E.; Fracassi da Silva, J. A.; Lucio do Lago, C.; Carrilho, E. *Lab on a Chip* **2007**, *7*, 931-934.
- (4) Caduff, A.; Hirt, E.; Feldman, Y.; Ali, Z.; Heinemann, L. *Biosens Bioelectron* **2003**, *19*, 209-17.
- (5) Dolgin, M., Einziger, P. D. *Physical Review Letters* **2004**, *93*, 148101/1-148101/4.
- (6) Liu, Y.-S.; Walter, T. M.; Chang, W.-J.; Lim, K.-S.; Yang, L.; Lee, S. W.; Aronson, A.; Bashir, R. *Lab on a Chip* **2007**, *7*, 603-610.
- (7) Sun, T.; Holmes, D.; Gawad, S.; Green, N. G.; Morgan, H. *Lab Chip* **2007**, *7*, 1034-40.
- (8) Yang, M.; Lim, C. C.; Liao, R.; Zhang, X. *Biosensors & Bioelectronics* **2007**, *22*, 1688-1693.
- (9) Felmet, K.; Loo, Y.-L.; Sun, Y. *Applied Physics Letters* **2004**, *85*, 3316-3318.
- (10) Wu, J.; Stark, J. P. W. *Measurement Science and Technology* **2006**, *17*, 781-788.
- (11) Wu, J.; Stark, J. P. W. *Measurement Science and Technology* **2005**, *16*, 1234-1240.
- (12) Lee, J. N.; Park, C.; Whitesides, G. M. *Analytical Chemistry* **2003**, *75*, 6544-6554.

Scheme

Scheme A2-1. Print-and-peel fabrication of a capacitance cell.



i – master preparation;

ii – casting PDMS;

iii – curing of the PDMS “stamp”;

iv – reversible adhesion to glass;

v – consequential flows of aqueous solutions of dextrose and AgNO_3 ;

vi – electroplating with Cu;

vii – coating with PDMS;

viii – PDMS-to-PDMS permanent adhesion.

Figures

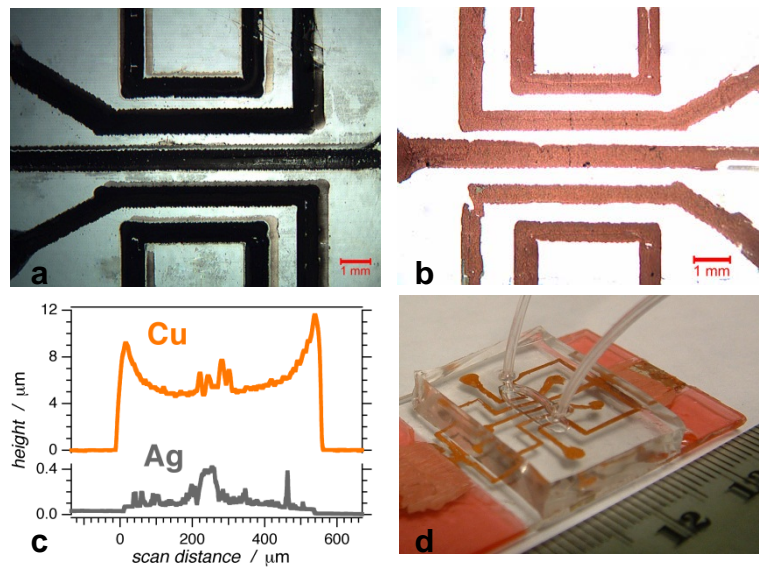


Figure A2-1. Print-and-peel fabricated capacitance cell. Reflection / transmission optical microscopy images of (a) silver and (b) copper electrode arrays. (c) Profilometry traces across silver (three consecutive dextrose/AgNO₃ treatments) and copper electrodes. (d) Photograph of a cell with 1.5 mm center-to-center electrode separation.

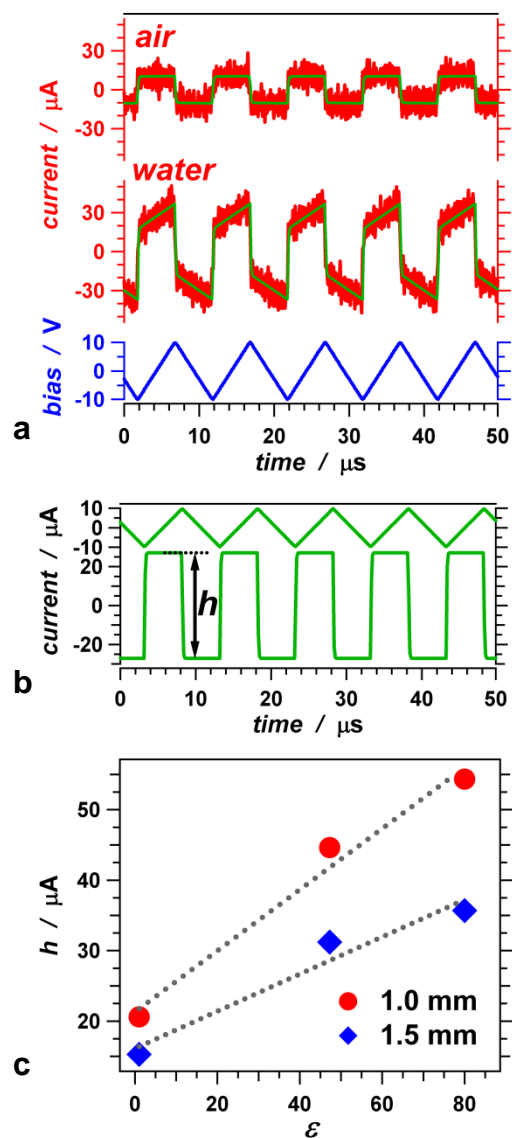


Figure A2-2. Triangular waveform (TW) impedance measurements. **(a)** Applied voltage (in blue) and current signals (in red) for air and water in a capacitance cell with 1 mm center-to-center electrode separation. The data fits are shown in green. **(b)** Deconvolution of the current signal for water (from b) into triangular and rectangular waves. **(c)** Linear correlation between the height of the rectangular current waveforms and the dielectric constant of the fluid (air, DMSO and water) in the sample chambers, measured with devices with 1 and 1.5 mm center-to-center electrode separation.